Bridging the Gap in Sustainable Continuous Chemicals Manufacture: Integrating Upstream Synthesis and Downstream Crystallisation

Scott, C. Daniel

Award date:
2020

Awarding institution:
University of Bath

Bridging the Gap in Sustainable Continuous Chemicals Manufacture: Integrating Upstream Synthesis and Downstream Crystallisation

submitted by

C. Daniel Scott

for the degree of Doctor of Philosophy

of the

University of Bath

Department of Chemistry

November 2019

Abstract

Continuous manufacturing (CM) is effective for sustainable chemical manufacture, but production of pharmaceuticals and fine chemicals requires complex, multi-step procedures often carried out in batch. Gaps in the CM supply chain, such as between upstream flow synthesis and downstream continuous crystallisation form a major bottleneck in the take-up of CM. The motivation for the research presented in this thesis was to demonstrate integrated CM of pharmaceuticals and multi-component complexes.

The oximation of 4-hydroxyacetophenone (4HAP) to 4-hydroxyacetophenone oxime (4-HAPO) and subsequent Beckmann rearrangement of 4HAPO to paracetamol (PCM) was investigated. A one-pot method was transferred to flow using a packed bed column, but leaching into the feed limited downstream integration. A two-step approach was transferred into flow to give 4HAPO and PCM respectively. Synthesis of 4HAPO was integrated with a compact flow crystalliser with partial success, while a semi-batch approach showed 4HAPO could be directly crystallised from the flow synthesis effluent.

The catalytic flow hydration of pyrazinecarbonitrile (PyCN) to the drug pyrazinamide (PZA) was integrated with the segmented flow kinetically regulated automated input crystalliser (KRAIC). A cooling step introduced controlled nucleation and resulted in a five-fold reduction in crystal size. The crystallisation technique selectively formed the γ-PZA polymorph from the aqueous solution without the need for additives.

Production of multi-component complexes, 4-bromo-2-methylaniline (4Br2MA):3,5-dinitrobenzoic acid (35DNBA) and 4-iodo-2-methylaniline (4I2MA):35DNBA, was investigated using antisolvent crystallisation. Crystallisation of 4Br2MA:35DNBA was transferred into a segmented flow crystalliser and off-line isolation of the precipitate allowed characterisation of 4Br2MA:35DNBA crystals. A novel form of 4I2MA:35DNBA was isolated and characterised from batch crystallisation experiments. Thermal analysis of the thermochromic behaviour of the cocrystals showed that the single-crystal-to-single-crystal (SCSC) phase transition may be enabled by water in the bulk sample.

Two flow crystallisers (a tubular mixer reactor and a periodic withdrawal, continuous stirred tank reactor (CSTR) system) were evaluated for production of a commercial active pharmaceutical ingredient (API) salt. Crystallisation in the tubular mixer reactor was effective only for short periods at high velocity flow rates. Crystallisation in the CSTRs successfully operated for twelve residence times (RTs); with a 70 % yield of the API salt. The API salt formed spherical agglomerates in flow which showed higher uniformity and lower cake resistance compared to the batch sample.

Acknowledgements

Firstly, a huge thank you to my supervisor Prof. Chick Wilson for all his support, guidance and enthusiasm from start to finish in this research. Thank you also, for your support for the visit to the University of Cambridge and your help in securing the industrial placement at AstraZeneca. A further thank you to my co-supervisor Prof Matthew Davidson for his help, insight and feedback with the synthetic chemistry aspects of this PhD, as well as his support for my placement opportunities.

A special thank you to Dr. Karen Robertson for her help, expertise and feedback throughout this work. Thank you as well for inviting me to continue to be a part of your efforts at Diamond Light Source and for your help proof reading this thesis. Wishing you all the best in your position at Nottingham.

A big thank you to the members of the Wilson group, particularly for putting up with me commandeering loads of lab equipment in the twilight months of this PhD. An extra thank you to Lois and Polly who helped me to set-up and run flow experiments in the lab when I needed an extra hand. Thank you to Aneesa, for the office chats and putting up with me while I was writing this thesis. Best of luck with the remainder of your PhDs to you all. Thank you to all the past members of the Wilson group for the good times. Special thank you to Lauren Hatcher for her help with single crystal X-ray diffraction measurements, Anuradha Pallipurath for her help and expertise with the thermochromic crystals and especially Piba for his hands-on training and help with flow chemistry and engineering.

Thank you to the EPSRC Centre for Doctoral Training in Sustainable Chemical Technologies for funding this work and contributing to conferences, research visits and placements. Thank you to the Royal Society of Chemistry and the Armourers and Brasiers Company for additional funding for conferences and special thank you to AstraZeneca for additional funding for the industrial placement.

Thank you to Prof. Steven Ley, Dr. Claudio Battilocchio, Dr. Ricardo Labes as well as the rest of the Ley group for making me feel welcome during my visit to the University of Cambridge. The expertise you gave me was invaluable and I'm extremely pleased to have continued to collaborate with you afterwards. It was a pleasure to work with you all and I hope we cross paths again in the future.

Thank you to the Right Particle team and Research and Development department at AstraZeneca, who made me feel extremely welcome. It was an absolute pleasure working with you all and it was over far too soon. Thank you especially to my placement

supervisors Amy Robertson and Anna Jawor-Baczynska for their help during and after the placement. Without your support, it would never have been possible to share some of the work conducted over those twelve weeks, thank you so much.

Thank you to the researchers at Research Complex at Harwell for access to their expertise and equipment over the duration of this work. Thank you to Dr. Ryan Skelton and Duncan Guthrie for their support and guidance from Vapourtec. Thank you as well to Diamond Light Source and Dr. Mark Warren and Dr. Lucy Saunders for their help and enthusiasm during long nights on the beamline.

Thank you to the University of Bath Kickboxing club as well as coaches Rob Tettmar and Scott Harris for the training sessions that got me out of the lab. Thank you as well to Kirsty Dougall, for the squash games that kept me sane while writing this thesis. Thank you to all my friends at Bath, past and present, for keeping me in good spirits when I needed it.

Thank you to my family, for all their love and support when I endeavoured to start a PhD. Thank you mum, for believing in me.

Lastly, thank you Beth, for foolishly saying yes when I asked you to go ice skating with me. You make it all worth it.

Contents

List of Figures

List of Tables

List of Acronyms

35DNBA 3,5-Dinitrobenzoic Acid.

4Br2MA 4-Bromo-2-methylaniline.

4HAP 4-Hydroxyacetophenone.

4HAPO 4-Hydroxyacetophenone Oxime.

4I2MA 4-Iodo-2-methylaniline.

ACN Acetonitrile.

AcOH Acetic Acid.

ACS American Chemical Society.

AH Aliskiren Hemifumarate.

AIDS Acquired Immunodeficiency Syndrome.

API Active Pharmaceutical Ingredient.

AZ AstraZeneca.

BPR Back Pressure Regulator.

CSTR Continuous Stirred Tank Reactor.

CM Continuous Manufacturing.

CNT Classical Nucleation Theory.

COBC Continuous Oscillatory Baffled Crystalliser.

CQA Critical Quality Attributes.

CRD Cambridge Reactor Design.

CSCT Centre for Sustainable Chemical Technologies.

DPH Diphenhydramine.

DSC Differential Scanning Calorimetry.

ES Electrospinning.

EtOH Ethanol.

FBRM Focused Beam Reflectance Measurement.

FDA Food and Drug Administration.

FEP Fluorinated Ethylene Propylene.

GCI Green Chemistry Institute.

GMP Good Manufacturing Practice.

HOA Hydroxylamine Hydrochloride.

HPLC High Performance Liquid Chromatography.

HSM Hot Stage Microscopy.

ICCA International Council of Chemical Associations.

ID Inner Diameter.

ITC Innovative Technology Centre.

KRAIC Kinetically Regulated Automated Input Crystalliser.

m-KRAIC Mini-KRAIC.

MSMPR Mixed Suspension Mixed Product Removal.

MeOH Methanol.

MZW Metastable Zone Width.

NaAc Sodium Acetate.

NMR Nuclear Magnetic Resonance.

PAT Process Analytical Technology.

PCM Paracetamol.

PEEK Polyether Etherketone.

PFA Perfluoroalkoxy Alkane.

PFPE Perfluoropolyether.

PFR Plug Flow Reactor.

PP Polypropylene.

PSD Particle Size Distribution.

PTFE Polytetrafluoroethylene.

PXRD Powder X-ray Diffraction.

PyCN Pyrazinecarbonitrile.

PZA Pyrazinamide.

RF Radio Frequency.

RCaH Research Complex at Harwell.

RT Residence Time.

RTD Residence Time Distribution.

Re Reynolds Number.

SCSC Single-Crystal-to-Single-Crystal.

SA Succinic Acid.

SAB Succinate Salt.

SCXRD Single Crystal X-ray Diffraction.

SDGs Sustainable Development Goals.

SEM Scanning Electron Microscopy.

TFA Trifluoroacetic Acid.

TGA Thermal Gravimetric Analysis.

UN United Nations.

Chapter 1

Introduction

1.1 Sustainability and Manufacturing

In 2005, the American Chemical Society (ACS) Green Chemistry Institute (GCI) established a round-table for the pharmaceutical industry. Drawing on the expertise of companies including AstraZeneca, GlaxoSmithKline, Novartis and Pfizer; the ACS GCI pharmaceutical round-table aimed to motivate the adoption of the *12 Principles of Green Chemistry*.[1] In 2007, they established a list of important research areas in which significant progress is needed in order to adopt green chemistry practices. A second list was released in 2010, where ten complementary green engineering targets were identified.[2] Of those highlighted, continuous manufacturing and integration of chemistry and chemical engineering were recognised as top priorities.[3] In 2015, United Nations (UN) launched the 2030 agenda for sustainable development in which they listed 17 Sustainable Development Goals (SDGs). Adopted by every member state, SDGs are a global strategy to improve health, education, reduce inequality, tackle climate change and stimulate economic growth for the betterment of people and planet.[4] In order to achieve these goals, the International Council of Chemical Associations (ICCA) has recognised the important role that the chemical and pharmaceutical industry must play in order to achieve long-term sustainable practices.[5]

However, the development of cleaner and more robust chemical manufacturing is a challenging problem. The chemical industry faces increasing pressure from social, economic and environmental factors to deliver greener chemistry while still meeting continually increasing consumer demand. This is particularly difficult in sectors such as the pharmaceutical industry, where developing life saving medicine for patients is of equal importance to tackling pollution. Meeting these growing challenges will require technologies and processes that reduce environmental impact, improve efficiency and shift away from depleting finite resources.

The Centre for Sustainable Chemical Technologies (CSCT) at the University of Bath aims to address current issues from a multidisciplinary approach, drawing on expertise across faculties. One of the core themes is processes and manufacturing. The CSCT aims to consider the total supply chain and whole life cycle impact, collaborating with both industry and international partners to achieve this.[6] One of the key areas identified by the CSCT for development is the use of continuous manufacturing for the production of fine chemicals and pharmaceuticals.

1.2 Continuous Manufacturing

Continuous manufacturing (CM) is the concept of continuously charging and discharging material(s) and product from a system without interruption.[7] Within chemical industries, continuous processing is not a new technique. The most well known modern continuous chemical process is the Haber-Bosch process, which was developed in the early 20th century for the production of ammonia (Figure 1-1).[8,9] The Haber-Bosch process, still in use today, was largely fuelled by the economic demand for nitrogen based compounds. Approximately 80 % of the worldwide ammonia output is used in fertilisers for agriculture.[10] Since then, continuous processing is now used widely for the mass production of commodity chemicals, polymers and petrochemicals.[11,12] In modern times, effectively all the steps in a petrochemical process from crude oil distillation through to separation of the final product is performed in a series of continuous flow reactors and separators.[13]

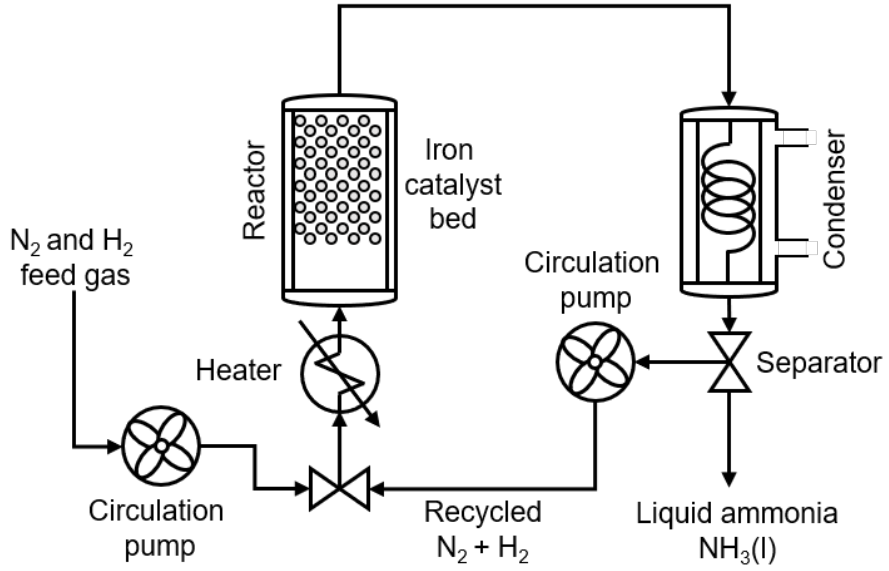

Figure 1-1: Schematic of the Haber-Bosch process for production of ammonia

The take-up of continuous process design in most bulk chemical production is relatively high, however the use of CM in the pharmaceutical and fine chemicals sectors has been much slower. There are several reasons for this, for example, in the pharmaceuticals sector stricter quality regulations (required to ensure the product is safe for human consumption) compared to bulk chemicals limits CM uptake.[14] Furthermore, pharmaceutical and fine chemical compounds tend to be structurally more complex than bulk chemicals. As a result, manufacturing fine chemical and pharmaceuticals often requires intensive, multi-step units of operation. Because of this, CM practices are generally

less attractive, as the conversion of existing batch processes to continuous systems requires purchasing of expensive new equipment and complementary control systems. As an example of the difficulties faced, a recent paper outlined the synthetic route to a promising anti-tumour drug C52-halichondrin-B amine (E7130) (Figure 1-2).

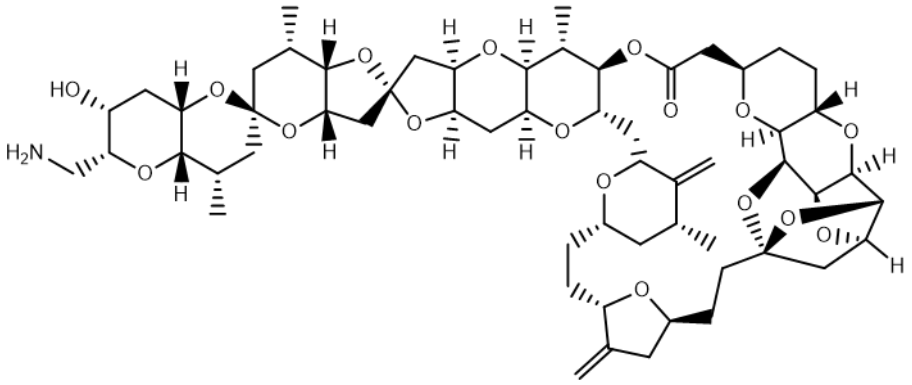

Figure 1-2: Chemical structure of C52-halichondrin-B amine (E7130)

E7130 is a synthetic derivative of halichondrins, a natural product isolated from marine sponges. E7130 requires 92 individual synthetic steps to produce E7130 suitable for clinical trials.[15] E7130 is currently produced on the lab-scale in a series of batch reaction and work-ups. This makes sense from a development standpoint, as it is easy to imagine that implementing a CM strategy for a 92 step continuous reaction would be extremely complex. In the adoption of CM, the plight facing the drug development industry is the fact that the molecular structures of drug molecules are becoming increasingly complex, which sparks an aversion to modern continuous manufacturing practices.

In contrast to drug development, commodity chemicals require much simpler preparation procedures and their is a clear economic driver to adopt CM in this case. The bulk chemicals industry produces huge stockpiles of chemicals in order to meet the demand. The amounts needed would be impossible to facilitate without the use of CM to reduce costs (see Table 1.1).[9] While the economic driver is still present in fine chemical and pharmaceutical sectors, this is a much smaller incentive for using CM technology, as annual product tonnage is orders of magnitude smaller than bulk chemicals production.

Instead other drivers have begun to push the adoption of continuous processing practices including, reducing development costs,[16] increasing production flexibility,[17,18] improving health & safety,[19,20] decreasing environmental impact,[21] increasing product quality,[7,11] greater process automation[14,22] as well as sector regulators pushing for modernisation of fine chemical processing.[7,23] Many of these drivers are influenced by the growing need for sustainable manufacturing practices. As shown in Table 1.1, the

Table 1.1: Comparing annual product tonnage and waste across industry sectors[12]

Industry sector	Product tonnage	kg waste[a] / kg product
Oil Refining	10^6 - 10^8	< 0.1
Bulk Chemicals	10^4 - 10^6	1 - 5
Fine Chemicals	10^2 - 10^4	5 - 50
Pharmaceuticals	10 - 10^3	25 - 100

[a] Defined as all materials except the desired product (including inorganic salts, solvent loss, etc.)

amount of waste per kg of product in the fine chemicals and pharmaceutical industry is orders of magnitude higher than bulk chemical production. CM has the potential to help offset waste and can be aligned closely with the principles of green chemistry (Table 1.2).

Table 1.2: 12 Principles of Green Chemistry[24]

Number	Green Chemistry Principle
G1	Waste Prevention
G2	Atom Efficient
G3	Reduce hazardous chemical usage
G4	Safer molecules by design
G5	Use benign solvents and auxiliaries
G6	Energy efficient
G7	Renewable feed-stocks
G8	Reduce derivatives
G9	Use catalytic amounts of reagents
G10	Design products for degradation
G11	Real-time analysis for pollution prevention
G12	Design safer processes

In particular CM has an affinity with G1, waste prevention, but a range of the other potential advantages are summarised in Table 1.3.[25] While CM offers many advantages, there are still significant gaps in the technologies available for continuous manufacturing. For instance, many of the downstream technologies concerned with extraction, separation, isolation and purification can become more complex when transferred into a continuous process.[26] While the use of CM in synthesis is becoming routine, examples of continuous downstream process operations in fine chemical and pharmaceutical manufacturing are relatively rare. In particular, continuous crystallisation is proving to be one of the most challenging aspects in continuous flow and there is a notable gap in the advances made in continuous crystallisation compared to flow chemistry. However, if the industry is to adopt an end-to-end manufacturing approach, then significant strides need to be made in bridging the gap between fields of continuous processing.

Table 1.3: Relationship between specific benefits of continuous manufacturing and green chemistry[7,11,25]

Feature	Potential Benefits	Green chemistry principles
Decreased reactor volume	Reduce solvent waste Smaller space requirements	G1, G3
In situ processing of hazardous intermediates	Safer handling of toxic material Shorter supply chains Reduction in unit operations	G1, G2, G12
Improved mass & heat transfer	Reduced energy costs Shorter reaction time Improved product consistency	G6
In situ analysis	Real-time reaction monitoring Greater process control	G11
Operate safely under pressure	Easier process intensification Reaction efficiency improvement Reduce required reagent amounts	G12, G9

1.3 Aims and Objectives

The overarching theme of the research presented in this thesis is to address current challenges in the development of continuous manufacturing for the production of pharmaceuticals and fine chemicals. The research herein aims to approach continuous processing challenges from a holistic perspective, establishing procedures and reactor designs that will allow the bridging between upstream synthetic technologies with downstream crystallisation platforms (Figure 1-3). The ability to seamlessly transfer from one chemical process to another without downtime or off-line work-up would lead to greater adoption of continuous processes in the pharmaceutical sector and will be an essential step in the development of a sustainable chemical industry. The work presented in this thesis will cover a range of flow technologies and attempt to develop continuous processes for a range of target molecules. The work carried out will be split into chapters covering each target molecule and discuss the development of various flow procedures, with the overall goal of achieving integrated continuous systems. The main targets will be active pharmaceutical ingredients (APIs) or important intermediates towards API production. These will be covered in Chapter 3, 4 and 6. The other aspect of the work presented here will cover more novel molecular systems and attempts to move their production from a small scale batch process to continuous production, this will be covered in Chapter 5.

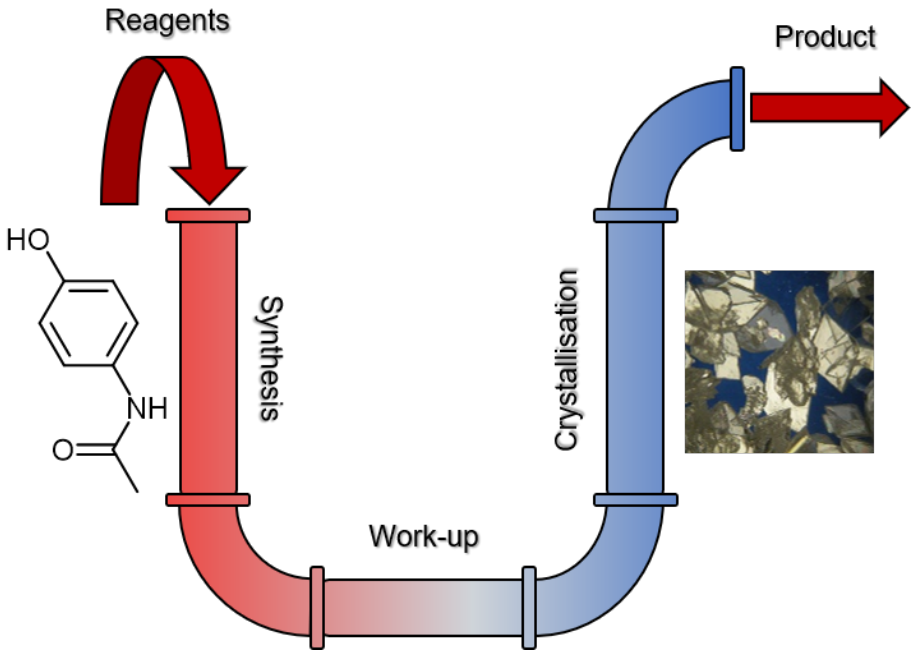

Figure 1-3: The continuous manufacturing pipeline (adapted from Mascia *et al.*)[27]

Chapter 3 discusses efforts towards the development of a continuous process for the delivery of paracetamol (PCM) in a continuous process. The work carried out within the Centre for Sustainable Chemical Technologies (CSCT) aims to develop a continuous process, using PCM as a model API. The overarching aim of the work is to develop a route to PCM from renewable feedstocks, circumventing the need for finite resources. This chapter will be concerned with the final synthetic step in the method and attempting to add further value to the process by integrating the route with a continuous crystallisation platform. The work will also outline efforts to develop an integrated, continuous process for the production of an important intermediate in the synthetic procedure, 4-hydroxyacetophenone oxime (4HAPO).

Chapter 4 will present the development of a continuous process for the delivery of pyrazinamide (PZA). The work was carried out as a collaboration between the University of Bath, Chick Wilson group and the University of Cambridge, Steven Ley group. The aim of the work was to couple an established flow chemistry route to PZA with a bespoke crystallisation platform, known as the kinetically regulated automated input crystalliser (KRAIC). The KRAIC was developed at Bath by Dr. Karen Robertson. The chapter will discuss the development and optimisation of a continuous synthesis and crystallisation process for PZA.

Chapter 5 will move towards the downstream process, concentrating on the development of a cocrystallisation procedure for the delivery of thermochromic materials. Previous work by the metastable materials group at Bath has produced crystalline products with desirable colour-changing properties. However, efforts to scale-up production in batch have been difficult. The main objective of the work is to develop a suitable continuous crystallisation process for scale-up without changing the desired properties. This in turn would allow for sufficient material to be produced for further studies in device applications.

Chapter 6 will cover the investigation into a reactive crystallisation procedure for the production of commercial API salt product. The work carried out was conducted during a three month placement at the AstraZeneca (AZ) Research and Development site, Macclesfield, UK. The overall aim was to investigate, develop and evaluate a continuous crystallisation process for the API salt formation. In particular, the development process was considered from an integrated manufacturing perspective. For confidentiality reasons, the identity of the API cannot be disclosed. Instead, this chapter concentrates on downstream process development and discusses the possible benefits of integration within a wider continuous manufacturing framework.

1.4 Continuous Chemistry Concepts

When considering continuous chemical reactions, it is important to identify a number of fundamental differences between batch and flow processes. This section is concerned with introducing some of the key concepts commonly encountered when considering continuous chemical processing, a brief summary is outlined in Table 1.4.

Table 1.4: Comparison of the characteristics of batch and flow[28]

	Batch	Flow
Stoichiometry	Defined by the concentration/molar ratio of the components	Defined by concentration/ratio of the flow rates
Reaction time	Time spent under the reaction conditions	Time spent in the reactor; dependent on the flow rate and reactor volume
Reaction progress	Dependent on time spent in reaction vessel	Dependent on distance travelled along reactor length
Steady state	Concentration of components throughout the vessel at any given time is uniform	Reactant concentration is steady with time but different along the reactor length

1.4.1 Residence Time (RT)

In traditional chemistry, the vast majority of reactions are carried out in batch processes. In a batch reaction, the reaction time is determined by the time that the vessel is held under the set reaction conditions. In continuous processes this is not the case, instead the reaction is controlled by the residence time (RT). This is the time between initiation and termination of a continuous transformation, or how long the reagents spend inside the reactor conditions (Figure 1-4).[28,29] RT is dependent on the reactor volume and the flow rate (Figure 1-5). In a tubular reactor, RT can be calculated using Equation 1.1. Where V is the volume (mL), Q is flow rate ($\mathrm{mL\,min^{-1}}$), l is length (cm) and r is the radius (cm). By adjusting the reactor size or flow rate, precise control can be exerted on the RT of a chemical process. This is important, as the RT has a profound effect on the success of a process. Should the residence time be too short, then the reagents are discharged from the reactor before the reaction is complete. If the RT is too long, then the solution is occupying reactor space for no benefit.[30] This not only decreases the productivity of the process, but risks decomposition of the product(s) if the reaction requires harsh conditions or the product is unstable.

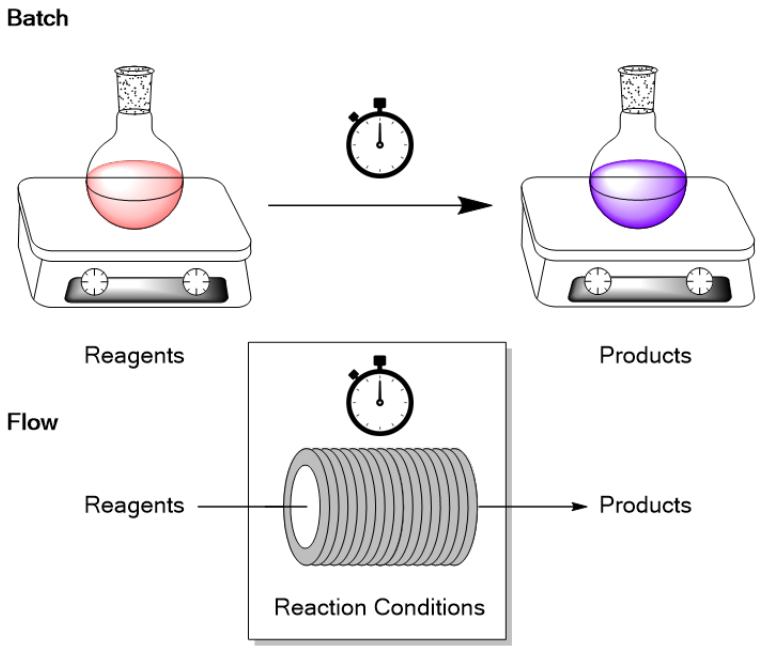

Figure 1-4: Reaction time in batch and flow systems[31]

$$R_T = \frac{\pi r^2 l}{Q} \equiv \frac{V}{Q} \tag{1.1}$$

Figure 1-5: Residence time

If a reaction is run in a batch environment, then the concentration of the reagents and products is uniform throughout the vessel at any given time. However in an optimal flow process, the concentration of reagents and products changes along the reactor length. Thus, the reaction time in a continuous process is related to the distance travelled from the inlet of the reactor.[30,32] The ideal situation to maximise productivity would be to ensure that the residence time is equal to the reaction time.[28] In other words, the flow rate and reactor volume is set so that the chemical transformation is completed at the point of reaction termination. However it is important to note that in the real world, not all molecules that enter the reactor spend the same length of time within the

reactor zone. In any flow system, there will exist a distribution of residence times that is influenced by the fluid dynamics. This dispersion of the RT from the ideal is denoted as the residence time distribution (RTD).[29,33] In general, the tighter the RTD, the more consistent the process will be.[34] There are a number of methods to improve the consistency of the RT including: enhancing mixing, segmentation of flow,[35] changing reactor geometry or decreasing solution viscosity.[36]

1.4.2 Steady State Conditions

Continuous reactors are preferably operated at steady state. At steady state, the movement of chemical species into and out of the reactor is the same. At steady state, the temperature and concentration at a specific spatial point does not change with time.[30] The yield and conversion at steady state is usually significantly different to the overall process yield and conversion.[29] This is because a continuous process will likely undergo a period of unsteady state during operation start-up, shutdown, or after a change in the process variables (Figure 1-6).[33]

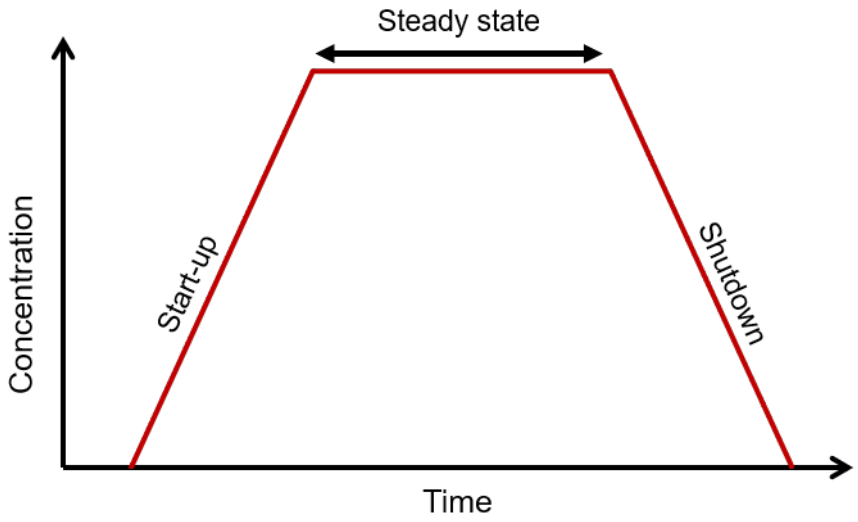

Figure 1-6: Diagram of a flow process with steady state operation

It is possible to measure approximately when a system has reached steady state using a tracer. The tracer can be monitored either offline or *in situ* but must be inert to the reactor conditions.[33] A typical example of a tracer would be a coloured dye, whose concentration could be measured using a spectrometer. Once the dye concentration is no longer changing with time, the system is said to have reached equilibrium.[33,36,37] While steady state is a useful term, in reality most real continuous processes are prone

to disturbances or fluctuations in temperature, pressure or chemical composition and so never truly reach steady state. However, measuring experimentally does help to determine when these disturbances in a process have reached a minimum, allowing measurements to be made when the system is at its highest consistency. This is a significant advantage in continuous processing over batch processing, as a batch reactor operates under unsteady conditions. Hence it can be much easier to control critical quality attributess (CQAs) in a continuous system if quality control focuses around operation at steady state.[14,38] Systems that operate close to steady state include plug flow reactors (PFRs) and continuous stirred tank reactors (CSTRs).[39]

1.4.3 Mixing, Mass and Heat Transfer

One of the advantages observed in using continuous processes is the improved surface area-to-volume ratio. This is mainly the case for tubular reactor platforms, such as in microreactors or macro-scale coiled reactors, but it can be extended to include CSTRs if they are run in series (i.e. multiple small CSTRs in contrast to a single stirred reactor of the same total volume). Since most processes require an outer heating jacket in order to regulate temperature, in larger batch vessels where surface-to-volume ratio is low, heat transfer is inefficient.[29] This in turn can lead to thermal gradients which increase the likelihood of unintentional side reactions occurring. In the case of flow reactors, if the surface area-to-volume ratio is high this allows greater control over the heating/cooling cycle resulting in a more consistent product. In the growing sector of microwave-chemistry for example, a good surface-volume ratio is a key factor in ensuring equal heating of the mixture.[40]

As with heat transfer, both mass transfer and mixing can be similarly improved in flow. In large scale processes, these factors can have a significant influence in the time required to establish homogeneity and this in turn can have a direct influence on a processes efficiency. Generally, the higher surface-to-volume ratio of flow reactors makes them superior to equivalent batch vessels in this regard. This is also true on the bench-top scale, when comparing a flow reactor to a flask. For example Nagaki *et al.* demonstrated how moving from a batch reactor to a microreactor significantly improved synthesis of a series of biaryls.[31,41] The improved surface-to-volume ratio led to better heat and mass transfer in the system which was essential in facilitating the conversion of the reactants to the products. Furthermore, by reducing the diameter of the tubing and therefore increasing mass transfer and mixing, the conversion and selectivity to the desired product was increased by 14 %.

In continuous processing, it can often be beneficial for a system to approach plug flow.

A plug flow reactor (PFR) consists of a vessel (or series of vessels) in which only radial mixing occurs (Figure 1-7).[42] This model assumes no back-mixing in the system and demonstrates a tight RTD. Essentially, the flow moves through the reactor as a single "plug" in the axial direction from inlet to outlet without any chemical dispersion.

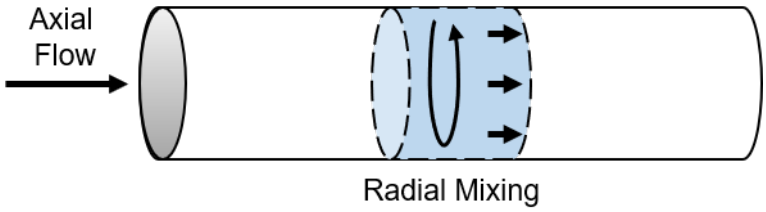

Figure 1-7: Plug flow through a tubular reactor

Typically a single continuous stirred tank reactor (CSTR) is described as "perfectly" mixed, that is, the vessel has a homogeneous composition.[33] However, in practice a single CSTR does not perform ideally and can suffer from a wide RTD, resulting in poor reactor performance.[43] This can be circumvented by running CSTRs in series. As the number of CSTRs approaches infinite, plug flow is achieved.[44] In reality, increasing the number of CSTR stages has repercussions on the amount of equipment needed and so is usually limited to less than ten. The benefits of a plug flow system are particularly pronounced in continuous crystallisation; where back-mixing leads to variation in particle size distribution, impurity retention and crystal morphology.[45–47] There are three forms of mixing in a conventional tubular reactor, which can be categorised as laminar, transitional and turbulent (Figure 1-8).[29]

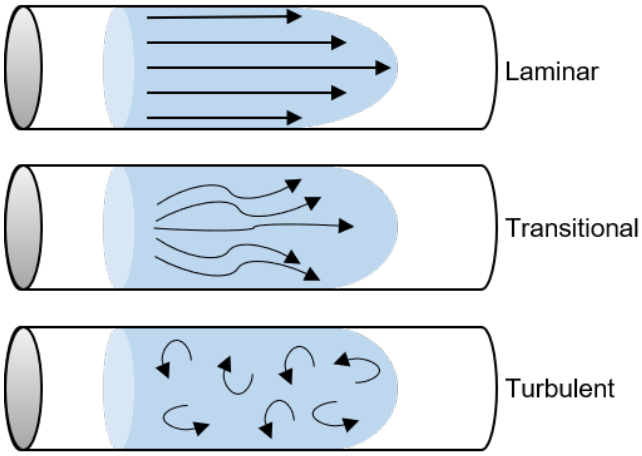

Figure 1-8: Types of fluid flow

Mixing in these systems is described using the dimensionless Reynolds number (Re).

Re is determined from Equation 1.2:

$$Re = \frac{\rho u d}{\mu} \tag{1.2}$$

Where is ρ is the fluid density ($\mathrm{kg\,m^{-3}}$), μ is the dynamic viscosity ($\mathrm{kg\,m^{-1}\,s^{-1}}$), u is the net flow velocity ($\mathrm{m\,s^{-1}}$) and d is the tube diameter (m).[37] Generally an $Re < 2300$ results in laminar flow, an Re between 2300 and 4000 is transitional and an Re above 4000 is turbulent.[28] In laminar flow, fluid motion is mostly parallel to the tube axis. In microreactors (where tubing diameter is less than 10^{-5} metres) laminar regimes can provide efficient mixing.[28] For larger reactors however, turbulence is needed to provide intense, random motion to improve mass transfer and heat transfer.[42] Most lab-based batch mixing is either laminar or transitional.[48] To achieve plug flow in a tubular system requires a high velocity flow rate that generates turbulent mixing. However, a secondary mechanism (such as segmentation) can be implemented to generate plug flow, independent of flow rate.

The fundamental differences in continuous flow offer chemists greater control and efficiency that cannot be easily replicated under batch conditions. These advantages, coupled with the drive for greener manufacturing has made CM increasingly attractive to the fine chemical and pharmaceutical industries. As a result, this has spawned the development of new technologies and applications in two distinct fields of research - flow synthesis and continuous crystallisation.

1.5 Flow Synthesis

Flow synthesis is concerned with the continuous flow reaction of a chemical species to a desired product.[49] Generally flow synthesis has had much success in organic chemistry to produce pharmaceuticals and petrochemical products, but flow synthesis has also been extended for the production of inorganic materials such as metal-organic frameworks, quantum dots and nanoparticles. There are several advantages in flow synthesis compared with batch synthesis. In particular, tubular flow reactors offer fast mixing, excellent heat and pressure control, good mass transfer and heightened safety, all factors that can influence the success of a synthetic reaction.[50]

1.5.1 Equipment and Technologies

In a simple flow synthesis set-up (Figure 1-9) there are a series of key equipment parts required to carry out a reaction. This usually consists of a series of pumps, tubing,

mixer pieces and a core reactor unit. The pumps are used to move solutions around the system and the choice of pump is dependent on the application. Some typical examples include peristaltic, gear and syringe pumps.[29,51] Each have a number of advantages and disadvantages and the choice of pump is dependent on the application. For instance, a peristaltic pump is capable of handling small solid loadings, such as when transporting a slurry. However a peristaltic pump can induce back-mixing, caused by the motion of the moving parts. Aspects to consider in pump selection include: what range of flow rates may be required? What reaction conditions (e.g. handling high pressure reactions or pumping gas-liquid reactions mixtures) must be maintained? Is the pump compatible with any corrosive or oxidising agents present?[52] Mixing of two reagent phases is facilitated by a mixer piece. In most cases a T-piece (as depicted in Figure 1-9) or Y-piece is used to combine two or more streams into a single channel. This is sufficient for slow reactions or small reactors, but where faster mixing is required the process can be intensified by in-line structures (such as static mixers) to ensure completely homogeneous mixing.[53] Other elements to consider are the need for elevated temperatures or pressures; in this case a back pressure regulator (BPR) will be needed for safe operation above a solvent's boiling point. The benefits of high pressure or high temperature are well documented, including increasing reaction rate, improving selectivity and raising process intensification.[54]

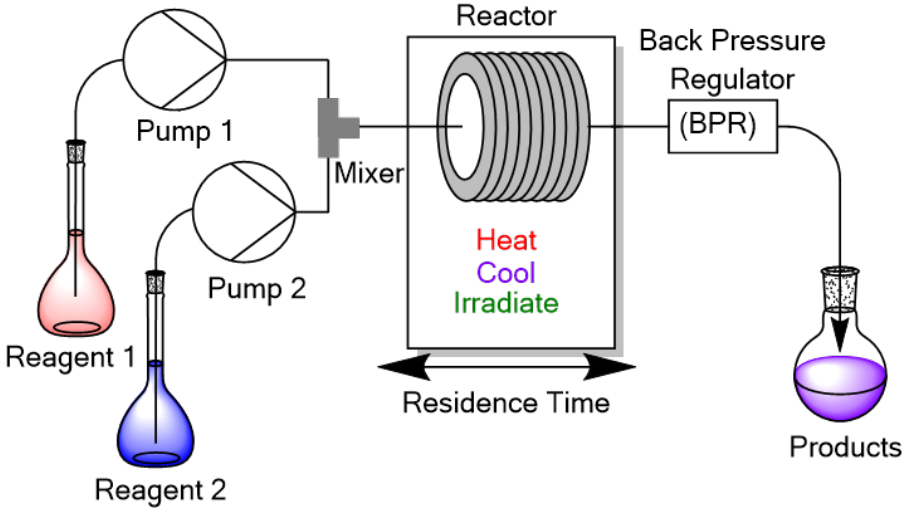

Figure 1-9: Typical flow chemistry scheme

The reactor lies at the heart of the process and is where the chemical transformation should take place. There are number of different types of reactors available. Some of the common examples encountered are shown in Figure 1-10. Much like pumps, the reactor type will largely be dependent on the nature of the reaction and the scale of the

process. Chip reactors (Figure 1-10a) offer very high levels of heat and mass transfer due to the large surface-to-volume ratios.[50] This results in the reduction of side reactions compared to batch where mixing and inefficient heat transfer can lead to unwanted by-products. The internal volume of a chip reactor can range from below 1 µL and up to and above 1 mL. This allows for optimisation of a synthesis using minimal amounts of reagents.[51] They can be machined from a range of materials including glass, stainless steel, polymers and ceramics suitable for a range of chemistry.[54] Chip based reactors are an attractive flow technology for liquid-liquid or gas-liquid reactions but they suffer from some disadvantages. In particular the system's inherent small diameter increases the likelihood of clogging and blockages occurring.[17] Roberge *et al.* has shown that statistically, over 50 % of all fine chemical and pharmaceutical reactions could benefit from using micro or chip reactors for synthesis. However, their inability to handle solids limits their application to less than half of these cases.[55] Furthermore, scaling up chip reactor technology can have high upfront costs, making it difficult for chip reactors to compete with established batch processes at the kilogram scale.[56]

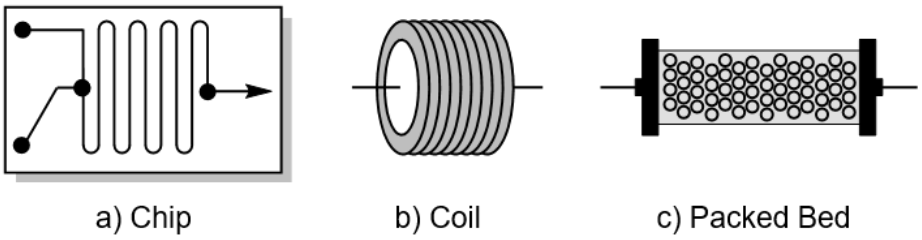

Figure 1-10: Typical reactors used in flow synthesis

Tubular coiled reactors (Figure 1-10b) are the simplest and most adaptable flow reactors available. Coil reactors typically operate between 1 µL up to a few litres in volume, with a wide range of internal diameters. Coil reactors are commercially available in a range of inert materials but the most commonly used are fluoropolymer derivatives such as polyether etherketone (PEEK), perfluoroalkoxy alkane (PFA), polytetrafluoroethylene (PTFE) and fluorinated ethylene propylene (FEP).[18] Where high temperatures (over 150 °C) or pressures (over 20 bar) are needed, stainless steel (or another suitable metal) coils may be more suitable.[29] The advantage of coil reactors is their versatility and ease of use. The RT can be set by adjusting the length or internal diameter of the coil, as well as the flow rate. They can be heated or cooled in a water bath or by a programmable heater unit. Coil reactors can be connected in series and subjected to different conditions making them suitable for multi-step reaction schemes. Much like chip-based reactors, coiled reactors can also suffer from blockages from particulates however, the larger diameter in coiled reactors makes it easier to clean and cheaper

to replace than chip reactors.[51] However the larger diameter in coil reactors tends to increase the RTD compared to those typically seen in chip reactors. This can be overcome by introducing mixer pieces or segmentation to narrow the RTD in coils. Chip reactors tend to offer better surface-to-volume ratio than coil reactors, making them most suitable for very fast or highly exothermic reactions which benefit from the superior mass and heat transfer rates.[54] Slower processes benefit from the longer RTs coil reactors offer as well as their higher productivity.

The third reactor type in Figure 1-10 is the packed bed unit. A packed bed unit is generally utilised when a heterogeneous reagent or catalyst is required. The unit consists of a column or cartridge filled with solid material where each end is plugged with a filter frit end-piece. A solution containing the reagents is pumped through the reactor to begin the reaction. An effective packed bed reactor allows for heterogeneous reactions to proceed without the need for a subsequent separation process. The performance of a packed bed reactor is highly dependent on particle size, solid loading and RT.[51] The greater the surface-to-volume ratio of the solid particles, the better a reaction performance is likely to be.[29] However, if the particles are too small or partially soluble in the feedstock, then leaching of the solid into the reaction stream can occur. This can lead to blockage issues, or a reduction in catalytic activity over time. Such problems can limit the run time of a flow process before a replacement cartridge is needed.[57] Nevertheless reagents immobilised within a packed bed benefit from localised high molarity, which can help drive a reaction to completion while simultaneously preventing side reactions via continuous removal of the effluent.[58]

There is an extensive range of advanced reactor technologies available on the market, most of which are designed to fit the chemistry. The range of applications include photochemistry,[59,60] electrochemistry,[61] microwave-assisted chemistry[40,62] and gas-liquid phase chemistry.[63] Each sector is a ongoing area of study but these advanced reactors are designed to take advantage of the inherent attributes of continuous flow processing. Much of the equipment is modular and allows for combinations of pumps, mixers, pressure regulators, reactors, heating and cooling zones to be assembled into versatile 'plug and play' platforms. As such, the development of flow technologies gives additional versatility compared to batch-based synthesis.

1.5.2 Pharmaceutical Synthesis

The use of flow technology can contribute towards improved sustainability, safety and productivity making flow synthesis an attractive procedure for the manufacturing of APIs or important intermediates. But the pharmaceutical industry still relies predom-

inantly on batch or semi-batch reactors, despite the evident interest in continuous flow manufacturing.[64,65] In academia, the growth of flow technology for API generation can be traced to the early 2000s. Examples of successful flow synthesis of drug products include the production of ciprofloxacin, rimonabant and efaproxiral (Figure 1-11).

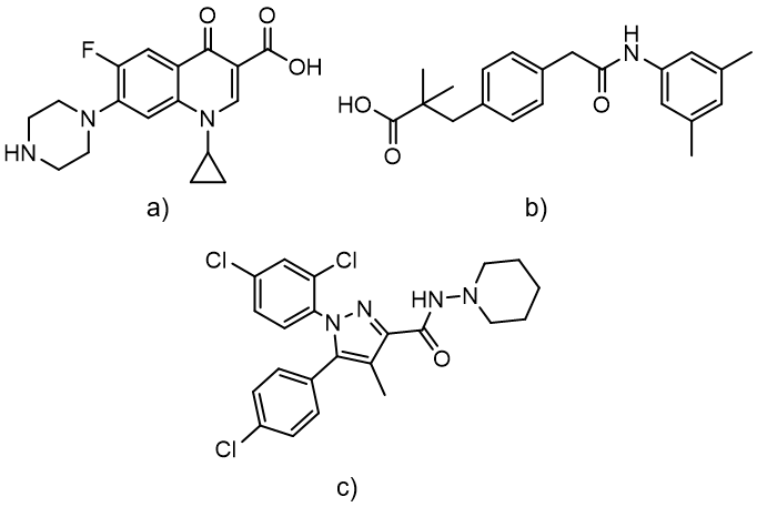

Figure 1-11: Chemical structure of a) ciproflaxin b) rimonabant and c) efaproxiral

In the case of ciprofloxacin, application of microreactor technology showed flow synthesis could be applied sequentially to assemble the antibiotic and derivatives using flow synthetic methods. In producing ciprofloxacin, the use of microreactor technology offered greater control of the subsequent product formation compared to batch.[66] For rimonanbant and efaproxial, Gustafsson *et al.* demonstrated how a small coiled reactor could be used to safely carry out an amide bond formation using the highly pyrophoric reagent trimethylaluminium. Process intensification in flow meant lower volumes of the hazardous reagent were needed and the process was much safer than the equivalent batch system.[67] More recently, the portfolio of high profile drugs that have been successfully synthesised in a series of single or multi-step flow synthetic processes has expanded rapidly, some notable examples include ibuprofen,[68,69] artemisinin,[70] imatinib[71,72] and nabumetone.[73]

A good example of a flow approach to pharmaceutical synthesis on an industrial scale was published by Bristol-Myers Squibb. Here a batch process was developed for the conversion of buspirone (an API for the treatment of anxiety disorders) to the metabolite 6-hydroxybuspirone, a promising candidate under clinical study.[74] While the batch process was successful, several issues remained. Scaling up of the process to the pilot plant significantly increased reaction time and raised concerns over the safety and po-

tential for a run-away reaction. This was important as the reaction is exothermic and required cryogenic temperatures to avoid unwanted side reactions. As such a consecutive three-stage flow synthesis approach was implemented to overcome these challenges (Figure 1-12).[75]

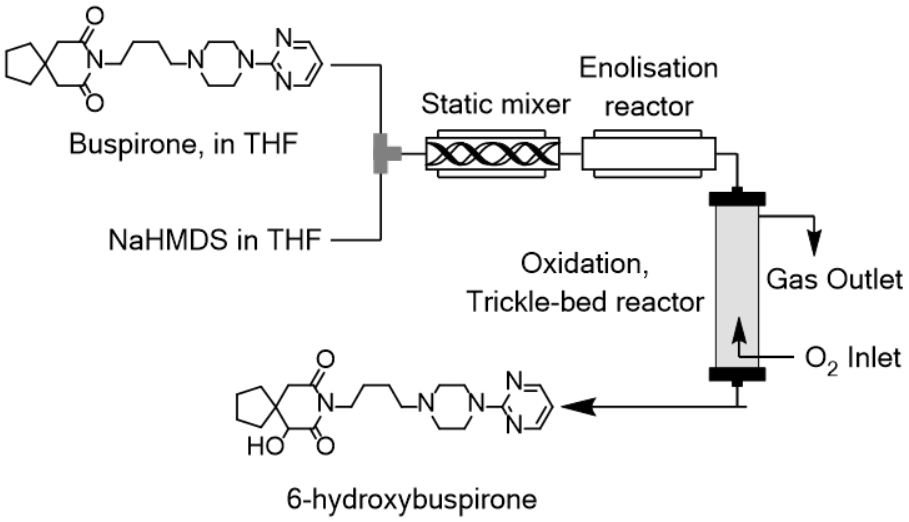

Figure 1-12: Schematic diagram for the flow synthesis of 6-hydroybuspirone

The process involved using a temperature controlled, jacketed reactor vessel for the conversion of buspirone to its enolate derivative. Gaseous oxygen is then bubbled through the enolate solution. The gas is fed counter to flow in a trickle-bed reactor to yield 6-hydroxybuspirone.[76] The process implemented the use of microstructures (static mixers) to ensure good mixing of the starting materials before the enolisation reactor. Using a flow reactor meant that temperature was easier to control compared to the batch process, as the improved surface area-to-volume ratio enabled the efficient removal of excess heat and easier maintenance of the cryogenic conditions. The static mixer ensured homogeneity of the feed and shortened the reaction time. The system was run for 50 hours under steady state operation producing over a 100 kg of the API with a comparable quality to the batch product.[75] Other examples of API flow chemistry on an industrial scale include the synthesis of vildagliptin,[77] 2,2-dimethylchromenes derivatives[78] and production of intermediates towards etodolac synthesis.[79]

While production of pharmaceuticals using flow chemistry is beginning to grow, there are some issues that have prevented widespread adoption. Issues include controlling complex multi-step processes, integration of downstream processes, in-line purification as well as an embedded culture and aversion to flow technologies. This is partly fuelled by the high up-front costs of flow equipment and a lack of trained personnel in

flow practices.[18,80] Despite this, the pharmaceutical sector is generally supportive of continuous processing practices, while regulatory bodies like the Food and Drug Administration (FDA) have begun accepting continuous manufacturing procedures.[7,81–83] Furthermore, key practitioners in pharmaceutical development have highlighted flow chemistry as a key enabling technologies in the adoption of green chemistry ideals.[3]

1.6 Crystallisation

Crystallisation plays a critical role in the fine chemicals industry with the majority of products requiring a precipitation or purification step at some point.[84] In the pharmaceutical sector, more than 90% of APIs are crystalline organic molecules.[53] Crystallisation is used to control important parameters in APIs such as purity, shape, size distribution and polymorphism (Figure 1-13). Without proper control, poor crystal performance can impact work-up, filtration, formulation and productivity.[44,46] As such, crystallisation has both a large effect on the performance of the final product and the efficiency of the manufacturing process.

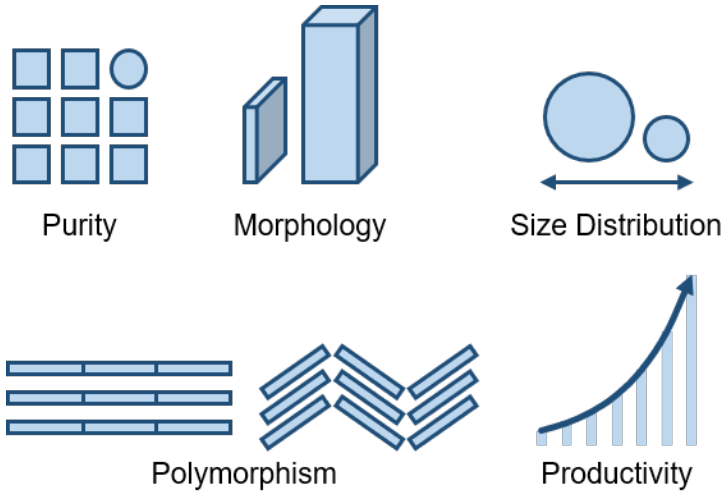

Figure 1-13: Important parameters in crystallisation control[46]

In order for crystallisation to occur, a system needs to be supersaturated. A system is considered supersaturated when the amount of dissolved solute at a given temperature and pressure exceeds the equilibrium solubility.[85,86] This is can be described in terms of concentration using Equation 1.3:

$$\ln S = \ln \frac{c}{c^*} = \frac{\Delta\mu}{RT} \tag{1.3}$$

where S is the supersaturation, c is the solute concentration, c^* is the equilibrium solubility, $\Delta\mu$ is the difference between the chemical potential of the solute and the chemical potential at equilibrium, R is the gas constant and T is the temperature.[38] For more practical uses, supersaturation is usually expressed as a ratio, or as the relative supersaturation (σ) as shown in Equation 1.4 and 1.5 respectively.

$$S = \frac{c}{c^*} \tag{1.4}$$

$$\sigma = \frac{(c - c^*)}{c^*} \tag{1.5}$$

So long as $S > 1$ (or $\sigma > 0$) the system can be considered supersaturated. Establishing the equilibrium composition under a given set of conditions provides the basis for a crystallisation process. Figure 1-14 shows a typical temperature vs concentration solubility diagram.The solubility curve represents the solubility at equilibrium and the dashed line represents the metastable zone limit. When the concentration of the solute is below the solubility curve, the system is considered undersaturated and any crystals will be dissolved in solution. The region between the solubility curve and the metastable zone limit is termed the metastable zone width (MZW). Within this region, the system is minimally supersaturated and thus only crystal growth and secondary nucleation events will occur. Above the metastable zone limit is the supersaturated labile region, where spontaneous primary nucleation occurs.

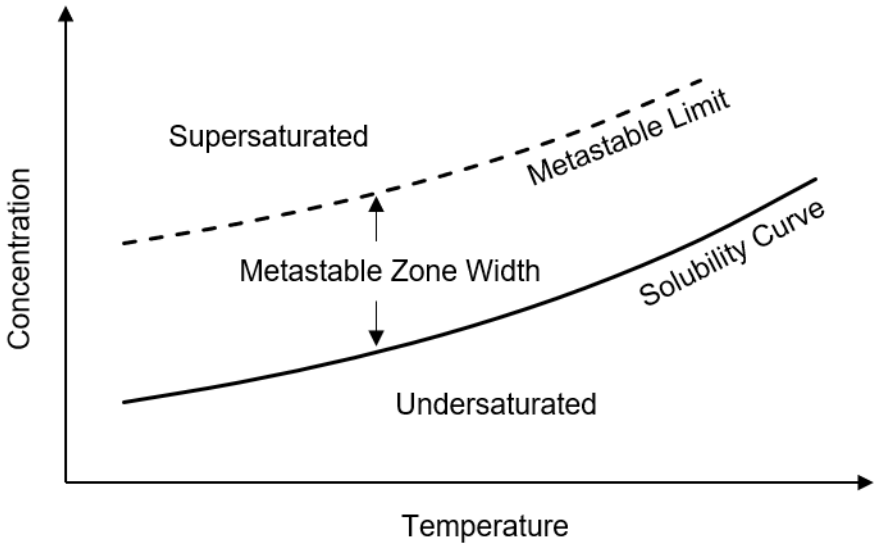

Figure 1-14: Solubility curve and the metastable zone width

When designing a crystallisation process, knowledge of the MZW is a useful tool in ensuring controlled nucleation and crystal growth. However, the MZW is highly dependent on many factors. In a cooling crystallisation for example the MZW can be influenced by cooling rate, impurity levels, additive concentrations, stirring rate, flow

rate, crystalliser scale and crystalliser geometry.[38,44,85,86] As such, the MZW should be considered a useful approximation rather than a fixed region.

1.6.1 Nucleation and Crystal Growth

Nucleation is the formation of a crystalline nucleus in a system. Nucleation can occur via several different pathways, the classical examples are primary and secondary nucleation (illustrated in Figure 1-15). Primary nucleation occurs in the absence of any crystalline solute. It has two distinct pathways, heterogeneous or homogeneous nucleation. In homogeneous nucleation, the formation of crystals occurs without the assistance of an interface or existing crystals. In primary heterogeneous nucleation, nucleation is induced by a foreign particle or interface, such as a dust particle or the crystalliser vessel walls.[87] In comparison, secondary nucleation is the formation of new crystals initiated by the presence of an existing crystal suspension. The source of crystalline solute could be from ongoing primary nucleation, or can be induced by an additive such as a seed crystal or template molecule.[38,88]

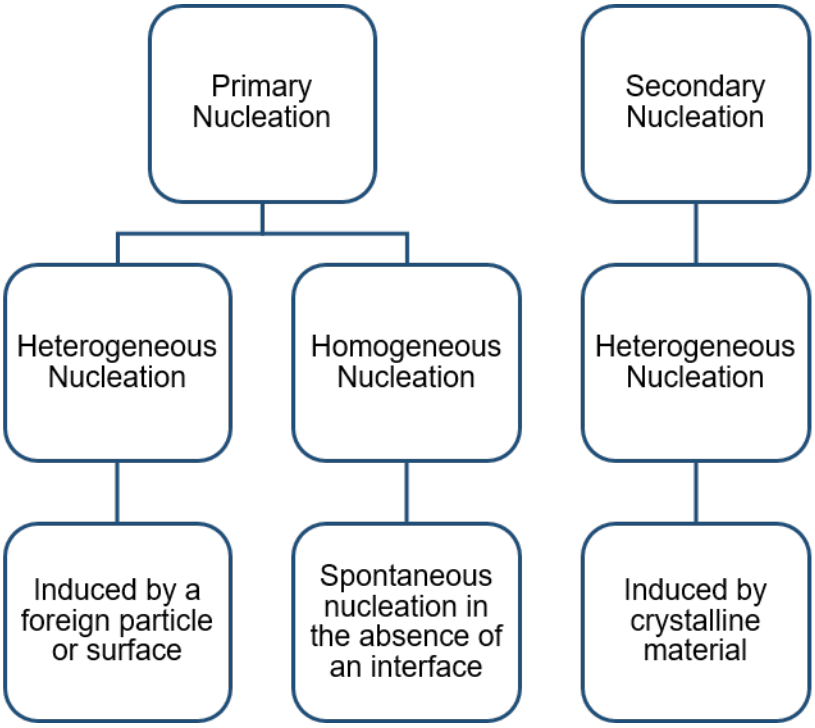

Figure 1-15: Nucleation pathways in crystallisation[88]

In primary nucleation, there are two nucleation pathways widely accepted within the crystallisation community: classical nucleation theory (CNT) and two-step nucleation theory (Figure 1-16). In CNT, fluctuations in the composition of a supersaturated

solution lead to the formation of a small nucleus which acts as a focal point for crystallisation.[45] In this model, small molecules of the solute are added one after another until it reaches a stable, critical size. The critical size of the cluster can be interpreted as the activation energy barrier to the formation of a crystal. In the two-step model, density fluctuations cause the formation of a highly disordered aggregate in the liquid phase, which subsequently crystallises after long-range order has reached a critical size.[45,89] In this model, crystalline order occurs progressively over time. In comparison, CNT builds one molecule at a time, with the cluster array having the same structure as the resulting crystal.[45]

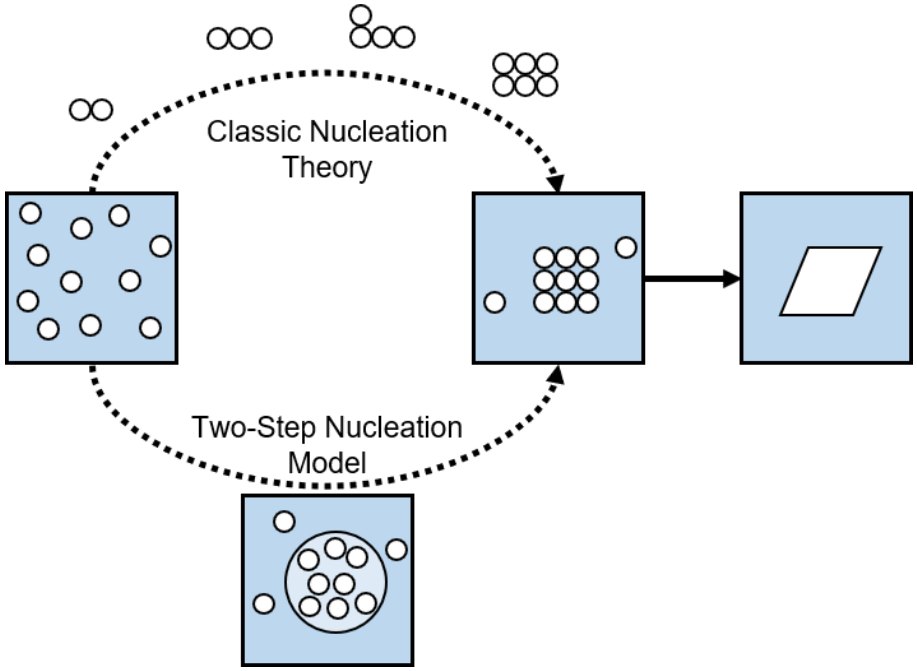

Figure 1-16: Nucleation models in crystallisation: classical nucleation (top) and two-step nucleation (bottom)[89]

In order for a cluster to crystallise, a free energy barrier must be overcome. The relevant phenomenon known as the critical cluster size (r_c), can be explained using a free energy diagram (Figure 1-17).[87] The free energy required for a cluster formation (ΔG) depends on the competition between the free energy for the formation of a surface (ΔG_s) and the free energy for the phase transformation (ΔG_v). The term ΔG_v favours growth, as there is a decrease in free energy when a molecule in a supersaturated system moves from the solution phase to the solid state. However, the ΔG_s term will increase as the introduction of a liquid/solid interface results in a positive free energy. This is proportional to the surface area of the cluster.[89] Therefore, small clusters where the

ΔG_s term dominates tend towards dissolution, but as cluster size increases, ΔG_v begins to exert greater influence. Once the total free energy passes through a maximum size (r_c), the total free energy will decrease continuously with growth becoming energetically favourable, resulting in the formation of crystal nuclei.[45] As supersaturation increases, the height of the energy barrier and the value of the critical size decreases, once the energy barrier is small enough, nucleation becomes spontaneous.[87]

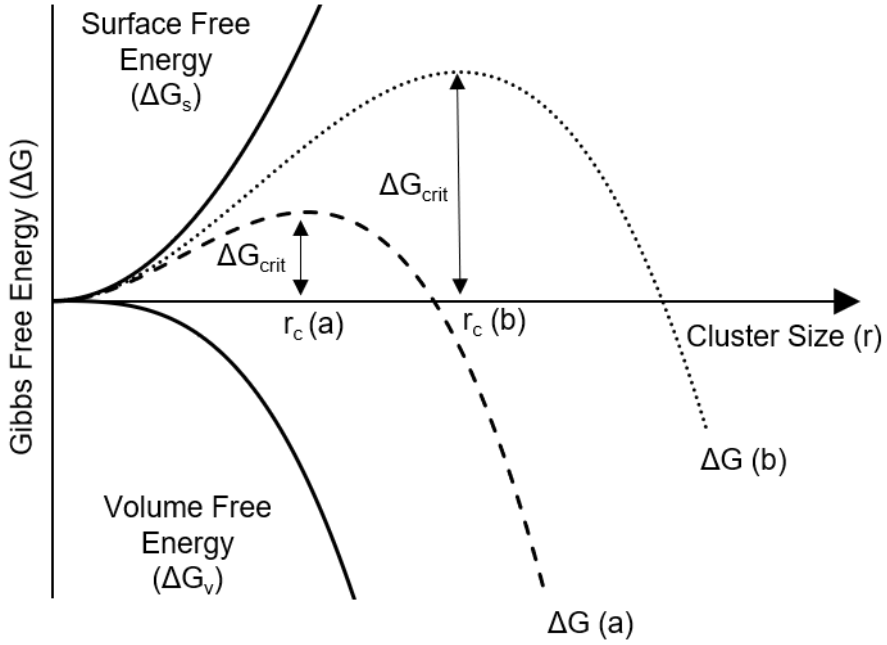

Figure 1-17: Free energy diagram for nucleation a) at high supersaturation, b) at low supersaturation[87,89]

In regards to heterogeneous nucleation (both primary and secondary), the presence of a foreign body or surface allows for nucleation at lower levels of supersaturation compared to homogeneous. This is due to the fact that adsorption onto a surface lowers the energy barrier (ΔG_{crit}) for a crystallising material. The amount that ΔG_{crit} is reduced by is strongly dependent on the degree of similarity between the structure of the crystallising material and the interface.[87] Thus, it can be inferred that secondary nucleation (e.g. by using seeding material) can be an effective strategy for controlling nucleation.[38] Once a nucleation event has occurred, the cluster can continue to grow into a larger, faceted crystal. The growth rate is dependent on a number of factors, such as the type of impurities present, the local mixing environment, the amount of particle breakage, agglomeration and the current supersaturation level.[38] Both particle size distribution and crystal morphology are influenced by the relative rates of nucleation and crystal

growth amongst other factors.[90]

1.6.2 Crystal Morphology

The overall shape of the crystal, termed either as the crystal habit or morphology, is an important parameter in crystallisation. In pharmaceuticals, the external shape of a crystal can influence important physicochemical properties such as bulk density, flowability, compressibility, melting point, solubility, stability, dissolution and bioavailability. As such, the crystal shape can have a direct impact on a drugs performance and processability.[87,90] As an example, Beck *et al.* investigated the influence of the size and morphology of calcium carbonate ($CaCO_3$) crystals on pressure filtration.[91] Crystals of $CaCO_3$ could be crystallised in several different morphologies including spherulites (polycyrstalline spherical particles), plates, cubic and needle shaped crystals. The spherical particles of $CaCO_3$ exhibited a similar polycrystalline behaviour to that of an aromatic amine derivative product of industrial interest, which suffered from filtration issues. Using calcium carbonate as a model compound, filtration experiments were performed at a constant pressure. Results indicated that a large particle size and narrow distribution improved the filtration of the spherical particles. The work also confirmed that $CaCO_3$ plate and needle-like crystals performed worse than spherical and cube-like particles during pressure filtration. This was attributed to the higher specific surface area, compressibility and tendency to break (leading to a larger particle distribution) in plate-like and needle crystals, which results in a higher cake resistance (Figure 1-18).

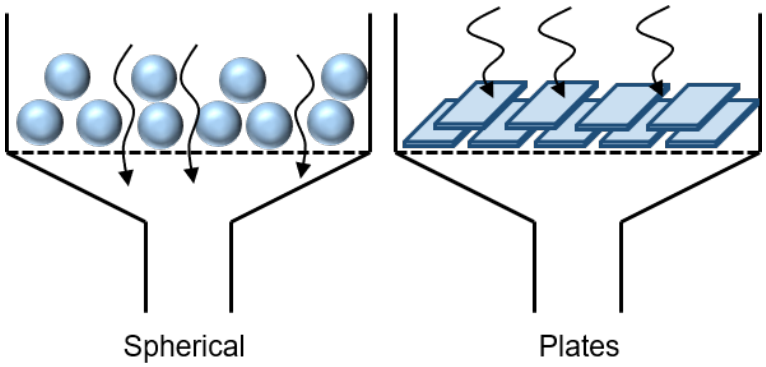

Figure 1-18: Effect of crystal morphology on filtration for spherulites and plate-like crystals. Adapted from Davey *et al.* with reference to Beck *et al.*[87,91]

1.6.3 Polymorphism

Polymorphism is defined as the ability of a chemical species to exist in two or more crystalline forms with different structural arrangements. Polymorphism is a widespread physicochemical characteristic and is observed in more than half of all APIs.[92] The strong interest in crystal polymorphism within the pharmaceutical sector can be attributed to the fact that differences in chemical and physical characteristics can arise with changes to the crystalline form.[93] These characteristics can often increase an API's effectiveness, such as increasing solubility or rate of dissolution, which can influence a drug's bioavailability. Polymorphism can also improve an API's mechanical properties such as compactability or flowability which can reduce the intensity of downstream processing steps like filtration or tableting.[93] Of course, polymorphism can also negatively alter such properties.

Control of the polymorphic form is of vital importance in drug development and is best illustrated by the well known example of ritonavir. Ritonavir, (marketed as Norvir® in 1996) was distributed as an oral liquid and as a semi-solid capsule for treatment of acquired immunodeficiency syndrome (AIDS).[94] Ritonavir is not bioavailable in the solid state and therefore a water/ethanol based solution was used to transport the API. Since the drug was solution-based, polymorphic control was deemed unnecessary and only one polymorph was identified (form I). However, an unknown but thermodynamically more stable polymorph (form II) of Ritonavir began to regularly crystallise over time. Form II was found to be more than 50% less soluble in the formulation than form I.[92] Ultimately, ritonavir had to be withdrawn from the market because the manufacturing process could not reliably produce the desired polymorph. The product was eventually relaunched, after an expensive and rigorous investigation was conducted to control polymorphic behaviour in the manufacturing procedure.[95]

Generally, there are two kinds of polymorphic systems - either packing or conformational polymorphism. Packing polymorphism arises when molecules can arrange in different structures within a crystal lattice. Conformational polymorphism occurs when different conformational isomers of a compound crystallise as distinct polymorphs.[94] Ritonavir is an example of conformational polymorphism, as the molecule can crystallise in a *trans* (form I) or *cis* (form II) formation and exhibits different bulk properties as a result.[96]

Under defined conditions, one polymorph is usually thermodynamically more stable. Polymorphic forms that deviate from the thermodynamically favoured structure are termed metastable. The metastable form will often undergo a phase transition to the

stable form.[93] The relative stability of polymorphs can be determined by calculating the difference in free energy. The Gibbs free energy of transition (ΔG_T) at a constant temperature and pressure is given by Equation 1.6:

$$\Delta G_T = \Delta H_T - T\Delta S_T \tag{1.6}$$

where ΔH_T represents the enthalpy difference between polymorphs, which reflects the difference in the lattice or structural energy. ΔS_T is the entropy difference, which relates the difference in disorder and structural vibrations. When $\Delta G_T < 0$, a transformation from the least stable polymorph can occur spontaneously. When $\Delta G_T = 0$, the two phases are in equilibrium while if $\Delta G_T > 0$, the transformation is not possible under the specified conditions.[92] ΔG_T can be estimated from the solubility ratio of two polymorphs (denoted form A and form B) in any given solvent from Equation 1.7:

$$\Delta G_T = RT \ln \left(\frac{\gamma_B c_B}{\gamma_A c_A}\right) \cong RT \ln \left(\frac{c_B}{c_A}\right) \tag{1.7}$$

where R is the gas constant, T is the absolute temperature, c_A and c_B are the solubilities of polymorph A and B respectively and γ_A and γ_B are the activity coefficients.[97] In dilute solutions, form A and B will be indistinguishable when dissolved. In this case the ratio of activity coefficients (γ_B/γ_A) will be ≈ 1 and therefore the relative thermodynamic stability of two polymorphs can be estimated from the ratio of their solubilities.[97,98] As the solubility is directly proportional to the free energy of a polymorph, determination of solubility is an effective method for comparing the stability of polymorphic forms.[87,92]

The relationship between polymorphs can be enantiotropic or monotropic. Enantiotropic polymorphs have a transition temperature ($T_{\text{transition}}$) which is lower than the melting point of the lowest melting polymorph. In this case, the relative stability between two polymorphs changes before and after the transition point. In a monotropic system, the transition point is above the melting point and therefore, one polymorph is always the more stable over a given temperature range.[97] In a monotropic system the most stable polymorph will always be the least soluble, regardless of temperature. In an enantiotropic system, the most soluble polymorph (and therefore most stable) will be temperature dependent (Figure 1-19).[87]

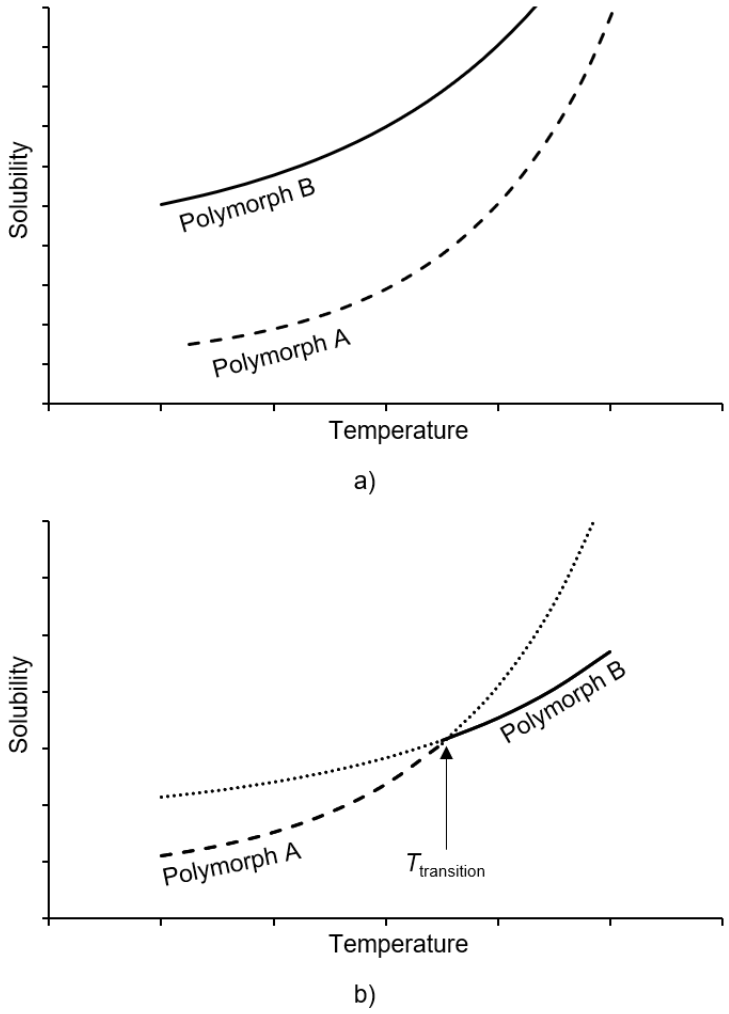

Figure 1-19: Solubility curves in a) monotropic and b) enantiotropic systems. Adapted from Davey *et al.*[87]

The overriding factor in pharmaceutical drug development is usually stability. As was demonstrated in the case of ritonavir, if the most stable form is not identified then this can have serious repercussions on a product's longevity. However, some metastable polymorphic forms are stable for extended periods and undergo a phase transition over extremely long time frames. In these cases, the choice of which polymorph to target will depend on which form demonstrates the most important and desirable properties.[88]

1.6.4 Multi-component Crystals

Multi-component crystallisation is the formation of crystalline solids containing two or more molecular species.[99] The incorporation of a second component (coformer or

solvate molecule) into a crystallisation can alter the crystal structure, providing a route to modifying the properties of a solid. In pharmaceuticals, multi-component crystallisation can be used to enhance solubility, dissolution rate, stability or increase mechanical properties.[92] Figure 1-20 depicts three common multi-component solid-states.

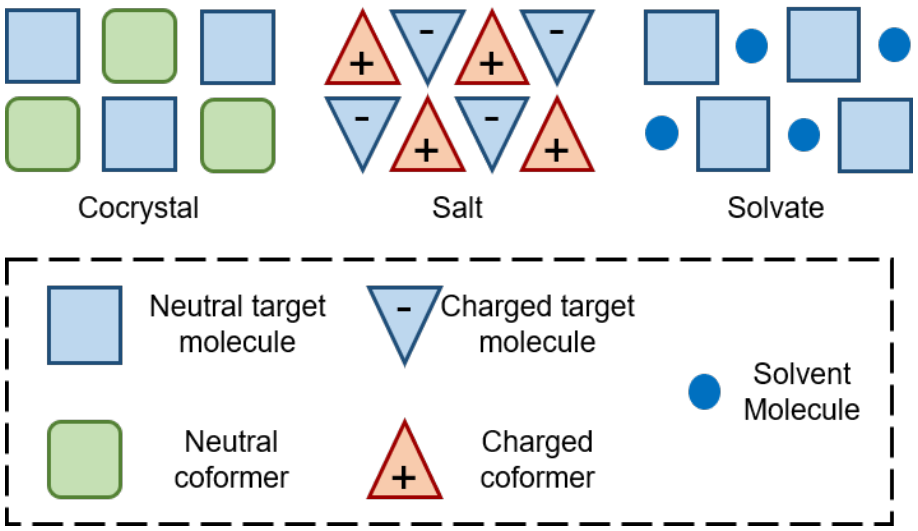

Figure 1-20: Representations of multi-component crystal systems

Solvates

A solvate is a crystalline solid that incorporates a solvent molecule into a crystal lattice.[100] A solvate usually exhibits different physicochemical properties than the original solid phase. In pharmaceutical development, hydrates (the incorporation of a water molecule into the crystal structure) are the most important solvate. Water's relatively small size and ability to serve as both a hydrogen bond donor and acceptor, make it likely to be incorporated within the lattice. As such, water can act as a stabilising force and prevent collapsing of a crystalline structure.[93] This factor along with its non-toxicity makes hydrates attractive targets for incorporating APIs.[100]

Salts

A salt consists of a crystalline solid that contains two or more components in which proton transfer is complete.[101] Salt formation is widely used with ionisable drugs. More than half of APIs approved by the FDA are pharmaceutical salts.[100] The most common salt formation is between an acidic and basic molecule, but zwitterionic salts are also prevalent. In the solid state, the pKa change during the reaction of an acid and a

base is used as a predictor of salt formation. If the pKa change is three or more, then the substance formed is predicted to be a salt.[101] As with hydrates, forming a salt is a simple, cost-effective method for improving low solubility and enhancing an API's bioavailability.[102]

Cocrystals

A cocrystal and a salt are relatively similar, however in a salt, a proton is transferred from the acidic molecule to the base component, whereas in a cocrystal no hydrogen transfer occurs; the components remain neutral.[92] It is generally excepted that there is a continuum that exists between cocrystals and salts. Cocrystals can be expected where a pKa change of less than one is observed. However, this leaves some ambiguity in defining a multi-component system with a ΔpKa between one and three.[101] Cocrystal formation is a viable alternative solid form when salt or polymorph formation does not meet the required specifications. Cocrystals do not rely on the target molecule being ionisable and bonding of the two components occurs through intermolecular forces (hydrogen bonding, $\pi - \pi$ interactions and van der Waals) in the crystal lattice. As such, the number of potential targets with respect to cocrystallisation (such as non-ionisable APIs) is greatly increased.[102]

As with single component crystals, solvates, salts and cocrystals are also capable of displaying polymorphic behaviour. Polymorphs of multi-component crystals can have significantly different properties. In pharmaceuticals this can influence bioavailability, stability and dissolution, while in materials science properties such as photoluminescence, mechanical strength and colour can be tuned using cocrystallisation.[103–105]

1.6.5 Thermochromism

Building multi-component crystals offers the potential to tune bulk physicochemical properties by changing intermolecular interactions within a crystal structure. Thermochromism refers to the phenomenon where a material changes colour in response to a temperature change. Materials which undergo a colour change in response to temperature have the potential for applications in imaging, sensing and smart devices.[106,107]

Thermochromism is not exclusive to multi-component crystals nor to small organic molecules.[106,108] However a number of cocrystal systems investigated by Jones *et al.* have been shown to afford a thermochromic change upon heating (Figure 1-21).[109] Thermochromism in these systems is facilitated by a proton transfer mechanism in the solid-state. While the isolation of these related crystal systems has been possi-

ble, reproducible production of the thermochromic cocrystal is difficult in batch.[110] This highlights that while cocrystallisation is an effective tool, it can still suffer from difficulties encountered in single-component crystallisation like reproducibility and elusive polymorphs.[111] As such, the finer control that continuous manufacturing offers could be an effective method for controlling the crystallisation of multi-component systems.[112,113]

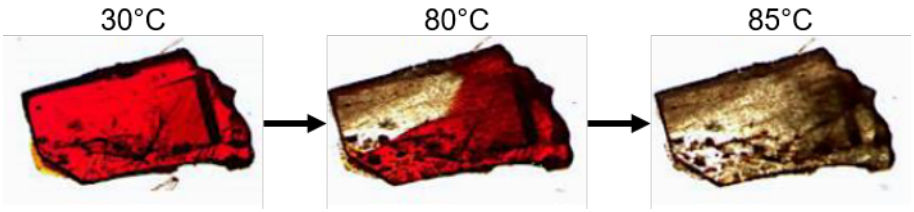

Figure 1-21: Thermochromism of the cocrystal 4-iodo-2-methylaniline:3,5-dinitrobenzoic acid.[109]

1.6.6 Crystallisation Techniques

In order to initiate crystallisation, it is necessary to generate first a supersaturated system. Figure 1-22 and Figure 1-23 depict common methods for generating supersaturation in solution mediated crystallisations. An overview of each method is outlined below. It is important to note that crystallisation techniques are not mutually exclusive, it is relatively common to employ more than one crystallisation technique in order exert greater control or improve the yield of a crystallisation. Examples of combined crystallisation methods include seeded-cooling[114] or reactive-antisolvent crystallisation.[115]

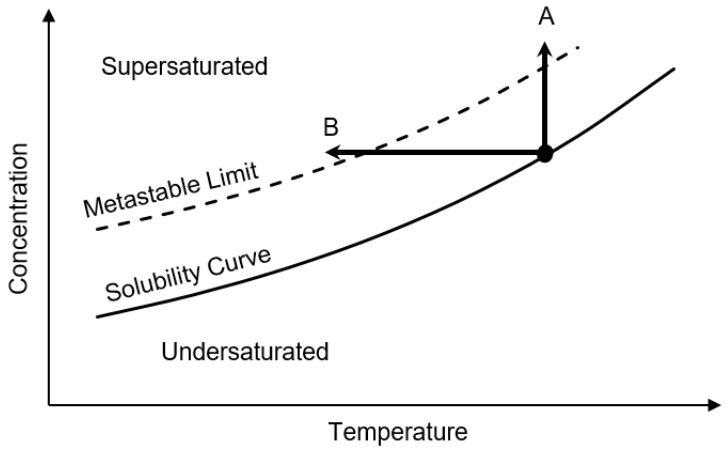

Figure 1-22: Crystallisation techniques: A - evaporative (increasing concentration over time), B - cooling (decreasing temperature over time).[38]

Evaporative Crystallisation

Evaporative crystallisation involves dissolution of the target material into a chosen solvent. The system is initially undersaturated, but as the solvent is left to evaporate over time, saturation gradually increases. Eventually the solution becomes supersaturated and nucleation occurs, the concentration will drop slightly and crystals begin to grow. As the solution continues to evaporate, the solution again becomes supersaturated and crystallisation proceeds further. This cycle is repeated until the crystallisation is completed.

Evaporative crystallisation is a fast and effective screening method. It requires a minimum amount of material and preparation time, making it a technique of choice for screening for desirable solid forms. However, it can be difficult to control as variations in temperature, solvent composition and encrustation results in difficulties in reproducing results.[88] Furthermore, evaporative crystallisation has limited scalability, as evaporation of large quantities of solvent is both energy intensive and unsustainable.[86] As such, once a desired crystal form has been identified from an evaporative crystallisation, the process is often transferred to a more controllable method such as cooling or antisolvent addition.

Cooling Crystallisation

Cooling crystallisation is an effective method in both batch and continuous crystallisation platforms. In cooling crystallisation, a solution is prepared where the target material is undersaturated at a heightened temperature. The solution is then cooled until the system becomes supersaturated and nucleation occurs. As the solution is cooled further, the system becomes increasingly supersaturated and more crystal growth takes place. Cooling crystallisation offers much greater control over a crystallisation process than evaporative. For example, a crystallisation can be designed so as to promote crystal growth and prevent encrustation issues by ensuring that the level of supersaturation remains within the MZW.[86] In controlled systems, one can also program a cooling profile to reflect the desired level of supersaturation at each stage of the crystallisation. As such, cooling crystallisation is often employed in API production where control of the cooling process allows greater control over particle size, crystal shape and purity.[88]

Antisolvent Crystallisation

Antisolvent crystallisation induces crystallisation by reducing the solubility of the material to trigger nucleation. The method requires identification of a solvent in which

the substance has a very low solubility (i.e. the antisolvent). Addition of the antisolvent (sometimes termed drowning out) changes the solvent composition, reducing the solubility of the substance and therefore generating supersaturation (Figure 1-23). As the level of supersaturation is dependent on the solvent composition at a constant temperature and pressure, one can use antisolvent addition rate to finely control crystal growth. This method makes antisolvent crystallisation processes attractive where a material's solubility has a low dependence on temperature.[116,117] However, antisolvent crystallisation is also dependent on mixing and issues can arise with encrustation where localised supersaturation occurs.[45]

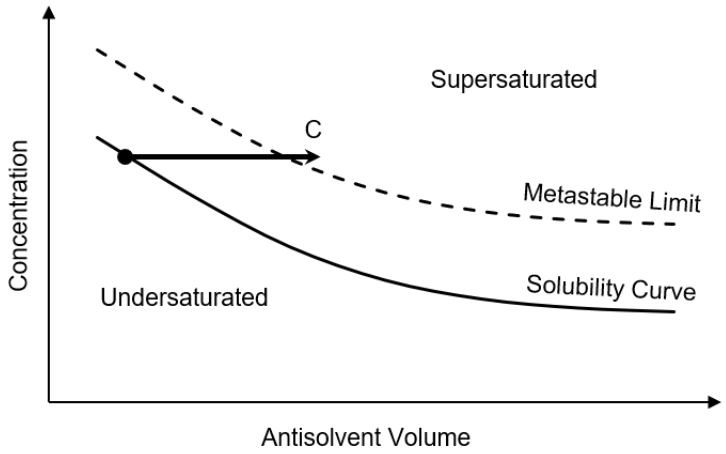

Figure 1-23: Antisolvent crystallisation: arrow indicates increasing ratio of antisolvent to solvent composition

Seeding Crystallisation

Seeding crystallisation can be an effective method for controlling a crystallisation process. For instance, seeding with a desired polymorph can allow for the selective growth of the desired crystalline form.[114] While some systems do nucleate spontaneously, controlling the nucleation rate, particularly on scale-up, can be subject to unanticipated process variation.[118] The addition of a seeding crystal allows for secondary nucleation to dominate at lower supersaturation values. Seeding impacts all aspects of a crystallisation process; including crystal morphology, particle size distribution, crystal growth, nucleation rates and product purity.[119] From a phase diagram perspective seeding eliminates the need for primary nucleation and so crystal growth can be contained to be within the metastable zone (Figure 1-24).

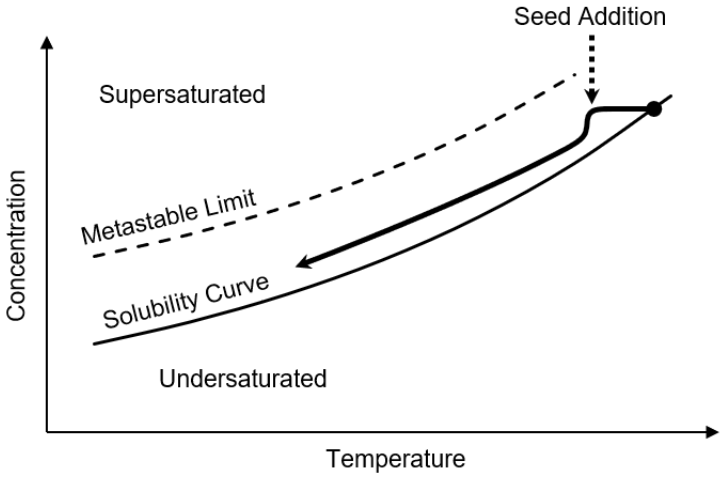

Figure 1-24: Schematic diagram for a seeded-cooling crystallisation, arrow tracking decreasing concentration of solute in solution as seeding/cooling progresses.

Reactive Crystallisation

Reactive crystallisation is the formation of an insoluble crystalline solid from freely soluble parent molecules.[120] Like antisolvent crystallisation, reactive crystallisation does not rely on temperature dependent solubility. However both antisolvent and reactive crystallisation are dependent on solution homogeneity. Good mixing is needed to ensure crystal growth control. While this can be limiting in batch, both antisolvent and reactive crystallisation techniques are particularly amenable to flow where they can benefit from the improved mixing regimes.[115] Often the driving force for supersaturation in a reactive crystallisation is a change in pKa. Hence, reactive crystallisation is usually limited to salt formation or cocrystallisation in organic molecules.[121]

1.7 Continuous Crystallisation

Crystallisation in fine chemical and pharmaceutical manufacturing is traditionally carried out as a batch operation, but the current drive towards implementing continuous manufacturing in pharmaceuticals has led to increased interest in developing and applying continuous crystallisation methods.[18] Continuous crystallisation relies on many of the same crystallisation techniques as batch (cooling, antisolvent, evaporation, seeding etc). However, operation of the feed solution is constant and a slurry is steadily withdrawn from the reactor (Figure 1-25), this is analogous to flow synthesis, where reactants are fed into the reactor and product(s) continuously withdrawn.[46]

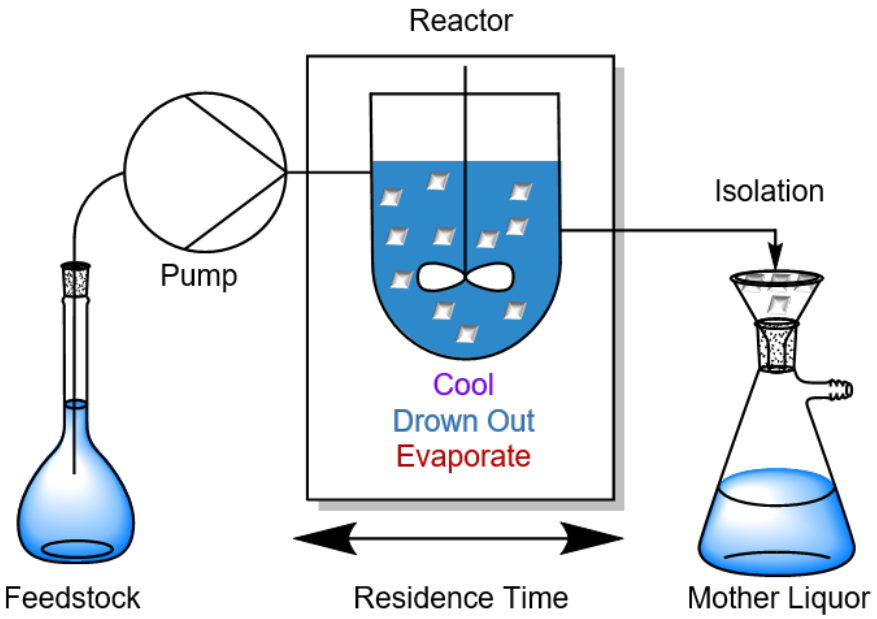

Figure 1-25: Simple set-up for continuous crystallisation

There are two main categories of continuous crystallisers: continuous stirred tank reactors (CSTRs) and tubular crystallisers.

1.7.1 Continuous Stirred Tank Reactors (CSTRs)

The continuous stirred tank reactor or mixed suspension mixed product removal (MSMPR) is one of the most commonly employed continuous crystallisers. The CSTR can be run as a single unit of operation or in series of cascading reactors (Figure 1-26). Generally a single CSTR is used for crystallisation kinetics studies.[122] However, as outlined in Section 1.4.3, a single CSTR tends to have a wide residence time distribution (RTD) and imperfect mixing. As such crystallisation processes typically use CSTRs in tandem, where the outlet of one stage is fed into another. In this way the system begins to approach plug flow and reduces the batch-to-batch variability of a process. A multi-stage CSTR system has a number of potential advantages. The design of each stage is analogous to a batch reactor so implementing a CSTR system is easier from pre-existing batch equipment. Careful design of the transfer method for the solid suspensions between vessels ensures the system is effective at handling high solid loadings. The addition of the feed and withdrawal of the product can be controlled, allowing adjustment of the residence time. Furthermore, transfer between vessels can be paused temporarily to extend the crystallisation operating cycle (periodic

steady state) or operated continuously (steady state).[123] Each individual vessel can be heated or cooled as needed, allowing a step-wise cooling profile to control crystal growth. Multi-stage CSTRs are relatively versatile, but the systems can suffer from encrustation, impurity build-up and lower yields (in comparison to batch). Methods have been devised to reduce these drawbacks, such as recycling the mother liquor,[124] *in situ* process monitoring[122] and in-line separation of impurities.[125]

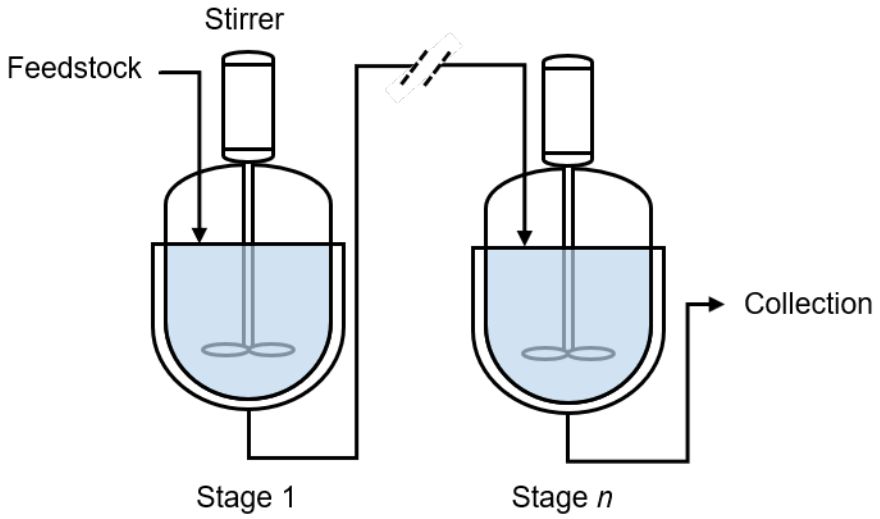

Figure 1-26: Schematic diagram for a series of CSTRs, where n = the number of CSTR operations

The potential benefits for using an CSTR are demonstrated by Agnew *et al.* Here researchers demonstrated the scaling-up of batch production of paracetamol (PCM) form II in a CSTR system. Form II is the metastable polymorph but displays enhanced physical and mechanical properties compared to PCM form I. A structurally similar molecule (metacetamol) was used as an additive in solution to preferentially crystallise PCM form II. In both batch and continuous operation, high purity of the desired form II polymorph was achieved. However continuous crystallisation in CSTRs showed superior purity compared to batch, as no traces of PCM form I or metacetamol impurities were found in the final product.[126] The authors highlight the ease in which the batch process could be transferred to the CSTR system, as well as indicating the improved reproducibility exhibited by the continuous process.

1.7.2 Tubular Crystallisers

The other common reactor design for continuous crystallisation is the tubular crystalliser. In this system the feedstock is pumped through a tube where crystallisation is

controlled by increasing supersaturation. The crystalline product is continuously withdrawn from the reactor outlet. In theory, a cascade consisting of an infinite number of CSTR crystallisers is equivalent to a plug flow tubular reactor, but the amount of equipment required to reach this stage is practically unfeasible.[46] Therefore plug flow is generally far simpler to achieve and more cost-effective in a tubular reactor. Figure 1-27 outlines some common methods for achieving plug flow in tubular crystallisers.

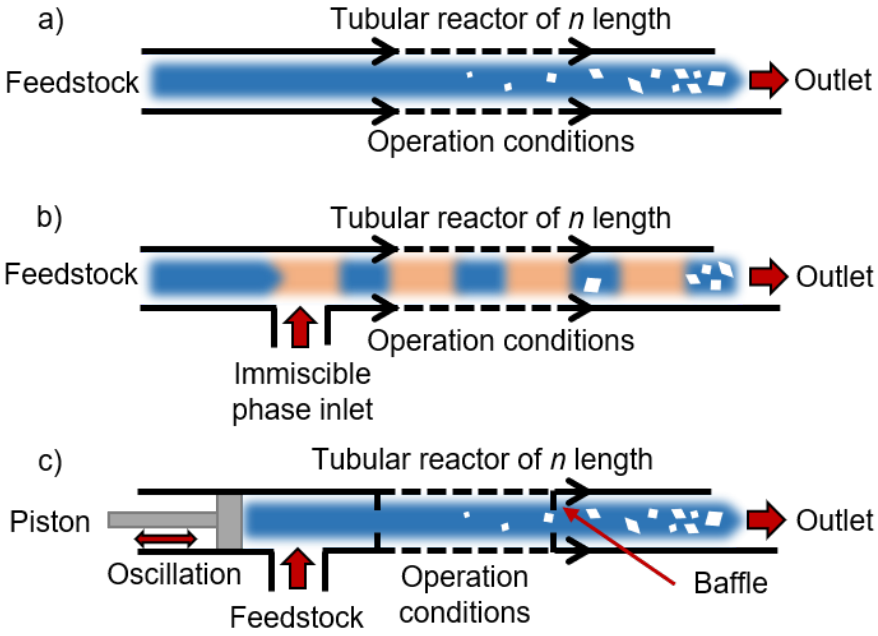

Figure 1-27: Schematic diagram depicting methods for achieving plug flow in tubular crystallisers via: a) high velocity flow, b) segmented flow or c) using an oscillatory baffled reactor

The simplest method to achieve the desired plug flow dynamic is to pump the feedstock at high velocity. As determined from Equation 1.2, generating a Reynolds number around 4000 results in a turbulent system and plug flow. However in this case, the required velocity is so high that an unfeasibly long tube is required, thus a high velocity system is usually only ever useful for very fast crystallisation processes. To overcome this drawback, a secondary mechanism is usually employed to achieve plug flow. One possibility is the introduction of a series of static mixers. Static mixers promote the mixing of fluids without using moving parts (Figure 1-28).[127] The introduction of static mixers has been demonstrated to enhance the mixing between feedlines, help suspend particles in solution and to narrow the particle size distribution.[53,128]

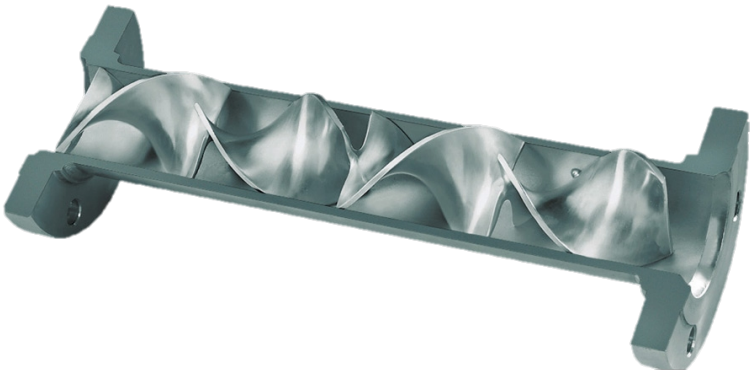

Figure 1-28: Photograph of a Kenics^{TM} KM static mixer where helical structures direct the flow of material[129]

Another method is to introduce an immiscible phase to segment the feedstock into discrete slugs. The introduction of a secondary phase ensures no back-mixing can occur, thereby achieving plug flow. The secondary phase can be an immiscible liquid or a gas. The benefit of this design is that plug flow can be achieved while maintaining slow, laminar pump regimes. As such, the residence time distribution in segmented flow tends to be narrow.[130] Furthermore, the introduction of a secondary phase can also improve the mixing within each slug. The slugs circulate within the tubing, forming eddies which ensures a homogeneous environment.[131] The size and number of slugs can be controlled by the frequency of the immiscible phase. The downside to this technique is that separation of the phases is often required for collection of the crystalline product. In most cases this can be relatively straightforward, but surface interactions can sometimes lead to the two liquids forming an emulsion. Therefore, careful selection of the immiscible phase is necessary. Some of the work in this thesis will be concerned with the development and optimisation of the kinetically regulated automated input crystalliser (KRAIC) which is categorised as a segmented flow crystalliser. Further detail on the KRAIC design will be supplied in Chapter 2.

A continuous oscillatory baffled crystalliser (COBC) consists of a series of tubes with baffles periodically arranged inside. A piston or bellow is used in combination with pumps to generate a pulsating flow regime. As the flow moves through the tube the baffles restrict the movement of the fluid. This leads to the generation of eddies within each baffled segment, which provides turbulent mixing (Figure 1-29). As the mixing regime is dissociated from the net flow rate and each baffled segment is homogeneous, the system is essentially running at plug flow without the need for a high velocity flow rate or the introduction of a immiscible phase.[44] Additional advantages have been

described, including good suspension of solids and slurries, enhanced heat and mass transfer capabilities and easier scale-up. Limitations of the technology in crystallisation has been encrustation issues, fluid viscosity and particle density limits as well solid loading limit.[37]

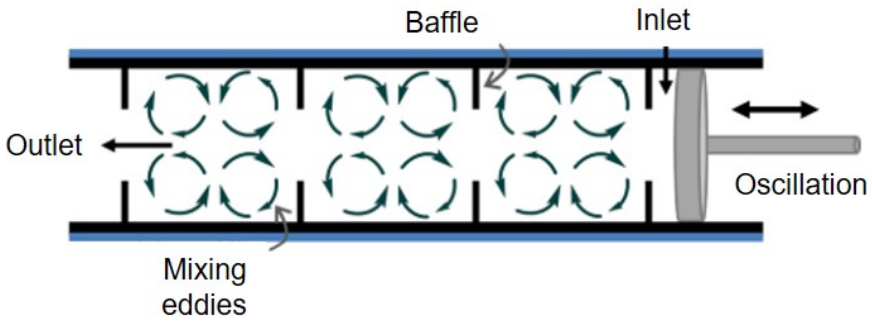

Figure 1-29: Generation of eddies in a COBC system[37]

Several examples exist of successful API crystallisation in a COBC system including; paracetamol (additive-cooling crystallisation),[126] β-l-glutamic acid (seeded-cooling crystallisation),[132] α-lipoic acid:nicotinamide (cocrystallisation) and salicylic acid (antisolvent crystallisation).[133] Of particular note, Brown *et al.* demonstrated the continuous operation and production of salicylic acid (commonly used in aspirin) for more than 100 residence times. During the work, operation under steady state conditions produced over 800 g in 6 hours (a productivity of 3.2 kg day^{-1}) with a narrow particle size range 35.1 ± 3.2 µm.[133]

The attraction of operating under plug flow in a COBC or similar plug flow system, is that under controlled steady state conditions, each particle in theory experiences an identical environment during operation. This leads to a uniform and consistent product. In addition, unlike a CSTR, tubular reactors do not have impellers, which can cause particle breakage and uncontrolled secondary nucleation events. While it is important to note that the current research scale crystallisers cannot compete with established batch mass production methods, the potential to deliver consistent particle size, scalable processes and other critical attributes over an extended period could prove attractive for delivering high value-low production chemicals. As these practices become more established, this may eventually lead to the adoption of continuous crystallisers across a wider field of the fine chemical and pharmaceutical industry.

1.8 Integration

One of the largest challenges facing continuous manufacturing (CM) is integration of processing technologies. While great strides have been taken in the areas of flow synthesis and continuous crystallisation, the amount of research dedicated towards integrating these operations is relatively sparse. When considering the potential benefits of CM it is important to consider the holistic viewpoint. Complex small molecule production requires multiple stages of operation. For instance, API processes will likely require several stages including synthesis, crystallisation, filtration and formulation of the drug (Figure 1-30). If a process is only partly converted to continuous operation, then inadvertently, the batch steps could become a process bottleneck. In these cases, this can add unnecessary complications to a system such as holding times, material transportation, chemical storage and safety issues. Ideally an integrated (end-to-end) approach to CM will provide more benefits than a partially continuous (multi-stage) approach. However, it is not always possible or indeed necessary to pursue an end-to-end CM process. Ideally, the mode of operation should suit the chemistry and a continuous multi-stage or semi-batch approach may be the most viable.

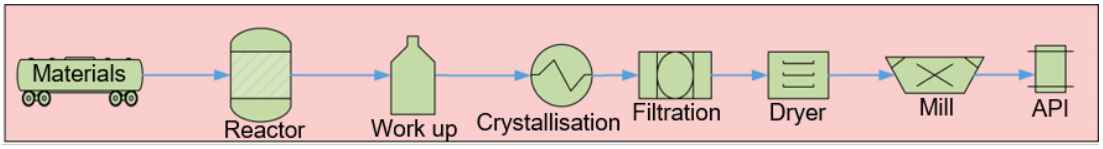

Figure 1-30: Typical workflow for API production[134]

Nonetheless, an integrated or partially-integrated process offers some key advantages including increasing production speed, greater cost effectiveness, minimising environmental impact, simplifying product supply chain, reducing materials inventory, *in situ* processing of unstable intermediates, reduction in plant space requirements as well as easier scale-up.[27]

1.8.1 Multi-step and Telescoped Processing

Multi-step processing or telescoped processes involve two or more continuous chemical transformations that are carried out within the same unit of operation (i.e. multiple synthetic steps in flow) or, where the output of one stage of operation is fed into another continuously (e.g. flow synthesis followed by continuous crystallisation). In both cases, the set-up can be considered a partially integrated mode of operation, but not end-to-end continuous manufacturing.

There are plenty of examples of telescoped reactions where two or more synthetic reactions are carried out in tandem, sometimes eliminating the need for intermediate work-up or purification.[135–137] However, most processes require a purification step at some stage, which is often carried out in batch. In order to deliver integrated systems, the replacement of batch processes with continuous downstream technologies is necessary for multi-stage and end-to-end continuous manufacturing.

There are examples of multi-step reactions which use in-line crystallisation or purification techniques, but the sector is relatively underdeveloped compared to telescoped flow synthesis. In-line work-up methods that have been used include liquid-liquid extraction,[138,139] scavenger columns,[21,140] column chromatography,[141,142] distillation[143] and crystallisation.[144] As a recent example, Loren *et al.* showed the synthesis and in-line crystallisation of diphenhydramine (DPH).[145] DPH is an antihistamine commonly found in several medicinal products. In this work, researchers developed a novel, miniaturised pharmaceutical purification platform (MiniPharm), which was integrated with a microreactor and on-line monitoring system (Figure 1-31).

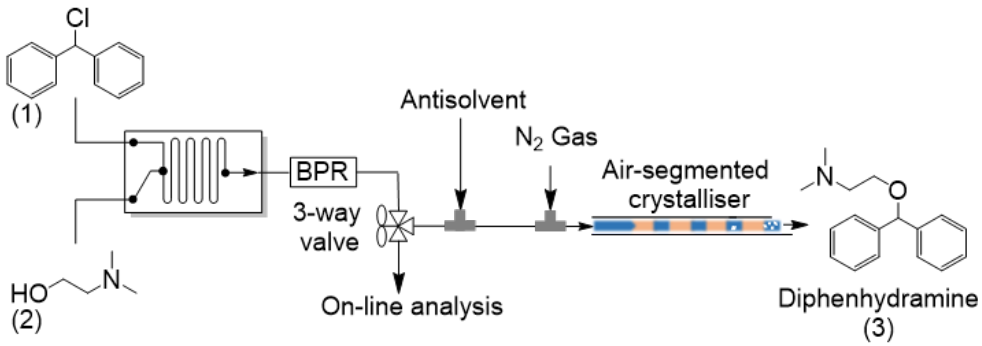

Figure 1-31: Simplified diagram of the flow synthesis and segmented flow crystallisation of diphenhydramine

In this set-up, DPH was prepared from chlorodiphenylmethane (1) and dimethylaminoethanol (2). A chip reactor was used to rapidly mix the streams, and a back pressure regulator (BPR) was used to maintain high pressure while operating above the solvent's boiling point. On-line monitoring and optimisation of the reaction was carried out using mass spectrometry methods. The introduction of a segmented flow crystallisation process reduced fouling issues encountered in the system, ensuring that $128\,\mathrm{mg\,h^{-1}}$ of DPH could be processed without issues.[145] While this work provides a good example of integrating synthesis, crystallisation and on-line monitoring, the system is limited to the microfluidic scale. In order to process high solid loadings or large crystal sizes, it will be necessary for the integration of macro or meso-scale crystallisers into multi-step

processes. Without the development of versatile, continuous work up and purification technologies that can handle a range of solid-state parameters, the delivery of integrated flow in the fine chemicals industry will remain challenging.[146]

1.8.2 End-to-End Integration

End-to-end integration of continuous manufacturing (CM) is the idea of delivering a final product from raw materials without isolation or downtime. While end-to-end manufacturing maximises the benefits of integrating units of operation, examples of end-to-end manufacturing in pharmaceuticals and fine chemicals are relatively few. End-to-end CM faces many challenges including complex control and feedback loops for product quality control, in-line reaction monitoring, solid and slurry handling, accumulative dilution problems in multi-step processes and bridging gaps in units of operation.[25]

An interesting example of bridging operational technologies was developed by Balogh *et al.* In this work continuous production of a drug was developed by coupling flow synthesis with formulation, via electrospinning (ES) (Figure 1-32).[147] The work describes a bench-top scale coupling of flow synthesis and drug formulation targeting acetylsalicylic acid as a model drug compound. In the work, ES is the key enabling technology to turn the API-polymer solution into a fibrous solid product which was applied to a water-soluble film. The work represents one of the few examples to incorporate formulation in an integrated process and while the authors demonstrate formulation directly after synthesis of the API-polymer solution, it is entirely possible that the ES unit could also be applied after a purification step in a more complex workflow.

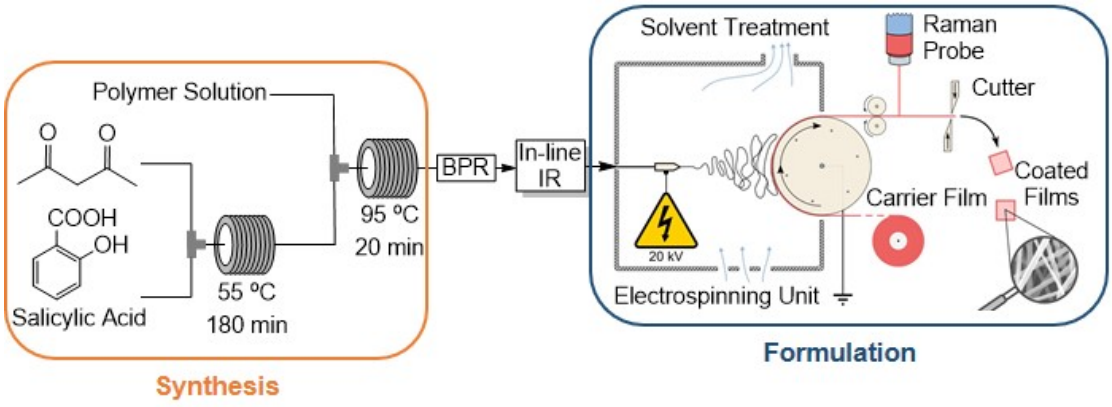

Figure 1-32: Schematic diagram of the end-to-end production of acetylsalicylic acid fibres in flow (adapted from Balogh *et al.*)[147]

Perhaps the biggest breakthrough in delivering pharmaceuticals end-to-end was carried out by Mascia *et al.* Here researchers delivered a continuous integrated process for the delivery of the API, aliskiren hemifumarate (AH). The chemical transformation proceeds through 14 operation units including; two synthetic reactions, two crystallisations, four separations, two washes and dilutions followed by an extrusion and mould process. The result is a platform capable of producing AH from a stable precursor through to formulation of the tablet in an unbroken, continuous process (Figure 1-33). The total end-to-end residence time was 47 hours, which was more than six times faster than the batch process. The process throughput was 41 $\mathrm{g\,h^{-1}}$ which corresponds to over 8500 tablets a day. Notably, researchers reported several advantages to running the process end-to-end. For instance, the synthesis was shown to be much faster in flow (3-4 hours vs 72 hours in batch). The reaction in batch usually needs to be cooled before separation (due to reactor conditions being above the solvents boiling point) however, in flow the separation can be carried out in-line at high pressure without issue. Furthermore, the CSTR crystallisers acted as buffer units, as their long residence times mean fluctuations in the upstream concentration can be mitigated and adjusted for without interrupting the process. Finally, the melt extruder unit streamlined the process, avoiding the need for milling, blending or granulation of the drug product. The melt can be directly fed into the tablet moulding process. This significantly decreased the energy footprint and time required to go from drug substance to the final tablet.[27,38,144,148]

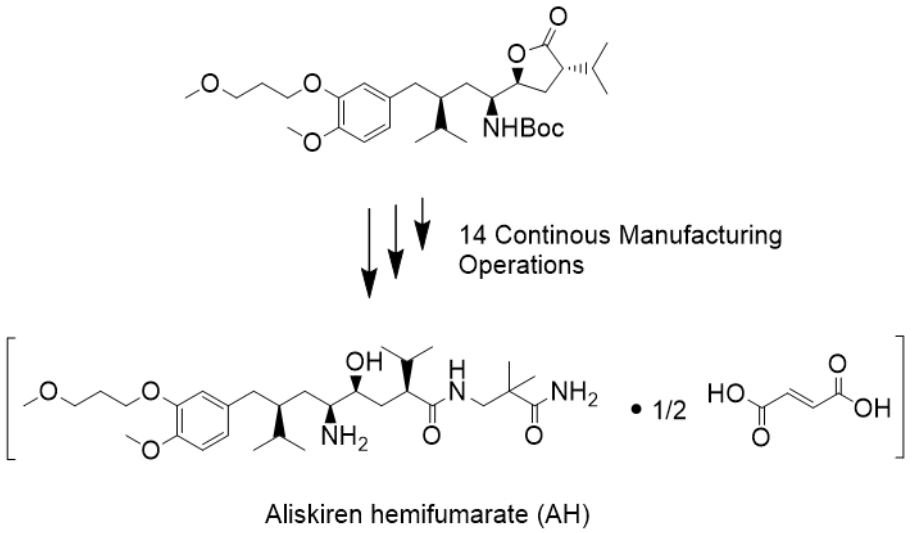

Aliskiren hemifumarate (AH)

Figure 1-33: Structure of the precursor (top) and tabulated product: aliskiren hemifumarate (bottom) in the integrated, continuous plant.

Following on from this pioneering work, a continuous manufacturing platform that combines both synthesis and final drug product formulation into a single, highly compact unit was developed (Figure 1-34). The modular system uses a series of reconfigurable tubular reactors, membrane separators, gravity separators, filtration units and CSTR crystallisers.[26,149] The platform has demonstrated continuous synthesis and crystallisation of several drug compounds, including rufinamide, diphenhydramine, fluoxetine, lidocaine and diazepam.

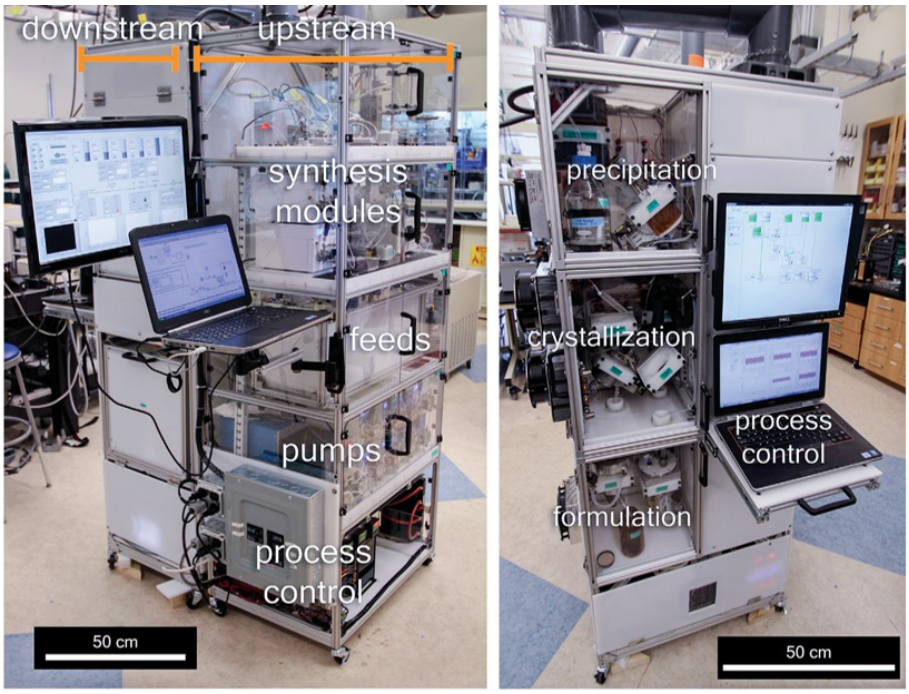

Figure 1-34: Photographs of the reconfigurable compact plant by Adamo *et al.* for continuous production and formulation of APIs[149]

Finally, the first continuous process that delivers a drug product meeting good manufacturing practice (GMP) was developed by Eli Lilly for the synthesis of prexasertib. The plant, consisting of eight continuous operations, resulted in the production of 3 kg day^{-1} of material for clinical trials. However, the process had to be separated into three-stages due to size restraints, while the final crystallisation, filtration, and drying stages were conducted in batch systems.[11] As the authors note, because of time constraints, the development of a continuous downstream process was not implemented. This reflects the need for greater understanding and development of robust continuous crystallisation and other downstream processes that can be integrated with upstream systems routinely.[150,151] Despite this, the work does demonstrate how integrated process development and CM can be applied to and successfully meet current GMP standards.

Chapter 2

Experimental Methods

2.1 Introduction

For specific experimental procedures, see the individual chapters. This chapter details the general experimental and analytical methods commonly utilised throughout the study.

2.2 Materials

Starting materials and solvents were sourced from commercial suppliers Sigma-Aldrich® and VWR International with no further purification.

The carrier fluid used in segmented flow crystallisation experiments was a fluorinated perfluoropolyether (PFPE), commercially known as Galden SV110, which was sourced from Solvay.

In Chapter 4, the manganese dioxide catalyst and the starting material pyrazinecarbonitrile were provided by the Steven Ley group, University of Cambridge.

In Chapter 6 all raw materials were supplied by AstraZeneca for the duration of the project. The reference succinate salt of the target active pharmaceutical ingredient (API) was sourced from the current commercial process after isolation.

2.3 Gravimetric Solubility

Gravimetric solubility studies were carried using the Cambridge Reactor Design (CRD) Polar Bear Plus reactor. The Polar Bear Plus is a platform for programmable heating and cooling cycles over a temperature range of −40 to 150 °C. It has interchangeable inserts that allow scaling up of systems from 1.5 to 250 mL (Figure 2-1). Solubility measurements were carried out in 20 mL, screw cap glass vials. A known volume of solvent was decanted into each vial and heated or cooled to the desired temperature. The vials were stirred continuously at a controlled stirring rate of 500 rpm. Excess solid matter was added until a persistent slurry was achieved. The slurry was left for at least 4 hours to equilibrate before filtering using a disposable syringe into a pre-weighed vial. The vial was sealed and weighed before being allowed to evaporate and dry in an oven at 50 °C overnight. The change in the mass of solution vs the dry solute allowed the concentration to be determined. Using this data, a solubility vs temperature graph was constructed to give a solubility curve. Each run was repeated in triplicate. The same procedure was used to determine the solubility of 4-hydroxyacetophenone (4HAP) and 4-hydroxyacetophenone oxime (4HAPO) in ethanol/water mixtures at 20 °C.

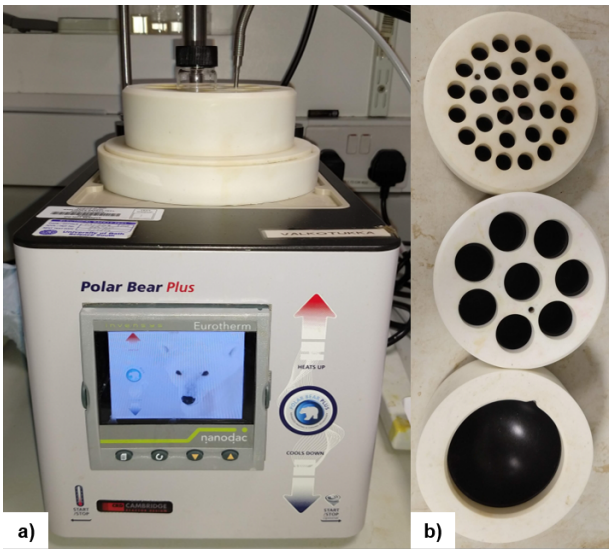

Figure 2-1: Photographs of a) the Polar Bear Plus reactor b) the interchangeable inserts

2.4 Synthesis

2.4.1 One-pot Amidation of 4-Hydroxyacetophenone

The batch method in the direct amidation of 4HAP for production of paracetamol (PCM) was based on the work by Rancan *et al.*[152]

Stoichiometric amounts of 4HAP and hydroxylamine hydrochloride (HOA) were weighed out and transferred to a vial in a 1:3 ratio. A stirrer bar and 5 mL of solvent were added to each vial. The vial was then placed on a hotplate and stirred vigorously at 90 °C for one hour. The solvent was then reduced on a rotary evaporator. The resulting solid was then taken for sample analysis.

In later experiments, the screw cap vial was replaced with a biotage reaction vial and sealable cap. To each vial, stoichiometric amounts of 4HAP and HOA were added with 5 mL of solvent. In these experiments, the vials were heated to 120 °C for one hour in a sand-bath with constant stirring. The samples were allowed to cool before analysis.

2.4.2 Preparation of 4-Hydroxyacetophenone Oxime

4-hydroxyacetophenone oxime (4HAPO) was prepared using a combination of the batch methodologies outlined by Tokmadzhyan *et al.* and Quartarone *et al.*[153,154]

A glass three-necked round bottom flask of 250 mL volume was placed in a oil bath with a reflux condenser attached (Figure 2-2). To a mixture of water and ethanol, stoichiometric amounts of 4HAP and sodium acetate (NaAc) were added. The system was heated to 90 °C before adding HOA. Regular samples were taken and diluted with deuterated DMSO before analysis by nuclear magnetic resonance (NMR). Once the reaction had reached completion, rotary evaporation was used to remove excess solvent to leave a crude solid. The solid was washed with a saturated aqueous solution of NaCl and $NaHCO_3$ at 0 °C. The solid was recrystallised using diethyl ether and hexane to leave a pure white solid.

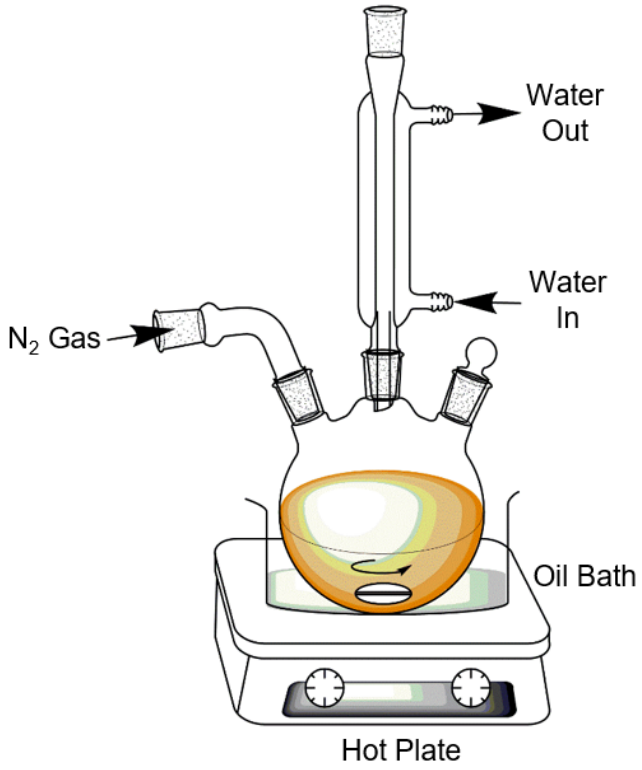

Figure 2-2: Diagram depicting the configuration in batch synthetic experiments for 4HAPO production

2.4.3 Beckmann Rearrangement of 4-Hydroxyacetophenone Oxime

Batch methodologies were investigated for the the Beckmann rearrangement of 4HAPO to PCM using trifluoroacetic acid (TFA). The procedure used was developed by Quartarone *et al.*[154]

The apparatus set-up is the same as outlined in Figure 2-2. To a 250 mL glass round

bottom flask under nitrogen gas, 9.8 mL of acetonitrile (ACN) and 1.0 mL (13 mmol) of TFA was added. The solution was stirred at 250 rpm and heated to 70 °C. Stoichiometric amounts of 4HAPO (1.3 mmol, 0.2 g) was added to the solution and the reaction was allowed to proceed for 1 hour. Regular 0.1 mL samples were removed and diluted with 0.3 mL of DMSO-d_6 for reaction monitoring using NMR. The resulting solution was rotary evaporated to remove excess solvent to leave a crude brown oil. The viscous oil was diluted with diethyl ether and washed with water at 0 °C. The final product was recrystallised from the diethyl ether layer using hexane. The off-white solid was then separated from the solution using filtration and allowed to dry overnight before analysis.

2.5 Flow Synthesis

Flow synthesis experiments were carried out using the commercially available Vapourtec R-series Flow Unit (Figure 2-3).

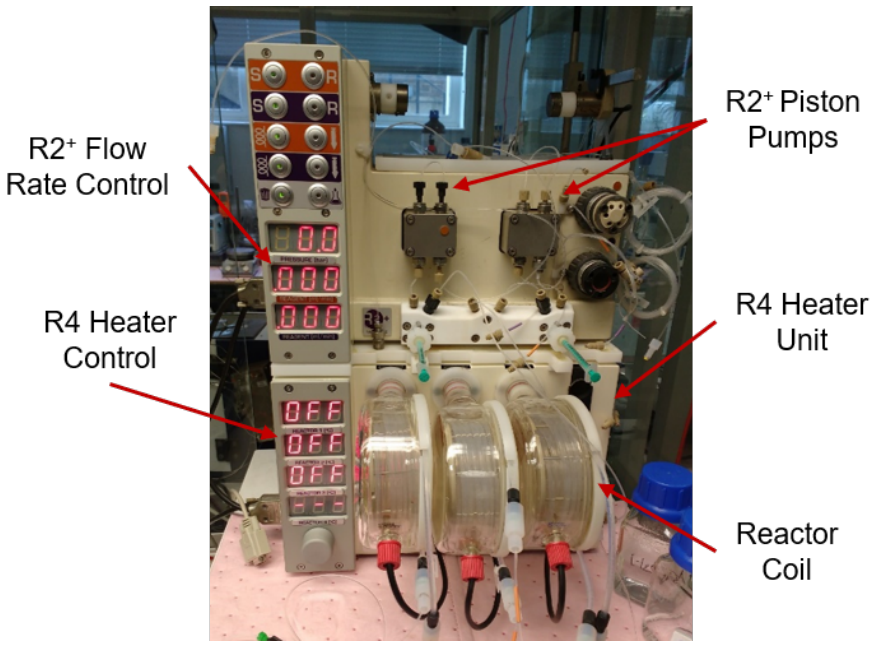

Figure 2-3: Photograph of the Vapourtec R-Series

The system is a reconfigurable, modular device that allows for a range of flow chemistry reactions to be carried out. The system consists of an $R2^+$ pumping module which is equipped with two high performance liquid chromatography (HPLC) pumps. Each HPLC pump has a chamber volume of 10 mL, with accurate flow rate range of 0.01 to 10 mL min^{-1}. A built-in manifold controls the pressure. The pumps are primed manu-

ally using a syringe to remove any air bubbles in the pump chamber before pumping at the set flow rate. The second module is the R4 heater unit. The R4 unit consists of four independent heated zones which allow for variable temperature control. Depending on the exact experimental set-up, a reactor coil or column is plugged into a heating zone and the temperature is monitored via a temperature probe. Each modular unit can be controlled via the in-built controls, but the system can also be connected to and controlled via a laptop, using the Flow Commander^{TM} software.

Specific reactor set-ups will be illustrated and discussed in the relevant Chapters 3 and 4 of this thesis. The range of reactors used throughout this work is however, outlined below:

- A perfluoroalkoxy alkane (PFA) tubular coil reactor of volume 10, 12 or 27 mL (1 mm inner diameter (ID))
- A static mixer coil with a volume of 20 mL (3.2 mm ID)
- A static mixer coil with a volume of 65 mL (5.6 mm ID)
- An adjustable omnifit packed bed column (100 mm length, 6.6 mm ID) of variable volume (0.1 to 2.4 mL)

All reactor equipment is commercially available from Vapourtec Ltd.

2.5.1 Steady State Measurements

For steady state measurements, a calibration curve was constructed using Eosin Y dye in ethanol (EtOH) at various concentrations (Appendix Figure 9-1). The extinction coefficient of the dye in EtOH at 478 nm was determined using the Beer-Lambert law (Equation 2.1):

$$A = \epsilon c l \tag{2.1}$$

Where A is absorbance, ϵ is the molar extinction coefficient, c is the concentration and l is the optical path length. A plot of absorbance vs concentration was used to determine the molar extinction coefficient of the dye in EtOH.

Steady state measurements were carried out on the flow process by pumping a stock solution of the dye through the reactor and sampling the effluent at periodic intervals. Measuring the absorbance of the dye in solution using offline UV/Vis spectroscopy on

a Jenway 6305 spectrometer allowed the concentration change to be plotted against time. The time taken to reach steady state was then be determined from the graph.

2.6 Crystallisation

2.6.1 Evaporative Crystallisation

Evaporative crystallisation was employed in the pursuit of multi-component molecular complexes. The work was carried out in order to replicate the thermochromic cocrystal complexes developed by Jones *et al.*[155] In each case, stoichiometric molar quantities of the target components were weighed into a clean 7 mL glass vial (approximately 10 - 50 mg). The solids were dissolved using the minimum amount of solvent to form a saturated solution (1 - 5 mL). In some cases, it was necessary to gently heat the solutions or use a sonicator bath to ensure complete dissolution. Once dissolved, the vials were sealed with a plastic lid. The lid was then punctured five times to allow the solvent to evaporate. Sample solutions were then left to evaporate free from agitation either at room temperature or at fixed temperatures of -4, 30 or 40 °C.

2.6.2 Antisolvent Crystallisation

Antisolvents were identified by screening the solubility of the target materials in a number of different solvents. Candidates where no visible or only partial dissolution occurred were identified as potential antisolvents. The choice of antisolvent was then limited to those that were miscible with the saturated solution of the coformers.

The antisolvent crystallisation was scaled up to 20 mL vials and temperature was controlled using the Polar Bear Plus reactor. In these studies, stoichiometric amounts of the starting materials (around 50 mg) were added to the chosen solvent with gentle stirring. Samples were transferred to the Polar Bear Plus stage and held at the desired temperature for at least 1 hour to ensure complete dissolution. The antisolvent was prepared as a stock solution in a separate 20 mL vial and subjected to the same conditions. A known volume of antisolvent was then transferred quickly using an Eppendorf pipette, from the antisolvent stock to the saturated solution to induce nucleation. Crystallisation was then monitored over the next hour. The solid was separated using gravity-assisted or vacuum filtration. In later attempts to understand the role of solvent on stability and thermochromic behaviour for multi-component complexes containing halo-anilines, the samples were left undisturbed in the vials at room temperature until the solvent/antisolvent had fully evaporated.

2.7 Continuous Crystallisation

2.7.1 Kinetically Regulated Automated Input Crystalliser (KRAIC)

2.7.2 Theory

The kinetically regulated automated input crystalliser (KRAIC) is a modular flow crystallisation platform (Figure 2-4) designed by Dr. Karen Robertson at the University of Bath. It is an open tubular crystalliser that uses segmentation to achieve a plug flow without the need for high velocity flow rates. Feed solution, a carrier fluid and air are pumped independently into a mixer piece resulting in a tri-segmented flow regime which is then propelled through three coils, each of which can be independently heated or cooled before a filtration step (Figure 2-5).[131] The residence time is controlled by adjusting the pump velocity or by changing the reactor length. The main body of the KRAIC consists of a 15 metre length of fluorinated ethylene propylene (FEP) tubing (3.2 mm inner diameter) through which the segmented flow will proceed. Segmentation and mixing can be controlled by adjusting the independent flow rates of the air, feedstock or carrier fluid. As the KRAIC is a modular unit, additional mixer pieces, tubing lengths and feed inlets can be added. In this thesis, several variations on the design of the KRAIC will be outlined and the merits discussed.

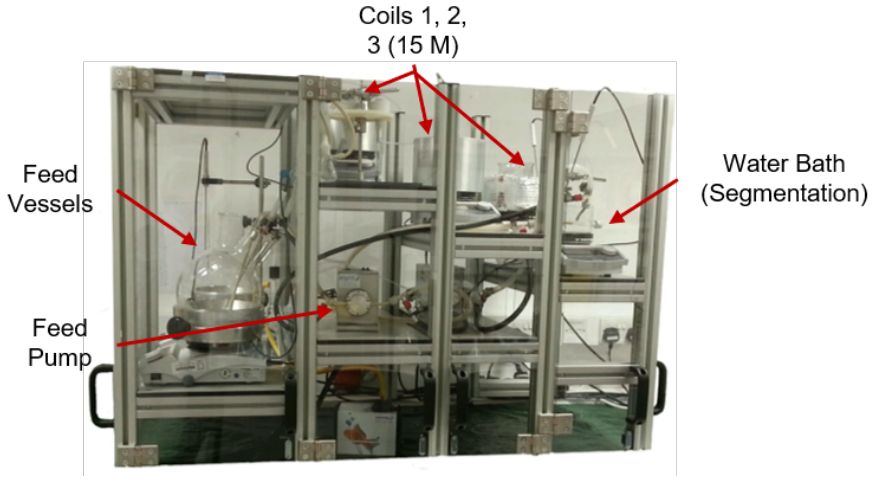

Figure 2-4: Photograph of the KRAIC crystalliser housing unit

The main driver for crystallisation in the KRAIC is cooling, however other configurations are possible. The carrier fluid is liquid fluorinated PFPE, known commercially as Galden SV110. The Galden and FEP are both hydrophobic in nature and thus, the carrier fluid preferentially wets the surface of the tubing over the solution phase. This isolates the segmented solution from the walls of the tubing, ensuring that nucleation

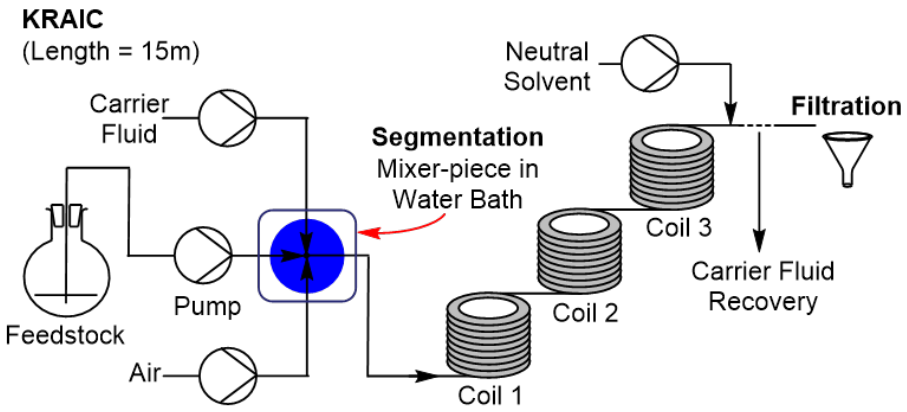

Figure 2-5: Schematic representation of the KRAIC configuration

in the KRAIC is generally driven by primary homogeneous crystallisation. The air provides an effective barrier between the solution slugs and helps to prevent unwanted back-mixing or coalescence of individual slugs, thereby ensuring the desired plug flow. Furthermore, air can be used to adjust slug size, the smaller the slugs, the more intense the mixing regime due to the generation of eddies. This helps to ensure the slugs remain homogeneous and promotes controlled crystal growth. In order to separate the carrier fluid from the solution phase before filtration, an end-piece is employed (Figure 2-6) .

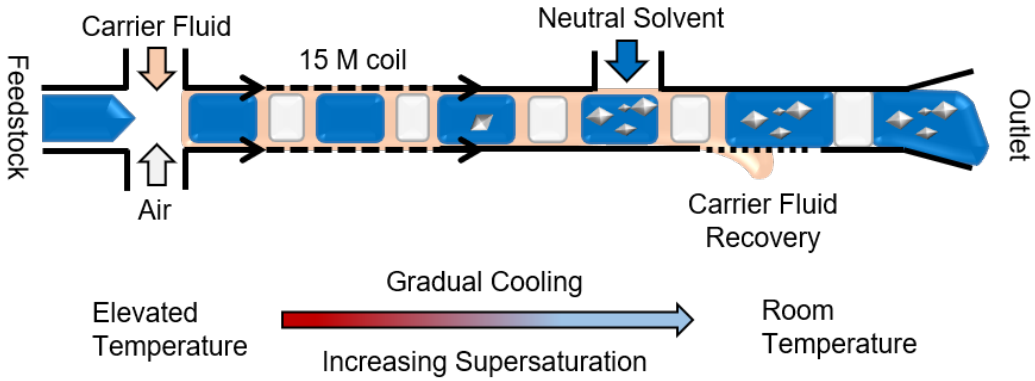

Figure 2-6: Diagram of tri-segmentation and carrier fluid recovery in the KRAIC during a cooling crystallisation

The end-piece is a small piece of FEP tubing that consists of an inlet (for a neutral solvent), followed by several small pores and an wider bore outlet. The neutral solvent is a miscible solvent which does not alter the solubility of the solution; it is used to increase the velocity of the net flow, reducing the chances of fouling around the outlet

by reducing contact time of the crystals with the reactor walls. The small pores in the end-piece allow separation of the carrier fluid. Galden easily passes through the pores as it displays a low contact angle and surface tension with the FEP tubing. In this way, the carrier fluid can be recovered and recycled, while the more hydrophobic properties displayed by the solution phase will pass over the pores without falling through. However, there is loss in flow velocity with the absence of the Galden as well as a change in the diameter of the end-piece as it reaches the outlet, this is made up for by the additional velocity of the neutral solvent phase. Crystals are then separated from the effluent by standard vacuum filtration in most cases.

2.7.3 Experimental

For specific reactor designs and experimental set-ups for the KRAIC and related segmented flow crystallisers, please refer to Chapters 3, 4 and 5. Here, a generic outline will be given for setting up a standard KRAIC crystallisation experiment.

A saturated solution of the target system is prepared to the desired concentration and volume. In a cooling crystallisation, the solution is heated and stirred until fully dissolved using Asynt hot plates equipped with an Asynt DrySyn basin and temperature probe. Carrier fluid, air and pure solvent are pumped through a 15 metre coiled tubing of FEP with inner diameter (ID) of 3.2 mm to prime the system. Flow rates of the carrier fluid, air and solution are adjusted to provide uniform slugs. The system is allowed to equilibrate for at least 1 to 3 residence times before swapping to the solution feed. The crystalline product is collected at the end of the tubular reactor and extracted using Büchner filtration. The filtered samples were allowed to dry before weighing the product and conducting analysis.

2.8 Single Crystal X-ray Diffraction (SCXRD)

2.8.1 Theory

To determine a crystal structure it is necessary to probe the positions of individual atoms within the crystal's molecular framework. In order to do this an incident beam of light is needed to "see" the structure of molecules. Visible light has too long a wavelength to probe these small distances, so a wavelength close to typical atomic distances is required. X-rays posses a wavelength in the nanometre range (0.01 to 10 nm), which lies close to the typical atomic spacing in a crystal structure.[156] As X-rays pass through a sample, interactions with the atoms will cause a scattering of the transmitted light. The strength of scattering is dependent on the number of electrons in

the atom and can thus be used to identify the atom type. Furthermore, the scattering of the light can be recorded and the resultant pattern can be recombined to determine the crystal structure.

While a single molecule is unlikely to give a strong scattering pattern, a perfect crystalline solid material is made up of a large number of identical molecules which are arranged in a precise pattern. The pattern is repeated in all directions, to give a highly ordered structure. This regular arrangement of many atoms or molecules not only enhances the scattering, but gives the scattering in turn a regularity that can be used in structural analysis. Each molecule can be represented as a single point, the result is a regular array of dots. This two-dimensional repeating unit of molecules is known as the the crystal lattice. Lattice points that are extended into three dimensions form a unit cell. The unit cell is defined as the smallest repeating volume of lattice points that are representative of the crystal structure. There are four types of unit cells depending on the positioning of the lattice points (Figure 2-7).

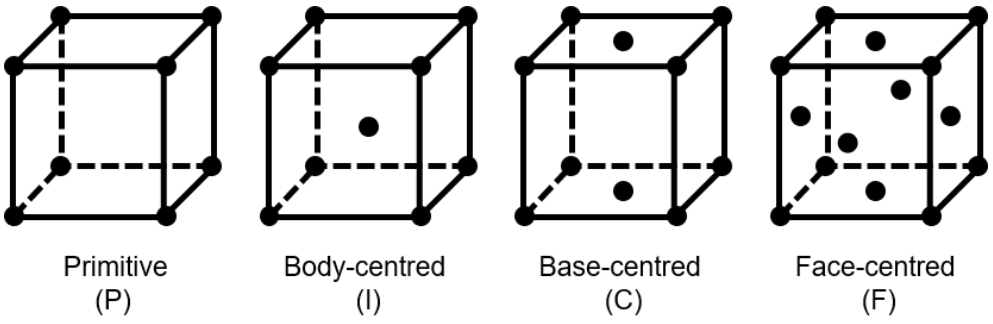

Figure 2-7: The four types of unit cell derived from lattice points

Based on the reflection and rotation symmetry elements present in the unit cell, constraints on the geometry of the unit cell gives rise to seven possible crystal systems summarised in Table 2.1. The combination of the seven crystal systems and four unit cells gives rise to the fourteen Bravais lattices. Furthermore, a crystal has symmetry elements that are regularly arranged in space and relate to the inherent lattice symmetry within its unit cell. The combination of all allowed symmetry translations distributed across the Bravais lattices gives raise to 230 possible arrangements. These arrangements, known as the 230 space groups, define all the ways a crystal structure can be arranged according to their symmetry.[156]

Having defined the regular, long range order present in a crystal structure, it is possible to predict when X-rays will interact with molecules in such a way as to provide a detectable scattering of light. Unless the radiation scattered by the lattice points are

Table 2.1: Table of the seven crystal systems and their symmetry restrictions

Crystal System	Unit Cell Restrictions	Lattice Types
Triclinic	None	P, I ,F
Monoclinic	$\alpha = \gamma = 90°$	P
Orthorhombic	$\alpha = \beta = \gamma = 90°$	P
Tetragonal	$a = b$; $\alpha = \gamma = 90°$	P, I
Rhombohedral	$a = b = c$; $\alpha = \beta = \gamma \neq 90°$	P, I, F, C
Hexagonal	$a = b$; $\alpha = \beta = 90°$; $\gamma = 120°$	P, C
Cubic	$a = b = c$; $\alpha = \beta = \gamma = 90°$	P

Where a, b and c are the unit cell axis and their associated angles α, β and γ

all in the same phase, then destructive interference will lead to zero intensity overall and no detectable diffraction. Bragg *et al.* described how constructive interference can be modelled from a set of parallel lattice planes (where a plane consists of a series of regular lattice points). Each set of parallel planes is represented by a set of Miller indices (denoted using the integers h, k, l). As shown in Figure 2-8, Bragg indicated that constructive interference between waves requires the X-ray beam and scattered radiation to have an angle of incidence and angle of reflection that is equal to each other. In this way, the lattice plane acts like mirror and the diffracted beam is reflected off the surface. Rays reflected from adjacent planes will interfere constructively when Bragg's law is satisfied. Bragg's law is defined in Equation 2.2, where d represents the spacing between lattice planes, λ is the wavelength, n is an integer and θ is the angle of incidence.

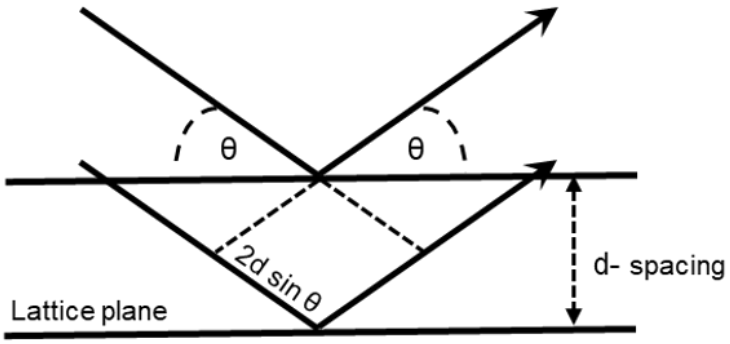

Figure 2-8: The Bragg model depicting the diffraction of X-rays by sets of parallel lattice planes

$$\text{Path difference} = 2dsin\theta = n\lambda \tag{2.2}$$

The Bragg equation forms the basis for all methods of obtaining the lattice geometry from the diffraction pattern. A single crystal will give a discrete set of diffraction patterns based on the orientation of the crystal in reference to the incident X-ray. However, Bragg's law describes only the necessary geometric constraints required to observe diffraction, it cannot predict the intensity of the reflection. The intensity of diffraction relates to the scattering of the incident ray by the atoms present and therefore contains all the information on the spatial positions of the molecules within the structure. In order to determine the intensity of the reflection, experimental data is required. The variation in intensities within an X-ray diffraction pattern is an indication of the distribution of electron density. The intensity of the scattering by the electrons around an atom is known as the the atomic scattering factor (f_j), which is proportional to an atom's atomic number at low Bragg angles.

An X-ray diffraction experiment measures the intensity of a series of reflections at different positions. Each reflection corresponds to diffraction from a set of lattice planes. Rearrangement of Bragg's law shows that there is an inversely proportional relationship between sin θ and d-spacing (Equation 2.3). A diffraction pattern is constructed in units of $\frac{1}{d}$. The diffraction pattern describes the reciprocal lattice, which is inversely related to the direct lattice. The distance of each individual spot from the central point in the diffraction pattern is proportional to sin θ and $\frac{1}{d}$.

$$\sin\theta = \frac{n\lambda}{2} \times \frac{1}{d_{hkl}} \tag{2.3}$$

The structure factor (F_{hkl}) describes the dependence of the intensity for each reflection on the crystal structure. It consists of the sum of the individual atomic scattering factors and is expressed in Equation 2.4:

$$F_{hkl} = \sum_{j=1}^{j=n} f_j exp2\pi i(hx_j + ky_j + lz_j) \tag{2.4}$$

Where f_j is the atomic scattering factor of the j$^{\text{th}}$ atom and x,y,z are the direct coordinates of the j$^{\text{th}}$ atom in the lattice. Each set of reflections with indices h, k and l, are represented by a specific structure factor. Fourier transformation of the sum of the structure factors produces an electron density map which allows for the assignment of atoms:

$$\rho_{xyz} = \frac{1}{V} \sum_{hkl} F_{hkl} exp[-2\pi i(hx + ky + lz)] \tag{2.5}$$

Where ρ_{xyz} is the electron density in position x, y, z and V is the volume of the unit cell. Experimentally the observed structure factor magnitudes are obtained, but the phase information is lost.[157] In order to solve the structure, the phases must be determined; for small organic molecules, the direct method is the norm. This process relies on using an approximation to determine the phases of the structure factor through statistical relationships between reflections. Successful use of the direct method yields the location of most non-hydrogen atoms in the structure.

Refinement is carried out using the least squares method. This procedure relies on approximating some of the atomic identities and positions within the crystal structure. From this, a series of calculated structure factors (F_{obs}) can be obtained which can be compared with the experimental structure factors (F_{calc}). A least squares process then cycles the atomic positions and vibrations to minimise the difference between observed and calculated structure factors. An R factor is then calculated to measure the agreement between the calculated and observed structure factors (Equation 2.6). The R factor value should decrease throughout the refinement process. A good refinement is typically indicated by an R factor of less than 5 %.

$$R = \sum \frac{F_{obs} - F_{calc}}{F_{obs}} \tag{2.6}$$

2.8.2 Experimental

Single crystal X-ray diffraction (SCXRD) experiments were carried out using the Rigaku Oxford Diffraction Supernova diffractometer. The Supernova platform is able to operate with either a Mo-K_α and Cu-K_α radiation. All single crystals were first coated in fomblin (a non-diffracting fluid) before being mounted onto the looped filament attached to the goniometer. The mounted crystal was then subjected to X-ray diffraction experiments using the monochromatic Cu-K_α radiation source at 150 K where the temperature was controlled using Oxford Diffraction Cryostream 700 series.

Data collection and processing were carried out using the CrysAlisPro 171.37.33 software. Diffraction data was refined with the help of Dr. Lauren Hatcher using SHELX-213 software by applying direct methods in the WinGX interface and applying the least square refinement method in SHELXL, before visualising the structure in the Mercury software.

2.9 Powder X-ray Diffraction (PXRD)

2.9.1 Theory

Powder X-ray diffraction (PXRD) is used in the determination of the crystal structure for a bulk, crystalline material. The technique has a variety of uses including determining polymorphic forms, confirming cocrystal or salt formation and identifying impurities in a material.[156] In a powder sample, multiple crystals with different orientations will be present. A beam of X-rays is fired at a powdered sample, some of the randomly orientated crystals will be in the correct position to give raise to a diffraction pattern. This will result in diffraction from multiple crystals and lattice planes. These collections of diffraction spots become superimposed on one another, forming a cone of diffraction (Figure 2-9). Each set of planes will give off its own cone of radiation.

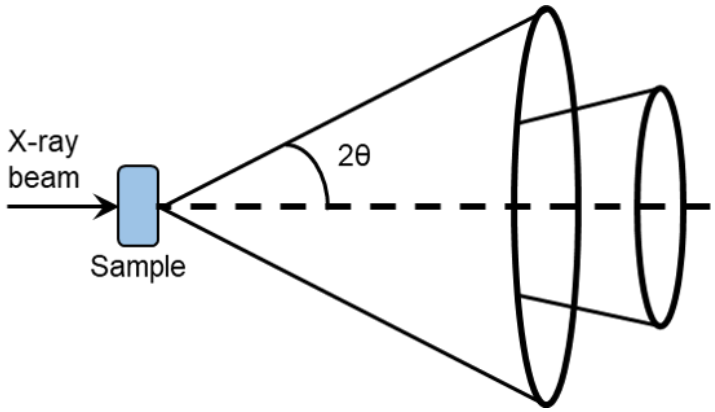

Figure 2-9: Cones of diffracted X-rays produced from a crystalline powder sample

If a detector is placed perpendicular to the X-ray beam, these cones will appear as a series of complete rings. The sample is rotated in relation to the X-ray source to collect a complete data set. The PXRD pattern is produced by plotting the integrated intensity of the rings against the 2θ angle.[158] PXRD patterns are characteristic of the crystal and notably the $2d$ positions of the PXRD peaks reflect the underlying unit cell. PXRD can therefore act as fingerprinting technique for identification of the molecule. Furthermore, a simulated powder pattern can be constructed from SCXRD data. The simulated PXRD pattern can be an effective method for confirming polymorphic form or identifying the bulk material.

2.9.2 Experimental

Bruker D8 Advance Diffractometer

PXRD data was collected using a Bruker D8 Advance diffractometer equipped with a monochromatic Cu-Kα radiation ($\lambda = 1.540\,56$ Å) source. Unless otherwise stated, crystalline samples were ground to a powder using a mortar and pestle before PXRD collection. The sample was mounted onto a glass slide and attached to a zero background sample holder using a non-diffracting adhesive plasticine. Samples were subjected to X-rays at room temperature (298 K) during analysis. Collection was carried out from 5 to 40° 2θ angles. Rotation of the sample holder was necessary to remove preferred orientation effects.

STADI P Diffractometer

Later analytical measurements were taken using a STOE STADI P diffractometer in transmission mode, equipped with a Cu-Kα radiation ($\lambda = 1.540\,56$ Å) source. Powder samples were placed between two non-diffractive transparent films and mounted onto the equipment via sample holder discs. The samples were subjected to X-rays at room temperature and collection was carried out between 2° and 75° 2θ angles. The samples were rotated throughout the measurements.

In both cases, comparisons were drawn between experimental data and simulated powder patterns produced from single crystal X-ray diffraction data in literature; this allowed determination of the polymorphic forms present.

2.10 Differential Scanning Calorimetry (DSC)

2.10.1 Theory

Differential scanning calorimetry (DSC) is a thermal analysis technique that allows the measurement of phase changes or solid-state transitions. The technique compares the heat flow of a sealed pan containing a sample with that of a reference pan (usually an empty, sealed pan). As the two pans are heated or cooled during a programmed temperature cycle, there should be no noticeable difference in the amount of heat flow required to maintain the same temperature in both pans until a thermal event occurs in the sample. As a phase change or transition occurs, a reduction or increase in heat flow will be required depending on the change. For instance, melting is an endothermic process and so the sample absorbs heat. In order for the temperature to remain the same, more heat flow will need to be supplied to the sample pan in comparison to

the reference pan. This data is recorded against temperature in a DSC trace and any exothermic or endothermic events can be detected (Figure 2-10).[159] The technique is useful as thermal events such as the melting point, glass and polymorphic transitions can be detected in the trace and used for identification or characterisation of a material. The techniques can also be effective for screening potential cocrystals, as the cocrystal will likely display a different melting point to the individual components.

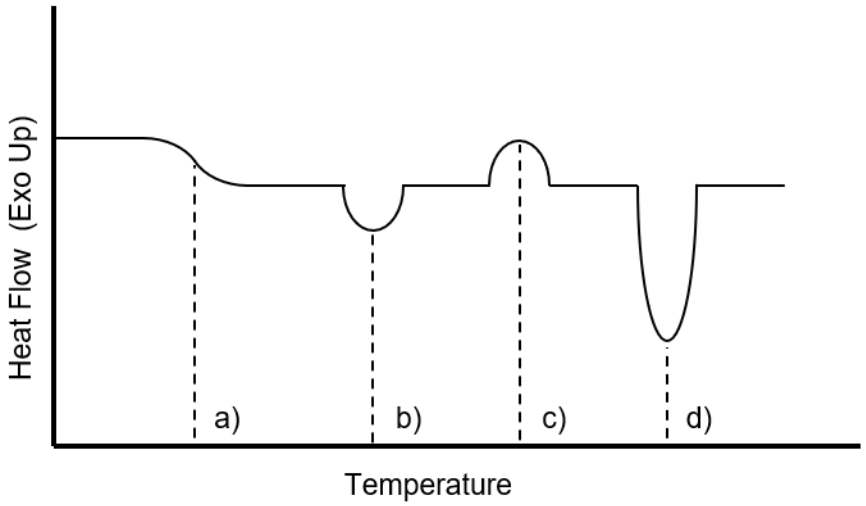

Figure 2-10: DSC trace depicting a) glass transition, b) an endothermic phase transition, c) solidification/recrystallisation and d) a melting point

2.10.2 Experimental

Thermal events were investigated using a Thermal Advantage Q20 DSC instrument equipped with a Thermal Advantage Cooling System and operated under a dry nitrogen gas purge of 18 mL min^{-1}.

Between 1.0 and 8.0 mg of sample was weighed into a Tzero aluminium pan. Samples were sealed by crimping an aluminium lid onto the pan before being transferred to the heating chamber. The heating and cooling profile was programmed using the Advantage for Qseries software© (ver. 5.40, 2001-2011, TA Instruments-Waters LLC) and the resulting trace was interpreted with TA Universal Analysis software.

2.11 Nuclear Magnetic Resonance (NMR)

2.11.1 Theory

A nucleus possesses a spin angular momentum, whose spin state is determined by the number of unpaired protons and neutrons. The magnitude of the spin angular momentum is given by Equation 2.7:

$$\text{Magnitude of spin angular momentum} = \sqrt{I(I+1)}\hbar \tag{2.7}$$

Where I is the spin quantum number and $\hbar$ is the reduced Planck's constant. Electrons, neutrons, and protons have a spin quantum number of a $\frac{1}{2}$. A nucleus with an even number of protons and neutrons (e.g. C^{12}) generally has an a total spin angular momentum of zero, as all nucleons are paired up. For nuclei with an odd number of proton or neutrons, a non-zero quantum number is encountered because each unpaired nucleon contributes $\frac{1}{2}$ to I. Based on this, it is possible to predict the spin quantum numbers of various isotopes as shown in Table 2.2.

Table 2.2: Possible nuclear spin quantum numbers (I) from the numbers of protons and neutrons in a nucleus

Number of protons	Number of neutrons	Spin quantum number (I)	Example Isotopes
Even	Even	0	C^{12}, O^{16}
Odd	Odd	1, 2, 3...	B^{10}, N^{14}
Even	Odd	$\frac{1}{2}$, $\frac{3}{2}$, $\frac{5}{2}$...	C^{13}
Odd	Even	$\frac{1}{2}$, $\frac{3}{2}$, $\frac{5}{2}$...	H^{1}, N^{15}

Because angular momentum is a vector, it has both a magnitude and direction (+ or -). A nucleus with an angular momentum of $\boldsymbol{I}$ will have 2I + 1 possible orientations in the z axis (Equation 2.8):

$$I_z = m\hbar \tag{2.8}$$

Where m is the magnetic quantum number with values between (Equation 2.9):

$$m = -\boldsymbol{I}, -\boldsymbol{I}+1, -\boldsymbol{I}+2, ... + \boldsymbol{I} \tag{2.9}$$

The nuclear magnetic moment (μ) of an atomic nucleus arises from the spin of the protons and neutrons. The magnetic moment of a nucleus is related to I by Equation 2.10.

$$\mu = \gamma I \tag{2.10}$$

Where γ is the gyromagnetic ratio of a nucleus. In the absence of a magnetic field, the energy levels of a spin active nucleus are degenerate. However, when a magnetic nucleus is placed within a magnetic field, the spin energy levels are split into allowed magnetic quantum number (m) orientations. For example, the nucleus of the hydrogen atom has two permitted orientations. In general terms, it can point either in the same direction as the field or in the opposite orientation (Figure 2-11).

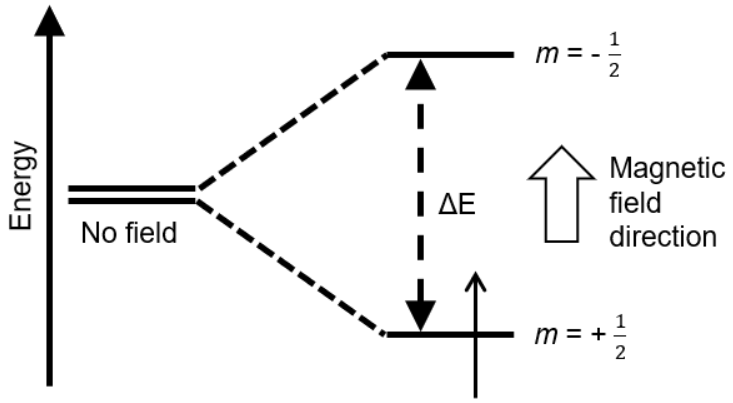

Figure 2-11: Splitting of hydrogen energy levels in a magnetic field

These energy levels are separated by an energy barrier, the size of which can be increased by the strength of the magnetic field. The selection rule for NMR spectroscopy is $\Delta m = \pm 1$, the allowed transitions therefore occur between adjacent energy levels.[160] By applying an external radio frequency (RF) equivalent to the spacing between the non-degenerate energy levels (ΔE), the spin state of a nucleus can be flipped so that it's magnetic moment now opposes the applied field (Figure 2-12). The RF absorbed is referred to as the resonance frequency.

The resonance frequency of the nucleus will vary slightly depending on the local chemical environment and therefore, a slightly different external RF is required to cause different nuclei to resonate. This is the result of local shielding effects which reduce the effectiveness of the external magnetic field felt by the nucleus, this is observed as a chemical shift. In order to generate a detectable signal, the nuclei are allowed to relax

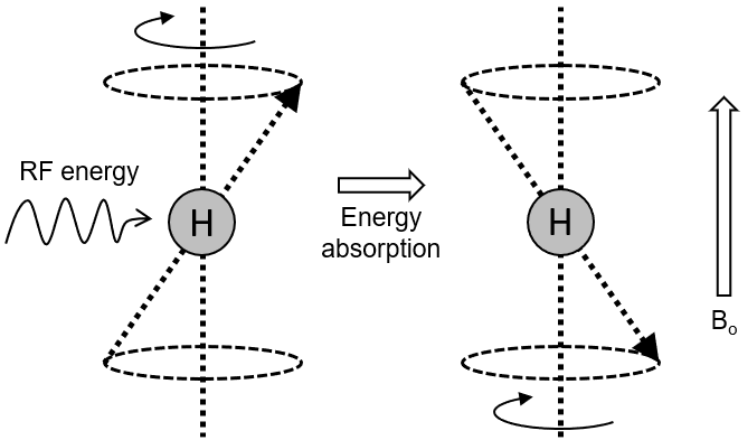

Figure 2-12: Absorption of the radio frequency (RF) causes the magnetic moment of a nuclei to flip and oppose the magnetic field (B_0).

back to the preferred orientation state before pulsing another dosage of RF radiation. This is cycled several times to generate an averaged signal. From the RF pulse, any radiation that is absorbed correlates to a resonance frequency. As the sample relaxes, a decaying, oscillating signal is generated which can be converted to a NMR spectrum using Fourier transformation (Figure 2-13).[161]

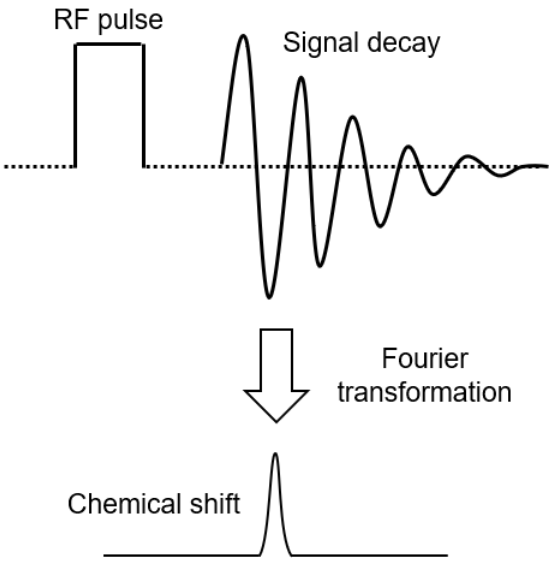

Figure 2-13: NMR spectrum obtained from the Fourier transformation of the signal decay generated after an RF pulse

2.11.2 Experimental

Routine NMR analysis was carried out using a Bruker Avance 300 MHz spectrometer. A small amount of sample was dissolved into 0.3 ml of deuterated dimethyl sulfoxide (DMSO) and transferred to a 5mm NMR tube for analysis. A proton spectrum was collected using TopSpin (3.6.1.). All spectra and corresponding peaks were analysed with MesResNova Software.

The relative conversion and selectivity for synthetic reactions was measured from the integral of the NMR peaks. As the limiting reactant will produce an equivalent amount of product, the starting material was used as a reference to give the molar ratio using the Equation 2.11

$$R_{A/B} = \frac{n_A}{n_B} = \frac{integral_A/N_a}{integral_B/N_B} \tag{2.11}$$

Where $R_{A/B}$ is the molar ratio of A to B, $integral_A$ is the integral of peak A, N_a is the number of protons corresponding to peak A, $integral_B$ is the integral of the peak B, N_a is the number of protons corresponding to peak B.

2.12 Hot Stage Microscopy

2.12.1 Experimental

Real-time analysis of phase transitions was conducted using a Mettler Toledo FP82 hot stage equipped with a Leica DM1000 microscope. A small amount of sample was placed onto a glass slide and transferred to the hot stage chamber. The sample was then subjected to a temperature program using the FP90 Central Processor. The microscope was equipped with an Infinity 2 camera to record any changes in real time. The Studio86Designs software was used capture the video. Playback of the videos was carried out using Studio Player.

In a typical experiment, a sample is heated at 5 °C min^{-1} from a start temperature of 35 °C until the sample has visibly melted. The video would be logged and played back to observe any visible changes in colour; a loss of crystallinity; solvent precipitation or a melting point over a specific temperature range.

2.13 Optical Microscopy

2.13.1 Experimental

An optical microscope with a Nikon Coolpix P5100 camera attached was used to evaluate crystal size, morphology and colour. Samples were placed on a glass slide under the microscope and the Nikon Coolpix camera was used to take digital images of the crystalline material.

Where particle size measurements were taken; a microscope calibration slide equipped with a grid net with divisions of 0.01 mm was placed under the sample slide. Pictures of the crystalline samples were taken using the Nikon Coolpix digital camera. By calibrating the number of pixels equivalent to 0.01 mm, the scale of the picture could be determined. Using this, the particle size could be determined by measuring the length and width of individual crystals by converting the number of pixels into the equivalent length in millimetres using the imageJ^{TM} software.

2.14 Scanning Electron Microscopy

2.14.1 Theory

Scanning electron microscopy (SEM) is a tool used for materials characterisation and provides information about the surface, shape, composition and defects in solid materials. It is used to produce high resolution images in the micron and nanometre range. SEM is used to overcome the limits of resolution in optical microscopy, which makes it possible to discern details which would otherwise be indistinguishable to the human eye. SEM uses electrons fired from an electron gun to probe the surface of a material. A typical SEM consists of three parts; an electron column, the specimen chamber and a computer interface system.[162] The electron gun is held within the electron column, which generates an electron beam. A series of electromagnetic lenses located within the column focuses the beam into nanometre-sized probe. The gun, the column, and the specimen chamber are kept under vacuum to prevent particulates from interfering with the electron beam generation. The electrons in the beam are directed at the sample and penetrate a few microns into the surface. Interaction with the atoms results in the emission of a variety of detectable signals.

Some of the electrons in the incident beam undergo elastic and inelastic scattering upon colliding with the sample. The elastically scattered electrons are eventually deflected out of the specimen without any kinetic energy loss. These electrons are backscattered, originally belonging to the incident electron beam that struck the samples surface. Once

out in the vacuum, these electrons can be captured by a detector and used to form a backscattered electron image. A backscattered electron image gives compositional contrast information of the surface. In addition to backscattered electrons, some electrons belonging to the target material are ejected from the specimen. These electrons are generally loosely bound, outer shell electrons residing close to the specimen surface. They are struck by the electrons of the incident beam and if enough energy is imparted to them, they are ejected from the atom. If they escape from the specimen (due to their close proximity to the surface), these electrons can be detected. As these electrons originally belonged to the specimen, they are known as secondary electrons and can be used to form a secondary electron image, which provides topographic contrast information. Both forms of contrast are detected and processed to obtain high resolution images of a samples surface.

Elemental dispersion information is obtained from X-rays generated when the primary electron beam interacts with inner shell electrons of an atom.[163] The inner shell electrons are knocked from their orbits and ejected from the atom (much like in secondary electron generation). The loss of an inner electron results in a vacancy in the orbital and the atom enters an unfavourable, energised state. The vacancy is immediately filled using an outer shell electron, which is transferred to the inner shell. This brings the atom back to its ground state, with an accompanying release of energy equal to the difference in the binding energy of the two shells. This excessive energy is released in the form of an X-ray photon, whose value will be characteristic of the atom's molecular weight.

2.14.2 Experimental

SEM was carried out using a JEOL SEM6480LV at the University of Bath and a JSM-6610LV at the Research Complex at Harwell (RCaH). In both cases, the samples were coated beforehand using gold (Au) with a Sputter Coater Quorum Q150T ES depositing a 4 to 10 nm coat on the samples. After coating, the samples were transferred to the SEM vacuum chamber and mounted onto a motorised stage to be analysed.

2.15 Laser Diffraction

2.15.1 Theory

The Malvern Mastersizer uses laser diffraction to calculate the size of the particles in a sample. In this technique, the scattering pattern of laser light by a sample of dispersed particles is measured on a series of detectors positioned at different angles (Figure

2-14).[164] As the particles are fed past the laser, the angle of the emerging scattered light will be dependent on the particle size. The scattering angle will be larger the smaller the particles. The detected light intensities at various angles are processed by a computer. The measured signals are converted to a particle size distribution (PSD) using a mathematical model. Several theoretical models are currently used to extract particle size data from laser diffraction including: Fraunhofer, anomalous diffraction and Mie theory. Mie theory requires knowledge of the the refractive index of a particle and dispersion media, but is the most robust method for studying small particles.[165] In all cases the particles are assumed to be spherical. For non-spherical particles, particle orientation will affect the distribution of light scattering observed and this is a current limitation of the technique. Regardless of the model used, processing of the light scattering is used to determine the volume density of particles within a defined set of size classes. The data is then compiled into a distribution based on those size classes.

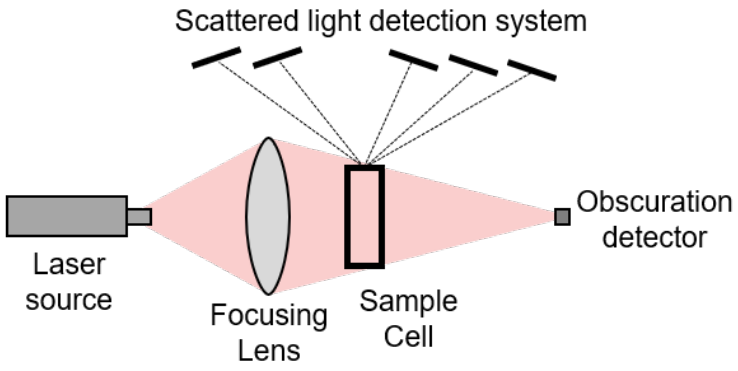

Figure 2-14: Simple laser diffraction set-up for particle analysis

2.15.2 Experimental

Measurements made using the Malvern Mastersizer 3000 were carried out with the help of Dr. Martin Depardieu. The Malvern Mastersizer 3000 (software version 3.36) was used to measure the distribution of controlled nucleation crystals produced during pyrazinamide (PZA) production. The particles were suspended in a saturated solution of pyrazinamide (PZA) in isopropanol to avoid particle dissolution. The refractive index of the dispersion solvent was supplied to the software and incorporated into the data analysis. A manual Malvern Hydro SM dispersion cell with a stirring rate of 2000 rpm was used to disperse the sample to avoid the formation of aggregates. After 30 minutes, the majority of these aggregates had dispersed without damaging the particles. The suspended sample was then fed past the laser, where the in-built software measured the

scattering of the particles and converted the raw data to a volume density vs particle size graph. The graph was then interpreted to determine the particle size distribution.

Chapter 3

Paracetamol

3.1 Introduction

The work in this chapter outlines the development of a continuous process for the production of paracetamol (PCM) and forms part of research effort to generate a route to PCM from renewable feedstocks. This research presented concerns the final synthetic step in this procedure and aimed to develop and evaluate a suitable flow synthetic process for coupling with continuous crystallisation.

3.1.1 Background and Aims

Paracetamol (PCM) or acetaminophen, is an important medicinal compound and common active pharmaceutical ingredient (API) in many over-the-counter pain relief medications. In 2014, the UK population was prescribed 42 million paracetamol-containing medicines while annual production worldwide exceeds 100000 tons.[166,167] Considering the high demand for PCM, pharmaceutical companies have developed a number of production methods to provide a cheaper and more efficient means of synthesis in order to maximise net profit. The most common industrial methods for PCM production involve the acetylation of 4-aminophenol to PCM. However, this method of production is not without its difficulties. The commercial routes to the 4-aminophenol intermediate suffer from moderate selectivity and produce large quantities of salt by-products that reduce the atom efficiency.[167] Strong acids such as sulphuric acid are used as a catalyst in most of these reactions but it is both strongly corrosive and large quantities are polluting. Therefore research has attempted to replace sulfuric acid with alternative catalysts with moderate success.[168,169]

In pursuit of the need for greater sustainability and efficiency, the development of alternative routes to medicinal compounds such as PCM have been developed using green chemistry principles. One particular route known as the Hoechst–Celanese procedure is used for the production of PCM from phenol (Figure 3-1).[170] This route involves the direct acetylation of phenol to the stable intermediate 4-hydroxyacetophenone (4HAP). This is followed by an oximation reaction using hydroxylamine hydrochloride (HOA) and an acid catalysed Beckmann rearrangement to deliver the final product.

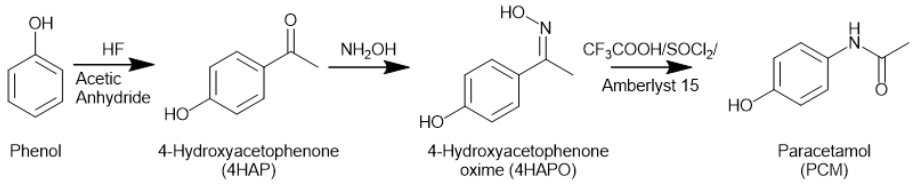

Figure 3-1: Hoechst−Celanese green synthesis of paracetamol from phenol

The Hoechst−Celanese process has been successfully scaled to industrial production, but a number of challenges remain. For instance, the stages employ mineral acids and inorganic bases each requiring significant work-up between operations. Furthermore, the starting reagents are derived from finite fossil fuels, which should be replaced with renewable feedstocks. Production of PCM could potentially benefit from an alternative synthetic approach within a holistic, continuous manufacturing framework. This could lead to improvements in the sustainability and efficiency of the process.

As such, the aim of this work is to develop and couple a flow synthetic method for the production of PCM with a continuous crystallisation work-flow for purification. The work forms part of a wider effort to produce medicinal products from green feedstocks. The proposed synthetic route developed by the Centre for Sustainable Chemical Technologies (CSCT) to produce PCM from limonene (which can be naturally sourced from citrus fruit) is shown in Figure 3-2.[171]

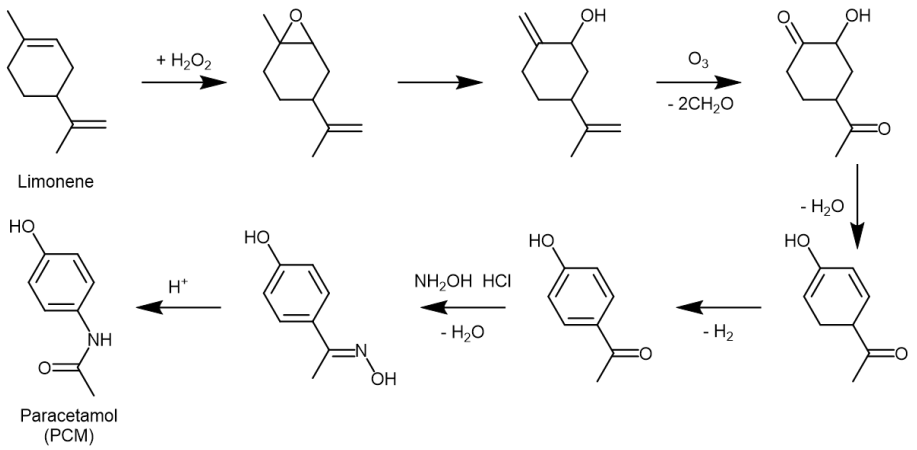

Figure 3-2: The proposed synthetic route from limonene to paracetamol[171]

The final step in this process was targeted for integration with continuous crystallisation. In pursuit of integration, the work aimed to develop an effective flow chemistry method compatible with downstream continuous processing technologies. While the primary target of this work was PCM, which is a well understood model compound for synthetic and crystallisation research, later research also investigated the integration and continuous production of the intermediate compound 4-hydroxyacetophenone oxime (4HAPO). 4HAPO represents a stable intermediate in the production of PCM. In this case, the research aimed to showcase how a holistic approach, incorporating flow synthesis and continuous crystallisation might benefit design of continuous manufacturing platforms.

3.2 Investigation into the One-Pot Synthesis of Paracetamol

In the Hoechst-Celanese process for the production of PCM, the ketone is first subjected to an oximation, followed by a Beckmann rearrangement in a multi-stage process. In general, the oximation step favours basic conditions, as the hydroxylamine reactant is stored as salt for stability, but in the presence of a base becomes a nucleophile. In contrast, a Beckmann rearrangement favours strongly acidic conditions.[172] As such, the process is generally a two-step reaction and requires significant work-up between steps, usually facilitated by ammonia to neutralise the base. To avoid this, initial attempts for the production of PCM concentrated on the investigation of a one-pot synthetic route to paracetamol from 4HAP. The synthetic procedure is outlined in Figure 3-3. The synthesis was developed by Rancan *et al.* for the self-catalysed amidation of ketones.[152]

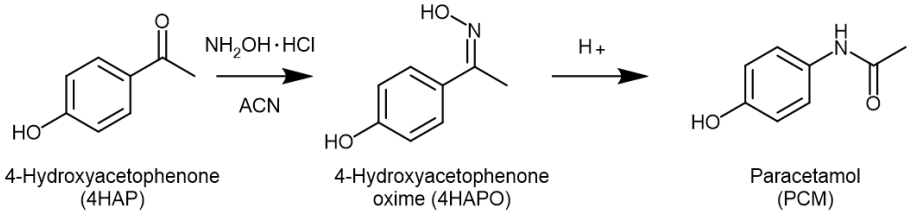

Figure 3-3: Direct amidation of 4-hydroxyacetophenone

In the self-catalysed mechanism demonstrated by Rancan *et al.* 4HAP readily converts to 4HAPO and subsequently to PCM without the need for additional acids or bases. At high temperature, the oximaton reaction between 4HAP and HOA occurs readily and subsequently releases a hydrochloric acid molecule, which catalyses the Beckmann rearrangement of 4HAPO to PCM. The process was shown to work well under solventless conditions or in the presence of a small amount of acetonitrile (ACN). A maximum conversion of 98% and selectivity to PCM of 97% was reached when heating between 90 and 110 °C for 1 hour. The reaction was further investigated by University of Bath Master's student Adam Steele, who replicated the reaction under solventless conditions. In subsequent kinetic studies under stoichiometric conditions, the production of paracetamol was shown to be completed within the first fifteen minutes at 120 °C.

Based on these initial findings the one-pot synthesis of PCM was targeted as a potentially attractive process for integrated continuous manufacturing. The almost quantitative conversion and high selectivity suggested the reaction could be linked directly to a developed crystallisation platform. Furthermore, the reaction proceeds well in less than an hour and could easily be improved by the higher mass and heat transfer ratios

typical in flow. While the use of ACN is not ideal as a solvent medium, it is recognised as the 'greener' alternative when considering dipolar aprotics as a reaction medium.[173] If the reaction can be translated into flow, this procedure could avoid the need for strongly corrosive acids typically required in the amidation of 4HAP.

Based on these observations, the work in this section aimed to replicate the work reported by Rancan *et al.* and transfer the solvent-based process to a flow chemistry platform. Particular attention was paid to the primary goal of integrated manufacturing and the flow chemistry route was therefore designed with the specific goal of integration with continuous crystallisation.

3.2.1 Batch One-pot Synthesis of Paracetamol

3.2.1.1 Experimental

The experimental parameters investigated in batch experiments for the direct amidation of 4HAP are outlined in Table 3.1. The experimental method was based on the work carried out by Rancan *et al.*[152]

Table 3.1: Experimental parameters for initial PCM investigations

Experiment	Molar Ratio (4HAP:HOA)	ACN Volume (mL)	Solvent Molar Ratio (ACN:4HAP)	Temperature (°C)	Reaction Time (min)
PCM1	1:3	5	10	90	60
PCM2	1:1	5	90	90	60
PCM3	1:3	5	38	120	60
PCM4	1:3	10	60	80	165
PCM5	1:1	100	250	70	1080
PCM6	1:1	100	250	90	1380

In PCM 1 and 2, stoichiometric amounts of 4HAP and HOA were added along with a specified volume of solvent to a 7 mL vial. A magnetic stirrer was added and the solution was heated on a hotplate to a temperature between 70 and 120 °C. The solution was allowed to react for one hour. Where the solid was extracted, the reaction was worked-up using rotary evaporation to leave a crude off-white solid. Routine nuclear magnetic resonance (NMR) analysis was carried out on the crude product and the conversion and selectivity were determined using the method described in Section 2.11.

In PCM3, the screw cap vial was replaced with a biotage reaction vial and sealable cap. Stoichiometric amounts of 4HAP and HOA were added with 5 mL of solvent. The vial

was heated to 120 °C for one hour in a sand-bath with constant stirring. The sample was allowed to cool before analysis.

In PCM4 to PCM6, the vial was scaled up to a 150 mL round bottom flask and stoichiometric amounts of 4HAP and HOA were added to the specified volume of solvent. The reaction was heated in an oil bath with constant stirring at 200 rpm. Samples were taken periodically to monitor reaction progress using routine NMR analysis.

PCM7 investigated the effect of water on the one-pot reaction and followed the same method as PCM3 to allow comparison. The parameters are summarised in Table 3.2.

Table 3.2: Influence of water on one-pot PCM reaction

Experiment	ACN Volume (mL)	Water Volume (mL)	Water Content (v/v%)
PCM7.1	4.5	0.5	10
PCM7.2	3.5	1.5	30
PCM7.3	2.5	2.5	50
PCM7.4	0	5.0	100

Reaction conditions: 2.5 mmol 4HAP, 7.5 mmol HOA, 120 °C, 1 hour

3.2.1.2 Results and Discussion

The isolated products from initial replications of the work carried out by Rancan *et al.* are shown Table 3.3. In this case, PCM1 and PCM2 underwent rotary evaporation after reaction completion to remove any remaining solvent, resulting in a crude solid. The crude was then recrystallised from hot deionised water. The isolated crystalline product was then subjected to analysis.

Table 3.3: Purity of PCM batch investigations from NMR

Experiment	Conversion (%)	Selectivity (%)	(%)
		4HAPO	PCM
PCM1	99	5	87
PCM2	96	5	88

Interestingly the addition of three molar equivalents of HOA in PCM1 as opposed to PCM2 did not change the selectivity to PCM, but did promote a higher conversion. Observations during the run however, indicated that a solid suspension was present during the reaction procedure. This was later determined to be undissolved HOA, which was not readily soluble in ACN. Nonetheless, the reaction proceeded well within

1 hour, producing PCM which was effectively isolated using recrystallisation. The products from each reaction were also tested using differential scanning calorimetry (DSC); the melting point was then compared to an experimental reference of PCM. The results are shown in Figure 3-4.

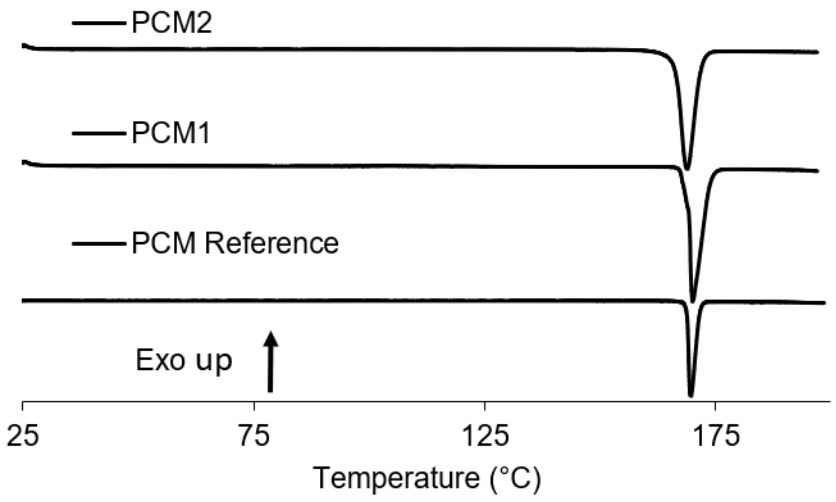

Figure 3-4: Comparison of DSC traces for PCM1, PCM2 and a experimental reference, note that values are offset in the Y-direction for clarity

As can be seen, the peak maximum for the endothermic melting peak matches well with the experimental reference of PCM. While the results are in good agreement with the reactivity described in literature, a better understanding of the reaction *in situ* was needed to develop a flow synthetic method. For instance, it was important to determine a suitable residence time (RT) to use in the flow set-up. Ideally the RT should allow for high conversion and selectivity to PCM without degradation of the product. As the reaction is a two-step process, the process would also need to balance and optimise both the oximation step and Beckmann rearrangement for maximum yield. Another issue was the poor solubility of HOA in ACN, which could lead to clogging in-line either due to precipitation or poor solid suspension depending on the set-up.

As such, experiments PCM3 to PCM6 tried to determine whether adjusting the reaction conditions could help facilitate the transfer of the one-pot process into flow. The results of the reactivity of the one-pot method in batch are shown in Table 3.4.

Table 3.4: Reactivity of PCM batch investigations according to NMR

Experiment	Conversion (%)	Selectivity (%)	(%)	Reaction Time (min)
		4HAPO	PCM	
PCM3	96	3	88	60
PCM4	74	9	88	165
PCM5	83	Traces	88	1080
PCM6	83	8	91	1380

From the data and parameters in Tables 3.4 and 3.1, a few trends emerge. As the amount of solvent increases, the time taken for the reaction to proceed increases. PCM3, PCM4 and PCM5 all showed little conversion to PCM after 1 hour. As stated earlier, increasing the stoichiometric ratio of HOA:4HAP improves conversion but has only a marginal effect on selectivity; in the literature, supplementary work showed the same trend. Increasing the temperature promotes a faster reaction but also leads to side-products forming. These were not actively identified, but have been noted in the literature as decomposition products.[152] The conversion has been calculated on the assumption that these impurities contribute to the conversion while the selectivity assumes that the decomposition products share the same signal-to-proton ratio as 4HAPO and PCM. This method does not produce quantifiable results, but does provide a quick method for screening and comparing the reaction progress using NMR spectroscopy. Identification and separation of these impurities is beyond the scope of this thesis. Despite the addition of solvent, reduction in molar ratio or increase in temperature, the solid suspension of HOA remained problematic. While some reactors are capable of handling solids in-line, equipment limitations in terms of pump capabilities meant that a high solid loading requirement would not allow the reaction to be transferred to flow easily. In order to overcome this, a solvent screen was carried out on the HOA salt to determine if this component could be effectively dissolved instead.

From the solvent screen, HOA salt was found to be readily soluble in water. Thus, batch reactions were conducted using a mixture of acetonitrile and water ranging from 10 to 100% water content (PCM7). These were compared to PCM3, run under the same conditions without water content. In this way, the effect of water on the reaction could be determined. The results are summarised in Figure 3-5. As can be seen from the graph, even the addition of 10 v/v% of water will reduce selectivity towards PCM by more than half. As water content increases, the preference for 4HAPO also increases. Furthermore, an unknown aromatic side product became more prevalent. A reduction

in conversion is also visible, with the exception of a small increase at 50 v/v% water. The increase may indicate a localised maximum for conversion, but selectivity to PCM is not improved. Regardless, the results do show that solvent choice has a clear role in the reaction progress. Care must therefore be taken to minimise the water content while maintaining dissolution of the reactants.

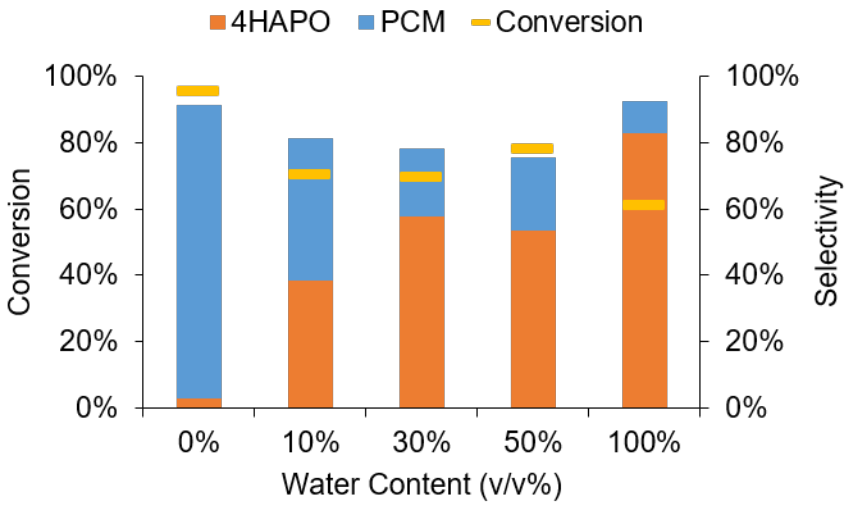

Figure 3-5: Effect of water on the one-pot synthesis of PCM. Reaction conditions: 2.5 mmol 4HAP, 7.5 mmol HOA, 5 mL solvent, 120 °C, 1 hour

Further attempts to find suitable conditions indicated that the reaction could be best run in a 95:5 v/v% ACN:H_2O mixture. This was found to be the lowest volume of water content that could effectively dissolve stoichiometric amounts of HOA at 80 °C. Here, the temperature was lowered to avoid thermal decomposition of the products. The results are shown in Figure 3-6. As can be seen, the selectivity to PCM is still very low after one hour. This gradually increases as the reaction progresses, but is significantly slower than the pure ACN process. In terms of dissolution of reactants, HOA did remain in solution at reaction temperature, but a biphasic solvent mixture and solid particulates were noted at room temperature. This indicates the dissolved salt reduces the miscibility of ACN and water at high concentrations. While the reaction had not fully completed after 22 hours, the selectivity to PCM had only reached 72% with an increasing amount of by-products noted in the spectra. The long reaction times and reduced conversion compared to the pure ACN process makes its application in bench-top flow equipment limited, particularly where integration with downstream technology is the aim.

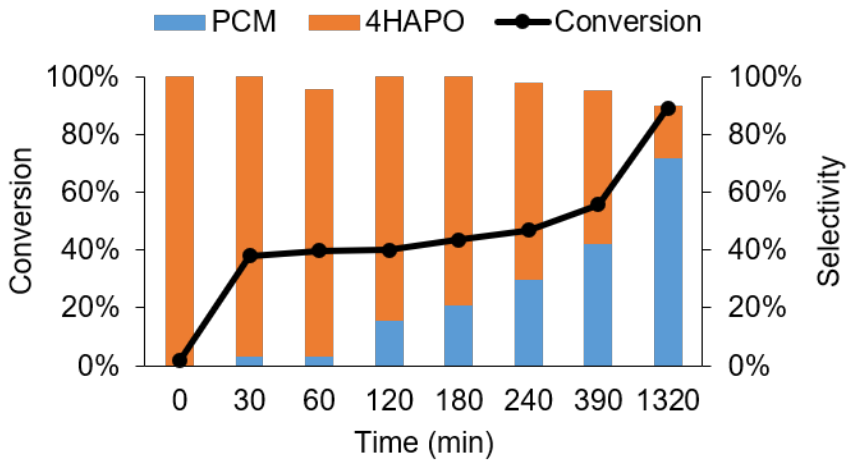

Figure 3-6: Effect of water on the one-pot synthesis of PCM. Reaction conditions: 2.5 mmol 4HAP, 2.45 mmol HOA, 10.5 mL solvent, 80 °C, 22 hours

Based on these results, the effectiveness of using a cosolvent to facilitate dissolution of the starting materials did not appear to be a viable approach. While it is possible that a balance could be found between a low water content, long RT and high temperature to optimise the reaction, the results show that the solvent may have the biggest impact on the reaction rate. A possible reason for the loss in rate could be related to pH.[152] Typically the oximation of 4HAP to 4HAPO uses a base as a buffer, while the Beckmann rearrangement is favoured by strongly acidic conditions.[172] The addition of water will neutralise the HCl component of the HOA salt, potentially stunting the reaction rate. With high solvent content, the reaction rate is reduced due to dilution. Hence, the reaction is most favourable under solventless conditions because a localised high concentration of hydrochloric acid is maintained as the oximation take place, which subsequently facilitates the Beckmann rearrangement.

3.2.2 One-pot Synthesis of Paracetamol in Flow

Since a cosolvent approach using water was not a suitable candidate for effective transference to a flow process, an alternative method was investigated. Instead of attempting to dissolve HOA, a packed bed column was used to support the reagent. Packed bed reactors have been previously used for in-line work up, scavengers, solid catalyst support or solid reagents in flow synthesis.[140,174,175] For the one-pot amidation reaction, the column could be used to house the HOA salt, thereby bypassing any need for dissolution.

3.2.2.1 Experimental

In flow, the one-pot amidation process was carried out using the Vapourtec R-series flow reactor. For full details of the Vapourtec apparatus, see Section 2.5. The packed bed reaction set-up is outlined in Figure 3-7.

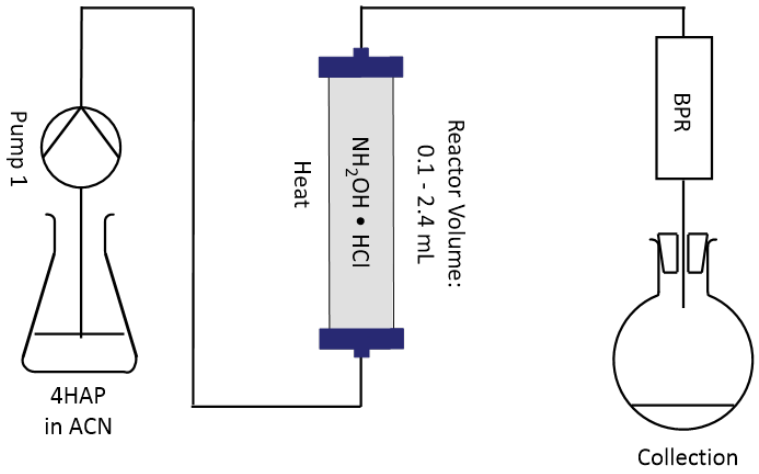

Figure 3-7: Experimental set-up for one-pot, flow synthesis of PCM

An adjustable omnifit fixed bed reactor of variable length was fitted to a heater zone on the Vapourtec R-series heater module. The column was packed with approximately 3.8 g of HOA. Celite was packed into both ends of the column to fill the void volume. Each end of the column was sealed with a frit and the length of the column was adjusted to pack the solid. The column was primed with pure ACN at the set flow rate for 1.5 RTs at 120 °C. A back pressure regulator (BPR) was fitted downstream (7 to 8 bar) to prevent solvent boiling in-line. After priming, the line was switched to the stock solution of 4HAP dissolved in ACN. Aliquots were collected at periodic intervals and reaction monitoring was conducted using NMR spectroscopy. The parameters used in one-pot packed bed flow synthesis experiments are outlined in Table 3.5.

Table 3.5: Parameters for the packed-bed flow synthesis of PCM

Experiment	4HAP ($mol\,dm^{-3}$)	HOA (mmol)	Solid Volume (cm^3)	4HAP Flow Rate ($mL\,min^{-1}$)	RT (min:sec)
PCM8.1	0.28	27.9	2.1	0.50	4:10
PCM8.2	0.28	27.9	2.1	0.25	8:20
PCM9	0.27	26.7	1.8	0.22	8:10

Reaction conditions: Solvent = ACN (100 mL), Temperature = 120 °C, Column volume = 2.4 mL, BPR = 7 - 8 bar

3.2.2.2 Results and Discussion

PCM8

In PCM8, the solution of 4HAP was initially pumped at 0.5 mL min^{-1} (PCM8.1). This was later lowered mid-run to 0.25 mL min^{-1} (PCM8.2). The reaction was monitored with off-line NMR and the results are shown in Figure 3-8. As can be seen from the graph, conversion of 4HAP remained low, reaching a maximum of 33% after running the reaction for 50 min. However, selectivity towards PCM was high, reaching 75%. While the selectivity towards PCM was not as high as delivered in batch, the total time spent within the column was only approximately 4 to 5 min. The presence of localised excess HOA readily promotes the Beckmann rearrangement. However, the lower conversion suggests that conditions were unfavourable for the oximation step. To improve this, the flow rate was halved mid-run to increase the residence time to 8 minutes. The effect was a noted increase in both the conversion and selectivity towards the desired product, with conversion reaching 72% at 70 minutes. Selectivity to PCM also reached a value of 97%. The remaining 3% was assigned to thermal decomposition products, as no peaks for 4HAPO were visible in the spectrum.

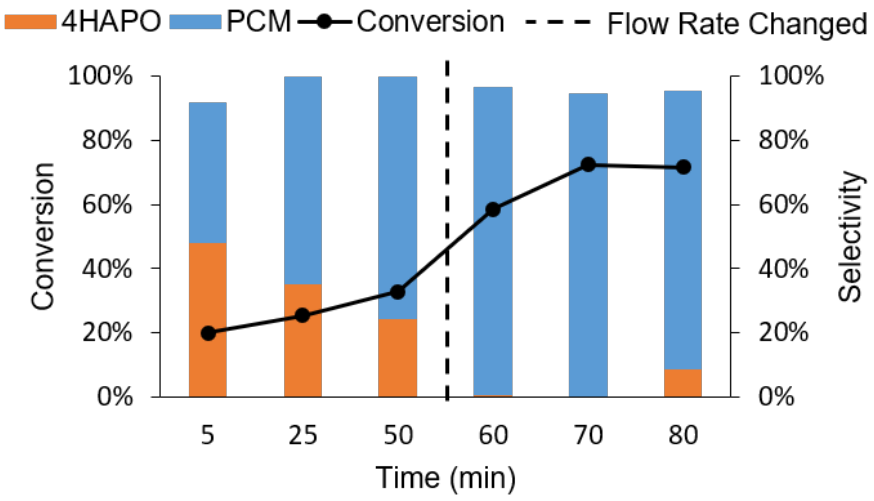

Figure 3-8: Conversion and selectivity to PCM using off-line NMR monitoring in PCM7. Flow rate changed to 0.25 mL min^{-1} after 50 min

Results suggest that the majority of the oxime intermediate can be converted to paracetamol within 8 minutes. While the oxime intermediate was detected again at 80 minutes the high selectivity towards PCM remained. The run was ended at 85 minutes, as the BPR became blocked with solid particles. Based on earlier observations in batch

regarding the poor solubility of HOA in ACN, the HOA salt was determined to be leaching from the column into the solution stream at the reaction temperature but as the effluent cooled, precipitation of HOA occurred and the BPR became a choke point for solid particles.

PCM9

Based on the good conversion and selectivity evident in PCM8.2, PCM9 aimed to replicate the work carried out over a longer period. The results are depicted in Figure 3-9. The flow rate was adjusted to give an equivalent RT to PCM8.2. However, in PCM9 the reaction was less productive. Here the reaction reaches a conversion between 60 to 70 %. Furthermore the selectivity towards PCM was reduced, with an average of 78%. It is difficult to discern the exact cause for the reduced reaction progress. A possible reason may be that the active surface area of the column was reduced compared to PCM8.2, as the exact column conditions and length (and therefore the column RT) are difficult to reproduce accurately. As a consequence the volume-to-surface area ratio may have been lower, which can affect the reaction rate of flow processes using packed beds.[29,58]

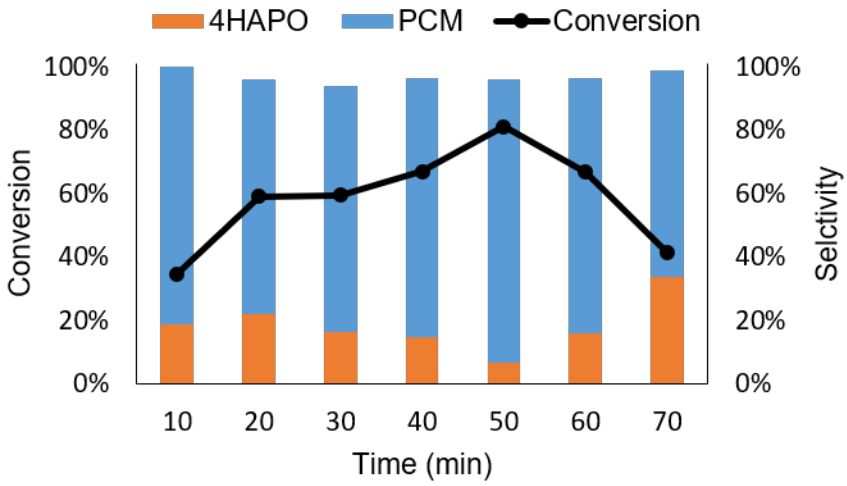

Figure 3-9: Conversion and selectivity to PCM using off-line NMR monitoring in PCM9

As was the case with PCM8, difficulties still remained in PCM9, which suffered from large pressure oscillations during the process. Eventually a blockage formed 37 minutes into the run, this was alleviated by raising the flow rate briefly, however the spike in conversion and yield at 50 minutes is likely a consequence of the blockage increasing the RT in the column. The upside of this is that the reaction yield and conversion to PCM could likely be increased by lowering the flow rate. The major difficulty in

doing this is that a BPR relies on a regular flow rate to maintain pressure. As the flow rate is lowered, it becomes more difficult to maintain safe operating pressures that prevent ACN from boiling in-line. This would in turn lead to precipitation and further blockage issues. Several attempts were made to apply temperature control to the BPR unit. These included insulating the tubing and actively heating the BPR in a water bath. However, neither approach was sufficient to prevent blockages or severe pressure oscillations in the process.

3.2.2.3 Summary

From the results discussed, the one-pot reaction showed promise in translation of 4HAP to PCM production into flow, some of the problems encountered could be mitigated by careful optimisation of the reaction and subsequent temperature and pressure control. In particular, PCM8.2 and PCM9 display the closest conversion and selectivity to the batch approach, with appreciable conversion to PCM in less than 10 minutes. However, oscillations in the column pressure caused issues with maintaining the high temperatures safely, while particulates leaching from the column caused blockages during the operating period.

In terms of integration, the process developed is currently not suitable for coupling with continuous crystallisation. While translation of the amidation was partially successful, the significant blockages and pressure oscillations in the packed column cause issues. One possible solution to this might be to introduce a quenching agent to the reaction after the column and before the BPR. This could redissolve any particulates and prevent blockages, however this would also dilute the product, making crystallisation more difficult. Scaling up would remain an issue, as the pressure oscillations may become worse even with quenching and this could have a knock-on effect on the crystalliser flow rate. A further problem would be the reactivity, which would decrease slowly as the HOA in the column is used up. This would lead to a build-up of starting material impurities during crystallisation. To compensate, the column would require periodic replacement or two columns would need to be run alternatively, along with *in situ* monitoring to determine when the columns needed swapping. While this is still a potential route for continuous manufacturing (CM), most of these additions add significant complexity to the process before even the integration with a crystallisation process can be evaluated. A possible viable approach to scale-up and integration of the one-pot method might be to use continuous stirred tank reactors (CSTRs). Individual CSTRs are more analogous to batch reactors and thus better capable to handle solid suspensions; in this case the HOA would not need to be fully dissolved and therefore

leaching would be less of a problem. However the reaction rate and purity might decrease, as mass and heat transfer would be less effective. To compensate for this, the CSTR set-up would need to be run with a longer RT. Alternatively a solventless approach could be most effective. The reaction has been previously shown to work best under these conditions and this could be facilitated in flow by the use of a twin screw extruder process. Literature precedent has already shown that multi-step telescoped synthesis can be effectively implemented in extrusion processes.[176]

3.3 Two-Step Synthesis of Paracetamol

In continuing to pursue applications of integration of flow synthesis and continuous crystallisation, an alternative approach was investigated for PCM. In this case, the one-pot process was separated into two distinct steps, which could potentially be later linked. This section will discuss the development of flow synthetic approaches to the production of 4HAPO from 4HAP and the subsequent Beckmann rearrangement of 4HAPO to PCM as separate processes.

3.3.1 Oximation of 4-Hydroxyacetopheone Using Acetic Acid

Since the poor solubility of HOA salt in ACN made it difficult to translate the one-pot amidation process into a continuous tubular reactor, an alternative approach was investigated in early trials. HOA is usually supplied as a salt, as free hydroxylamine slowly decomposes in solution. However despite the reduced shelf life, hydroxylamine is readily available commercially in a 50 wt% aqueous solution. By replacing the salt form with the aqueous form, it was hoped that a solution based method could be developed. In pursuit of a green process, acetic acid was used to facilitate the reaction in the absence of the hydrochloric acid component.

3.3.1.1 Experimental

The Vapourtec R-series modular unit was used in all flow synthesis experiments. For a fuller description of the Vapourtec R-series unit, refer to Section 2.5. Stock concentrations of 4HAP and hydroxylamine solution were prepared in ACN and acetic acid (AcOH) respectively. Each pump was primed with the required pure solvent respectively. The feed streams were combined at a polyether etherketone (PEEK) T-piece mixer (1 mm inner diameter (ID)) before the reactors. A BPR with a pressure of 7 to 8 bar was used to avoid solvent boiling in line. The system was primeed at temperature for at least 1.5 RTs before switching to feed solution. Regular aliquots were

taken to monitor reaction progress and analysed using NMR spectroscopy. In initial experiments (PCM10) a perfluoroalkoxy alkane (PFA) tubular coil reactor with a volume of 27 mL (1 mm ID) was used. This was later replaced with a single or series of static mixer coils (PCM11 and PCM12). In PCM11, the reaction was carried out at the Innovative Technology Centre (ITC), University of Cambridge while visiting the Steven Ley research group. The set-up consisted of three 20 mL (3.2 mm ID) static mixer coil reactors placed in series and heated individually to 120 °C (Figure 3-10).

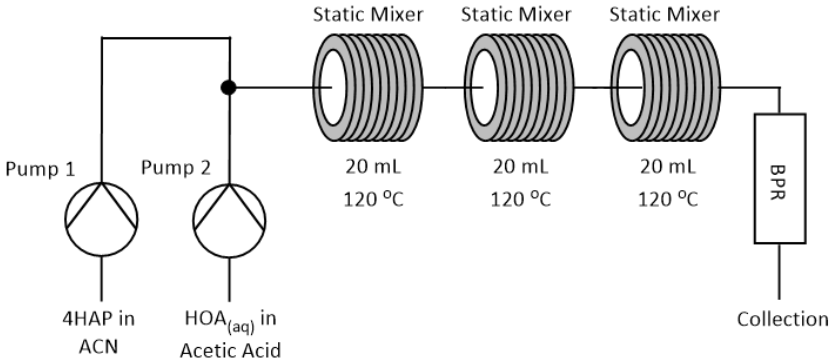

Figure 3-10: Schematic diagram for the flow oximation of 4HAP in acetic acid using three static mixers in series.

In experiments at the University of Bath, the three static mixers were replaced with a single, 65 mL (5.6 mm ID) static mixer coil. The single coil was wrapped around a glass water bath which was actively heated on a hotplate to 60 - 70 °C. All other features of the reaction set-up remained the same (Figure 3-11).

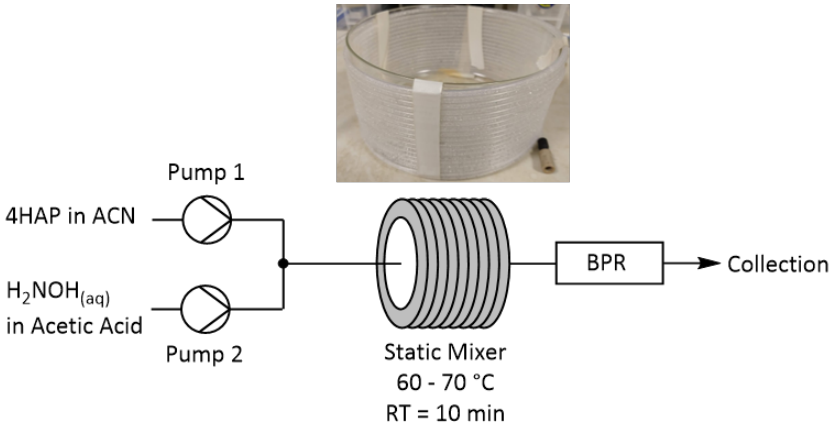

Figure 3-11: Schematic diagram for the flow oximation of 4HAP in acetic acid using a single 65 mL static mixer coil.

The parameters used in each experiment are outlined in Table 3.6.

Table 3.6: Experimental parameters for oximation investigations using aqueous hydroxylamine and acetic acid

Experiment	4HAP Concentration ($mol\,dm^{-3}$)	Flow Rate ($mL\,min^{-1}$)	HOA Concentration ($mol\,dm^{-3}$)	Flow Rate ($mL\,min^{-1}$)	AcOH Concentration ($mol\,dm^{-3}$)	Reactor Volume (mL)	Temperature (°C)
PCM10	0.25	2.25	2.45	0.45	5.00	27	120
PCM11.1	0.50	5	4.90	1.00	10.00	60	120
PCM11.2	0.50	5	4.90	1.00	0.00	60	120
PCM12	0.13	5.42	5.25	1.08	5.00	65	60 - 70

Residence Time = 10 min

3.3.1.2 Results and Discussion

PCM10

In PCM10, the reaction was carried out in a standard PFA coil. During the run, it was noted that the acetic acid and HOA solution did not mix well with the 4HAP solution in ACN. Off-line testing revealed that the high HOA/Acetic acid content made AcOH solution immiscible with ACN. After leaving the reactor, the solution remained biphasic and formed two layers in the collection vessel. Reaction monitoring was carried out using off-line NMR (peaks can be seen in Appendix Figure 9-2). A clear consistency is maintained throughout the run, with a mixture of the starting material (peak at 7.8 ppm, 4HAP) and the product (7.5 ppm, 4HAPO) detected at the time of extraction. While the reaction went selectively to the oxime product, the conversion remained steady throughout the run at 70 to 80 % (Figure 3-12). At 80 minutes the feed was switched to pure solvent, which is reflected in the NMR spectra at 90 minutes where a lack of NMR peaks is observed. While the conversion was not complete within 10 minutes, the reaction was unproblematic and simple to run; showing steady production of 4HAPO was achieved over nine RTs without issues.

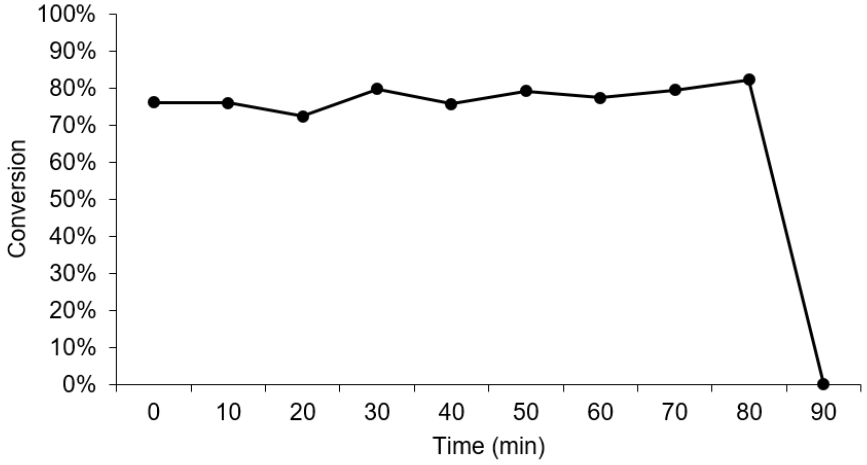

Figure 3-12: Conversion of 4HAPO using off-line NMR monitoring in PCM10

The reaction was worked up after completion and the solvent removed under vacuum. However, the resulting product remained as a viscous brown oil. This was unexpected, as 4HAPO is usually an off-white solid at room temperature. Further washing with water and subsequent extraction using ethyl acetate resulted in a crude solid product. The product was then recrystallised from hot water to leave an off-white solid. The isolated yield was 41 %, with trace amounts of 4HAP present.

While initial results were promising, an improved isolated yield and conversion were required for further integration with downstream technologies. The closely related molecular structures of 4HAP and 4HAPO meant that separation using crystallisation techniques would be difficult as their solubility behaviour could be similar. While they could be separated using in-line chromatography, this would slow and complicate the production process. On the other hand, if the conversion and selectivity to 4HAPO was sufficiently high, then separation in-line could be avoided. Therefore to improve conversion, the reaction was transferred into a series of static mixer coils at heightened temperatures. This would encourage mixing of the biphasic solutions and increase reaction rate.

PCM11

In PCM11.1, PCM10 was transferred to a series of static mixer reactors in tandem, which were heated to 120 °C. In PCM11.2 the reaction was repeated in the absence of acetic acid. The results are summarised in Figure 3-13.

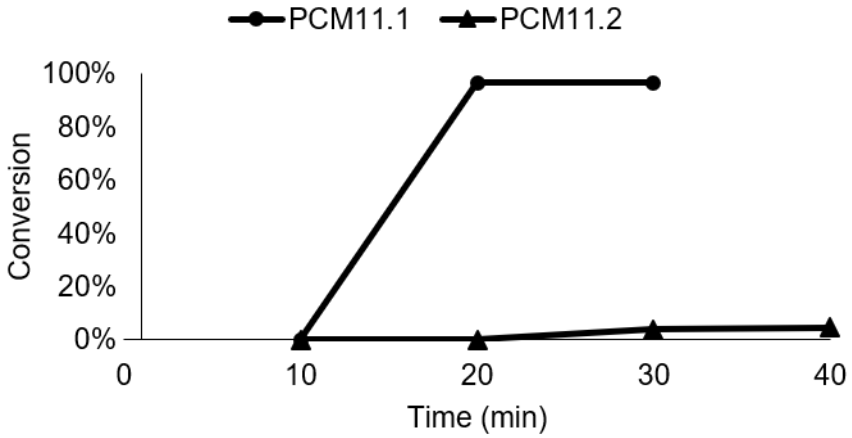

Figure 3-13: Conversion to 4HAPO using off-line NMR monitoring in PCM11.1 and 11.2

As can be seen from the graph, the reaction proceeded to produce almost quantitatively the 4HAPO product in PCM11.1. Comparison of the NMR spectra at different time stamps showed that almost no trace of 4HAP remained in PCM11.1 (See Appendix Figure 9-3 for stacked spectra). A minor intermediate was seen to form, but was not visible in the isolated product. During the run, the reaction mixed well in the static mixer coils and the biphasic nature of the solution was lost within the first coil. Separation of the phases occurs gradually upon collection and cooling. In PCM11.2,

the reaction was run without the high concentration of acetic acid to check whether the acetic acid played a purpose in the oximation. Based on the results in PCM11.2, the acetic acid is needed to initiate the oximation process. Without its presence, the conversion remains less than 5 %. This was a clear indication that the presence of acetic acid catalyses the reaction. This behaviour was also seen by Ren *et al.* when preparing ketoximes using aqueous hydroxylamine in ionic liquids.[177]

PCM12

Having established that selective production of 4HAPO was possible in a ten minute flow reaction, PCM12 attempted to improve the process further by reducing the temperature to avoid thermal decomposition of the product while increasing the concentration of aqueous hydroxylamine and AcOH to promote 4HAPO formation. To replicate the set-up from PCM11 (carried out at the University of Cambridge), a single, large 65 mL static mixer coil wrapped around a water bath was used. This was close to the equivalent volume of the three 20 mL static mixers used in Cambridge. The water bath was heated to 80 °C. The reaction was monitored using quantitative NMR where maleic acid was used as a reference standard. The reaction was run for 9 RTs and the results from reaction monitoring in PCM12 are shown in Figure 3-14.

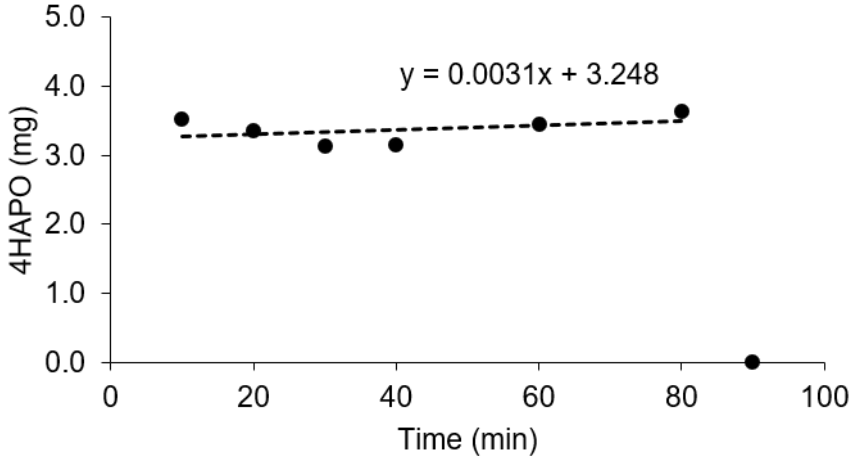

Figure 3-14: Quantitative NMR measurements for 4HAPO production from 4HAP using acetic acid as a cosolvent

As was the case with PCM11.1, PCM12 produced 4HAPO in quantitative yields. The expected yield per aliquot was calculated to be 3.1 mg and was based on the flow rate and collection period. As can be seen from Figure 3-14, the mass of product per sample is close to the expected value, with an average of 3.3 mg at steady state. Analysis of

the individual NMR spectra showed the small shoulder peak from PCM11.1, which is believed to be a solution-based intermediate, as the peak was lost after removal of the solvent. Further investigation is required to confirm this. However literature precedent has indicated that an intermediate complex can form between 4HAPO and trifluoroacetic acid (TFA).[154] It is possible that a similar intermediate may form in the presence of high amounts of AcOH and an analogous behaviour may be being observed.

The reaction was worked up using a more robust method than PCM10. The isolated yield was 63%, but significant improvement was still required. The high amounts of acetic acid encouraged the product to form a viscous oil before recrystallisation. In order to effectively crystallise, large amounts of sodium bicarbonate were required to neutralise the acid. The reaction then had to be separated from the solution using liquid-liquid extraction facilitated by ethyl acetate and water. The isolated product was tested using DSC and NMR to confirm the major product was 4HAPO. The results can be seen in Figure 3-15 and Table 3.7.

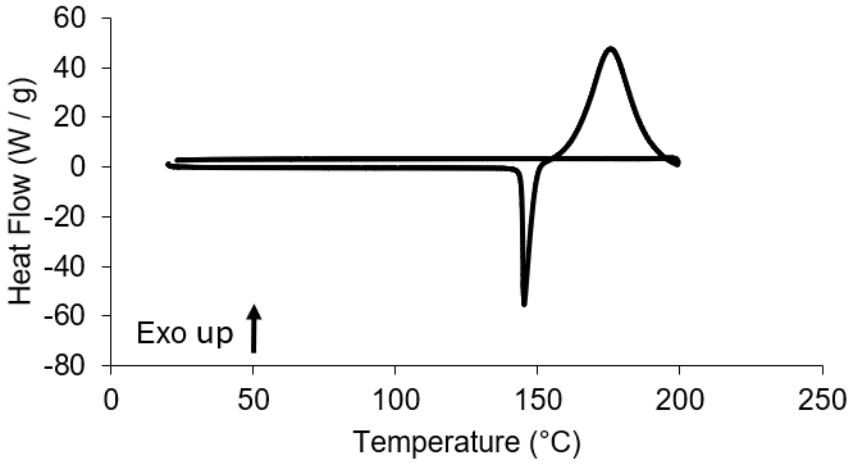

Figure 3-15: DSC of trace PCM12

Comparison of the melting point from the DSC trace and NMR peak shift with values taken from literature gives firm indication that the isolated compound from PCM12 is 4HAPO. It is also worth noting that 4HAPO undergoes exothermic decomposition at temperatures above the melting point (visible as a large exothermic peak centred on 175.7 °C). This is confirmed by the lack of a recrystallisation peak in the DSC trace on cooling the sample. Oxime products can be unstable and this thermal behaviour has been observed in other analogous organic oximes, such as benzaldehyde oxime.[180]

While the reaction was successful in producing 4HAPO with a high throughput, the

Table 3.7: Proton NMR chemical shifts of PCM12 and melting point from the DSC trace

Experiment	Chemical Shift (ppm)	Melting Point (°C)
PCM12	(300 MHz, DMSO-d6) 2.08 (3 H, s), 7.12 - 6.32 (2 H, m), 7.47 (1 H, d, J 7.3 Hz), 9.63 (1 H, br, s), 10.87 (1 H, br, s)	144.8
4HAPO[154]	(200 MHz, DMSO-d6) 2.09 (3 H, s), 6.73 - 6.78 (2 H, d), 7.45 - 7.49 (2 H, d), 9.60 (1 H, br, s), 10.84 (1 H, br, s)	140 - 145
4HAP[178,179]	(500 MHz, DMSO-d6) 2.47 (3 H, s), 6.84 (2 H, d, J = 8.5 Hz), 7.83 (2 H, d, J = 8.5 Hz), 10.32 (1 H, br, s)	108 - 110

See Appendix Figure 9-4 for the experimental spectra

need for intensive extraction and purification does not lend itself well to coupling with crystallisation procedures. However, the reaction could potentially prove useful as a telescoped oximation process for other applicable compounds such as the precursor to nylon-6, ϵ-caprolactam, which is typically made from cyclohexanone oxime.[181]

3.3.2 Oximation of 4-Hydroxyacetophenone Using Sodium Acetate

While the production of 4HAPO using acetic acid was successful, the procedure is not currently well-suited for coupling with continuous crystallisation processes without a offline work-up procedure. Another approach was therefore investigated. The reaction scheme is shown in Figure 3-16. Here 4HAPO is readily prepared using the salt form of HOA in the presence of sodium acetate dissolved in an aqueous/alcohol solvent mixture.[182]

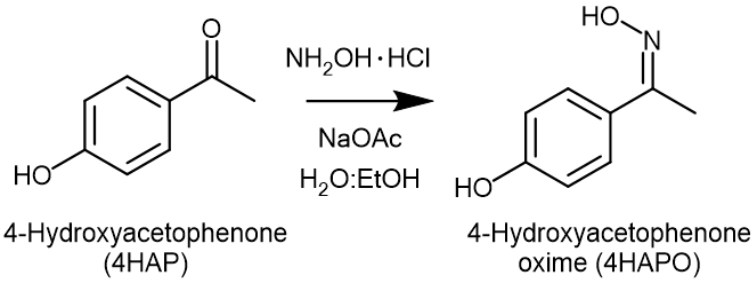

Figure 3-16: Reaction scheme for the production of 4HAPO

The batch synthesis is described in the experimental Section 3.3.1.1 and is based on the

preparation procedure for 4HAPO described by Mo *et al.*[182] This work was replicated in PCM13 for evaluation as a flow synthetic route to 4HAPO.

3.3.2.1 Experimental

For PCM13, the apparatus set-up is the same as depicted in Figure 2-2. To a 100 mL glass round bottom flask under nitrogen gas, 4 mL of ethanol and 12 mL of water were added with stirring to HOA (0.52 g, 7.5 mmol) and sodium acetate (NaAc) (1.03 g, 12.5 mmol). The solution was stirred at 250 rpm and heated to 85 °C. A stoichiometric amount of 4HAP (0.68 g, 5.0 mmol) was added to the solution once the set temperature had been reached. The reaction was allowed to proceed for 90 minutes. Regular 0.1 mL samples were removed and diluted with 0.3 mL of DMSO-d6 for reaction monitoring using NMR.

In flow synthesis experiments, the flow rates and the concentrations were set to provide an analogous reaction mixture to the batch process within the reactor. Flow rates were set to give a total RT of 15 minutes in a polytetrafluoroethylene (PTFE) tubular coil (ID = 1 mm) heated to 85 °C. The output from the reactor was pumped directly into a round bottom flask held in an ice bath. The set-up is shown in Figure 3-17. Reaction monitoring was carried out using NMR spectroscopy.

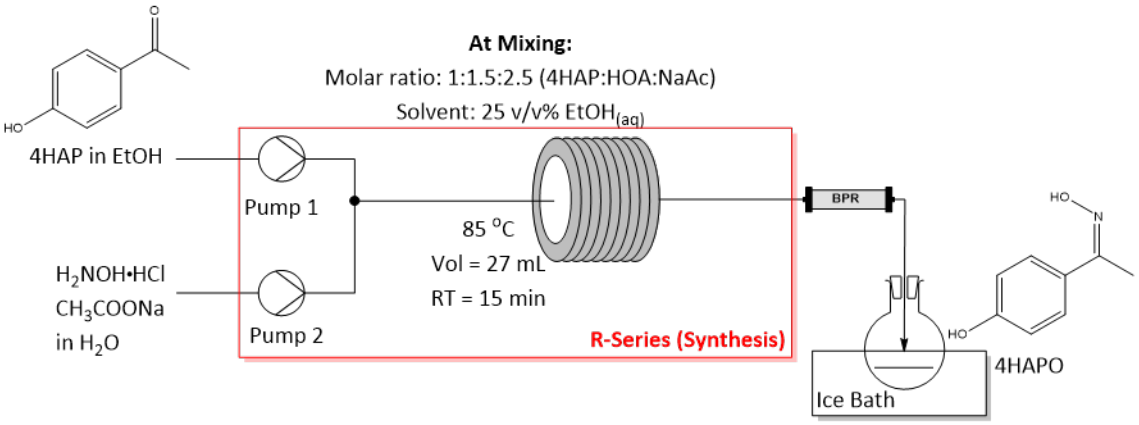

Figure 3-17: Schematic diagram for the flow oximation of 4HAP in ethanol/water

Table 3.8 shows the pump rates, feedstock concentration and molar ratios (after mixing) for PCM14 experiments.

Table 3.8: Concentration and feed rates for oximation investigations in ethanol/water

	Pump 1 (P1)		Pump 2 (P2)			Reactor	
Experiment	Flow Rate ($mL\,min^{-1}$)	4HAPO ($mol\,dm^{-3}$)	Flow Rate ($mL\,min^{-1}$)	HOA ($mol\,dm^{-3}$)	NaAc ($mol\,dm^{-3}$)	Molar Ratio 4HAPO:HOA:NaAc	Temperature (°C)
PCM14.1	0.45	1.25	1.35	0.63	1.05	1:1.5:2.5	85
PCM14.2	0.45	3.74	1.35	1.89	3.15	1:1.5:2.5	95
PCM14.3	0.45	2.47	1.35	0.83	1.24	1:1:1.5	95

Reaction conditions: reactor volume = 27 mL, RT = 15 min, pump 1 = ethanol, pump 2 = water, after T-piece solution = 25 v/v% ethanol

3.3.2.2 Results and Discussion

PCM13

The results of the reaction monitoring vs time are summarised in Figure 3-18.

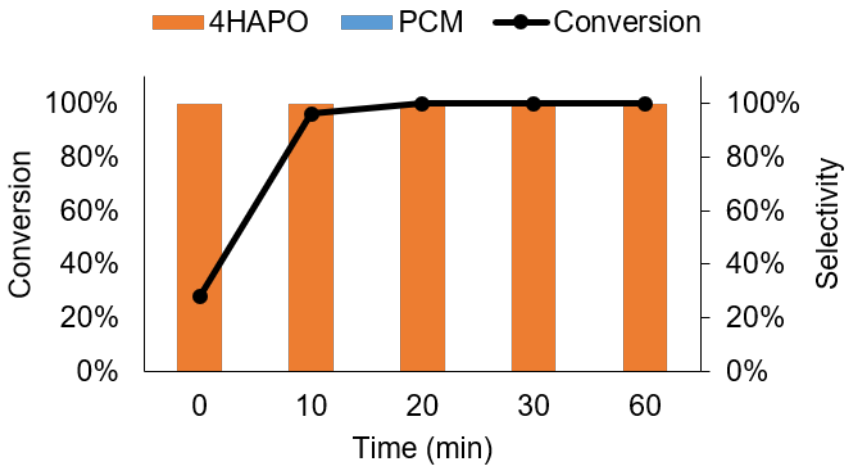

Figure 3-18: Production of 4HAPO from 4HAP using the method outlined by Mo *et al.*

As can be seen from the results, 4HAP was readily converted to 4HAPO within 10 minutes and the reaction was completed in 20 minutes. The product was then isolated using an ice bath, where 4HAPO was allowed to crystallise for 3 hours. The isolated yield was 57%.

Like the acetic acid experiments, the method was effective for production of 4HAPO in a short reaction time. However, isolation and crystallisation of the product was much more straightforward, not requiring solvent neutralisation and removal. In addition, an ethanol/water solvent is preferable to ACN and acetic acid in terms of crystallisation medium and green solvent selectivity. As the product could be readily isolated using an ice bath, a cooling crystallisation profile might be an effective method for integrated continuous crystallisation. Based on the initial batch test, the reaction was determined to be potentially applicable for direct integration with continuous crystallisation.

PCM14

While the reaction proceeded well in batch, the synthetic process had to be tested in a continuous system. In PCM14, PCM13 was translated into a flow synthesis platform, as shown in Figure 3-17.

In all runs, NMR reaction monitoring showed the reaction proceeded to 4HAPO selectively and with high conversion (Appendix Figures 9-5 and 9-6). PCM14.3 in particular, indicated that the molar ratio of HOA and NaAc with respect to 4HAPO could be decreased without compromising the selectivity and conversion. However care must be taken with high concentrations, as PCM14.2 and PCM14.3 both showed signs of encrustation around the T-piece and BPR. To compensate, the reactor temperature was increased to 95 °C and potential choke points were insulated where possible to prevent precipitation and encrustation. In each case, the effluent from the reactor was fed directly into a round bottom flask, where crystallisation began to occur after 30 minutes of operation. The crystallisation was allowed to proceed undisturbed in an ice bath overnight before extraction via Büchner filtration. In the case of PCM14.1 and 14.2, the effluent was worked-up using rotary evaporation to determine loss to the liquor. The results are shown in Table 3.9.

Table 3.9: Isolated yields of 4HAPO in ethanol/water flow reactions

Experiment	Crystallisation (%)	Work-Up (%)	Total Yield (%)
PCM14.1	13.5	56.3	69.8
PCM14.2	41.1	28.7	69.8
PCM14.3	29.7	Not worked up	29.7

As can be seen from the results, the crystallisation yield increases as the concentration of the reactant increases. There is however, a large loss of product to the mother liquor, though this is decreased at higher supersaturation levels. The loss to liquor compared to batch is likely a consequence of dilution during the collection period. This happens primarily during start-up and shutdown, as the pump flow is laminar, the concentration of reactants is lower than at steady state. The crystallisation recovery would likely be improved by collecting only once steady state is achieved. However, the mother liquor can also be easily worked up to improve total product recovery. The crystalline product was tested using powder X-ray diffraction (PXRD) and DSC. The corresponding melting and decomposition peak from the DSC trace are summarised in Table 3.10. The values are compared to PCM13 and show good similarity.

Table 3.10: Melting point and decomposition peaks in DSC traces for PCM13 and PCM14

Experiment	Melting Point (°C)	Exothermic Peak (°C)
PCM13	144.1	162.1
PCM14.1	144.6	166.0
PCM14.2	143.8	159.8
PCM14.3	143.6	158.9
4HAPO[154]	140 - 145	-

The PXRD pattern matched well with the simulated pattern of 4HAPO generated from the reported single crystal X-ray diffraction (SCXRD) structure (Figure 3-19).[183] In conjunction with the DSC melting points obtained from the isolated crystalline product, this confirmed the production of 4HAPO.

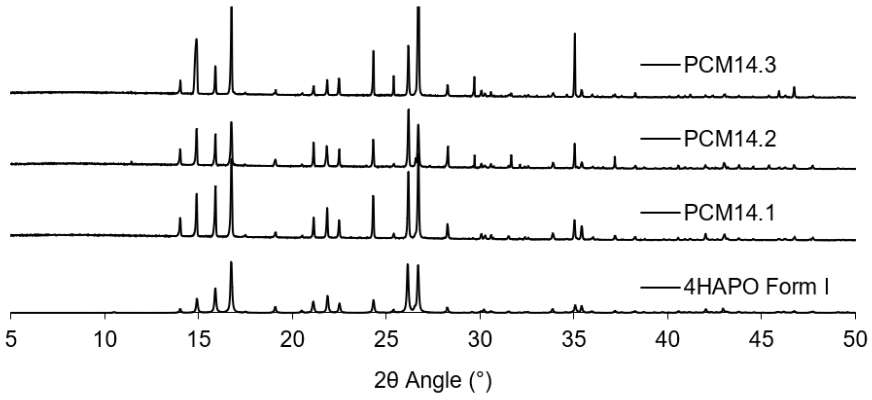

Figure 3-19: PXRD patterns for PCM14 vs simulated 4HAPO powder pattern from the SCXRD structure[183]

Some minor issues remained, however. The yield obtained from the crystallisation was relatively low and required a long induction time. Furthermore, close analysis of the PXRD pattern suggests that NaAc may be a trace impurity in the isolated product. Ideally, this should be reduced where possible, while raising the supersaturation level of 4HAPO. To achieve this, a better understanding of the solubility was needed to create an optimised crystallisation procedure. Development of the crystallisation process is described in Section 3.4.

3.3.3 Beckmann Rearrangement of 4-Hydroxyacetophenone Oxime

While the production of PCM via direct one-pot amidation of 4HAP was not transferable to flow within the scope of this project, isolation of 4HAPO product within the oximation flow process allowed the opportunity for the development of a second step-wise flow method. Investigations thus moved towards subjecting the 4HAPO intermediate to a Beckmann rearrangement. While the two-step process does not benefit from direct integration, partial translation into flow may still have beneficial productivity and efficiency advantages compared to batch and also represents a useful proof of concept within the integrated CM research scope. Work carried out by Quartarone *et al.* had previously shown that the Beckmann rearrangement of 4HAPO could be realised using TFA as an organocatalyst.[154] The reaction scheme is shown in Figure 3-20 and formed the start point for the current investigation.

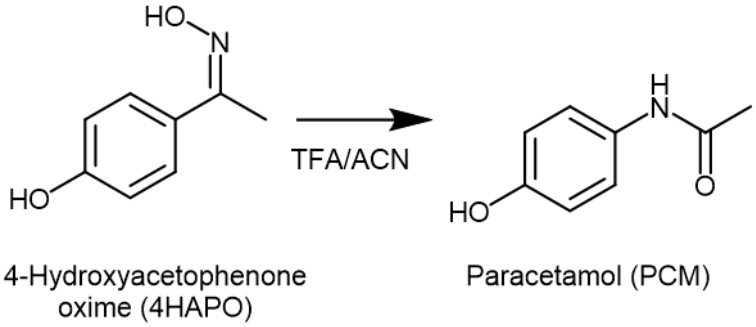

Figure 3-20: Reaction scheme for the production of PCM using TFA

3.3.3.1 Experimental

The experimental set-up in the batch methodology is described in Section 2.4.3. The experimental conditions for batch experiments are summarised in Table 3.11.

Table 3.11: Parameters for batch organocatalysed Beckmann rearrangements experiments

Experiment	4HAPO (mmol)	TFA (mmol)	ACN (mL)	Reaction Time (min)
PCM15.1	1.3	13.1	10.8	120
PCM15.2	1.3	13.1	10.8	120
PCM15.3	1.3	13.1	10.8	120

Reaction conditions: 70 °C, 250 rpm

3.3.3.2 Results and Discussion

PCM15

PCM15 aimed to repeat the procedure carried out by Quatarone *et al.* and determine if the reaction would be applicable in a flow system. In all PCM15 experiments, 4HAPO readily dissolved in the TFA/ACN solution at 70 °C. The reaction was run for 2 hours as described in the literature. NMR analysis in PCM15.2 indicated that the reactant 4HAPO was depleted within the two hour period (Figure 3-21) with the majority of the reaction already proceeding within 1 hour. A high selectivity towards PCM was achieved, though a small amount of what appeared to be 4HAP was detected (Appendix Figure 9-7). The formation of ketones has been shown to be possible via hydrolysis of the ketoxime.[154] This may have been facilitated in the present case by trace amounts of water in the solvent mixture. However, only a small amount of 4HAP is detected, as such the formation of PCM is more favourable under the current conditions.

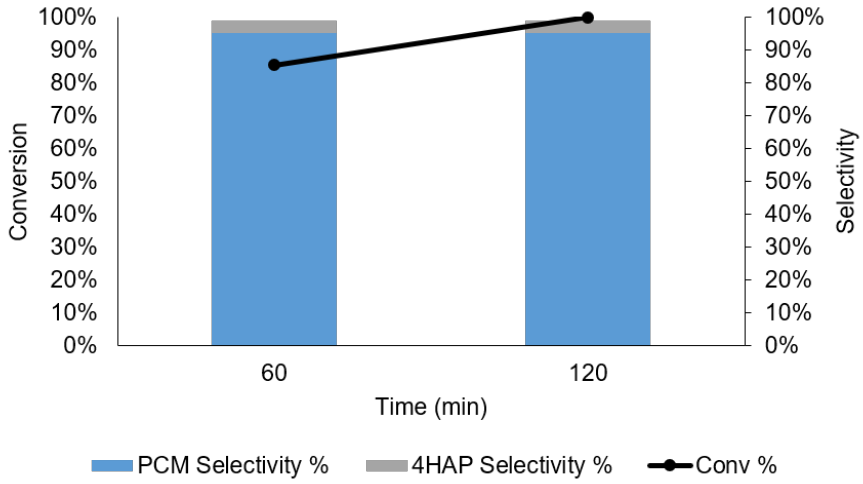

Figure 3-21: Conversion and selectivity to PCM using off-line NMR monitoring in PCM15.2

Once the reaction had reached completion, the product was isolated by removal of the solvent, leaving a viscous oil. Addition of ice cold diethyl ether, ethyl acetate or water caused precipitation of a pink solid which was extracted. The crude product was purified by recrystallisation using hot water. The results for the isolated yield are shown in Table 3.12. As was the case with acetic acid experiments, the strongly acidic environment favours the formation of a viscous oil during rotary evaporation. However, precipitation of the solid can be induced by the addition of a small amount of antisolvent and subsequent recrystallisation gave PCM as the desired product.

Table 3.12: Isolated yield of the batch organocatalysed Beckmann rearrangements experiments

Experiment	Extraction Solvent (Antisolvent)	Mass (g)	Yield (%)
PCM15.1	Diethyl Ether	0.054	27
PCM15.2	Water	0.081	40
PCM15.3	Ethyl Acetate	0.042	21

The isolated yield was variable, but this was due to experimental differences in work-up and extraction. While the extraction method needed further improvement to increase the isolated yield, the relatively fast and simple synthetic reaction showed high potential for translation into a continuous environment. The isolated product was tested using NMR and DSC. The peak positions and subsequent melting points of the product are shown in Table 3.13. The results clearly indicated that the isolated product matched well with the expected chemical shifts of PCM and the melting point also showed good agreement with literature. Therefore, the extracted product showed a high selectivity towards PCM, even if the isolated yield was lower than anticipated.

Table 3.13: Analysis of PCM15 after isolation

Experiment	Chemical Shift (ppm)	Melting Point (°C)
PCM15.1	(300 MHz, DMSO-d6) 1.97 (3 H, s), 6.62 - 6.71 (2 H, m), 7.28 - 7.38 (1 H, m), 9.14 (1 H, br, s), 9.65 (1 H, br, s)	168.8
PCM15.2	(300 MHz, DMSO-d6) 1.97 (3 H, s), 6.60 - 6.72 (2 H, m), 7.27 - 7.39 (2 H, m), 9.15 (1 H, br, s), 9.66 (1 H, br, s)	168.2
PCM15.3	(300 MHz, DMSO-d6) 1.97 (3 H, s), 6.66 (2 H, d, J = 8.9 Hz), 7.33 (2 H, d, J = 8.9 Hz), 9.15 (1 H, br, s), 9.66 (1 H, br, s)	169.0
4HAPO[154]	(200 MHz, DMSO-d6) 2.09 (3 H, s), 6.73 - 6.78 (2 H, d), 7.45 - 7.49 (2 H, d), 9.60 (1 H, br, s), 10.84 (1 H, br, s)	140 - 145
PCM[184]	(400 MHz, DMSO-d6) 1.98 (3 H, s), 6.68 (2 H, d, J = 8.8 Hz), 7.34 (2 H, d, J = 9.2 Hz), 9.14 (1 H, br, s), 9.65 (1 H, br, s)	170.2 - 170.6

See Appendix Figure 9-8 for the experimental spectra

Platform Development

For flow chemistry experiments using TFA as an organocatalyst, the schematic diagram of the reactor set-up is shown in Figure 3-22. The set-up used the Vapourtec R series pump and heater modules (as described in Section 2.5) to control the flow rates and reactor temperature respectively. The flow was transported from the feedstock to the reactor using PTFE tubing (1 mm ID) and the streams were pre-mixed using a PEEK T-piece (1 mm ID) at room temperature before entering the reactor. Pressure was maintained using a BPR (4 to 7 bar). Two PEEK valves were installed either side of the reactor in order to allow the system to be isolated while maintaining the pressure, should a safety issue arise. The PTFE reactor (27 mL, 1 mm ID) was heated to 70 °C. Regular aliquots were taken to monitor the reaction progress using NMR. The effluent was collected in a round bottom flask and reduced under vacuum to isolate the product.

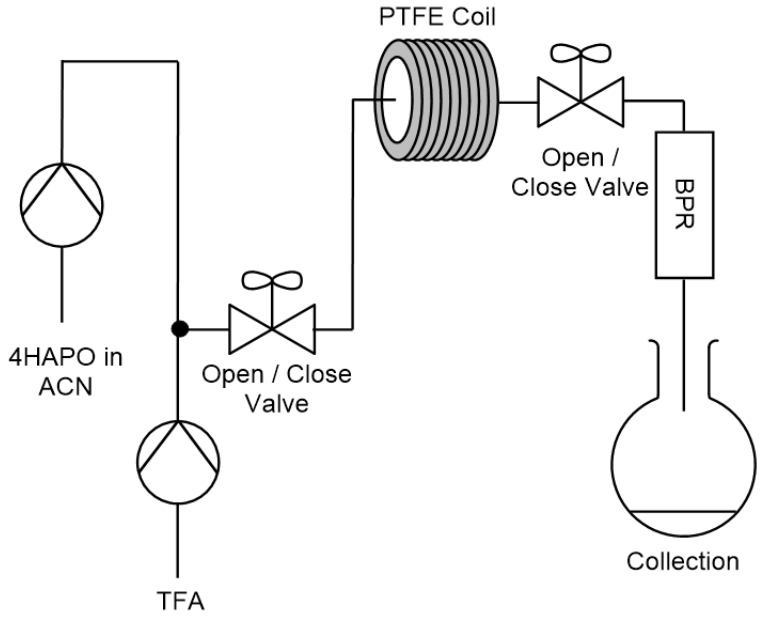

Figure 3-22: Set-up for the flow synthesis of paracetamol using 4HAPO and TFA

In terms of extraction, the process used in the batch system was refined further. In this case, the formation of the viscous oil was avoided. The majority of the solvent was reduced under vacuum to leave a small amount of pink oil. To the pink oil, a small amount of ethyl acetate or water was added. Rotary evaporation of the solvent/cosolvent mixture left a pink solid. The pink solid is extracted using ice cold water and left to dry overnight; no further purification was required. The experimental parameters used in Beckmann rearrangement flow experiments are shown in Table 3.14.

Table 3.14: Parameters for Beckmann rearrangements of PCM investigations

Experiment	4HAPO Flow Rate ($mL\,min^{-1}$)	TFA Flow Rate ($mL\,min^{-1}$)	Molar Ratio (at mixing) TFA:4HAPO	Residence Time (min)	Run Time (min)
PCM16.1	0.41	0.04	9	60:00	180
PCM16.2	0.82	0.08	9	30:00	120

Run conditions: 4HAPO = $0.14\,mol\,dm^{-3}$ in ACN, TFA = 8 mL, Temperature = 70 °C.

PCM16

Translation of the batch methodology to a flow environment was relatively straightforward in this case. The concentration of 4HAPO in the feedstock was adjusted to ensure that after mixing, the conditions in the coil reactor reflected those used in the batch process. Despite the increased concentration of 4HAPO in the feedstock, the solute remained in solution. The reaction was run over 2 to 3 hours. As the mass and heat transfer in a coil reactor tends to be superior to batch vessels, the residence time was reduced to 1 hour in PCM16.1 and 30 minutes in PCM16.2. As the reaction was shown in literature to be sensitive to the TFA/substrate molar ratio, the flow rate and therefore mixing ratio was kept the same.

The results from the NMR monitoring of PCM16.1 are shown in Figure 3-23. As can be seen, despite the reduced reaction period, the process is still highly selective to PCM with conversion that matches the batch procedure. The improved productivity and reaction efficiency is not surprising, as the use of TFA in Beckmann rearrangements has been demonstrated for the production of caprolactam from cyclohexanone oxime in a microchemical flow system.[185] For caprolactam, the reaction time was decreased from 100 min to 40 sec, though this does not necessarily translate to higher productivity due to the difference in reactor scale.

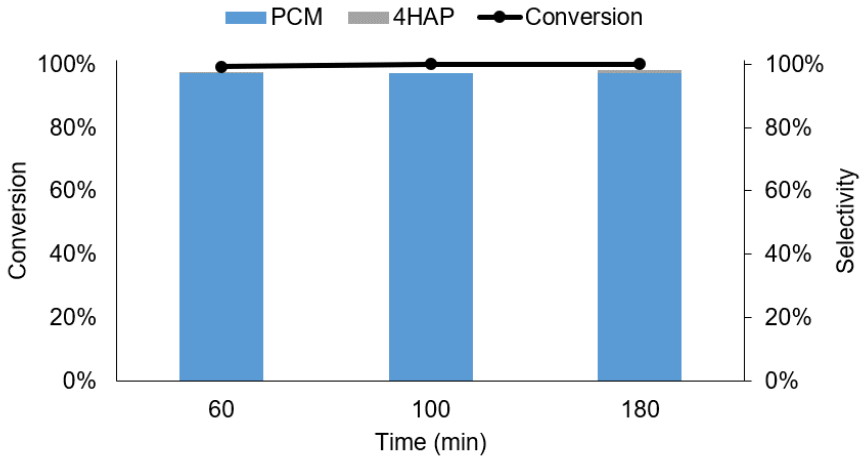

Figure 3-23: Conversion and selectivity to PCM using off-line NMR monitoring in PCM16.1

For PCM16.2, the RT was decreased further to boost efficiency, however the reaction does not go to completion (Figure 3-24). Instead, the conversion averages 83% over 4 RTs, though the selectivity towards PCM remains high.

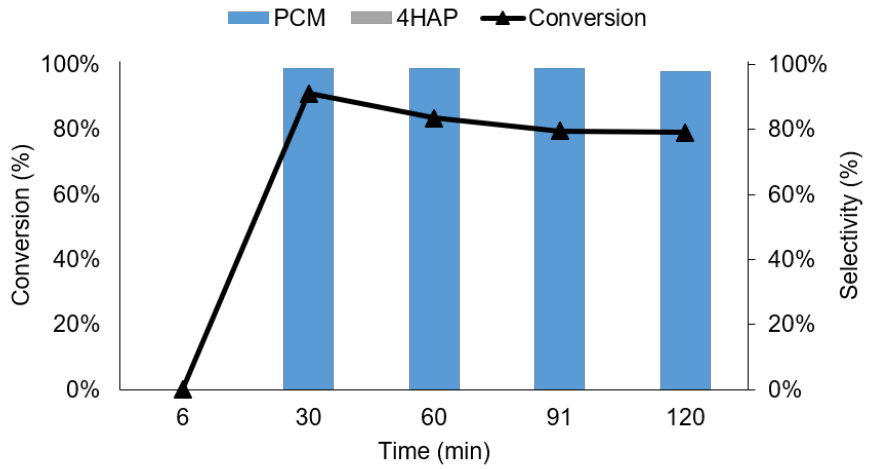

Figure 3-24: Conversion and selectivity to PCM using off-line NMR monitoring in PCM16.2

Based on these results, a 60 minute RT is effective under the current conditions, however it is possible that a 30 minute RT could still be facilitated by adding a static mixer reactor or by increasing reactor temperature. The latter however, may lead to thermal decomposition under extreme conditions. While the batch process contained a small amount of 4HAP and an unknown side product, the flow reactor appears to reduce this complication. While traces of both impurities are still visible in the raw NMR spectra above the baseline, both appear significantly reduced relative the PCM peak integral (See Appendix Figure 9-9).

Analysis of the isolated product is shown in Table 3.15. The experimentally determined melting point was similar to the values found in the batch experiments. The NMR peak shift was also close to the value found in batch experiments and literature. The isolated yield was also improved, the addition of a small amount of water and ethyl acetate to the rotary evaporation process helped to avoid the formation of the viscous brown oil previously encountered. Of note however, was the higher than anticipated isolated yield of PCM16.2. This was unexpected as conversion was monitored as lower than PCM16.1 while the product showed a similar purity after isolation. The likely cause was that the reaction continued in the collection vessel, or during rotary evaporation. In further work, this could be avoided by the addition of a quenching stream after the reactor. Earlier work in this thesis during the one-pot amidation procedure, along with

results shown by Zhang *et al.*, indicate that water would be effective at preventing further reactivity in the presence of TFA.[186]

Table 3.15: Isolated yield and analysis of the flow organocatalysed Beckmann rearrangements experiments

Experiment	Isolated Yield (%)	Chemical Shift (ppm)	Melting Point (°C)
PCM16.1	71	(300 MHz, DMSO-d6) 1.97 (3 H, s), 6.66 (2 H, d, J = 8.8 Hz), 7.33 (2 H, d, J = 9.0 Hz), 9.15 (1 H, br, s), 9.66 (1 H, br, s)	168.5
PCM16.2	83	(300 MHz, DMSO-d6) 1.97 (3 H, s), 6.66 (2 H, d, J = 8.9 Hz), 7.33 (2 H, d, J = 8.9 Hz), 9.15 (1 H, br, s), 9.66 (1 H, br, s)	169.2

Raw spectra in Appendix Figure 9-10

While the methodology discussed here is effective as a single flow synthesis reaction, it is not well suited for integrated continuous crystallisation. In order to initiate crystallisation, supersaturation must be induced. TFA is a strong acid and potentially hazardous, thus it would make a poor crystallisation solvent medium. Currently, 9 molar equivalents are needed to facilitate the reaction. As well as safety concerns, addition of TFA has the effect of diluting the reaction medium, which makes it more difficult to induce crystallisation. Therefore TFA would likely need to be removed prior to crystallisation. Ideally a solvent swap would be used, however current available methods are limited in dealing with complex solvent mixtures such as ACN/TFA. However, the work does show that the conversion from 4HAP to PCM can be achieved using a series of stepwise, flow synthetic reactions with off-line workup.

3.4 Integrated Crystallisation of 4-Hydroxyacetophenone Oxime

While the amidation procedure from 4HAP to produce PCM in the work presented was unsuitable for integrated crystallisation investigations in its current state, during the course of these studies, the oximation synthesis in ethanol/water solutions for production of 4HAPO was identified as a possible alternative target. As has been demonstrated in this work and literature, 4HAPO is useful intermediate in the preparation of PCM. A fast and clean route has been designed to deliver 4HAPO in quantitative yields using a flow synthesis platform. In this section, investigations aimed to optimise the flow synthesis process for integration with a continuous crystallisation platform.

3.4.1 Gravimetric Solubility Studies

In order to best determine the suitable conditions for crystallisation, a gravimetric solubility study was carried out to measure the solubility of 4HAP and 4HAPO in ethanol/water solvent mixtures. The experimental procedure is outlined in Section 2.3. The solubility dependence of 4HAP and 4HAPO in different ethanol/water mixtures is shown in Figure 3-25 and the average solubility for each composition is shown in Table 3.16.

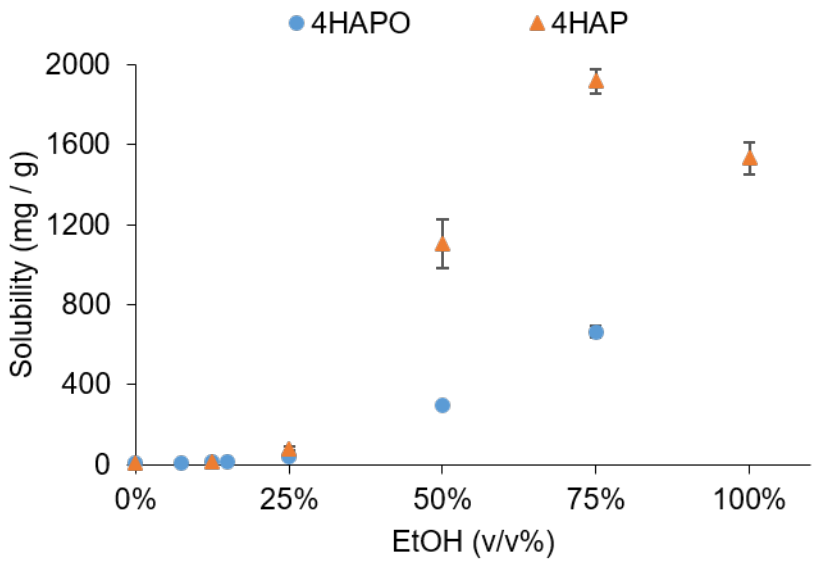

Figure 3-25: Solubility curves for 4HAP and 4HAPO in ethanol/water solvent mixtures at 20 °C

Table 3.16: Average solubility of 4HAPO and 4HAP in ethanol/water mixtures at 20 °C

EtOH (v/v%)	4HAP ($mg\,g^{-1}$)	4HAPO ($mg\,g^{-1}$)
0	7.2	7.3
7.5	-	11.9
12.5	18.3	16.8
25	81.7	40.0
50	1106.5	294.5
75	1916.6	665.8
100	1531.9	-

From the results, 4HAP and 4HAPO both have low solubility in pure water. As the amount of ethanol increases, the solubility of both components increases. The

solubility of 4HAP reaches a maximum at 75 v/v% EtOH. The degree of change is different between the two components; 4HAP is more strongly influenced by ethanol (EtOH) than 4HAPO. The largest solubility difference is at 50% EtOH where 4HAP is almost four times more soluble than 4HAPO. While this solvent ratio would be best to eliminate any remaining organic impurities, the high overall solubility would result in a significant loss of product to the liquor. Furthermore, the conversion of 4HAP to 4HAPO is high in the flow synthetic process, so there is a low probability that 4HAP impurities will exceed the solubility threshold, providing the reaction reaches completion.

The most ideal solvent ratios from the data for integration, would be 12.5 and 25 v/v% EtOH. 25 v/v% shows a larger difference in the solubility ratio of 4HAP and 4HAPO, while maintaining relatively low solubility at ambient conditions. This is also the set-up that has been tested in the flow synthesis reaction successfully. Reducing EtOH content to 12.5 v/v% would reduce the amount of product lost to the liquor, but may promote precipitation of unreacted 4HAP or by-products. While pure water offers the highest potential solid recovery, the synthetic reaction requires a degree of EtOH in the feedstock to achieve dissolution of 4HAP at ambient temperatures.

The temperature dependent solubility of 4HAP and 4HAPO in 25% and 12.5% EtOH is shown in Figure 3-26.

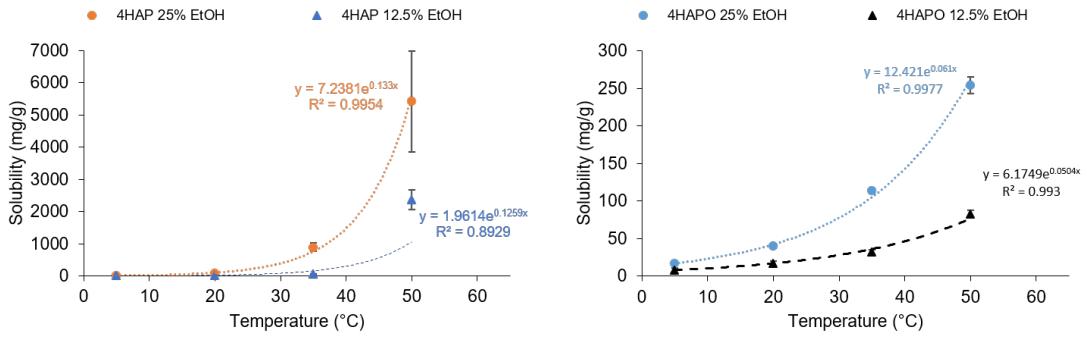

(a) 4HAP (b) 4HAPO

Figure 3-26: Temperature dependant solubility of a) 4HAP and b) 4HAPO in 25% and 12.5% ethanol/water solutions

From the data, the solubility of 4HAP and 4HAPO was found to be similar at 5 °C in both EtOH compositions. However, as the temperature increases 4HAP becomes more soluble than 4HAPO. The difference in solubility with temperature is larger for 25 v/v% EtOH solutions. For 4HAPO, both solvent compositions generated solubility curves from the data with a good exponential fit. For 4HAP, the solubility curve

generated was less accurate, particularly at high temperatures. This is due to the fact that the supersaturated solution of 4HAP became biphasic at high saturations (due to preferential dissolution in EtOH over water). This made it difficult to determine by eye when saturation had been reached and led to higher variation in repeat measurements. Another complication is that 4HAP forms a hydrate at high water content and low temperatures. This leads to a switch in the most thermodynamically stable polymorph, where form I is preferred above 29 °C and the hydrate form is more stable below 29 °C. Literature has shown that form I and the hydrate have different solubilities. Hence form I and the hydrate are enantiotropic and a change in the solubility curve is expected above and below 29 °C.[187] This could be corrected in Figure 3-26 by taking more solubility measurements above and below the transition temperature. However, it was deemed unnecessary for this work, as the important aspect was to ensure the solubility of 4HAP was low in relation to 4HAPO.

What is established clearly from the data is that a change in the solubility behaviour will occur after conversion of 4HAP to 4HAPO. Therefore, the system can optimised to be undersaturated with respect to 4HAP but supersaturated with respect to 4HAPO. Hence, it was potentially possible to crystallise directly from the reaction effluent. The work therefore, concentrated on developing a reaction procedure and cooling crystallisation process that would work within this framework.

3.4.2 Platform Development

Having established parameters within which to conduct continuous crystallisation experiments, the next aspect was to establish a suitable crystalliser. A number of conditions needed to be met for successful integration:

1. The synthesis and crystalliser needed to be similar in scale;
2. The flow rates between synthesis and crystallisation needed to be complementary;
3. The system needed to be safe and easy to operate;
4. The platform design needed to be versatile and modular for optimisation.

Based on these criteria, the kinetically regulated automated input crystalliser (KRAIC) described in Section 2.7.1 would meet most of the essentials. However, concern regarding safety prevented integration. The KRAIC is a large platform and requires significant lab space. The flow chemical reaction uses HOA, which is a suspected carcinogenic and while the current flow synthetic process reduced potential contact, precautions needed to be taken to ensure that the effluent from the crystallisation was safely housed in

a fume cabinet after exiting the reactor. To overcome this shortcoming, a compact miniature KRAIC, known as the mini-KRAIC (m-KRAIC) was built (Figure 3-27). The m-KRAIC uses the same concepts as the KRAIC and is a segmented flow crystalliser. In order to save space however, the main body of the KRAIC consisting of a 15 m fluorinated ethylene propylene (FEP) tubular coil (3.2 mm ID), is compacted onto a single custom size DrySyn basin.

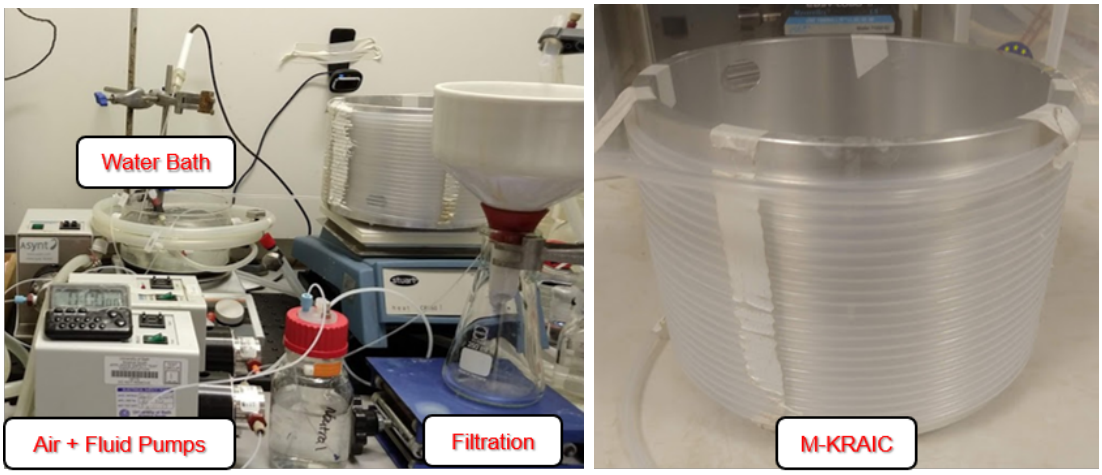

(a) m-KRAIC set-up (b) m-KRAIC coiled reactor

Figure 3-27: Photographs of the m-KRAIC

For comparison, the volume and length of the KRAIC is 121 mL and 150 cm respectively. The m-KRAIC has a volume of 115 mL and length of 143 cm. The compact design of the m-KRAIC could have a minor effect on the mixing regime within the reactor but it will not change the overall plug flow regime and therefore is not detrimental to the crystallisation process. The design is as versatile and modular as the KRAIC and so the crystalliser can be adjusted to the system. The m-KRAIC will also be easier to transport for off-site experiments and can fit into a conventional fume cabinet, which allows crystallisation experiments to be safely run where solvent vapour is a concern. For the purposes of this work, the more compact design meant that the additional space could be used to accommodate the synthetic reaction, allowing integration experiments to be tested within a smaller space, emphasising the potential for reducing future plant footprint.

3.4.3 Experimental

A schematic of the integrated, flow synthesis and m-KRAIC platform set-up is shown in Figure 3-28 and a photograph is shown in Figure 3-29. In decoupled runs, the flow synthesis output was collected in a round bottom flask and allowed to crystallise at room temperature unless otherwise stated.

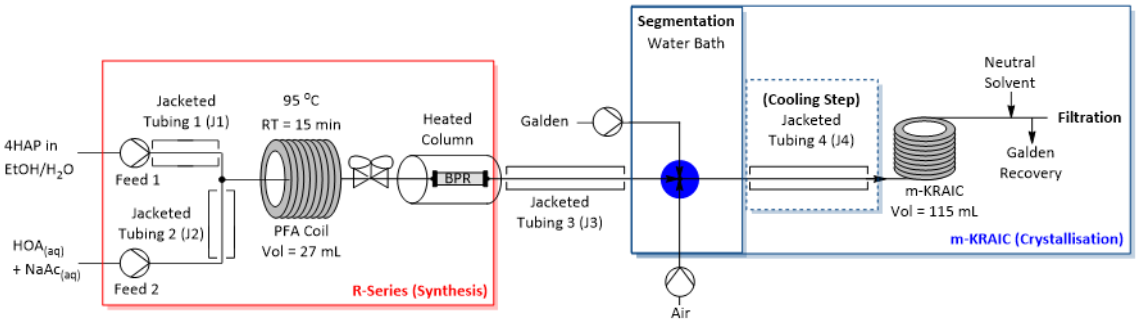

Figure 3-28: Schematic diagram of the integrated synthesis and crystallisation process for 4HAPO production.

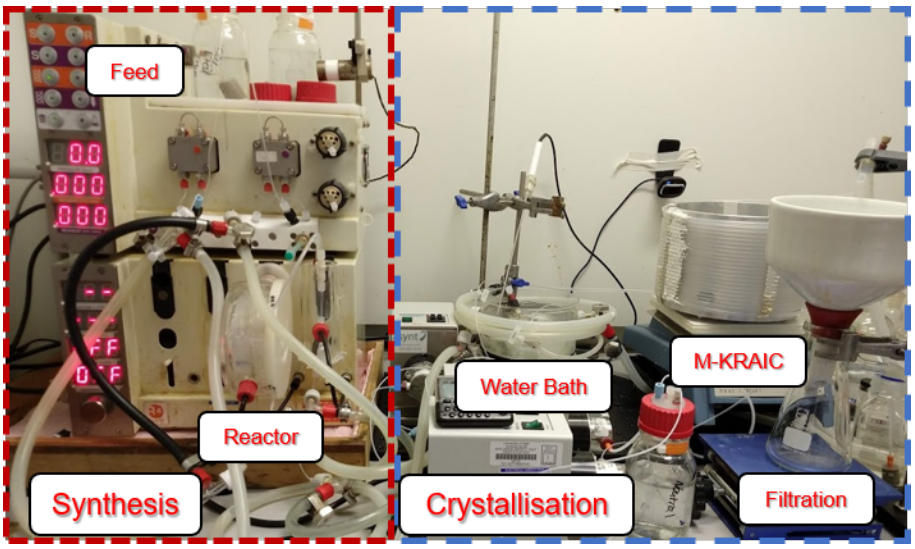

Figure 3-29: Photograph of the integrated synthesis and crystallisation process for 4HAPO production

Synthesis

The synthetic reaction was carried out in a 27 mL reactor coil consisting of PFA tubing (1 mm ID) housed in a glass reactor and equipped with a temperature probe. The coil is attached to an R-series heater unit which controls and monitors the temperature. Pumping of the reagent streams was facilitated by the Vapourtec R-series pump module

and heating the synthesis reactor was facilitated by the Vapourtec R-series heater unit. A BPR (2 to 4 bar) was used to maintain pressure in the reactor. The outlet from the flow synthesis was transported to the segmentation point using temperature-controlled jacketed tubing which was actively heated to avoid crystallisation before segmentation. In later experiments where supersaturation was particularly high, the BPR and feed-lines 1 and 2 were actively heated to avoid precipitation. The BPR was heated using a glass column with a temperature probe attached to the R-series heater unit. Temperature of the jacketed tubing was controlled using a Grant R3 TX150 circulator unit.

In investigations for decoupled synthetic reactions, the segmented flow crystalliser was not used and the effluent from the reactor was transported using jacketed tubing 3 (J3) to a round bottom flask stirred at 500 rpm.

Steady state operation was verified as follows. A 1.0 mmol dm^{-3} concentration of Eosin Y dye was prepared in EtOH. The Eosin Y solution was run at 0.45 mL min^{-1} in Feed 1 into the reactor and a corresponding feed of pure EtOH (Feed 2) was run at 1.35 mL min^{-1}. Aliquots from the reactor were taken at regular intervals and the absorption of the sample was recorded at a fixed wavelength of 478 nm using a Jenway bench-top Spectrometer. The same cuvette with a 1 cm length was used for all measurements and the absorption was calibrated against a reference containing pure EtOH. The cuvette was cleaned with EtOH and dried before the next measurement. The concentration was determined from the absorption using the Beer-Lambert law (Equation 2.1) and the corresponding values were then used to construct a concentration vs time plot to determine steady state in the flow reaction. The results from this calibration are assumed to be analogous with the flow synthetic reactions using the same flow rates.

Segmentation

Segmentation is achieved by introducing an immiscible fluid (i.e. a carrier fluid) and air to the feed line using a glass cross piece (3.2 mm ID). The air and carrier fluid were supplied using Ismatec (Reglo-Z series) gear pumps. The cross piece was kept submerged under a water bath which was actively heated. The carrier fluid used is a liquid perfluoropolyether (PFPE), known commercially as Galden SV110.

Crystallisation

Crystallisation was facilitated by the m-KRAIC. The temperature of the coil was not actively controlled and is left at room temperature. In some runs, an additional active

cooling step was added. This consisted of a 1.2 m (3.2 mm ID) section of FEP tubing jacketed with silicone tubing (J4). This cooling step was controlled using a designated circulatory bath. The cooling step was installed after segmentation but before the m-KRAIC coil. A zero volume FEP union was used to connect the jacketed tubing to the main crystalliser. Galden recovery, as well as filtration of the crystalline product, was achieved using an end-piece as described in Section 2.7.1.

The experimental parameters for synthesis and crystallisation of experiments in 25 v/v% EtOH are shown in Table 3.17 and 3.18 respectively. The experimental parameters for synthesis and crystallisation of experiments in 12.5 v/v% EtOH are shown in Table 3.19 and 3.20.

Table 3.17: Concentration and feed rates in 25% EtOH integrated continuous processing

	Pump 1 (P1)		Pump 2 (P2)		
Experiment	Flow Rate ($mL\,min^{-1}$)	4HAP ($mol\,dm^{-3}$)	Flow Rate ($mL\,min^{-1}$)	HOA ($mol\,dm^{-3}$)	NaAc ($mol\,dm^{-3}$)
HAPO1	0.45	2.16	1.35	0.73	1.09
HAPO2	0.45	2.16	1.35	0.73	1.09
HAPO3	0.45	3.70	1.35	1.24	1.86

Reaction conditions: Pump 1 = ethanol, Pump 2 = water

At reactor coil: solution = 25 v/v% ethanol, molar ratio (4HAPO:HOA:NaAC) = 1:1:1.5, temperature = 95 °C, RT = 15 min

Table 3.18: Feed rates for crystalliser in 25% EtOH integrated continuous processing

	Concentration ($mg\,mL^{-1}$)	Flow Rate ($mL\,min^{-1}$)			Set Temperature (°C)		
Experiment	4HAPO[a]	Feed	Air (P3)	Galden (P4)	Feed	Water Bath	Cooling Step
HAPO1	82	1.8	2.1	6.3	55	55	N/a
HAPO2	82	1.8	2.1	4.18	65	65	5
HAPO3	140	1.8	2.1	4.18	65	65	5

a: Calculated assuming quantitative conversion of 4HAP to 4HAPO

Table 3.19: Concentration and feed rates in 12.5% EtOH integrated continuous processing

	Pump 1 (P1)		Pump 2 (P2)		
Experiment	Flow Rate ($mL\,min^{-1}$)	4HAP ($mol\,dm^{-3}$)	Flow Rate ($mL\,min^{-1}$)	HOA ($mol\,dm^{-3}$)	NaAc ($mol\,dm^{-3}$)
HAPO4	0.45	3.75	1.35	1.26	1.90
HAPO5	0.45	3.75	1.35	1.26	1.90
HAPO6	0.45	3.75	1.35	1.26	1.90
HAPO7	0.45	3.75	1.35	1.26	1.90
HAPO8	0.45	3.75	1.35	1.26	1.90

Reaction conditions: Pump 1 = 50 v/v% ethanol, Pump 2 = water

At reactor coil: solution = 12.5 v/v% ethanol, molar ratio (4HAPO:HOA:NaAC) = 1:1:1.5, temperature = 95 °C, RT = 15 min

Table 3.20: Feed rates for crystalliser in 12.5% EtOH integrated continuous processing

	Concentration ($mg\,mL^{-1}$)	Flow Rate ($mL\,min^{-1}$)			Set Temperature (°C)		
Experiment	4HAPO[a]	Feed	Air (P3)	Galden (P4)	Feed	Water Bath	Cooling Step
HAPO4	142	1.8	n/a	n/a	65	n/a	n/a
HAPO5	142	1.8	2.1	4.18	65	65	n/a
HAPO6	142	1.8	2.1	4.18	65	50	20/15/5
HAPO7	142	1.8	4.18	6.3	65	50	10
HAPO8	142	1.8	n/a	n/a	65	n/a	n/a

a: Calculated assuming quantitative conversion of 4HAP to 4HAPO

3.4.4 Results and Discussion

25 v/v% EtOH

The isolated yield and residence times for flow synthesis and crystallisation experiments in 25 v/v% EtOH are shown in Table 3.21.

Table 3.21: Residence times and isolated yield for 4HAPO continuous synthesis and crystallisation for 25 v/v% EtOH

Experiment	Collection Period		Residence Time (min:sec)		
	Collection Time (min:sec)	Yield (%)	Cooling Step	m-KRAIC	Total[a]
HAPO1	57:00	11.4	n/a	39:40	55:50
HAPO2	60:00	15.1	01:30	20:40	38:20
HAPO3	71:00	16.7	01:30	20:40	38:20

a: Including synthesis and transfer stage (RT = 16:10 min)

As can be seen from the results, the isolated yield was relatively low. Even with the addition of a cooling step only a small increase was observed in the crystallisation yield. The concentration was also increased in HAPO3 with no major improvement in the isolated yield. The reason that no major change was observed was that the majority of crystallisation only occurred on contact with the filter paper. No crystallisation was visible to the naked eye within the m-KRAIC during the operation period. The relative supersaturation for HAPO1-3 at two key points are shown in Table 3.22.

Table 3.22: Relative supersaturation in 25 v/v% EtOH

Experiment	Cooling Step		m-KRAIC Outlet	
	Set Temperature	Rel. Supersat.	Temperature[a]	Rel. Supersat.
HAPO1	n/a	-	23.9	0.86
HAPO2	5	4.6	23.2	0.9
HAPO3	5	8.6	23.0	2.2

a: Measured using an external temperature probe at the m-KRAIC outlet. The relative supersaturation was calculated, using Equation 1.5. The equation from Figure 3-26 b) was used to calculate equilibrium solubility

As can be seen from the Table 3.22, all runs showed a degree of supersaturation in the system. However, as no visible crystallisation occurred within the m-KRAIC it is possible that the system remained within the metastable region throughout. As the m-KRAIC uses a segmented flow environment analogous to the KRAIC, the slugs are

suspended away from the walls of the tubing due to a capillary effect.[131] As such, heterogeneous nucleation via the crystalliser walls is removed. This environment favours primary homogeneous nucleation. This may have had a knock-on effect of extending the induction time compared to the batch process. As the filter paper acts as a surface, this lowers the energy barrier to crystallisation and hence induces nucleation. One method that would help in better crystallisation process design would be to use turbidity experiments to find an approximate metastable zone width (MZW). However, the MZW is dependent on both cooling rate and the crystalliser environment. Therefore, batch tests may not inherently reflect the m-KRAIC vessel, while internal measurements are difficult in the m-KRAIC due to equipment limitations. If it became possible to measure the MZW routinely in flow crystallisers such as the KRAIC, then this could help in the adoption of continuous crystallisation technology.

Another issue was that the flow rates from the air and carrier fluid were not always consistent; this was particularly the case for HAPO1. This was rectified by removal and cleaning of the pumps but RT could not be predicted from the combined set flow rates values, so the RT was measured experimentally. The pumping in the synthetic reaction feed was tested and found to be consistent. As a result only the downstream processing was affected. The reaction was monitored using offline NMR, carried out by taking aliquots from the m-KRAIC outlet. The reaction was tracked before, during and after the collection period, by observing the aromatic peak region between 6 to 10 ppm. The results for HAPO3 are shown in Figure 3-30.

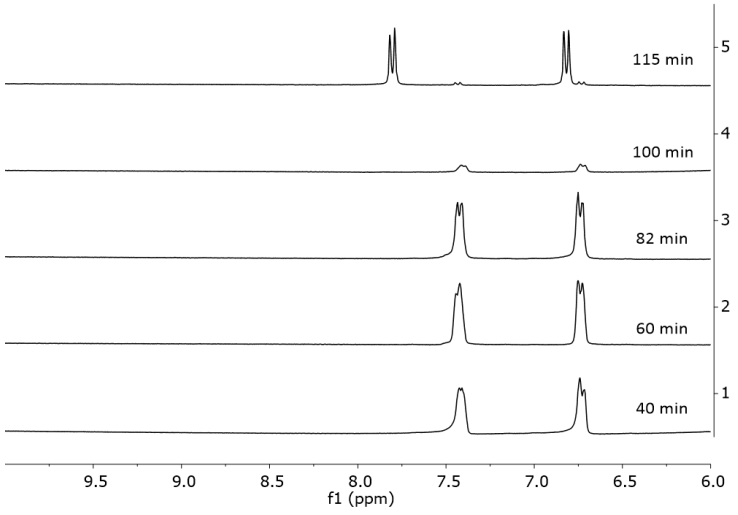

Figure 3-30: NMR spectra between 6 and 10 ppm at different time stamps during HAPO3

As the results show, the lack of peaks at 7.8 ppm and 6.8 ppm between 40 to 100 minutes indicates that 4HAP has converted to 4HAPO. The conversion is similar to the results observed the uncoupled flow synthesis processes. The resurgence of the 4HAP peak at 115 min occurs during the shutdown period, at which point the feed lines had been switched to pure solvent. HAPO1 and HAPO2 showed the same spectra trends to HAPO3 (See Appendix Figures 9-11 and 9-12).

Samples were taken from the isolated product and subjected to DSC. Traces from each run (HAPO1 to HAPO3) are shown in Figure 3-31, the corresponding values for the melting peak and exothermic peak are given in Table 3.23.

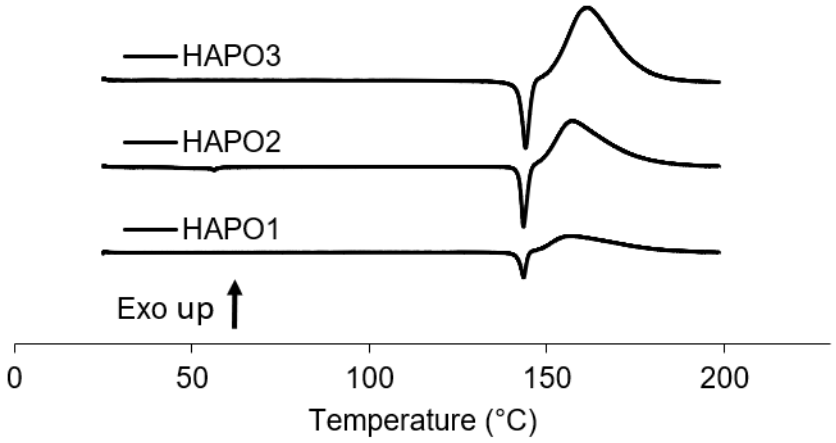

Figure 3-31: Comparison of DSC traces for HAPO1, HAPO2 and HAPO3, note that values are offset in the Y-direction for clarity

Table 3.23: Melting point and decomposition peaks in DSC traces for HAPO1 to HAPO3

Experiment	Melting Point (°C)	Exothermic Peak (°C)
HAPO1	143.5	156.2
HAPO2	143.4	157.6
HAPO3	144.0	161.5

As can be seen from the traces, there is a good overlap between the melting points, but the exothermic peak corresponding to decomposition of 4HAPO is more variable. This is reflected in the values in Table 3.23. Nonetheless, DSC results match those from flow synthesis experiments in Section 3.3.1. This confirms that the addition of a continuous crystallisation platform and filtration step have not affected product stability.

Samples from HAPO1 to HAPO3 were also subjected to PXRD analysis and the diffraction patterns are shown in Figure 3-32. These are compared to a simulated pattern derived from the SCXRD structure of 4HAPO.[183]

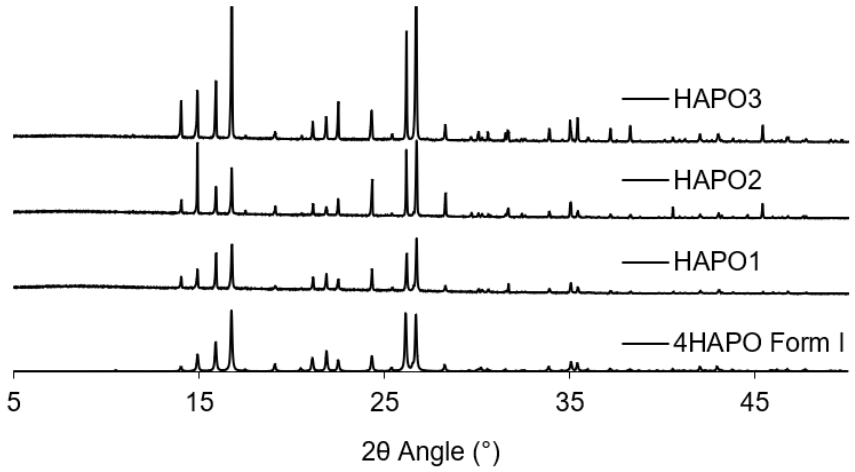

Figure 3-32: Comparison of PXRD patterns for HAPO1 to HAPO3 with the simulated pattern reported from SCXRD

A quick comparison reveals that the patterns show a good match with the simulated pattern, which confirms the presence of the known 4HAPO crystal form. As 4HAPO only has one reported polymorph, no other forms are expected to be isolated during crystallisation. Some differences in relative peak heights are observed, but this is likely a consequence of preferred orientation.

While the coupling of the compact m-KRAIC and flow synthetic method was effective in producing a small, self-contained integrated reactor space, issues remained with crystallisation. Previous work in direct batch crystallisation from flow synthesis had shown that crystallisation occurred within 30 minutes, but in the m-KRAIC process, no visible crystallisation occurred in-line during operation. Supersaturation appeared insufficient to induce primary nucleation as crystallisation mostly occurred during filtration. This in turn led to clogging of the filter which needed frequent changing. To induce crystallisation, the supersaturation level needed to be raised. As already noted during gravimetric measurements, reducing EtOH composition will increase supersaturation in the crystalliser. This would provide a simple method to increase supersaturation without changing the process equipment or flow rates.

12.5 v/v% EtOH

To ensure 4HAP and 4HAPO remained in solution during flow synthesis in 12.5 v/v% EtOH, the uncoupled 4HAPO reaction was tested. The synthesis was carried out as described in the experimental, Section 3.4.3, however the effluent from the reactor was decoupled from the segmentation bath and collected in a round bottom flask. The parameters for the synthesis-only (HAPO4) and all coupled flow experiments (HAPO5 to HAPO7) are outlined in Table 3.19 and 3.20.

HAPO4

In first attempts at running the reaction at the reduced EtOH composition, blockages occurred in the set-up. This was generally around the BPR, T-piece and reactor outlet. To mitigate this the glass column (pictured in Figure 3-28 in the experimental) was added and the BPR was actively heated to 65 °C. Up to this point, the BPR had not needed to be actively heated. The T-piece could not be actively heated, but the distance from the jacketed feed lines, T-piece and reactor were adjusted so as to minimise the portion of tubing without an active heat source. The reaction proceeded well after these changes and the resulting effluent crystallised at room temperature during collection. The samples were left overnight to crystallise and the isolated yield was 56.5% from a 75 minute collection period. NMR monitoring was carried out under the new conditions to determine if solvent composition affected the reaction rate. The peaks between 6 to 10 ppm were tracked and the results are shown in Figure 3-33.

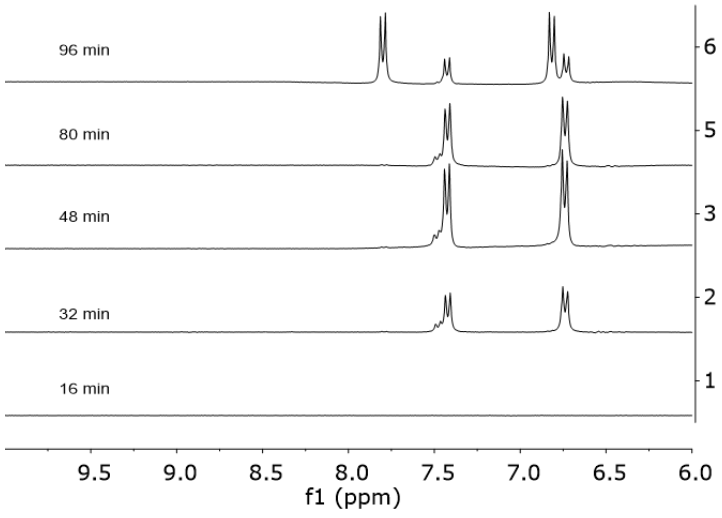

Figure 3-33: NMR spectra between 6 and 10 ppm at different time stamps during HAPO4

As can be seen, 4HAP was converted to 4HAPO readily and any residual peaks are below the baseline. 4HAPO is the major product, but a secondary peak is noted to overlap with the 4HAPO aromatic proton peaks. These shoulder peaks are most visible at 64 min. However, they are not seen in the isolated product, indicating they are likely the solution based-intermediate previously observed.

HAPO5 to HAPO7

After verifying that the synthetic reaction rate was unaffected by the reduced EtOH content, experiments HAPO5 to HAPO7 were reconnected to the segmented crystalliser. HAPO5 was run without the cooling step and HAPO6 and HAPO7 were run with the additional active cooling step. The isolated yield and residence times for coupled flow synthesis and crystallisation experiments are shown in Table 3.24, HAPO4 has been included for comparison.

Table 3.24: Residence times and isolated yield for 4HAPO continuous synthesis and crystallisation in 12.5 v/v% EtOH

Experiment	Yield (%)	Residence Time (min)		
		Cooling Step	m-KRAIC	Total[a]
HAPO4	56.5	n/a	n/a	16:10
HAPO5	61.6	n/a	23:30	39:40
HAPO6	Blocked	01:50	25:00	43:00
HAPO7	Blocked	01:20	15:40	33:10

a: Including synthesis and transfer stage (RT = 16:10 min)

In HAPO5 no blockages occurred during the run, however no visible (by eye) crystallisation occurred within m-KRAIC during the run. Crystallisation did occur readily around the m-KRAIC end-piece and on the filter paper. The crystallised product was collected and left to dry before weighing. The yield was 61.6%. The result does indicate that while no visible crystal growth is occurring within the m-KRAIC, work-up of the extracted product will result in similar solid recovery to batch crystallisation. To try to induce nucleation, the cooling step was added for HAPO6 and HAPO7 to increase supersaturation. In HAPO6 the cooling step was run at 5 °C initially but the system blocked within 30 minutes. After resetting, the cooling step was raised to 20 °C, but no crystallisation occurred after 28 minutes. The cooling step was then dropped to 15 °C but a major blockage formed at 40 minutes, 10 minutes after lowering the cooling step. As a result of the blockages in the m-KRAIC, the system had to be shutdown and reset without accurate yield collection.

In HAPO7 the cooling step was set to 10 °C. The air and carrier fluid pumps were also increased by one increment (equivalent to an increase of 2.1 mL min^{-1}). The additional velocity to the net flow during crystallisation was intended to reduce blockage formation and help better suspend any crystals in the slugs. A cooling step of 10 °C was used as a median between 20 °C which did promote nucleation and 5 °C which blocked readily. Despite these changes, the system blocked 40 minutes into operation.

The relative supersaturation of 4HAPO at the m-KRAIC outlet and during the cooling step in 12.5 v/v% EtOH is shown in Table 3.25.

Table 3.25: Relative supersaturation in 12.5 v/v% EtOH

Experiment	Cooling Step		m-KRAIC Outlet	
	Set Temperature (°C)	σ	Temperature[a] (°C)	σ
HAPO5	n/a	-	26.0	6.0
HAPO6	5/20/15	19.1/8.4/11.1	23.2	7.0
HAPO7	10	14.6	24.5	6.5

a: Measured using an external temperature probe at the m-KRAIC outlet. The relative supersaturation (σ) was calculated using Equation 1.5. The equation from Figure 3-26 b) was used to calculate equilibrium solubility

As can be seen, the relative supersaturation is much higher than compared with HAPO1 to HAPO3. As a result, the driving force towards nucleation is much higher. Importantly the higher supersaturation is maintained at ambient temperatures. This is confirmed by looking at the temperature profiles for HAPO5 and HAPO6 (at 5 °C) as shown in Figure 3-34.

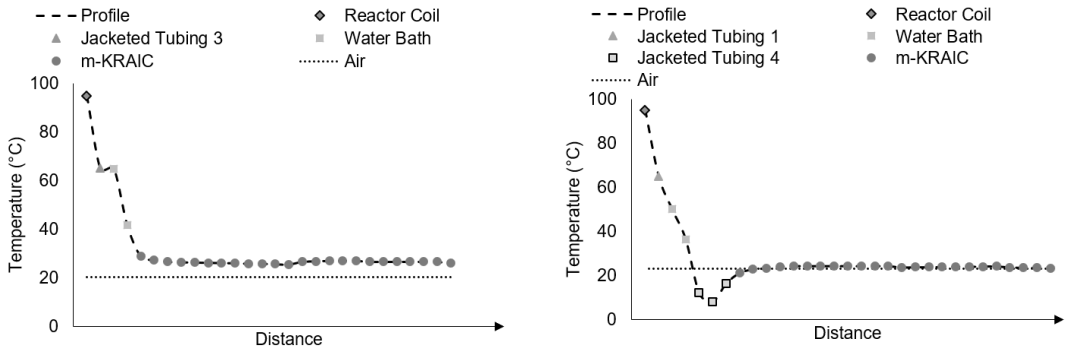

(a) No active cooling step

(b) Active cooling to 5 °C

Figure 3-34: Temperature profiles for a) HAPO5 with no cooling step and b) HAPO6 at 5 °C cooling step, as measured using an external temperature probe

As the feed proceeds into the m-KRAIC there is rapid heat loss after the water bath. In the case of HAPO6, the temperature decreases below room temperature for a short period during the cooling step before stabilising. Each data point of the m-KRAIC represents a different coil. The feed rapidly reaches ambient conditions in both HAPO5 and HAPO6 and this is maintained throughout the 20 to 25 min RT of the m-KRAIC. In combination with the examples given in Table 3.25, it is safe to assume that the supersaturation level is high and relatively constant in the m-KRAIC. However this did not lead to spontaneous nucleation, as a consequence of the wide MZW.

While the additional cooling in HAPO6 and HAPO7 may have caused some crystallisation, the major cause for blockages occurred around the join between the cooling step and the m-KRAIC. Despite attempts to form a flush connection, observed crystals appeared to snag on the join. This then became a point for secondary nucleation that caused rapid growth. In future, a more effective design may be to directly attach the cooling stage to the m-KRAIC tubing, thereby removing the uneven surface and avoid uncontrolled nucleation.

Analysis of the solid form of HAPO4 and HAPO5 using DSC and PXRD is shown in Figure 3-35. HAPO6 and HAPO7 could not be analysed as the blockages were not recovered.

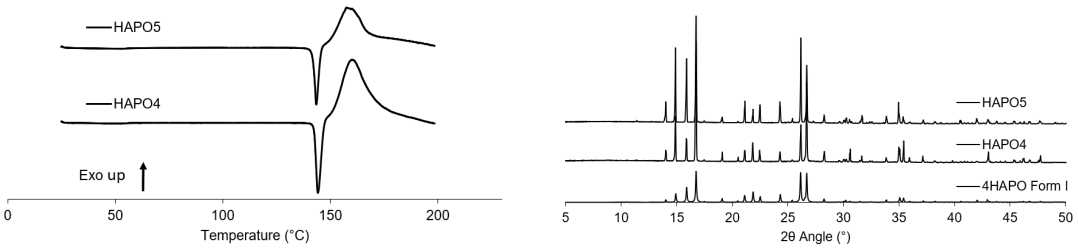

(a) (b)

Figure 3-35: Analysis of HAPO4 and HAPO5 a) DSC traces and b) PXRD patterns with simulated PXRD pattern of 4HAPO for comparison.

As was the case with HAPO1 to HAPO3, the solid form matches the expected PXRD pattern for 4HAPO. The DSC trace also shows the typical melting point between 140 °C and 145 °C followed by a decomposition peak. No major changes were observed in the polymorphic behaviour of the product extracted from the m-KRAIC compared to the batch crystallisation in HAPO4.

In summary, cooling crystallisation in the m-KRAIC for 4HAPO was not particularly

effective. The set-up in itself showed high versatility within a compact plant space, allowed control over the cooling profile, synthetic flow rate, crystallisation net flow and demonstrated direct coupling between flow platforms, but the cooling crystallisation did not initiate nucleation in a controlled manner. The apparent wide MZW of 4-HAPO in the m-KRAIC along with high solid loading (when nucleation did occur) within the tubular environment led to major blockages in the system. The system could be potentially optimised further by introduction of an antisolvent or seeding step for example, to drive controlled nucleation but this does add another layer of complexity to the process.

For instance, in seed addition, the delivery system would need to be carefully controlled to ensure that the same quantity of seeds were delivered to each slug to ensure controlled crystal growth. In the case of the antisolvent, increasing water content has been shown to decrease the solubility of 4HAPO and 4HAP ethanol:water mixtures. The effect of adding water on the solubility would be most pronounced in 50 v/v% ethanol or higher compositions. While this could be readily taken advantage of in a single, continuous crystallisation process, coupling with flow synthesis meant that HOA and NaAc were also present in the effluent. The coupled process needs to ensure that these reactants do not crash out of solution, which becomes more likely as the EtOH composition increases. This highlights the major difficulty of integration in this work, whereby the overall process needs to balance the requirements of both the synthetic reaction and crystallisation step without compromising the other.

HAPO8

While a high solid loading can be prone to blockages in the KRAIC and m-KRAIC. Alternative approaches may be more suitable. For example, CSTRs in series tend to be capable of handling high solid loadings. As a proof of concept, the reaction was repeated as described in HAPO4, where J3 was disconnected from the m-KRAIC and the effluent transferred to a round bottom flask. The reaction was run for a total of nine RTs to show that the system could be operated over a prolonged period. Collection was carried out during start-up, steady state and shutdown periods which were determined by UV-Vis measurements as described in the experimental Section 3.4.3 and the results are shown in Figure 3-36.

Based on Figure 3-36, the reaction reaches steady state by the second RT; this was used to infer when steady state was reached in HAPO8. During the HAPO8 run, no initial crystallisation occurred during the start-up procedure, but crystal growth did occur upon cooling to ambient temperatures. Once the system had reached steady state,

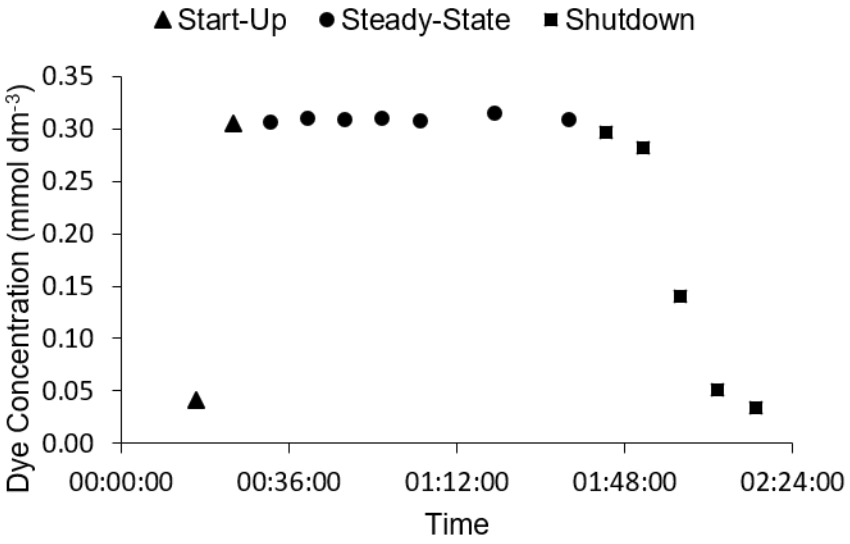

Figure 3-36: Change in concentration of the dye Eosin Y in the flow reactor during steady state measurements

collection was switched to a separate flask where immediate crystallisation occurred without the need for temperature control. Some encrustation formed over time at the tubing outlet, but this did not impede the flow over the three hour operation period. The collection was then switched to another flask during shutdown. The crystalline product was isolated after stirring under ambient conditions for three to four hours. The solid recovery is summarised in Table 3.26.

Table 3.26: Calculated solid recovery in HAPO8

Period	Time (h:min:sec)	Number of RTs	Yield (%)	Productivity ($g\,h^{-1}$)
Start-up	00:16:00	1	46.0	7.05
Steady State	01:52:00	7	62.3	9.54
Shutdown	00:32:00	2	42.4	6.49
Overall	02:40:00	10	57.7	8.68

The average solid recovery is slightly lower than HAPO4, but a higher solid recovery is achieved at steady state. HAPO4 has an overall higher yield as the system had more time to crystallise. The differnce in overall recovery suggests the recovery could be improved by using a temperature controlled holding vessel. The productivity of the synthetic reaction was found to be $8.68\,g\,h^{-1}$, but this excludes the time taken

for the crystallisation period. Even so, this would potentially be an improvement over the batch process since once the system reaches steady state, crystallisation readily occurs. Ideally, the collection vial could be replaced with a CSTR system. In this case, a temperature control profile could be applied to a series of vessels to induce nucleation and control crystal growth. However, the scale and number of vessels would be important as the net flow rate of the CSTRs would be dependent on the flow rate of the synthesis, unlike the m-KRAIC set-up in which air/carrier fluid can be used to adjust the crystalliser net flow without impacting the upstream synthesis. A pseudo-continuous CSTR system may be the most beneficial in this case. Although other issues could arise such as the build-up of impurities or encrustation in the CSTR vessels.

In terms of solid analysis, the NMR, PXRD and DSC of all three samples were reminiscent of previous runs and matched well the expected physical properties of 4HAPO (Figures in Appendix 9-13, 9-14 and 9-15 respectively). Hot stage microscopy (HSM) was also carried at 5 °C min^{-1} from 32 to 175 °C. The results are shown in Figure 3-37.

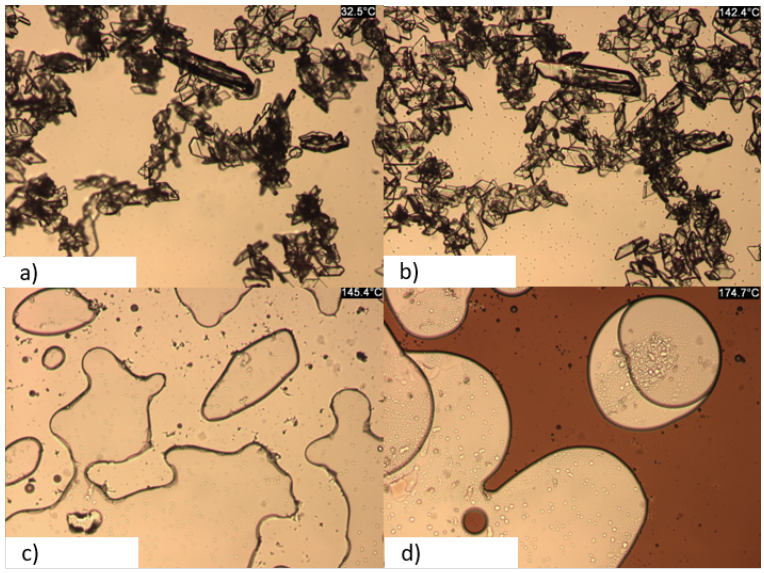

Figure 3-37: HSM images of HAPO8 at a) 32 °C b) 142 °C c) 145 °C and d) 175 °C

As can be seen, no changes are observed in the product until the melting point at 142 to 145 °C. This is followed by a darkening of the solution as 4HAPO decomposes up to 175 °C. The trend matches what has been observed in the DSC traces up to this point.

3.5 Chapter Conclusions

In this research, attempts were made to transfer the synthesis of paracetamol (PCM) from 4-hydroxyacetophenone (4HAP) into a integrated continuous synthesis and crystallisation process. In pursuit of this, a one-pot synthetic method was replicated in batch and investigated for transfer into a flow environment. Direct transfer was problematic as issues were encountered by the inability of traditional small-scale tubular reactors and pumps to handle solid suspensions of the reactant hydroxylamine hydrochloride (HOA). Attempts to fully dissolve the starting reagents in a mixture of ACN and water showed minimal success, as the addition of water generally stopped the reaction at the intermediate 4-hydroxyacetophenone oxime (4HAPO) or slowed the reaction progress significantly. To overcome this, a different approach was used involving packing excess HOA in an adjustable column. The attractiveness of this process was the high selectivity to the desired product, fast reaction time and the mild reaction conditions. However, issues occurred with precipitation and clogging. The best results were obtained using low flow rates, where PCM was produced as the major product within a 10 minute residence time (RT). However, the hydroxylamine hydrochloride reactant proved problematic, often leaching into the reaction stream and causing blockages. While further development might optimise the process to combat this, integration with downstream crystallisation technology appeared difficult without in-line work-up of the product, which would add complexities to the process procedure that ideally, could be avoided.

Instead, the reaction was separated into distinct steps; oximation of 4HAP to 4HAPO and a subsequent Beckmann rearrangement of 4HAPO to PCM. Oximation of 4HAP was successfully implemented in a tubular flow reactor using acetic acid and aqueous hydroxylamine. However, the reaction required neutralisation and liquid-liquid separation to extract the product, which interrupted the continuous framework. This flow reaction was later replaced with a simpler process using hydroxylamine hydrochloride and sodium acetate (NaAc) which had previously been demonstrated in batch. While both methods produced high conversion and selectivity to the 4-hydroxyacetophenone oxime intermediate, the second approach showed potential for integration, as the product could be crystallised directly from the reactor output.

In striving to achieve production of PCM from 4HAP, this work has also demonstrated that the Beckmann rearrangement of 4HAPO isolated from the oximation flow process could be redissolved in ACN and combined with the homogeneous organocatalyst trifluoroacetic acid (TFA) in flow to produce PCM with high selectivity. While the product

required offline work-up for isolation, the reaction showed a higher productivity and purity than the batch process due to the improved heat transfer and avoidance of thermal decomposition. In effect, a possible route to PCM from 4HAP has been developed which translates the important chemical steps into a continuous environment. This could be potentially integrated to form a telescoped continuous method with sufficient development of *in situ* separation and extraction technologies.

In order to demonstrate an integrated flwo chemistry and crystallisation continuous process, the synthesis and crystallisation of 4HAPO was taken forward as an alternative candidate. Here, a batch method for the production of 4HAPO was successfully transferred to a flow synthesis platform. Furthermore, a crystallisation profile was designed from the solubility of 4HAPO in ethanol/water mixtures. From this data, a continuous crystallisation process was investigated in a compact KRAIC design. The m-KRAIC used less reactor space than the KRAIC but displayed a similar reactor volume; allowing easier integration between the crystallisation and synthetic procedures. The m-KRAIC allows for safe operation and crystallisation using potentially hazardous materials or solvents. A cooling crystallisation profile was tested in 4HAPO production with partial success. In particular, 4HAPO showed a large MZW which resulted in little *in situ* crystallisation during the cooling crystallisation, but nucleation readily occurred during filtration. While beyond the scope of this work, an alternative route would be to introduce seeds to the system. If the seeding dosage in each slug could be regulated within the cooling profile, this could lead to the desired controlled nucleation.

While a purely cooling crystallisation process could not be demonstrated for 4HAPO in the m-KRAIC, a semi-batch model did indicate that coupling the flow process with a series of CSTRs could be demonstrated as successful integration of flow synthesis and crystallisation for 4HAPO. The direct crystallisation of high purity 4HAPO from the flow synthetic oximation of 4HAP opens the door to continuous crystallisation. A CSTR system would allow design of a cooling profile that could initiate nucleation and increase solid recovery. CSTRs are generally better at handling the high solid loading encountered during crystallisation of 4HAPO and could be particularly effective for integration between the flow synthesis step and continuous crystallisation process in this case. While the m-KRAIC may not be effective for crystallisation of 4HAPO under the current conditions, it has potential applications as a compact, segmented flow crystalliser that can be used in conjunction with other flow technologies to deliver small scale integrated processes on a lab scale. It could therefore be considered for wider applications in pursuing other pharmaceutical products or chemical commodities that would benefit from continuous crystallisation and continuous manufacturing.

Chapter 4

Pyrazinamide

4.1 Introduction

The work presented in this chapter has been published as a communication in *Reaction Chemistry and Engineering* under the heading:

'Integrated plug flow synthesis and crystallisation of pyrazinamide' C. Daniel Scott, Ricardo Labes, Martin Depardieu, Claudio Battilocchio, Matthew G. Davidson, Steven V. Ley, Chick C. Wilson and Karen Robertson, *React. Chem. Eng.* 3, 631-634, 2018.

Flow chemistry and continuous crystallisation techniques offer high levels of control over the resultant products and opens opportunities for leaner and more sustainable manufacturing. However, integration of the the two techniques is relatively novel. Most examples of integrated continuous manufacturing use continuous stirred tank reactors (CSTRs) to achieve the desired crystallisation.[27] Examples of integrated tubular crystallisation processes are uncommon.

The work in this chapter outlines the development of an integrated, telescoped synthesis and crystallisation process to deliver the pharmaceutical drug pyrazinamide (PZA). The approach involved the direct coupling of the flow synthesis method developed by the Steven Ley group (University of Cambridge) with the kinetically regulated automated input crystalliser (KRAIC) platform at the University of Bath.[131] The work formed a collaborative project between researchers at the University of Bath and the University of Cambridge. Support for the project on the synthetic reaction procedure was provided by Dr. Ricardo Labes (Cambridge) and crystallisation experiments were carried out with the help of Dr. Karen Robertson (Bath). Mastersizer particle size analysis was carried out with the help of Dr. Martin Depardieu (Bath). In this chapter, the development of the process along with analysis of the resultant product is described.

4.2 Background and Aims

Previous work carried out by Battilocchio *et al.* had shown that an effective method for the synthetic production of pyrazinamide could be achieved through hydration of pyrazinecarbonitrile (PyCN).[188] Pyrazinamide is an attractive target material as the relatively simple molecule is a common pharmaceutical drug used in the treatment of tuberculosis and is recognised as an essential medicine by the World Health Organisation (WHO).[189] The reaction proceeds quantitatively in the presence of a manganese (IV) dioxide (MnO_2) catalyst when heated to 80 °C. While MnO_2 is a cheap, reliable catalyst for hydration of nitriles, it can be difficult to use in batch.[190,191] The heterogeneous catalyst tends to adhere to surfaces and can become clumped together, reducing reaction efficiency and making the resulting product difficult to work-up and separate from the catalyst. However in a flow environment, the catalyst can be packed into a column. Here, the reactants can be pumped through the column to perform the reaction. This inherently separates the catalyst from the products as the effluent leaves the reactor column and therefore avoids a complex work-up and separation process (Figure 4-1).

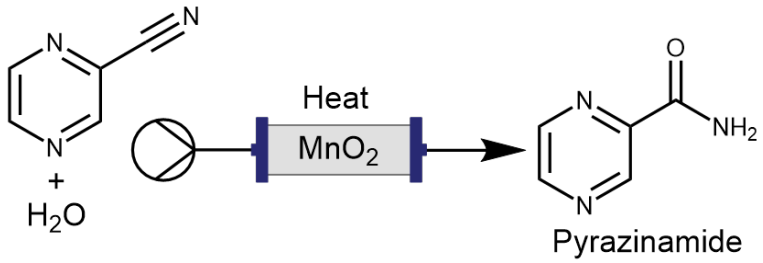

Figure 4-1: Hydration of PyCN under catalytic conditions

This reaction is attractive for the development of a flow synthetic method due to its mild reaction conditions and high atom efficiency, leading selectively to the desired product with few impurities. In order to determine if the synthesis of PZA would be applicable for integrated flow synthesis and crystallisation, preliminary work was undertaken to reproduce the results achieved by Battilocchio *et al.* Reproduction of the flow synthetic method would allow for evaluation of the crystallisation process and suitability of PZA flow synthesis for coupling with continuous crystallisation.

4.3 Investigation into the Flow Synthesis of Pyrazinamide

4.3.1 Experimental

Flow synthesis experiments were carried out using the Vapourtec modular flow reactor equipped with a R2$^+$ pump module and R4 flow heater system. For a full description of the Vapourtec unit see Section 2.5. An adjustable omnitfit column (100 mm, 6.6 mm inner diameter (ID)) of variable volume (0.1 to 2.4 mL) was attached to the heater unit and packed with between 0.7 g and 1 g of MnO_2 powder, mixed with 0.2 g of celite to prevent the build-up of back pressure. Each end of the column was capped with a small amount of celite to help prevent MnO_2 powder from exiting the column. A 12 bar back pressure regulator (BPR) was connected to the outlet of the omnifit column. Fluorinated ethylene propylene (FEP) tubing (1.0 mm ID) was used to connect the feed solution to the pump, the pump to the inlet of the reactor column and the outlet of the column to the BPR. Wider bore FEP tubing (1.50 mm ID) was used to connect the outlet of the BPR to the collection vessel. The column was heated to 80 °C under 12 bar pressure (Figure 4-2).

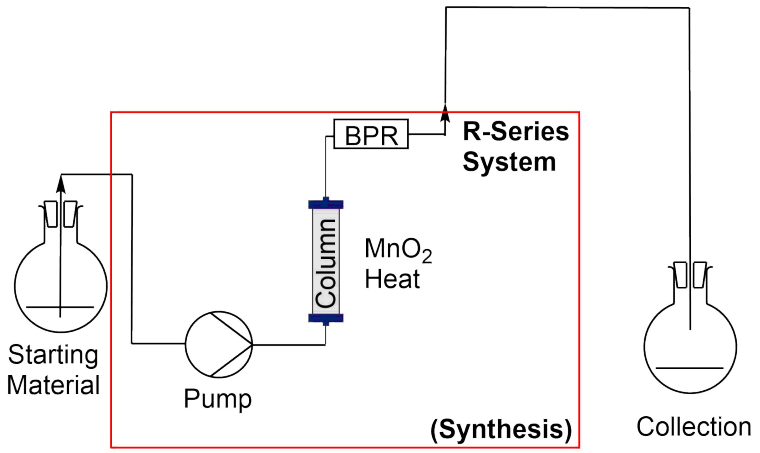

Figure 4-2: Schematic diagram of the uncoupled flow synthesis process

A feed solution of PyCN was prepared to a concentration of 0.28 mol dm^{-3} in water. The reactor column was equilibrated and primed with H_2O at 1 mL min^{-1} for 10 minutes before being switched to the feed solution. A 20 mL aliquot was collected for each PZA1 experiment, over a total collection period of sixty minutes. After collection, the resultant solution was evaporated on a rotary evaporator, leaving a white, crystalline solid. The solid was extracted using diethyl ether and allowed to dry before determining the synthetic yield. Collection was performed in triplicate and the average yield was calculated from the individual solid recoveries.

For comparison, nuclear magnetic resonance (NMR) spectroscopy measurements were taken of the starting material and the product on a Bruker Avance 300 MHz spectrometer and the resultant spectra were compared to known chemical shift values of PyCN and PZA from literature. Evaluation of the solid form was carried out using differential scanning calorimetry (DSC) and powder X-ray diffraction (PXRD) and comparisons were made with literature values.

4.3.2 Results and Discussion

PZA1

Using the experimental set-up in Figure 4-2, the production of PZA from PyCN in flow was successfully replicated in PZA1. The approximate residence time from inlet to outlet of the reactor was experimentally derived as 4 minutes. In Table 4.1 the isolated yields for the hydration of PZA are summarised.

Table 4.1: Flow synthesis of Pyrazinamide

Experiment	Flow Rate ($mL\,min^{-1}$)	Residence Time (min)	Run Time (min)	Isolated Yield (%)
PZA1.1	1.00	2	20	81.5
PZA1.2	1.00	2	20	63.1
PZA1.3	1.00	2	20	64.7
Average	1.00	2	60	69.8 ± 10.2

In the synthesis-only run (PZA1), PZA was found to be isolated in an average yield of 69.8 % over the total collection period of 60 minutes. While the values for the isolated yield were lower than anticipated, for the purposes of coupling the synthetic reaction with the continuous crystallisation these values were deemed sufficient. This was because PZA remained in solution at reaction temperature (80 °C), but was observed to begin to crystallise at room temperature. This was important, as a prerequisite to translation into the flow crystalliser under consideration for integration, was that the feedstock needed to be supersaturated at ambient temperatures. The spontaneous growth observed of crystals in the collection flask was a good indicator that this is the case and that cooling crystallisation may be a suitable approach for initiating precipitation.

Proton NMR analysis was carried out on the product of PZA1, to identify PZA and determine if any unreacted PyCN was present. The chemical shifts detected are outlined in Table 4.2, along with values taken from literature. There is only a small change

in the NMR spectra between the two compounds PyCN and PZA. However, the clear growth of two additional peaks at 7.89 ppm and 8.29 ppm indicates the formation of the amide. There is also a slight down-field shift of the aromatic protons compared to PyCN. The combination of these two factors confirms the conversion of PyCN to PZA. The peak shift values taken from PZA1 are close to those quoted in literature, although some residual solvent (H_2O) is still present when looking at the raw spectrum (Appendix Figure 9-17). Analysis of the NMR data would therefore suggest that the discrepancy in yield is due to difference in extraction and work-up, rather than reactivity.

Table 4.2: Proton NMR chemicals shift of isolated product in PZA1

Experiment	Chemical Shift (ppm)
PZA1.1	(300 MHz, DMSO-d6) 3.35 (H_2O), 7.88 (1 H, br. s), 8.28 (1 H, br. s), 8.72 (1 H, dd, J = 2.5, 1.5 Hz), 8.86 (1 H, d, J = 2.5 Hz), 9.18 (1 H, d, J = 1.5 Hz)
PZA1.2	(300 MHz, DMSO-d6) 3.35 (H_2O), 7.88 (1 H, br. s), 8.28 (1 H, br. s), 8.71 (1 H, dd, J = 2.5, 1.5 Hz), 8.85 (1 H, d, J = 2.3 Hz), 9.18 (1 H, d, J = 1.5 Hz)
PZA1.3	(300 MHz, DMSO-d6) 3.36 (H_2O), 7.89 (1 H, br. s), 8.29 (1 H, br. s), 8.72 (1 H, dd, J = 2.5, 1.5 Hz), 8.85 (1 H, d, J = 2.5 Hz), 9.18 (1 H, d, J = 1.5 Hz)
Starting Material, PyCN	(300 MHz, DMSO-d6) 8.83 (dd, 1H), 8.94 (d, 1H), 9.21 - 9.13 (1H, m)
Pyrazinamide[192]	(400 MHz, d6-DMSO) 7.84 (1 H, br. s), 8.24 (1 H, br. s), 8.70 (1 H, dd, J = 2.5 Hz, J 1.5 Hz), 8.85 (1 H, d, J = 2.5 Hz), 9.17 (1 H, d, J = 1.5 Hz)
Pyrazinecarbonitrile[193]	(300 MHz, d6-DMSO) 8.85 (1 H, dd, J = 2.5 Hz, J = 1.5 Hz), 8.95 (1 H, d, J = 2.5 Hz), 9.20 (1 H, d, J = 1.5 Hz)

The PXRD data for PZA1 was compared to the three most accessible polymorphs of pyrazinamide. The patterns were generated from the available single crystal X-ray diffraction (SCXRD) structures (Figure 4-3).[194–196] The powder patterns for PZA1 clearly indicate that the crystalline product corresponds closely to the α polymorph. Work by Cherukuvada *et al.* suggests that this is the most thermodynamically stable polymorph of PZA at room temperature.[197] However, PZA has enantiotropically related polymorphs, with the δ form being the most stable below 25 °C, α the most stable between 25 and 155 °C and the γ being the most stable from 155 to 191 °C. This highlights the need for careful crystallisation control to ensure polymorphic purity as

the crystallisation process may drive the formation of a kinetic polymorph product, or mixture of polymorphs.

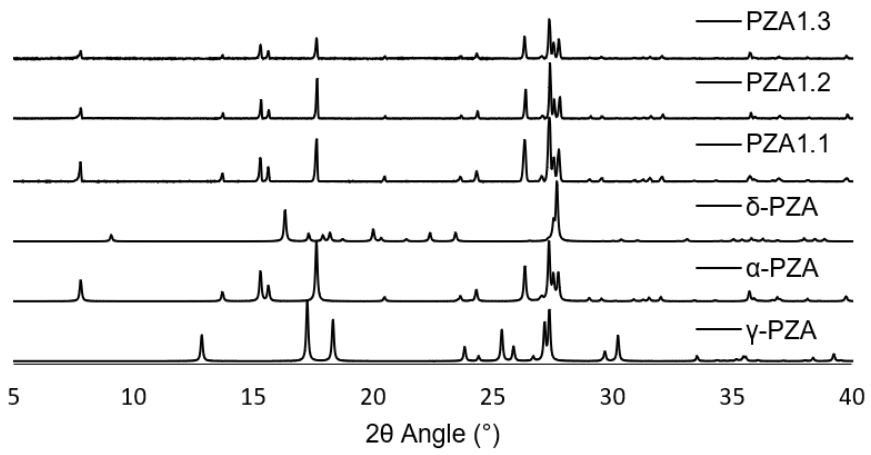

Figure 4-3: PXRD analysis for PZA1. Comparison with the simulated pattern for three PZA polymorphic forms

To confirm the results in the NMR and PXRD analysis; DSC was carried out on PZA1.1, the results are summarised in Figure 4-4. From the DSC trace, a clear melting point at 190.3 °C can be seen. This fits with the expected value between 190 and 194 °C.[197] Furthermore, a phase transition is visible above the baseline in PZA1.1, with a peak maximum at 151.6 °C. This is close to the expected phase transition from polymorph α to γ (140 to 155 °C) typically seen when heating a sample of α-PZA.

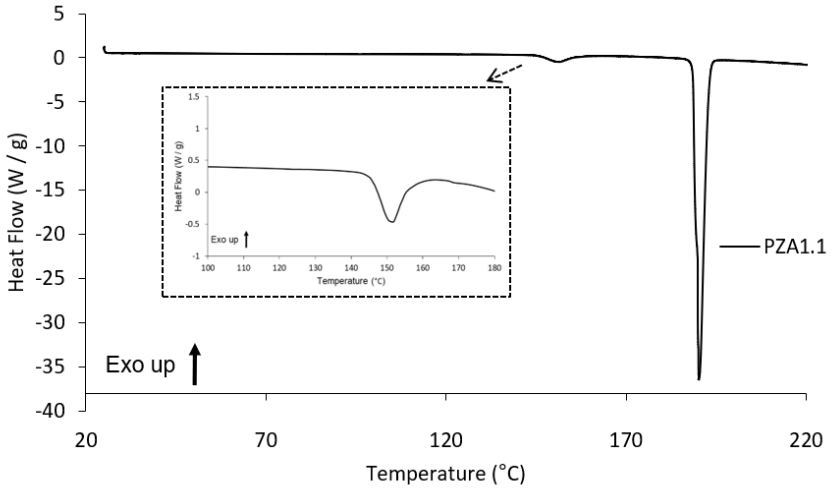

Figure 4-4: DSC of the Flow Synthesis of PZA1.1

Given the decreased yield, the reaction was retested using the same synthetic method but with a more efficiently packed column, where celite was mixed with MnO_2. The renewed column was run under the same conditions. The results for the yield are shown in Table 4.3.

Table 4.3: Second attempt at the flow synthesis of PyCN

Experiment	Flow Rate ($mL\,min^{-1}$)	RT (min)	Run Time (min)	Isolated Yield (%)
PZA1.4	1	2	20	88.4
PZA1.5	1	2	20	94.1
PZA1.6	1	2	20	92.7
Average	1	2	60	91.7 ± 3.0

As can be seen, the yield is 20 % higher than the first attempt, which was on average around 69.8 %. Since the reaction was run under the same conditions, the discrepancy was put down to poor packing of the column in the first attempt as well as greater care taken during work up and isolation of the product in PZA1.4 to PZA1.6.

In summary, the hydration of PyCN to pyrazinamide was replicated in a flow environment successfully. The desired product was produced in a high yield under the similar conditions to those outlined by Battilocchio *et al.* Analysis by NMR of the product showed no residual starting material (notable loss of the peak at 8.94 ppm). The polymorphic form isolated matched the α-PZA form, which was identified as the expected form under the aqueous cooling crystallisation conditions. Crystallisation occurred during collection, but in order to determine the most accurate solid recovery, work-up on a rotary evaporator was used to remove the solvent.

The system thus provides a good framework for an integrated continuous crystallisation approach. There are a number of factors that support this. The reaction set-up was straightforward and easy to control, making it simple to replicate. This ensures that during optimisation of the downstream process, performance of the upstream synthesis is reliable and non-variable. The reaction is well understood, atom efficient and performed in water. The synthetic process was found to be highly selective to the desired product, with no side products detected in NMR spectroscopy. Furthermore, water acts as a green solvent, making it attractive from a sustainability perspective. The resulting high selectivity ensures that the system becomes supersaturated as it cools to ambient temperatures. Under these conditions, it was deemed possible to directly couple the flow synthetic reaction to the continuous crystallisation platform without

the need for in-line work-up.

4.4 Coupling Synthesis and Crystallisation

4.4.1 Experimental

For a fuller explanation of the Vapourtec R-series equipment and KRAIC crystallisation platform, please see Sections 2.5 and 2.7.1 respectively.

Uncontrolled Nucleation

Flow synthesis was carried out as described in Section 4.3.1. A feed solution of PyCN was prepared to a concentration between 0.1 and 0.25 $\mathrm{mol\,dm^{-3}}$. The reactor column was equilibrated and primed with H_2O at $1\,\mathrm{mL\,min^{-1}}$. The column was heated to 80 °C under 10 - 12 bar pressure. In coupling experiments, the output from the flow synthesis of PZA was fed directly into a glass cross piece (1.25 mm ID) to undergo segmentation before crystallisation in the KRAIC. Carrier fluid (Galden SV110) and air were pumped using a pair of Ismatec (Reglo-Z series) gear pumps at set flow rates (Appendix Table 9.1) through 1 mm ID perfluoroalkoxy alkane (PFA) tubing. The effluent from the flow synthesis reactor was transported to the segmentation point using a temperature-controlled jacketed tubing (J1) which was kept at 75 °C to avoid early onset of crystallisation. The cross piece was kept submerged under a water bath which was actively heated to 70 °C.

In initial experiments, termed 'uncontrolled nucleation runs' the output from the segmentation bath was transferred into a 15 metre length (3.2 mm ID) FEP tubing via a 3.2 mm ID piece of marprene tubing. The segmented slugs were allowed to cool without assistance to ambient conditions (Figure 4-5). The temperature profile for uncontrolled nucleation runs is shown in the Appendix Figure 9-16. Once the feed cooled to ambient conditions, the resting temperature remained steady between 18 and 20 °C, depending on the external atmosphere. A neutral solvent (water) was used to help propel any crystals out of the end-piece of the KRAIC. The neutral solvent was used to provide additional velocity to the flow after carrier fluid recovery in the end-piece. The neutral solvent is defined as a solvent that will not cause dissolution or crystallisation of the product. The neutral solvent was turned on intermittently when needed to clear any solid build-up. The neutral solvent in later runs was chilled with an ice bath to reduce the observed dissolution of the product.

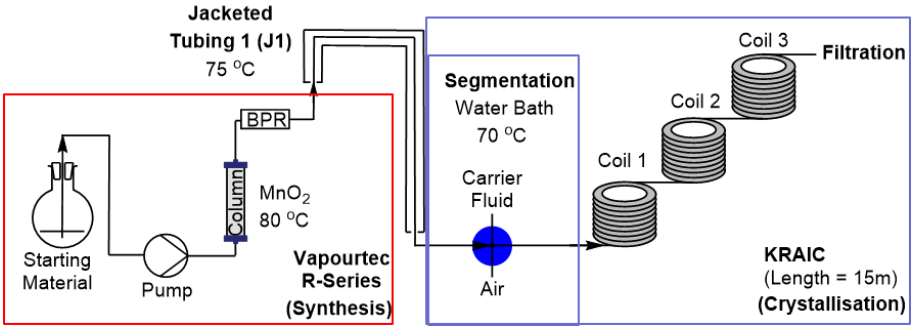

Figure 4-5: Schematic diagram of the direct coupling of the flow synthesis and crystallisation platforms in uncontrolled nucleation runs

Controlled Nucleation

The experimental parameters in later experiments (referred to as 'controlled nucleation runs') were the same as those described in the uncontrolled nucleation runs with the exception of the introduction of a controlled cooling step. The set-up is outlined in Figure 4-6. The active cooling step consisted of an additional 1.2 m section of 3.2 mm ID FEP tubing jacketed with silicone tubing (jacketed tubing 2, J2) which was actively cooled using a circulatory bath. J2 was installed between the segmentation bath and the 15 m main body of the KRAIC. A zero volume FEP union was used to connect J2 to the main crystalliser.

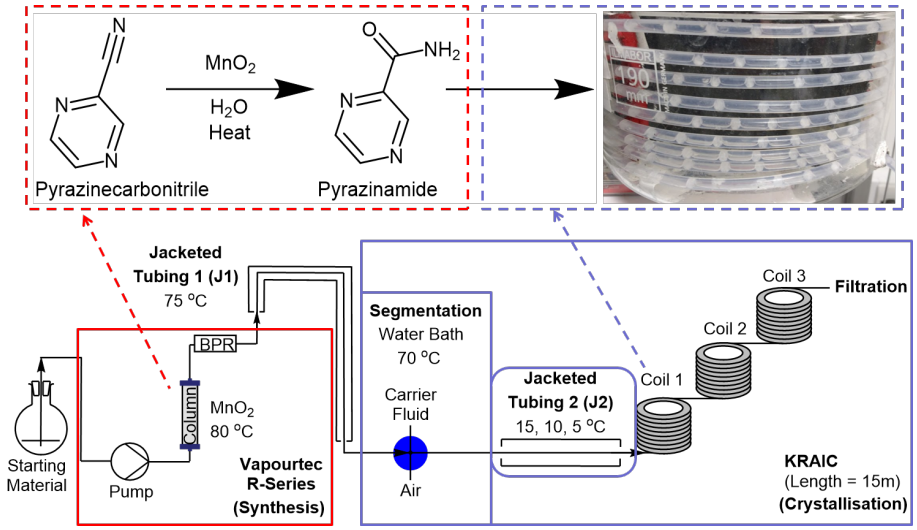

Figure 4-6: Schematic of the controlled nucleation run for coupling of the flow synthesis and crystallisation platforms for pyrazinamide

4.4.2 Platform Development

The initial experiment parameters are given in Table 4.4. These experiments aimed to scope what parameters were important in producing an effective crystallisation for PZA in a continuous manner.

Table 4.4: Experimental parameters for initial PZA investigations into coupled flow synthesis and crystallisation

Experiment	Concentration ($mol\,dm^{-3}$)	Synthesis Flow Rate ($mL\,min^{-1}$)	Crystallisation Flow Rate[a] ($mL\,min^{-1}$)	Crystallisation RT[b] (min:sec)
PZA2	0.1	1.00	2.9	41:45
PZA3	0.25	1.00	2.9	41:45
PZA4	0.25	1.00	7.4	16:16

a: Total of synthesis, air and carrier fluid flow rates. Calculated from the RT, as volume of the KRAIC is known to be 120.64 cm^3

b: Residence time experimentally derived after segmentation

PZA2

The hydration reaction of PyCN to PZA was monitored off-line by taking a sample after exiting the KRAIC. NMR analysis indicated that the synthetic reaction was proceeding well. Table 4.5 shows the NMR results for uncontrolled nucleation. In the case of PZA2, the sample was taken from the solution leaving the KRAIC. While the sample showed a high water content, the identifiable peaks in the aromatic region indicated no remaining starting material and confirmed the presence of PZA in solution.

Table 4.5: Proton NMR chemicals shift of pyrazinamide samples in uncontrolled nucleation runs

Experiment	Chemical Shift (ppm)
PZA2	(300 MHz, DMSO-d6) 7.78 (s, 1 H), 8.36 (s, 1 H), 8.67 (s, 1H), 8.78 (s, 1 H), 9.11 (s, 1 H)
PZA1.1	(300 MHz, DMSO-d6) 3.55 (H_2O), 7.88 (s, 1 H), 8.29 (s, 1 H), 8.72 (dd, J 2.5, 1.5 Hz, 1 H), 8.86 (d, J 2.5 Hz, 1 H), 9.18 (d, J 1.5 Hz, 1 H)

NMR spectra of PZA2 in Appendix Figure 9-18

However, during PZA2 no crystallisation occurred within the KRAIC even after taking steps to decrease the temperature of coil 1 using an ice bath. Work-up of the effluent leaving the KRAIC using rotary evaporation did leave a white powder, which was subsequently analysed by NMR and PXRD. The NMR peak shifts were in agreement

with those reported in PZA1 and powder pattern was indicative of the expected α-PZA polymorphic form (Figure 4-8).

PZA3

In PZA3, the concentration of the precursor PyCN was increased to $0.25\,\mathrm{mol\,dm^{-3}}$. Crystallisation in the KRAIC was visible in coil 1, within the first 20 minutes after switching feed. Coil 1 is approximately 5 metres in length, so crystallisation was occurring early in the residence time. Here, crystallisation began before a complete RT had passed through the system. As the transfer tubing from the pumps has a laminar flow regime, the concentration of PZA in solution is unlikely to have reached steady state at this point. The crystallisation was noted to be sporadic, with crystals appearing only intermittently within slugs. Furthermore, the crystals that did form began to cause blocking issues which affected the flow rates of the feed. Hence, an accurate solid recovery could not be determined. The system had to be stopped and cleared 25 minutes into the run, 5 minutes after crystals had been observed to be growing *in situ*. However, PZA3 achieved the first instance of crystallisation in coupling experiments. This confirmed that a concentration of $0.25\,\mathrm{mol\,dm^{-3}}$ was sufficient to provide adequate supersaturation levels of PZA that would result in crystallisation at ambient temperatures within the KRAIC. However, the low solid suspension and subsequent blockage issues were problematic, the nature of the blockages suggested that the PZA crystals were growing in a less than ideal morphology, which was leading to poor suspension in the segmented flow and consequently quickly formed blockages.

PZA4

In PZA4 the flow rate of the crystallisation process was increased in order to provide better mixing in the system and reduce the chances of a blockage forming. This was achieved by raising the flow rate of the carrier fluid and air components, while the RT of the synthetic process remained unchanged. In PZA4 crystallisation in the coils occurred visibly after 17 minutes, occurring in the latter half of coil 2 of the KRAIC. However a blockage began to form in coil 3, 29 minutes into the run. The blockage was removed by applying hot air via a heat gun to the area to partially redissolve the crystals. The run was continued, but required further interventions to remove small blockages. The crystals were collected after exiting the KRAIC, but an accurate solid recovery could not be taken as the blockage affected the flow rates.

In order to better understand why the PZA crystals were causing issues, analysis of the particle sizes under an optical microscope was carried out. Images were taken

that showed the PZA crystals had a tendency to form long elongated needle structures (Figure 4-7). Based on crystal size relative to the particle sizing grid, some crystals were growing regularly up to 1 mm in length. Some of the crystal growth reached close to the size of the tubing (3.2 mm ID). Table 4.6 shows the particle size distribution from optical microscopy measurements. The crystals show a large size distribution, indicating a non-uniform dispersion. The particle size distribution (PSD) indicates that the majority of crystals have a width between 118 and 150 µm and a length between 702 and 1032 µm. Therefore the crystals are forming in the KRAIC with an average length close to 1 mm and a width around 0.1 mm. However, the maximum length measured was 2.5 mm. Its likely that these elongated crystals are what led to blockages despite the low solid loadings in each slug. Once the crystals had grown to a size sufficient to begin touching the walls of the tubing, this perhaps provided an easier pathway for nucleation via the reactor wall, leading to a sudden growth in crystals and subsequent solid build-up.

Figure 4-7: Optical image of PZA4 crystals with scale bar (DIV = 0.1 mm)

Table 4.6: Particle size analysis of PZA4

	Length (µm)	Width (µm)	Particle Distribution (µm)
Average	867	134	501
Standard deviation	585	58	554
95% confidence limits	702 - 1032	118 - 150	390 - 611
Full range	160 - 2590	55 - 375	55 - 2590

PXRD analysis of PZA4 (Figure 4-8) resulted in noisy powder pattern, but seemed to indicate the preferential growth of the γ-PZA polymorph over the thermodynamically

favourable α-PZA form. This was in contrast from those isolated from PZA2 and literature, which showed the α form in the absence of crystallisation in the KRAIC. PZA2 crystals were isolated by rotary evaporation using the same method used during the development of the flow synthesis. In contrast, the results from PZA4 would indicate that continuous crystallisation in the KRAIC platform was influencing polymorphic behaviour.

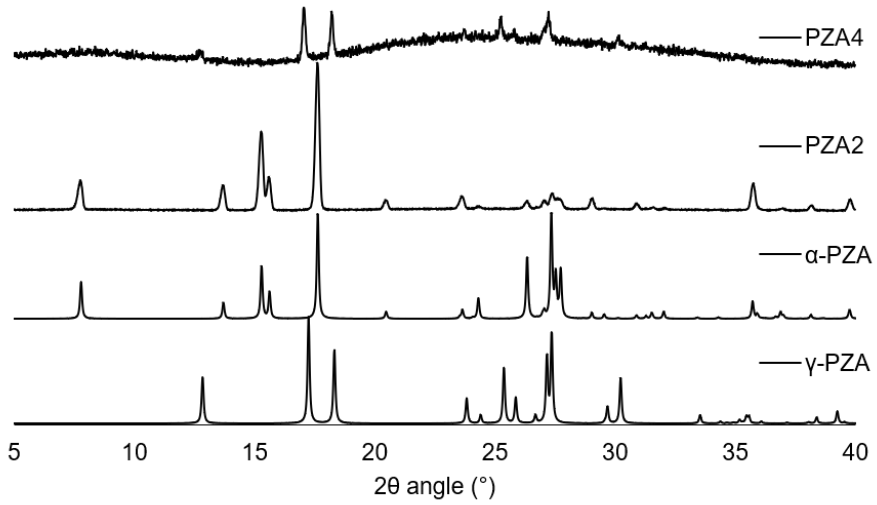

Figure 4-8: Powder diffraction pattern of PZA2, PZA4 and simulated patterns for α and γ polymorphic forms of PZA. Note that PZA4 is enhanced to allow easier comparison.

From these results, it was clear that greater control over the crystallisation process would be necessary to ensure successful integration of the two continuous manufacturing platforms. In particular, the large crystal size and shape was leading to blockage issues even at low yields. In order to eliminate these issues and allow a greater solid recovery, a secondary, cooling step was introduced to the process to influence the particle size and morphology. In this way, a coupling of flow synthesis and continuous crystallisation could be achieved without downstream processing issues.

4.4.3 Controlled Nucleation

The experimental parameters for the controlled nucleation runs are outlined in Table 4.7 and the set-up is described in Section 4.4.1.

Table 4.7: Parameters for controlled nucleation PZA investigations

Experiment	[PyCN] (mol dm^{-3})	Synthesis Flow Rate (mL min^{-1})	Crystallisation Flow Rate[a] (mL min^{-1})	Crystallisation Residence Time[b] (min:sec)	Run Time (hour:min)	J2 Set Temperature (°C)
PZA5	0.2	1.0	4.0	30:00[c]	1:20	15, 10, 5
PZA6	0.25	1.00	4.6	27:38	1:38	15, 10, 5
PZA7	0.28	1.00	4.4	27:28	1:48	10
PZA8	0.28	1.00	3.9	30:47	1:50	5
PZA9	0.28	1.00	3.7	34:24	0:54	Off
PZA10	0.28	1.00	4.6	28:10	1:37	10
PZA11	0.28	1.00	5.5	23:24	0:46	Off

a: Combined velocity of air, carried fluid and feed flow rate. Calculated from the RT, as volume of the KRAIC is known to be 120.64 cm^3

b: Residence time experimentally derived after segmentation

c: Pulsations in flow meant RT for PZA5 could only be approximated

PZA5

PZA5 was the initial screening experiment with the new controlled nucleation set-up. As such, the concentration was lowered to 0.2 mol dm^{-3} as it was thought that this may avoid further blockage issues at the reduced temperatures. It was also identified that the air and carrier fluid pumps were not working at capacity during the uncontrolled nucleation runs. As such, they were cleaned and repaired. Unfortunately this had the effect of changing the actual pump flow rates of the carrier fluid and air, despite being set to the same rate as previous experiments. In addition, pulsation and sudden drops in pressure (likely due to oscillations caused by pumping through a packed column) meant that it was not possible to determine an accurate RT for PZA5. Crystallisation of PZA did not occur within the KRAIC, even after the temperature of J2 was reduced from 15 to 5 °C. It was determined that the concentration of PZA was too low in solution. This was adjusted in later experiments to raise the supersaturation. The filtrate from PZA5 was collected and excess solvent removed using a rotary evaporator, which resulted in a white product. NMR analysis confirmed that the product was PZA (Table 4.8).

Table 4.8: Proton NMR chemicals shift of PZA5

Experiment	Chemical Shift (ppm)
PZA5	(300 MHz, DMSO-d6) 7.89 (1 H, br. s), 8.29 (1 H, br. s), 8.71 (1 H, dd, J 2.5, 1.5 Hz), 8.85 (1 H, d, J 2.5 Hz), 9.18 (1 H, d, J 1.5 Hz)

NMR spectra of PZA5 in Appendix Figure 9-19

PXRD analysis (Figure 4-9) shows that PZA5 is a mixture of the α and γ form of PZA. This indicates that there is some competition between the two forms during the crystallisation process. It is interesting that a physical mixture of two polymorphs is formed after subjecting the effluent from the KRAIC to rotary evaporation, rather than the pure α form seen in PZA1 and PZA2. This indicates that it is an aspect of the KRAIC crystallisation process that is changing the preference for the solid form. While no visible crystallisation could be seen during the run, it is possible some microcrystals formed either inside the KRAIC or at the end-piece.

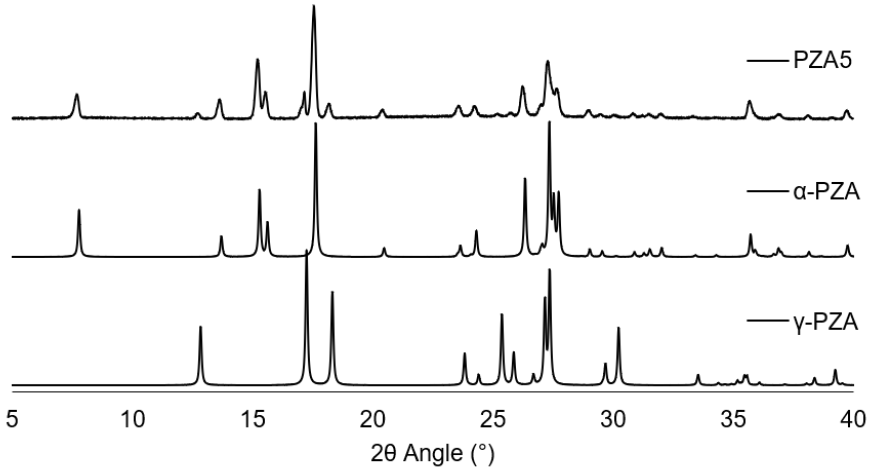

Figure 4-9: Powder X-ray diffraction pattern from the extracted solid in PZA5

PZA6

In the second screening experiment, PZA6, the concentration was raised to 0.25 mol dm^{-3}, as used in PZA3 and PZA4. The MnO_2 catalyst column was replaced and repacked to reduce the pulsations exhibited in the crystalliser. An accurate RT for the crystallisation was measured at 27 minutes 38 seconds. PZA6 showed no crystallisation with J2 set at 15 °C over one full RT. The circulator was then reduced to 10 °C. Crystallisation within the KRAIC occurred in coil 1, rung 3 at around 30 minutes after switching feeds and 50 seconds after the circulator had reached 10 °C (Figure 4-10).

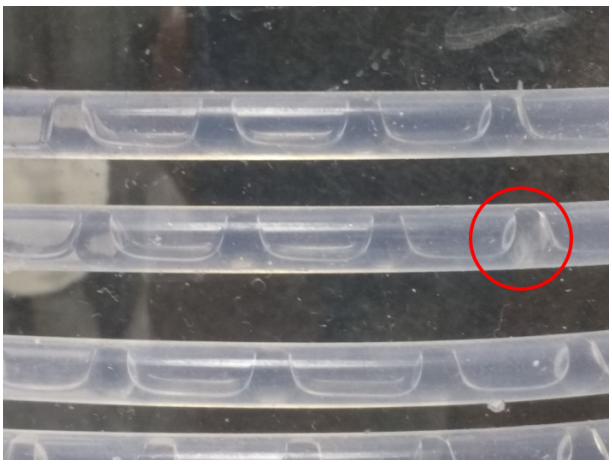

Figure 4-10: First instance of controlled crystallisation in flow synthesis and segmented flow crystallisation of pyrazinamide

As the system began to equilibrate to the new temperature profile, crystals were noted to appear as they were leaving J2. The slight increase in concentration with respect to PZA5 resulted in the first instance of *in situ* crystallisation after successful flow synthesis with no blockages encountered throughout the operational period. However, the yield was only 0.8 % after collecting for 40 minutes. The reduced yield was determined to be a side effect of the neutral solvent delivery, which appeared to be redissolving the product. In most KRAIC based crystallisation processes the neutral solvent is essential for ensuring no encrustation around the crystalliser outlet. However, as this was proving a detriment to the solid recovery, in future runs neutral solvent was only switched on briefly whenever solid mass began to build-up around the end-piece.

During PZA6, the average slug size was monitored during the crystallisation. The results are summarised in the Appendix Table 9.2. The average slug has volume of 0.08 ± 0.01 mL. The values show a good consistency and indicate that the segmentation is regular. Therefore, each slug should be crystallising under similar conditions, however while monitoring 60 slugs only 30 showed observable crystal growth at the outlet. This indicates the system may not have fully equilibrated. It is likely that changing the temperature of the cooling step led to some deviation in the process. In fact, crystal growth became more regular towards the end of the counting period. Furthermore, this method only takes into account the presence of observable crystals by eye; the introduction of a monitoring technique such as Raman spectroscopy would provide a more accurate hit rate for crystallisation in each slug. Unfortunately not enough product was isolated to carry out any reliable analysis of the polymorphic form using PXRD or DSC methods but the product was confirmed to be PZA via NMR spectroscopy (Table 4.9).

Table 4.9: Proton NMR chemicals shift of PZA6

Experiment	Chemical Shift (ppm)
PZA6	(300 MHz, DMSO-d6) 7.88 (1 H, br. s), 8.28 (1 H, br. s), 8.67 - 8.79 (1 H, m), 8.86 (1 H, d, J 2.5 Hz), 9.18 (1 H, d, J 1.5 Hz)

NMR spectra of PZA6 in Appendix Figure 9-20

PZA7

In PZA7, PyCN concentration was increased to 0.28 mol dm^{-3}. The column from PZA6 was reused without replacement. The residence time after segmentation was very close to the previous experiment at 27 minutes 28 seconds. J2 was set to 10 °C and the system was allowed to pump pure solvent for 45 minutes to ensure the temperature of J2 had reached full equilibrium. Crystallisation occurred in the 2nd rung of coil 1

of the KRAIC, 8 minutes after switching the feed line. This extended back towards J2 over time, stabilising within the first RT, with observable crystals forming halfway round the 1.2 m coil (Figure 4-11). This was consistent for the remainder of the run. Every slug showed crystallisation upon exiting the jacketed tube. The solid recovery over the collection period was 28.5 %, leading to a productivity of $0.6\,\mathrm{g\,h^{-1}}$. During the hour long collection period, no blockages occurred within the crystalliser. The samples were extracted with vacuum-assisted filtration and allowed to dry before analysis.

Figure 4-11: Initial nucleation within the cooled J2 tubing jacket during controlled nucleation run, PZA7. Crystal growth becomes visible to the naked eye within the upper rung of the cooling jacket.

The increase in concentration of PyCN was enough to significantly increase the supersaturation ratio at 10 °C, to the extent that spontaneous nucleation and visible crystal growth could be seen within the first 2 minutes of a residence time (RT). Furthermore, the high concentration improved the consistency of crystal growth in the slugs as well as leading to a much improved yield compared to PZA6. Despite the significant increase in solid loading, no blockages were encountered during the duration of the experiment.

Optical images of the crystals were taken under a microscope (Figure 4-12). The crystals are clearly significantly smaller than those isolated from PZA4. This indicates that the addition of a cooling step influences the size and shape of the crystals. The rapid heat loss provides a drive towards nucleation. This provides numerous points for crystals to grow and hence reduces the likelihood that crystals will grow to sizes exceeding the diameter of the tubing. This has significant advantages in processability compared to the uncontrolled nucleation runs. Furthermore, the rapid heat loss is facilitated by the high surface-to-volume ratio in a tubular crystalliser, which could not be as easily applied in a batch crystallisation process, clearly highlighting an advantage of tubular flow crystallisation over conventional batch crystallisation.

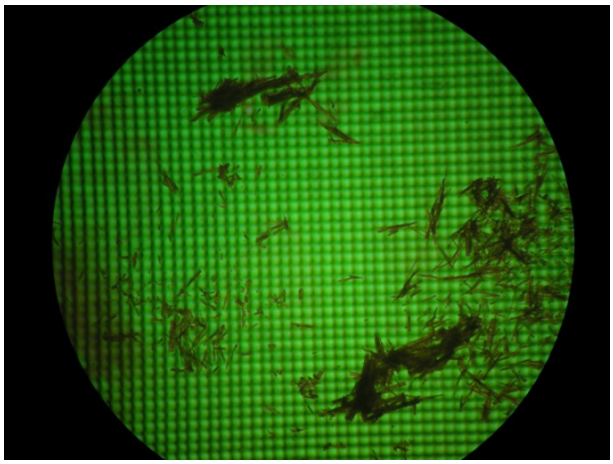

Figure 4-12: Optical image of PZA7 crystals with scale bar (DIV = 0.1 mm)

The particles were too small to accurately measure size under an optical microscope so a sample was taken for study using scanning electron microscopy (SEM). SEM images were taken of the crystals formed during PZA7 and the images at various magnifications can be seen in Figure 4-13. Particle size analysis was carried out on the SEM images and results are summarised in Table 4.10. The average particle size was 83 µm. A comparison of the elongated crystal axis of PZA4 and PZA7 shows a similar reduction in average size from 867 to 145 µm, respectively. The SEM images of the crystals from PZA7 show a rectangular shape, with one elongated axis.

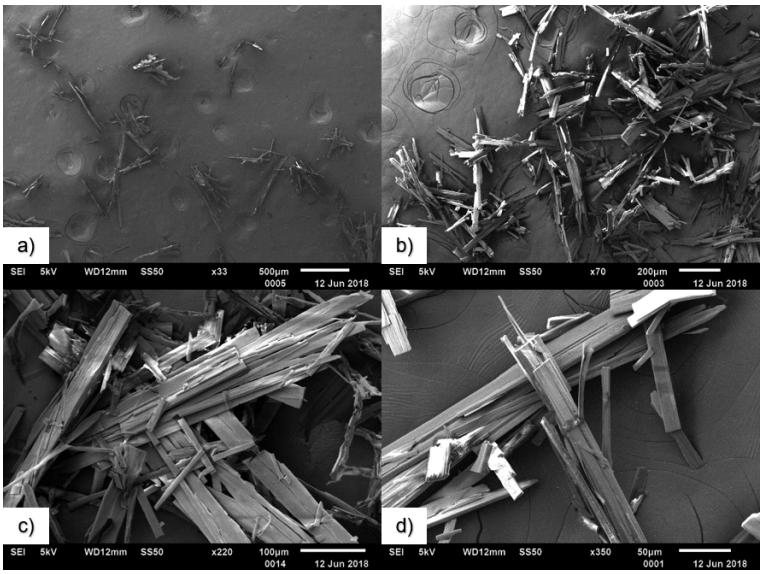

Figure 4-13: SEM images of PZA7 at magnifications of a) x33 b) x70 c) x220 d) x350

Table 4.10: Particle size analysis of PZA7 from SEM

	Length (µm)	Width (µm)	Particle Distribution (µm)
Average	145	21	83
Standard deviation	102	10	95
95% confidence limits	117 - 173	18 - 24	64 - 101
Full range	4 - 484	7 - 63	4 - 484

A sample of PZA7 was analysed by laser diffraction using the method outlined in Section 2.15. The Malvern Mastersizer 3000 software version 3.36 fits the diffraction data to an irregular sphere. The results from the particle size analysis data are depicted in Figure 4-14. As the particles have a rectangular shaped morphology, the data will reflect a combination of all orientations of the needle crystals with respect to the laser beam.

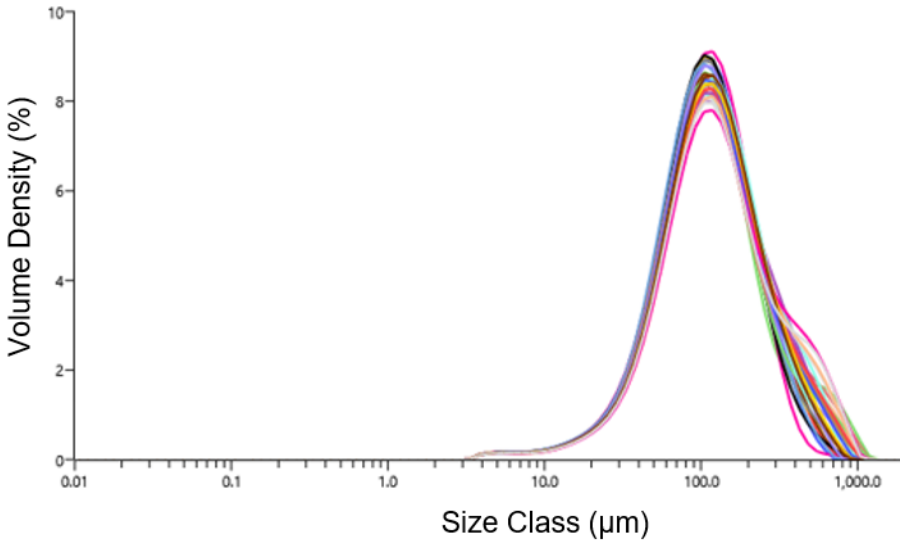

Figure 4-14: Particle size distribution of PZA7 from laser diffraction measurements

On closer inspection of Figure 4-14, there is a clear peak maximum centred around 100 µm. This is maintained over several recorded scans. The size range of the crystals was relatively large, ranging from 3 to 300 µm. This large range may be the result of the non-spherical nature of the crystals. Using the particle size analysis from the SEM images to interpret the data, it is likely that the lower range of the size class corresponds to the crystal width (3 to 60 µm). The long axis in Table 4.10 has a range of 4 to 480 µm, hence sizes above 60 µm may correspond to the crystal length. Above 300 µm and the

size class begins to vary on repeated scans in Figure 4-14. This might correspond to aggregates forming and breaking between PZA crystals in suspension during laser diffraction analysis. These aggregates generally ranged up to 1 mm in size. Comparison of these results with the particle size analysis from the SEM images indicates that the results are a good approximation. The average particle size from Table 4.10 was close to 100 µm with a range of sizes within the observed laser diffraction analysis distribution depicted in Figure 4-14.

Based on the results in PZA7, the introduction of a rapid cooling step increases the temperature gradient significantly as expected; Figure 4-15 shows a comparison of the temperature profiles of PZA7 and PZA4. As can be seen, the rapid temperature loss and resulting lower temperature will contribute to increasing the supersaturation. These factors contribute towards the onset of nucleation and crystal growth. Hence, the cooling step raises the supersaturation level in the KRAIC to above the metastable zone width (MZW) and into the labile zone, this resulted in spontaneous nucleation of many crystal nuclei rapidly.

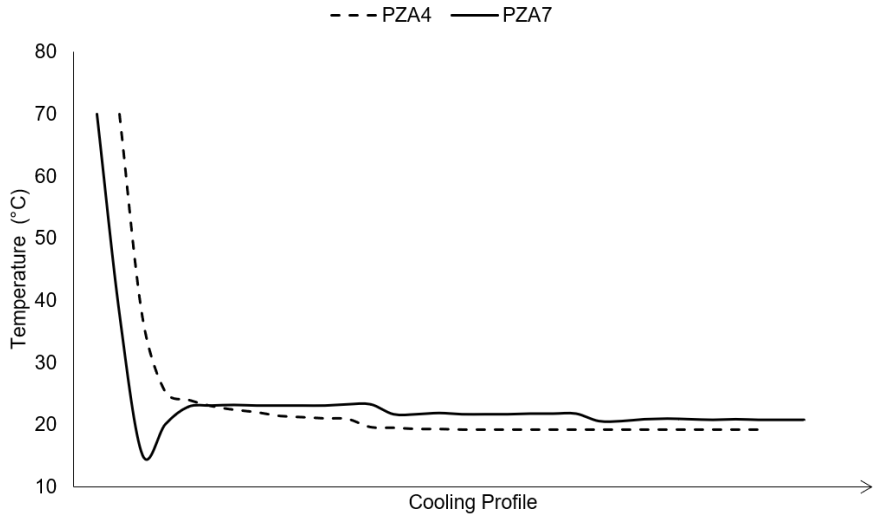

Figure 4-15: Cooling profile for the KRAIC in PZA4 and PZA7

As this provides several points for secondary nucleation, the crystals tend to grow smaller. Generally, excessive nucleation promotes encrustation issues, however the KRAIC benefits from a preferential wetting of the carrier fluid on the tubing. As a result, the solution slugs never encounter the walls of the tubing and this prevents encrustation. However, poor crystal suspension or elongated crystals can approach the tubing diameter and this can lead to blockages. In PZA7, the reduced crystal size

improves the processability of PZA compared to PZA4 as the smaller crystals no longer exceed the diameter of the tubing and remain suspended in the solution slugs. Hence, the result is that blockage issues were removed while solid recovery was simultaneously improved.

PXRD was carried out on a sample of PZA7 after filtration. The diffraction pattern is shown in Figure 4-16. It is apparent that the preferred polymorphic form is γ-PZA, in contrast to the batch crystallisation process which promoted the α polymorph.

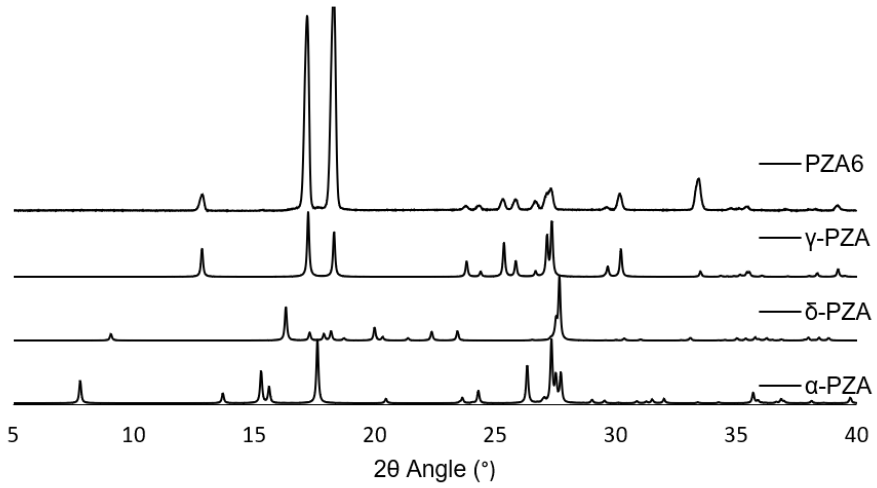

Figure 4-16: Powder diffraction pattern of PZA7 compared to simulated patterns of the accessible polymorphic forms of pyrazinamide

The result is in line with the polymorphic forms identified in previous experiments PZA4 and PZA5 both of which showed a mixture of α and the metastable γ polymorph when isolated from the KRAIC. In PZA7 however, the form identified is exclusively the γ form. Of particular interest, the γ polymorph of PZA is not usually accessible from an aqueous cooling crystallisation process. In two separate pieces of work carried out by Castro *et al.* and Hermanto *et al.*, both authors report the preferential crystallisation of the α polymorph from water.[189,198] In particular, Hermanto noted that during cooling crystallisation experiments, the α polymorph was the only accessible polymorph, regardless of cooling rates. The results obtained along with the literature cited indicate that the influence on polymorphic behaviour on PZA is likely due to the KRAIC crystalliser. However, it is important to note that the cooling rates experienced in the controlled nucleation runs here are significantly faster than the scope of the work presented by Hermanto. In runs that showed blockages (e.g. PZA5) a mixture of α and γ was detected, this perhaps indicates that nucleation on vessel walls leads to α-PZA

expression, while the absence of the crystalliser walls and no blockages (PZA7) leads to growth of γ-PZA. This observation is in line with previous work in the KRAIC that has seen a similar polymorphic change with succinic acid when moving from a batch to a segmented flow crystalliser and removing solid-liquid interfaces.[131] Confirmation of this relationship would require *in situ* polymorphic form analysis, which is outside the scope of this thesis but marks a clear need for the development of technologies and methodologies that could enable a better understanding of this phenomenon.

The change in polymorph is also reflected in the DSC trace, which shows a distinct lack of thermal transitions before the melting point (Figure 4-17). This is in contrast to Figure 4-4 from PZA1, which clearly shows an endothermic transition corresponding to a switch from α to γ-PZA around 145 °C. The melting point peak minimum for the PZA7 product corresponds to a value of 189.6 °C which is in agreement with the melting point of PZA from PZA1 (190 °C).

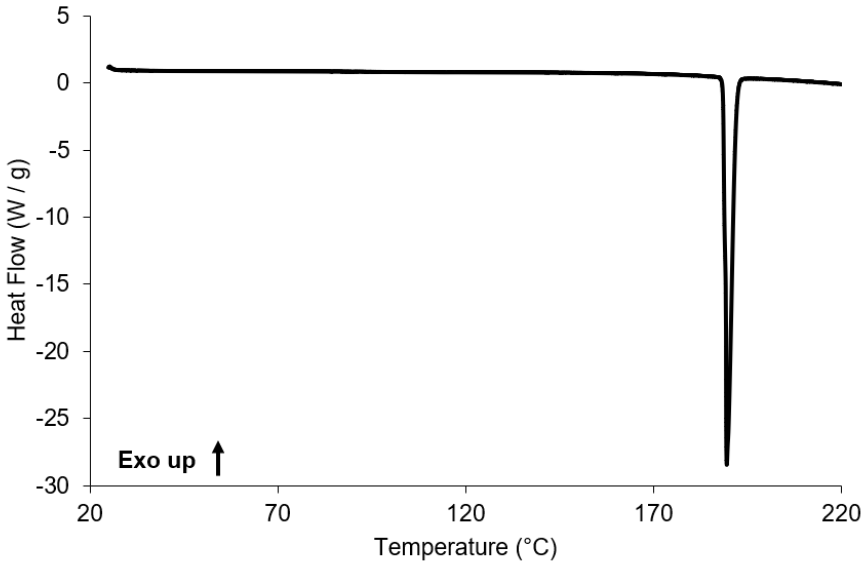

Figure 4-17: DSC trace of PZA7, showing a melting point at 189.55 °C.

PZA8

The results from PZA7 indicated that a successful coupling of flow synthesis and continuous crystallisation was possible. However the solid recovery was still relatively low compared to the batch crystallisation process which was 70 to 90 % on average. In order to improve the solid recovery, PZA8 reduced the temperature of the cooling step in order to increase supersaturation and hence increase overall crystallisation. The cooling step was lowered from 10 to 5 °C and the resulting temperature profile is shown

in Figure 4-18. The readings were taken using an external probe and indicate that the temperature of J2 is close to the expected 5 °C. After this, the solution gradually increases to ambient temperatures, stabilising at 21.7 °C.

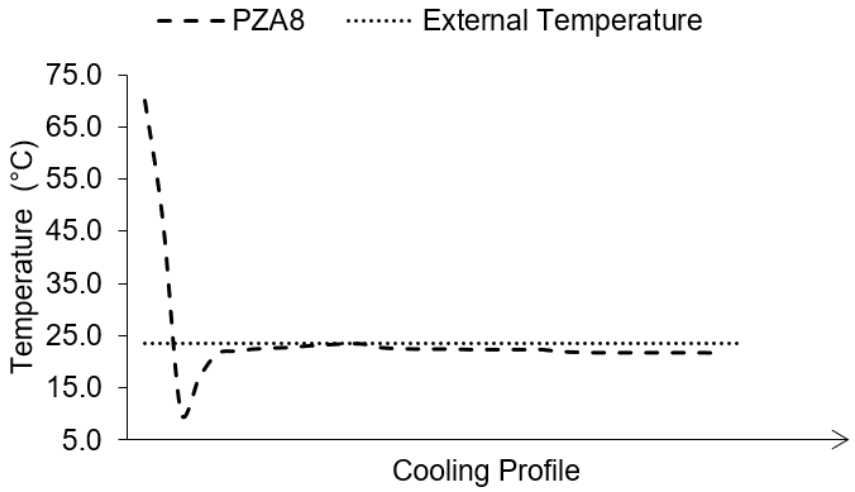

Figure 4-18: Cooling profile of the KRAIC in PZA8

During the run, it was noted that the onset for crystallisation after switching the feed to the PyCN solution was earlier than in PZA7. In PZA8, considerable crystal growth was visible within the first 60 cm of J2, whereas in PZA7 the onset of crystallisation occurred after the first 60 cm of J2. Crystallisation was noted to occur visibly in J2 within the first 7 minutes, similar to PZA7 (8 minutes) but solid loading was observably higher within the slug. This is not unexpected as the cooling profile for PZA8 is steeper, with a lower resting temperature. The residence time is also noted to be slightly longer (Table 4.7), but this could be down to a fluctuation in pump performance or accuracy in measuring the residence time. Unfortunately, the increased solid density in each slug eventually led to a major blockage issue and the run needed to be stopped. The blockage occurred 45 minutes into operation and was centred around the join between the 15 m FEP tubing and J2 (Figure 4-19).

The join has the advantage of that it could be disconnected, cleared and reattached without switching off the pumps. This allowed the run to continue for a further 30 minutes unimpeded and enabled collection of some product. However, the join was also responsible for the blockage, acting as a solid surface for nucleation and encrustation. Furthermore, the seam, while as flush as possible, may still act as a catching point for dense crystals that are not suspended well in the slug. In the case of PZA8, the extra solid loading before the join resulted in crystals getting caught at irregular intervals.

Figure 4-19: Union between Jacket 2 (J2) and the 15 m FEP tubing in the KRAIC

This was not an issue in PZA7, which would suggest that the crystals were better suspended or solid loading was lower in each slug when passing this point compared to PZA8. Potentially this could be resolved by increasing the flow rate, but this would have affected the residence time. Another solution and a possible improvement to the design used in these experiments would be to directly jacket the first metre of the 15 metre FEP tubing. This would avoid the need for a join between J2 and the FEP tubing and eliminate the unwanted surface interaction.

Some solid was recovered before the run blocked in PZA8 and was tested using PXRD and DSC analysis (see Appendix 9-21 and 9-22 for corresponding graphs). The PXRD pattern showed the formation of the γ form in-line, which was also the observed form detected in PZA7. DSC analysis shows a clear melting point of 190 °C with no thermal transitions indicating no polymorphic changes before melting. The lack of α-PZA may be due to the fact that the crystals collected were isolated before the blockage occurred and hence the polymorphic form maintained the γ phase.

Results from PZA8 would indicate the cooling step was too fast under the current parameters, leading to blockages around the union between J2 and the FEP tubing. Potentially this could be overcome by modifying the design to eliminate the union. In this case, the PZA crystals only appeared to cause blocking issues around the join, which would indicate that a greater solid recovery could be achieved by removing this point.

PZA9

In PZA9, the J2 was switched off and was filled with only air. In this case, crystallisation was allowed to proceed without active cooling, as in the uncontrolled nucleation runs,

but with an additional 1.2 m tubing extension. The experiment aimed to determine if the rapid cooling effect was causing the change in the polymorphic behaviour or whether this could be attributed to the KRAIC design. The cooling profile can be seen in Figure 4-20. In contrast to PZA8, the lowest temperature reading is found to occur at the outlet of the KRAIC, with a reading of 20.8 °C compared to 10 °C in the rapid cooling run. Unfortunately, over the course of the hour long run, no crystallisation occurred in-line. This would suggest that the conditions were not sufficient to cause spontaneous crystallisation.

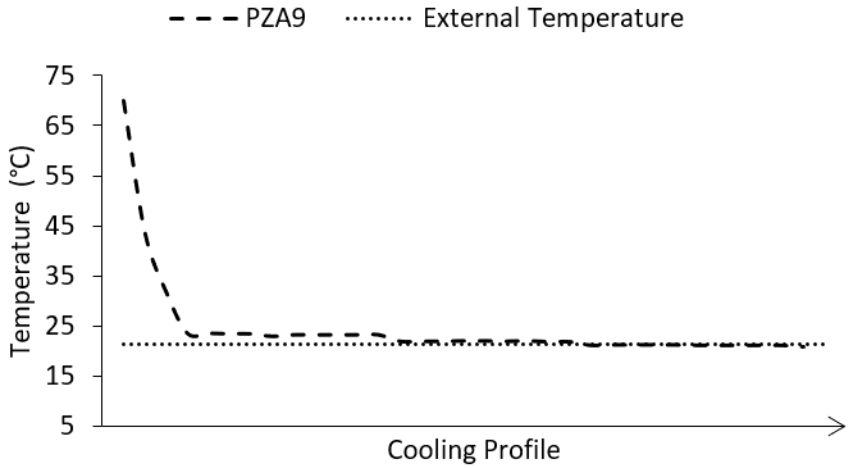

Figure 4-20: Temperature readings and cooling profile of PZA9

PZA10

In PZA10 the coupling experiment was carried out using the same conditions as PZA7. During the 40 minute priming period, the residence times for synthesis and crystallisation were monitored. These are summarised in Table 4.11.

Table 4.11: Residence times and process volumes for PZA10

Location	Residence Time (min)	Volume (mL)
Packed Column	1:56	1.9
Jacket 1 (J1)	2:11	1.8
Jacket 2 (J2)	1:52	9.2
KRAIC	26:18	120.6
Total	32:17	133.5

From this, it is clear that the total time spent in the column was relatively short, only 2 minutes. The crystallisation process is much slower than the synthetic reaction, with a total time of 28 minutes. In direct coupling of flow synthesis and continuous crystallisation this can cause difficulty due to the disparity in reactor volumes and process times. However, in a segmented flow regime, the addition of an air and carrier fluid allows control over the net flow of each set-up without detrimentally affecting the downstream processing.

Crystallisation occurred in J2, around the half-way point at 6 minutes 30 seconds, which is a similar to the induction time to PZA7 (7 minutes). Collection of product was carried out for 1 hour, with no blockage issues. Crystallisation occurred in every slug once steady state had been reached with the cloud point observed in J2 (Figure 4-21). Solid recovery was significantly improved, giving a yield of 57 % compared to 28.5 % in PZA7, representing a productivity of $1\,g\,h^{-1}$. The large improvement was likely due to a more robust process built on the observations of the previous attempts, along with the installation of a renewed MnO_2 catalyst column. Proton NMR of the product indicated the isolated crystalline product matched the signals typical of PZA (Appendix Figure 9-23).

Figure 4-21: Crystallisation of pyrazinamide in all slugs in coil 1 of the KRAIC in PZA10

SEM was used to image a sample of crystals isolated from PZA10. The crystals have a similar morphology to those produced during PZA7, showing one long axis resulting in

rectangular plate-like shaped crystals (Figure 4-22). Particle size analysis was carried out on the SEM images and the results are summarised in Table 4.12.

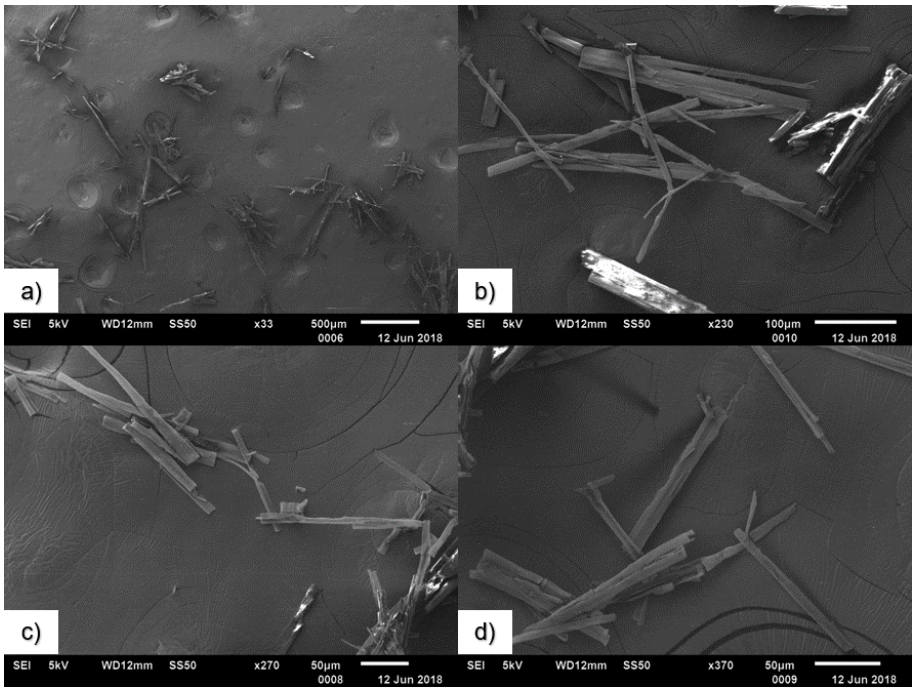

Figure 4-22: SEM images of PZA10 crystals at magnifications of a) x30, b) x230, c) x270 d) x370

Table 4.12: Particle size analysis of PZA10

	Length (µm)	Width (µm)	Particle Size (µm)
Average	171	17	94
Standard deviation	115	8	112
95% confidence limits	135 - 207	15 - 20	69 - 119
Range	36 - 618	5 - 35	5 - 618

Particle size analysis of the SEM images (Table 4.12) indicates that PZA10 has an average particle size of 94 µm which is similar to the crystals isolated from PZA7 (83 µm). The 95% confidence limits for the average length and width are within the expected distribution from the laser diffraction experiments carried out on PZA7. Here, a slightly wider range of lengths were detected but it is difficult to determine exactly why this is the case. One possibility is the neutral solvent. In PZA7, the neutral solvent was an aqueous solution at room temperature, but, it was noted halfway through the run that the neutral solvent was causing dissolution of the product. In this repeat

(PZA10), the neutral feed was kept off throughout the run as encrustation around the end-piece was not an issue. Therefore the change in crystal size may be a consequence of the improved solid recovery resulting from the reduction of product dissolution.

The polymorphic form was investigated using PXRD and DSC analysis and the results are summarised in Figure 4-23 and Figure 4-24 respectively. As was the case for PZA7, the γ polymorph is selectively isolated from the integrated process. The SEM images depict rectangular, plate-like crystals as previously observed in PZA7. DSC analysis lacks the thermal transitions associated with a phase change before the melting point, confirming γ-PZA to be present throughout, while the large endothermic peak at 190 °C matches the expected melting point. The sample of PZA10 was stored under ambient conditions after extraction and the stability of the γ-form was monitored using PXRD. The results are shown in Figure 4-23. As can be seen from the data collected, the metastable form was still present after a 2 year period, indicating that the sample, if left undisturbed, remains stable over an extended period.

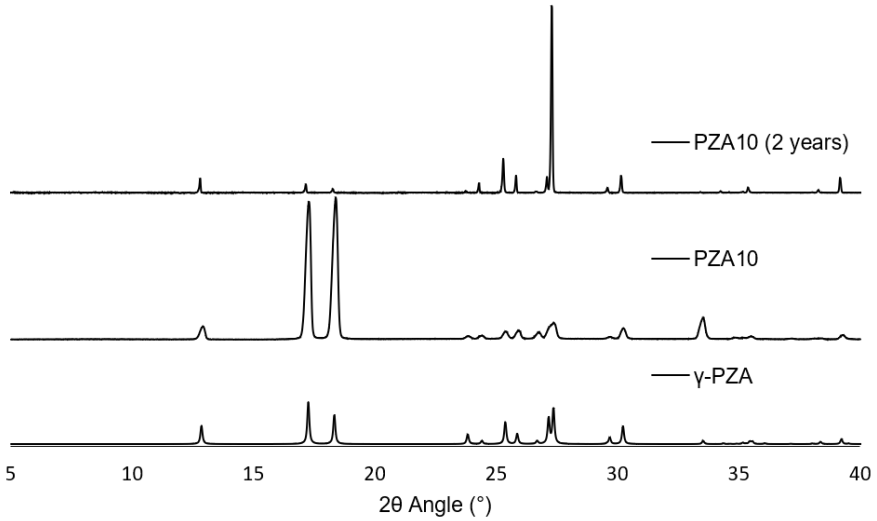

Figure 4-23: PXRD pattern comparison of PZA10 after 2 years under ambient storage conditions

PZA10 confirms that that the integrated production and crystallisation of the γ-form of pyrazinamde is effective and can be repeated with similar results. Furthermore, the greater solid recovery suggests that the process could be significantly improved with more optimisation. In particular, solid recovery values were calculated from depletion of the feedstock, assuming 100% conversion of the starting material to PZA. If the system was allowed to reach steady state before beginning collection, then solid recovery

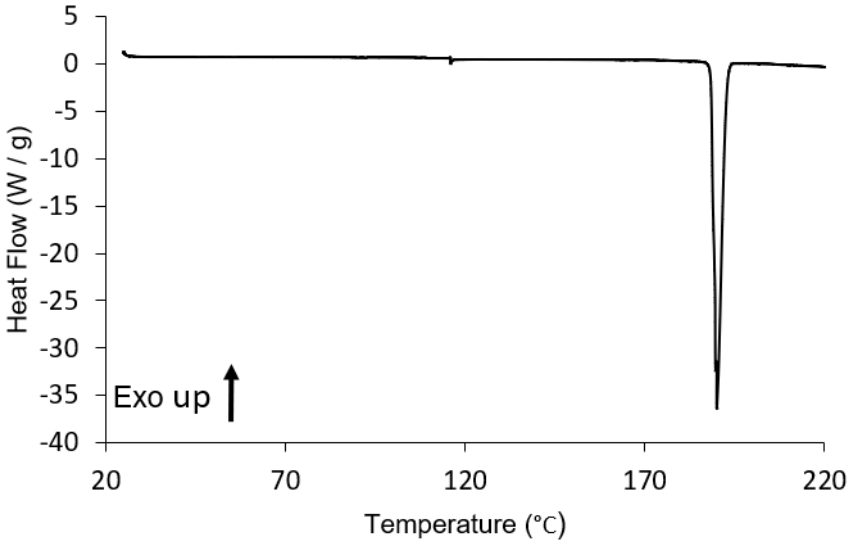

Figure 4-24: DSC trace of PZA10, showing melting peak at 190.02 °C

would likely improve over this period. Ideally, the system should be run for several more residence times, with separate collection periods allowing for an averaged solid recovery to be determined.

PZA11

A final attempt was made to isolate pyrazinamide crystals without the addition of controlled temperature stage in J2. The experiment was run at an increased concentration of PyCN ($0.32\,\mathrm{mol\,dm^{-3}}$) to encourage spontaneous crystallisation without the controlled cooling step. This would allow for insights into the cooling effect on polymorphism. Unlike in PZA10, crystallisation occurred around the exit of J2 after 8 minutes. Unfortunately, the crystals caused a blockage 25 minutes into the run (within the first RT). An external heat gun was applied to clear the blockage and the air flow rate was increased to extract the crystals before another blockage could develop. Solid recovery over this period was 12.2%. A sample was analysed using PXRD, results are summarised in Figure 4-25. In this case, PZA11 consists of a mix of the α and γ forms. Comparison of the DSC traces for PZA11 and PZA1 (α-PZA) indicate that a small peak is present above the baseline in PZA11 (Figure 4-26) which matches the expected α to γ transition. This correlates with the PXRD data.

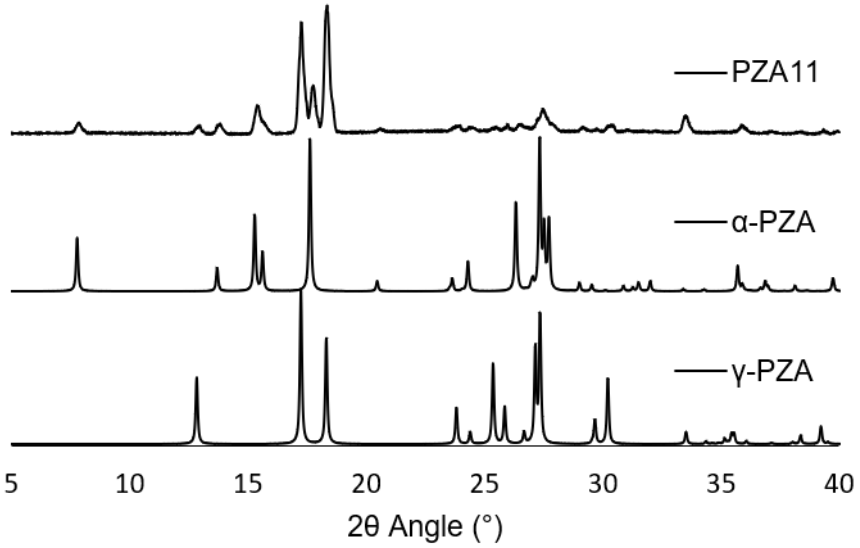

Figure 4-25: PXRD of PZA11, showing a physical mixture of the gamma and alpha forms

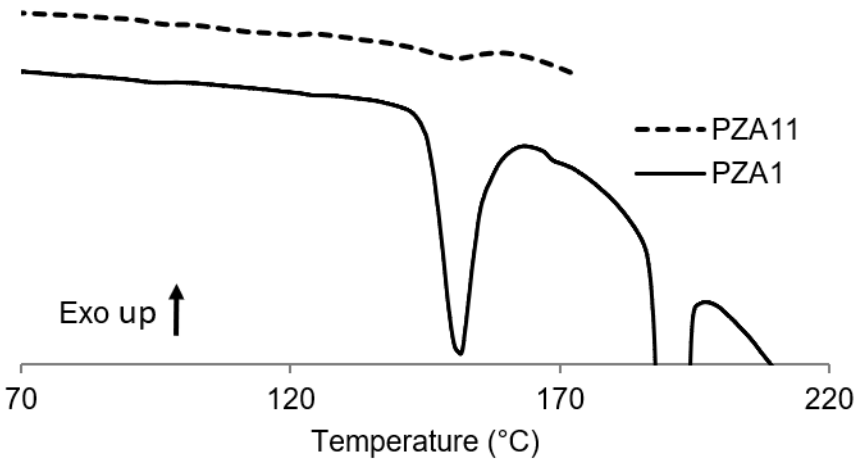

Figure 4-26: Endothermic peak in DSC traces of PZA11 (150.6 °C) and PZA1 (151.5 °C) indicating the α to γ transition in PZA. The DSC run for PZA11 was kept below 175 °C to avoid losing the phase transition to the baseline due to the large melting point peak.

Evaluation of this suggests that the mechanism for growth of the α form may be related to surface interactions with the tubing, as the α form has only been extracted from the KRAIC when major blockages have occurred. The results in PZA11 therefore indicate the α polymorph formation in the KRAIC is related to nucleation on the vessel walls,

rather than the cooling profile. This behaviour correlates with the fact that during both controlled nucleation in PZA8 and uncontrolled nucleation in PZA4, gave only γ-PZA as neither run suffered a major blockage.

4.5 Chapter Conclusions

This work constitutes a novel bench-top scale coupling of the flow chemical production of the drug substance PZA with integrated, in-line crystallisation process. Both the advantages of flow synthesis and continuous crystallisation are maintained by decoupling the net flow rates of the processes. Initial research resulted in poor crystallisation processing and a low overall solid recovery. The introduction of a controlled cooling step resolved blockage issues and improved the solid recovery. This was achieved through a rapid cooling step, which induced nucleation and reduced crystal size. The resultant five-fold smaller crystals of PZA were easily isolated without blockage issues. Potentially, the PZA crystals produced by this route could be incorporated into formulation after isolation. Furthermore, as a consequence of the crystallisation technique, the γ polymorph of PZA was selectively obtained. Literature indicates that γ-PZA shows enhanced dissolution and solubility properties compared to the thermodynamically stable α form.[198] This might be of industrial interest, as the γ-form is not usually accessible from a purely aqueous solution and may display an improved bioavailability compared to the α-form; the only example of acquiring the γ form from an aqueous solution was described by Zhang *et al.*, where a group of sulfonamide compounds were used as templates for the preferential crystallisation of the γ polymorph.[199] The work presented demonstrates the first crystallisation to selectively produce the γ polymorph from an purely aqueous solution, without the need for templates that would require off-line separation. This work presents a more streamlined production process for scale-up of a potentially desirable polymorph. However, further investigation is needed, particularly to determine the driving force for this preferred growth mechanism. It is a previously encountered phenomenon in the KRAIC to access unexpected polymorphic forms however, the exact mechanism is not well understood.[131] One possible explanation is that the distinct lack of primary nucleation sites or surface interactions within the KRAIC is the cause for the polymorphic selectivity. It is also possible that the surface boundary between the solution slugs and the air/carrier fluid is acting as a nucleation pathway for the metastable polymorph. It is difficult to study this phenomenon *in situ*, however such a study may shed some light on the possibilities for continuous crystallisation platforms allowing accurate control and selectivity towards a desired solid form.

The work presented in this chapter illustrates a bespoke working example of an inte-

grated synthesis and continuous crystallisation process. However there are still clear limitations. For example, in-line reaction monitoring and crystallisation monitoring techniques would be extremely useful in further optimisation of the process. Using available technology such as infra-red or Raman techniques would offer greater understanding of the process as well as determination of the optimum RT to achieve the greatest solid recovery and productivity. Monitoring of the synthetic reaction could be done in real-time, which would greatly improve the downstream crystallisation reproducibility. Another useful feature would be to include multiple temperature controlled zones in the KRAIC. In this work, a cooling step before running at ambient temperatures was enough to deliver selective solid form control. However, in a more complex crystallisation process being able to run processes below ambient temperatures over an extended period, or maintaining a step-wise temperature gradient would allow greater versatility in the KRAIC platform. In the long-term, extending the process to demonstrate continuous work-up after crystallisation would be a useful feature in addressing other significant gaps in integrated continuous manufacturing (CM), for example the addition of continuous filtration or formulation technologies as outlined in work by Heider *et al.*[144] Greater versatility in the available tools for engineering continuous crystallisation and work-up will allow for more integration with synthesis, which will be an essential step in the development of integrated continuous manufacturing.

Chapter 5

Thermochromics

5.1 Introduction

The work in this chapter forms part of the M4 (Make, Measure, Model, Manipulate) Metastable materials programme, which aimed to develop switchable materials. These switchable materials could be manipulated by the application of an external stimulus to change their properties. Amongst the systems developed, a series of multi-component crystals were produced which displayed thermochromic properties. The study in this chapter was carried out in conjunction with Dr. Anuradha R. Pallipurath, Dr. Pierre-Baptiste Flandrin and Dr. Lauren Hatcher.

5.1.1 Background and Aims

Thermochromism refers to the phenomenon where a material changes colour in response to a change in temperature. A material which undergoes a colour change in response to temperature has the potential for applications in imaging, sensing and smart devices.[106,107] A family of related, multi-component halo-aniline:3,5-dinitrobenzoic acid (35DNBA) molecular crystals were identified and characterised by Jones *et al.* at the University of Bath, which displayed thermochromic properties.[110] The coloured cocrystals were found to be metastable and convert via proton transfer to a more stable salt form on heating. These pairs of cocrystal/salt complexes included 4-iodoaniline:3,5-dinitrobenzoic acid, 4-iodo-2-methylaniline (4I2MA):35DNBA and 4-bromo-2-methylaniline (4Br2MA):35DNBA (Figure 5-1). In each case, the neutral and salt form were grown using slow evaporative crystallisation. However repeatable isolation of the desirable chromatic cocrystal was not always possible.

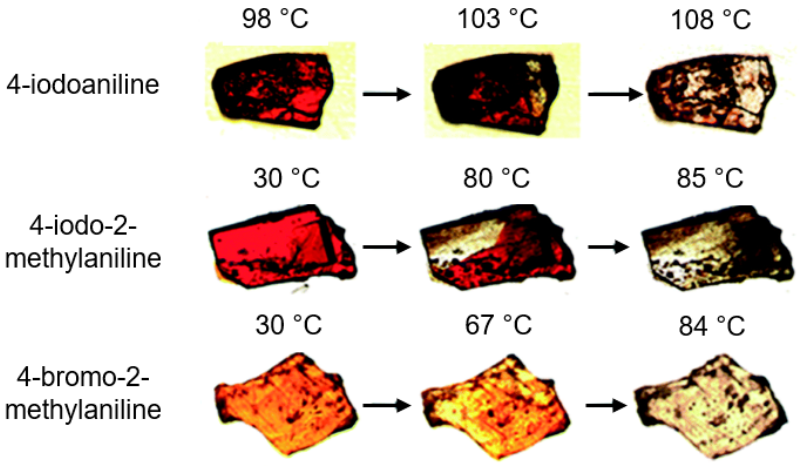

Figure 5-1: Thermochromic behaviour of halo-aniline:35DNBA cocrystals[110]

To improve the reproducibility of the crystallisation, the research presented here aimed

to investigate whether the use of flow chemistry and crystallisation platforms would allow scale-up and better control over the crystallisation of thermochromic materials. Some of the initial investigations were carried out by University of Bath Masters project student, Alex Mildon under the supervision of Dr. Pierre-Baptiste Flandrin. In their work, they successfully scaled-up and reproduced the 4-iodoaniline:3,5-dinitrobenzoic acid cocrystal and salt forms. The isolated cocrystal was also shown to be thermochromic and readily transformed to the colourless salt on heating. However, production of 4Br2MA:35DNBA complexes was not investigated and the chromatic 4I2MA:35DNBA cocrystal could not be produced. Therefore the work presented in this thesis aimed to investigate the use of flow crystallisation in the production of the multi-component systems of 4I2MA:35DNBA and 4Br2MA:35DNBA (Figure 5-2). The research focused on development of a suitable crystallisation process for translation into flow. Once identified, a series of efforts were made to control the formation of the multi-component crystals to preferentially form the elusive thermochromic cocrystals in a more consistent procedure with scale-up potential.

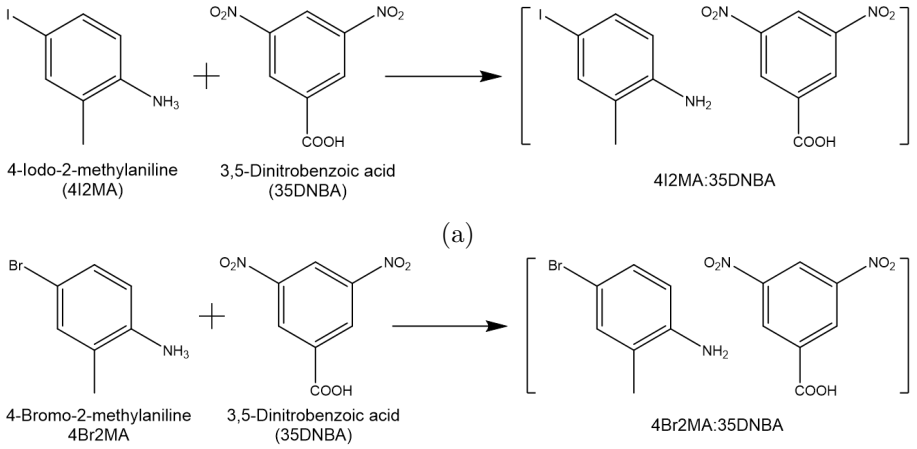

Figure 5-2: Cocrystallisation of a) 4I2MA and b) 4Br2MA with 35DNBA

5.2 Batch Crystallisation

5.2.1 Evaporative Crystallisation

Initial production of the thermochromic cocrystals began by replicating the slow evaporation procedure for the formation of 4I2MA:35DNBA and 4Br2MA:35DNBA cocrystal and salt forms reported by Jones *et al.*[109,110] The method used is described in Section 2.6.1. The conditions for producing the neutral and salt forms of the different cocrystal complexes are outlined in Table 5.1.

Table 5.1: Slow evaporation conditions reported for production of cocrystal complexes of 4I2MA and 4Br2MA with 35DNBA[110]

Compound	Complex	Formula	Solvent	Temperature (°C)
4-bromo-2-methylanilinium:3,5-dinitrobenzoate	**Cc1**	$[C_7BrNH_9]^+$ $[C_7O_6N_2H_3]^-$	Methanol	Room Temp
4-bromo-2-methylaniline:3,5-dinitrobenzoic acid	**Cc2**	$[C_7BrNH_8]$ $[C_7O_6N_2H_4]$	Methanol	40
4-iodo-2-methylanilinium:3,5-dinitrobenzoate	**Cc3**	$[C_7INH_9]^+$ $[C_7O_6N_2H_3]^-$	Ethanol	4
4-iodo-2-methylaniline:3,5-dinitrobenzoic acid	**Cc4**	$[C_7INH_8]$ $[C_7O_6N_2H_4]$	Acetonitrile	Room Temp

Using the conditions described by Jones *et al*, both the salt and neutral forms of the cocrystals could be replicated using evaporative methods. Of particular note, the production of **Cc1** and **Cc3** (the salt forms of 4Br2MA:35DNBA and 4I2MA:35DNBA respectively) were accessible in multiple solvents and across several temperatures. This is not surprising as the colourless salt complex is the most stable form. In contrast, **Cc2** and **Cc4** (the chromatic, metastable cocrystals) repeats of the evaporative method did not always produce the desired chromatic complex. Solid form analysis was carried out on a sample of **Cc2** isolated from slow evaporation using the conditions described in Table 5.1. The resulting powder X-ray diffraction (PXRD) pattern is shown in Figure 5-3, which is compared to simulated PXRD patterns taken from literature for **Cc1** and **Cc2**.[110]

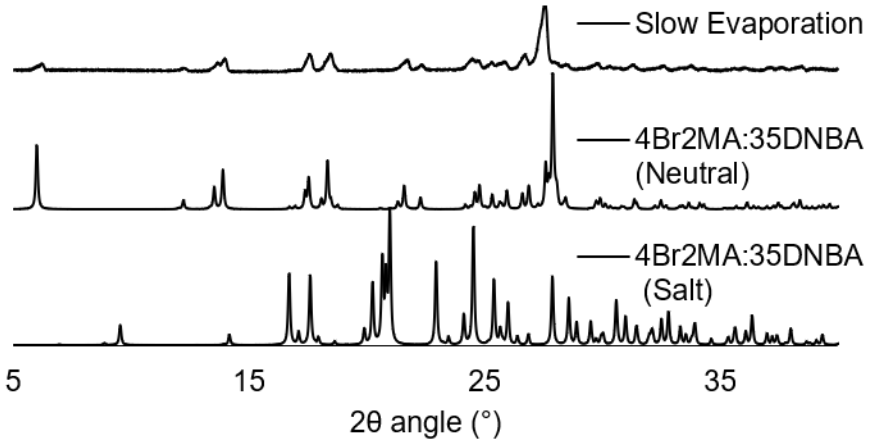

Figure 5-3: PXRD pattern for **Cc2** produced from evaporative crystallisation, compared to simulated patterns from single crystal X-ray diffraction (SCXRD) acquired by Jones *et al.*

As can be seen from the figure, there is close similarity between the neutral form of 4Br2MA:35DNBA and the sample isolated from slow evaporation at 40 °C. There is a clear distinction between the diffraction patterns for the neutral (**Cc2**) and salt (**Cc1**) forms of 4Br2MA:35DNBA, which corresponds to a change in the crystal structural arrangement. The measured diffraction intensity from the slow evaporation **Cc2** sample is quite weak, but further sample preparation to improve this could not be carried out, as grinding the isolated sample would cause a shift to the salt form. As noted by Jones *et al.* repeat experiments did not always result in production of the same complex. In this case, slow evaporation at 40 °C did result in the desired **Cc2** form, but it was produced as a powder, rather than the block crystal reported. This inconsistent behaviour was commonly encountered by Jones *et al.* during crystallisation attempts of **Cc2** under similar conditions. This highlights the difficulty in isolating the metastable, thermochromic cocrystal and provides further evidence of the need to replace the evaporative method.

The differential scanning calorimetry (DSC) trace for the slow evaporative sample of **Cc2** is shown in Figure 5-4. The sample shows a endothermic peak that corresponds to a melting point at 129.9 °C, close to the value reported by Jones *et al.* for a transformed sample of **Cc2** (128.6 °C). It is worth noting that Jones *et al.* were unable to determine the phase transition from **Cc2** to **Cc1** using DSC measurements, due to the rapid transformation of **Cc2** to **Cc1** with time. The transformation was confirmed visually using hot stage microscopy (HSM) in literature. In this repeat, the powder form of

Cc2 did show an exothermic phase transition just above the DSC baseline, with an onset of 82.4 to 125.3 °C. However, this is significantly shifted and over a larger range compared to the expected value of 61 to 83 °C reported by Jones *et al.* from HSM measurements. The shift may be due to the difference in morphology. Unfortunately, the powdered form of **Cc2** was opaque and no visible colour switch could be seen during HSM measurements to confirm thermochromism in the powder form.

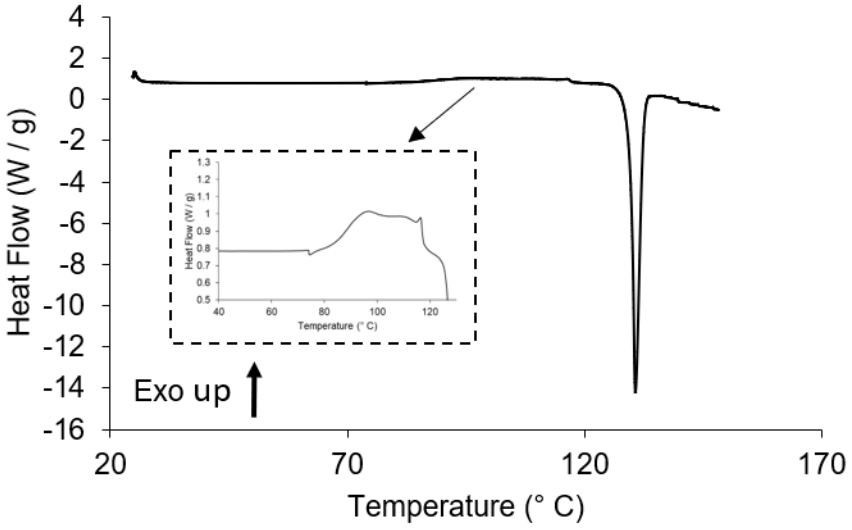

Figure 5-4: DSC trace of **Cc2** produced from evaporative crystallisation, showing a melting point of 130.9 °C and possible phase transition

For 4I2MA:35DNBA, slow evaporation of 4I2MA and 35DNBA in acetonitrile (ACN) resulted in red, plate-like crystals. These were analysed using HSM and DSC. The DSC trace is shown in Figure 5-5. An exothermic peak is observed in DSC analysis from 48.7 to 75.4 °C. This is close to the reported phase transition from **Cc4** to **Cc3** by Jones *et al.* (45 to 65 °C). The endothermic peak corresponds to a melting point and has an onset temperature of 117.9 °C. Jones *et al.* reported a value of 114 °C for the 4I2MA:35DNBA cocrystal complex. Thus, the results are in general agreement.

Figure 5-6 shows analysis using HSM, which was carried out as described in Section 2.12. A link to the video can be found in the Appendix Section 9.3. Here, the thermochromic behaviour is exhibited as a single-crystal-to-single-crystal (SCSC) phase transition from 94.9 to 100.5 °C resulting in a loss of crystallinity and the red colour.[200] This is followed by a melt and recrystallisation at 122.1 °C which corresponds to the loss of the cocrystal and recrystallisation of the 35DNBA coformer. The shift in the transition point compared to the DSC data may be related to analysis of the bulk ma-

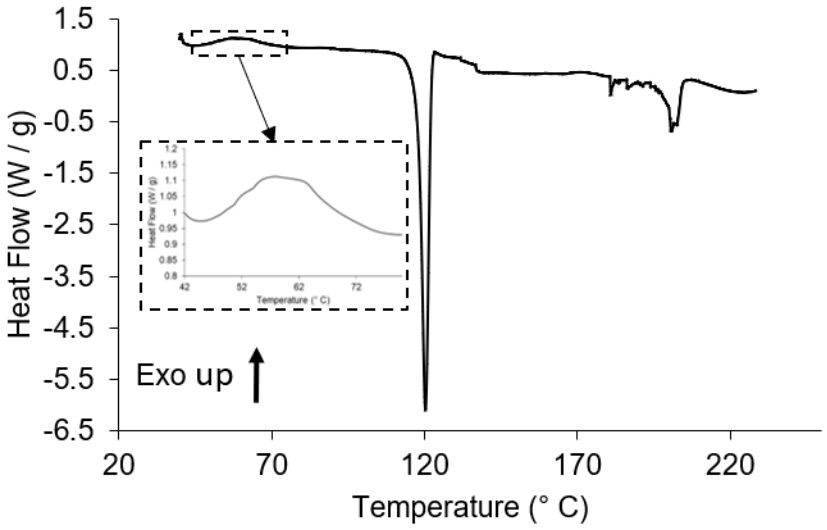

Figure 5-5: DSC trace of **Cc4** produced from evaporative crystallisation, showing a melting point of 120.3 °C and an exothermic event at 48.7 to 75.4 °C.

terial compared to a single crystal. A difficulty with reproducing the thermochromic behaviour in these cocrystals, was the variability in observed transitions. This may be due to differences in experimental set-up or variations in crystallisation conditions. As the framework of this work was to translate evaporative methods into a more consistent methodology, evaporative crystallisation was not pursued further. There was insufficient material to complete a PXRD experiment but the red colour and melting point in comparison to the pure starting materials of 4I2MA (Appendix Figure 9-24b) and 35DNBA (Appendix Figure 9-24c) suggested the formation of 4I2MA:35DNBA in the **Cc4** form.

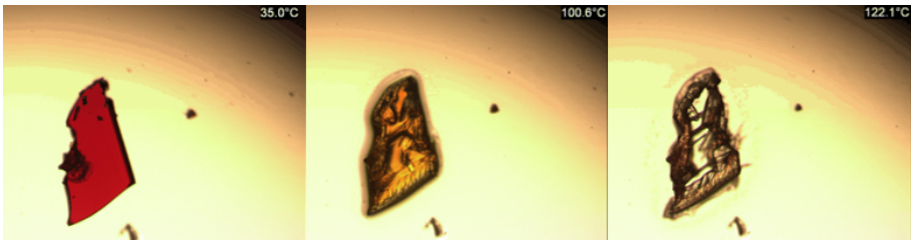

Figure 5-6: HSM images of thermal events for **Cc4** isolated from slow evaporation. The red colour is lost from 94.9 to 100.5 °C. The crystal melts at 122.1 °C.

While analysis of crystals isolated from evaporative methods indicated the complexes of 4Br2MA:35DNBA and 4I2MA:35DNBA could be replicated under the conditions outlined in Table 5.1, the isolated products were often poorly crystalline and incon-

sistent with the block crystals described in literature. This is often the case when producing metastable or multi-component crystal systems.[201] Furthermore, scaling up of an evaporative crystallisation process is difficult due to the inherent limitations of the technique, making it better suited to small scale, screening investigations.[202,203] For the thermochromic organic complexes, the metastable form of **Cc2** was difficult to acquire consistently as the transition of **Cc2** to the thermodynamically more stable **Cc1** form occurs under ambient conditions over time.[110] Therefore, the aim of this work was to replace the evaporative methods with an alternative crystallisation technique that could offer better control over crystallisation conditions, as well as the potential to scale-up production. In pursuit of this, previous work in the group had identified that an antisolvent methodology could be applied to replicate halo-aniline cocrystals from evaporative experiments.[204] These structures were analogous to the desired 4Br2MA:35DNBA and 4I2MA:35DNBA complexes. Hence, efforts concentrated on applying antisolvent crystallisation techniques for the production of **Cc1**, **Cc2**, **Cc3** and **Cc4** complexes.

5.2.2 Antisolvent Crystallisation

The experimental method used for antisolvent crystallisation in batch experiments is outlined in Section 2.6.2. In solvent screening tests, water was found to act as suitable antisolvent due to the low solubility of the coformer components, 4Br2MA, 4I2MA and 35DNBA. As such, antisolvent crystallisation experiments concentrated on solvents miscible with water and which had shown success in the formation of at least one of the multi-component complexes during evaporative crystallisation experiments. The first successful formation of 4Br2MA:35DNBA form **Cc2** was achieved during antisolvent crystallisation under ambient temperatures. To determine if temperature played a role in the preferential crystallisation of **Cc2** over **Cc1**, antisolvent crystallisation experiments were repeated under controlled conditions. The results for temperature dependent antisolvent experiments are shown in Table 5.2.

Table 5.2: Antisolvent crystallisation results at various temperatures

Experiment	Temperature (°C)	Coformer	Form
TC1.1	40	4Br2MA	**Cc2**
TC1.2	30	4Br2MA	**Cc2**
TC1.3	20	4Br2MA	**Cc2**
TC1.4	10	4Br2MA	**Cc2** to **Cc1**
TC1.5	5	4Br2MA	**Cc1**

Conditions: 4Br2MA (50 mg) and 35DNBA (56 mg) in methanol (MeOH) 1 mL. Addition of 2 mL equivalents of antisolvent (water) to precipitate. No stirring.

As can be seen from Table 5.2 a trend emerges, with a switch occurring from formation of **Cc2** to **Cc1** as temperature decreases. This is visually observed as the change in colour from orange to colourless, as depicted in Figure 5-7.

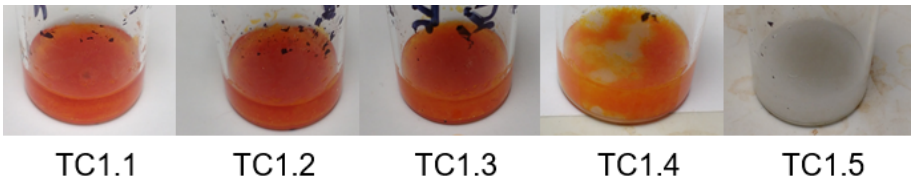

Figure 5-7: Antisolvent crystallisation of 4Br2MA:35DNBA at different temperatures

Of particular importance was sample TC1.4, which initially comprised of a mixture of orange and colourless crystals upon precipitation. However this changed over time, becoming completely colourless within 45 minutes (Figure 5-8) under ambient conditions.

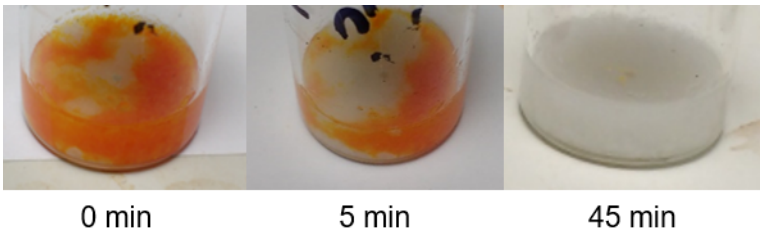

Figure 5-8: Colour change observed for sample TC1.4

For TC1.1 to TC1.3 no colour change was observed within the same time period, under the same conditions. However, removal of the solvent under vacuum in some cases did trigger the transformation from orange to colourless and a shift from **Cc2** to **Cc1**. This shift appears to indicate that the presence of the colourless complex will seed the transition of the whole sample over time and may indicate that the metastable, neutral form (**Cc2**) has a relatively small energy barrier for transitioning to the salt form (**Cc-1**). Even samples that visibly appeared unchanged after filtration would slowly switch under ambient conditions from the chromatic complex to the colourless complex over days, weeks or months. It may be that some **Cc1** is present but not visible to the naked eye in these cases. Certainly, it was observed that the transformation occurs more rapidly in samples with a visible **Cc1** presence. In contrast, some **Cc2** samples that were not separated from the solvent/antisolvent medium did not change colour, so long as **Cc1** was not present to initiate the change. In these cases, the samples were left to evaporate at room temperature until dry. In these cases, the orange colour remained stable if undisturbed for up to 1 year under ambient conditions (Figure 5-9).

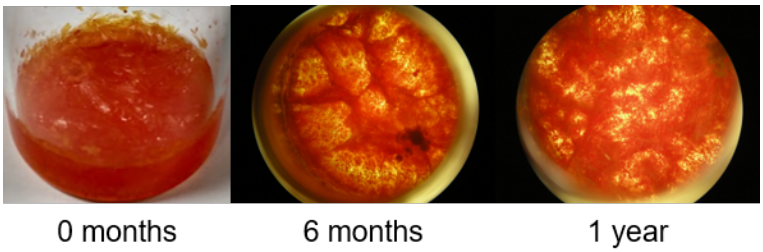

Figure 5-9: Orange crystals of 4Br2MA:35DNBA produced from a batch antisolvent crystallisation at 30 °C (a later repeat of TC1.2). Photos taken 6 months and 1 year later using an optical microscope.

Solid form analysis was carried out on TC1.2, TC1.4 and TC1.5. Unfortunately, TC1.1 and TC1.3 changed from orange to colourless during extraction emphasising again the metastable nature of the **Cc2** complex. The results for PXRD analysis are shown in Figure 5-10.

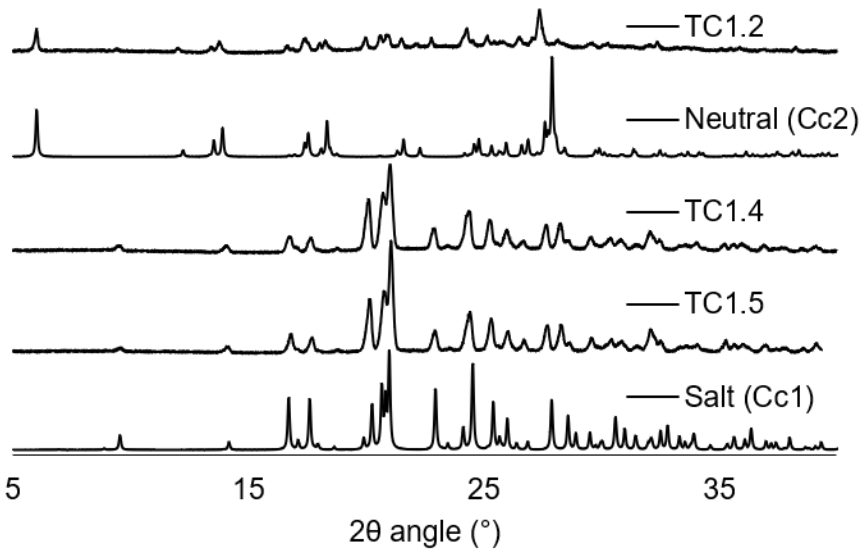

Figure 5-10: PXRD of antisolvent crystallisation samples of 4Br2MA:35DNBA in comparison to simulated PXRD patterns of the relevant complex

As seen, the complexes isolated match the PXRD patterns generated from SCXRD data reported by Jones *et al.*, suggesting the formation of both complexes is possible from antisolvent methods. However, TC1.2 does show signs of conversion of **Cc2** to **Cc1**, but this is believed to have been initiated during sample preparation for PXRD analysis. The onset temperature and melting points for each sample are shown in Table 5.3. DSC traces for TC1.2, TC1.4 and TC1.5 are shown in Appendix Figure 9-25.

Table 5.3: Melting points for DSC traces in antisolvent crystallisations of 4Br2MA:3-5DNBA

Experiment	Melting Point	
	Onset (°C)	Peak Max (°C)
TC1.2[a]	129.7	130.3
TC1.4[a]	129.3	130.3
TC1.5[a]	129.3	130.9
4Br2MA[b]	57.0	57.9
35DNBA[b]	205.4	206.5

a DSC traces for TC1.2, TC1.4 and TC1.5 are shown in Appendix Figure 9-25. *b* DSC traces for starting materials are in the Appendix Figures 9-24a and 9-24c

As was the case with the samples isolated from slow evaporation, the DSC traces show a clear endothermic peak that corresponds to a melt at 130 °C. The melting points are distinct from the starting materials and close to the onset temperature in literature for the complex **Cc1** (128.6 °C). Thermal analysis and PXRD data are therefore in general agreement. The close melting point of TC1.2 with TC1.4 and TC1.5 would suggest that a phase transition from **Cc2** to **Cc1** may have occurred in TC1.2 during heating. This may correspond to a display of thermochromism. Figure 5-11 shows an magnified view of two possible transitions in the DSC trace of TC1.2 before the melting point.

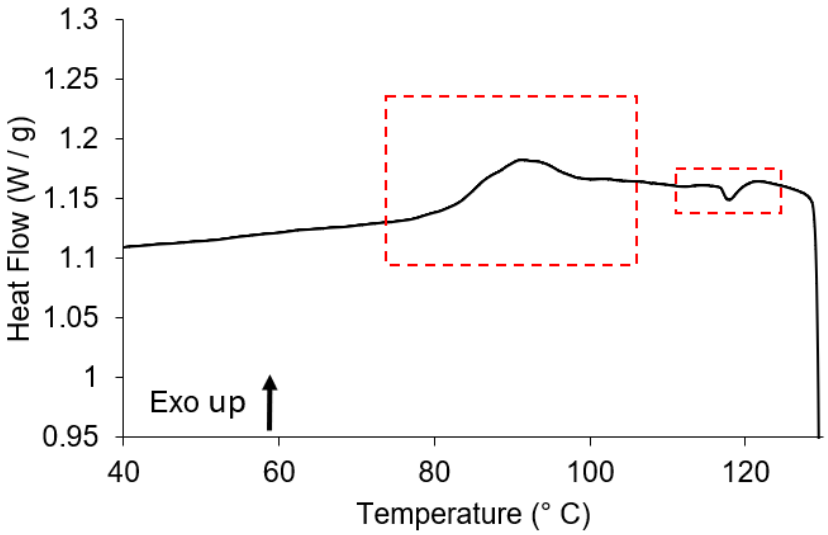

Figure 5-11: Possible phase transitions in TC1.2. The melting endothermic event is visible at the far right of the trace (129 °C)

An exothermic event is visible above the baseline from 81.1 to 112.7 °C. This is fol-

lowed by a small endothermic event at 117.9 °C. The exothermic event shows an onset temperature similar to that seen for the slow evaporation sample of 4Br2MA:35DNBA, as shown in Figure 5-4. This may correspond to a possible switch from **Cc2** to **Cc1**. The small endothermic peak at 117.9 °C has not previously been observed and may constitute a thermal event that may have been lost to the baseline in earlier evaporative measurements. This is not unsurprising, as computational modelling studies by Jones *et al.* calculated the formation energy difference between **Cc2** and **Cc1** to be 8.51 kJ mol^{-1}.[110] This is in the range of a typical polymorphic transition but the difference between the neutral and salt forms of 4Br2MA:35DNBA was the lowest of all the halo-aniline:35DNBA neutral/salt pairs reported for the computational studies. Hence, the transition enthalpy from **Cc2** to **Cc1** may be small and difficult to detect accurately using standard DSC experiment. The possible thermal transitions detected in the DSC trace for TC1.2 could not be cross-referenced with HSM as TC1.2 converted to **Cc1** after PXRD and DSC measurements. However, further discussion of the switching properties of 4Br2MA:35DNBA cocrystals can be found in Section 5.3.4.

For the neutral complex/salt pair, **Cc3** and **Cc4** the antisolvent crystallisation was tested in ACN, MeOH and ethanol (EtOH) over a range of temperatures from 4 to 40 °C. Key experiments are shown in Table 5.4.

Table 5.4: Antisolvent crystallisation results at various temperatures

Experiment	Temperature (°C)	Solvent (4**R**2MA)	Coformer	Form
TC1.6	40	ACN	4I2MA	**Cc3**
TC1.7	RT	EtOH	4I2MA	**Cc3**
TC1.8	30	MeOH	4I2MA	**Cc5**

Conditions: 4I2MA (46 mg) and 35DNBA (56 mg) in 1 mL of solvent. Addition of 2 mL equivalents of antisolvent (water) to precipitate. No stirring.

For **Cc3** and **Cc4** production using ACN as a solvent with H_2O as an antisolvent was not effective. The addition of the antisolvent gave rise to an emulsion of red oil. Even after the addition of excess water, 4I2MA:35DNBA did not readily crystallise (Figure 5-12). For TC1.7, a mixture of colourless/purple powder was obtained. This was common across a range of solvents and temperatures. However, in TC1.8 a series of yellow crystal clusters were obtained, indicating that antisolvent crystallisation at 30 °C in MeOH favoured the formation of a possible new crystal form.

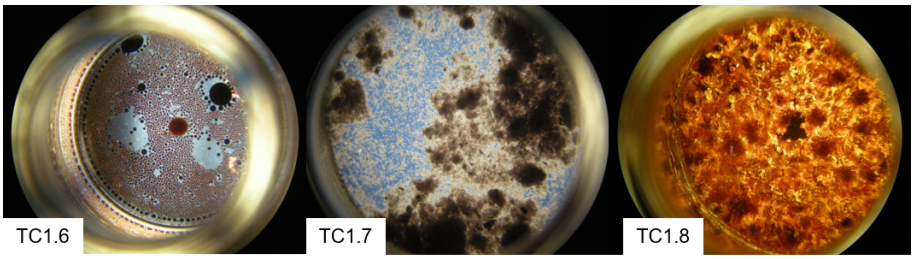

Figure 5-12: Optical microscopy of TC1.6, TC1.7 and TC1.8 after antisolvent crystallisation

These yellow crystal clusters rapidly transformed to colourless crystals on extraction, in a similar manner observed with **Cc2**. Unfortunately, unlike **Cc2** samples, attempts to isolate the yellow crystal cluster from solution seeded the transition to **Cc3** before analysis could take place. The cluster did remain stable if left submerged in solution and left undisturbed. The solvent was allowed to fully evaporate and TC1.8 remained sufficiently stable after this to perform solid form analysis. PXRD analysis was carried out on TC1.8 and compared with TC1.7, the results are shown in Figure 5-13.

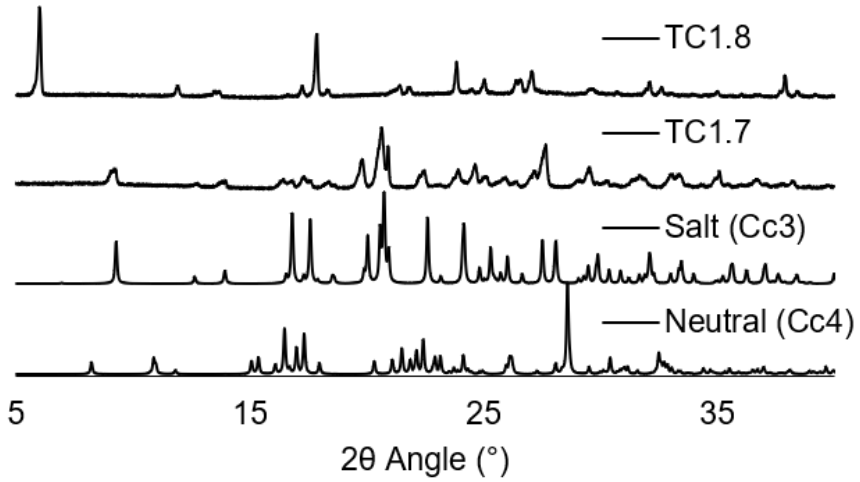

Figure 5-13: PXRD patterns for TC1.7 and TC1.8 compared to simulated data for **Cc3** and **Cc4** from literature.[109]

The diffraction pattern obtained from TC1.7 shows a match with the simulated salt form of 4I2MA:35DNBA. This confirmed that the colourless crystals seen in optical microscopy images for TC1.7 corresponded to **Cc3**. None of the antisolvent crystallisation methods tested reproduced the red, thermochromic cocrystal **Cc4** as seen in slow evaporation. However, the crystals produced in TC1.8 matched neither of the

two known forms of 4I2MA:35DNBA. The difference in the optical properties of the crystals along with the PXRD pattern suggested that a new cocrystal may be present.

A crystal from TC1.8 was analysed using SCXRD; the structure was solved with the help of Dr. Lauren Hatcher. The structural data can be viewed in Appendix Table 9.4. Analysis of the structure indicated that a new complex of 4I2MA:35DNBA (denoted herein as **Cc5**) had been produced. The SCXRD data was used to generate a simulated PXRD pattern which was compared to the PXRD pattern for the bulk TC1.8 (Figure 5-14). The data showed a relatively good match, suggesting that the crystal was representative of the bulk. However, the crystal was only weakly diffracting and hence the quality of the measured PXRD pattern needs improving at higher 2θ angles.

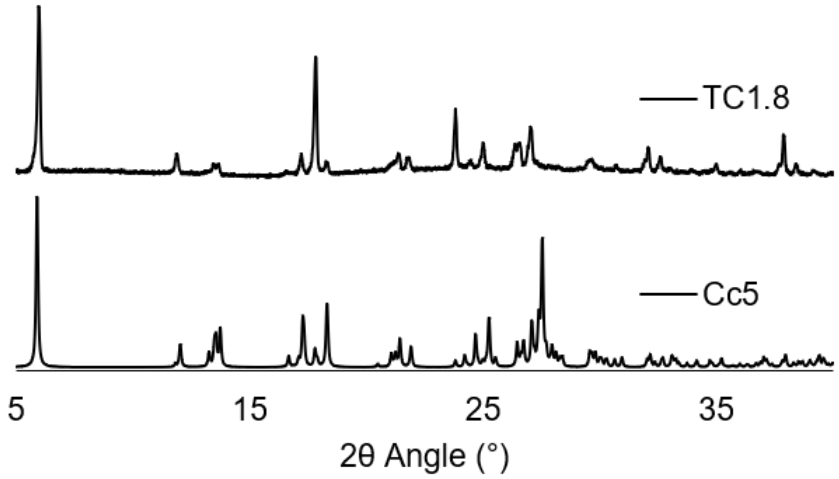

Figure 5-14: PXRD pattern for TC1.8 compared to simulated PXRD pattern for **Cc5** from SCXRD data.

TC1.8 was tested for thermochromic behaviour using thermal analysis. The DSC traces of TC1.8 and TC1.7 are shown in Figure 5-15a and 5-15b respectively. Observations in the DSC analysis of TC1.8 and TC1.7 show matching endothermic peaks representing melting points at 121.2 °C and 123.0 °C respectively. The values are close to the melting point observed for the slow evaporation sample of 4I2MA:35DNBA (120.3 °C) providing confirmation that TC1.8 is a complex of 4I2MA:35DNBA. However an exothermic event unique to TC1.8 is also observed from 96.8 to 106.4 °C. This potentially corresponds to a phase transition or recrystallisation event.

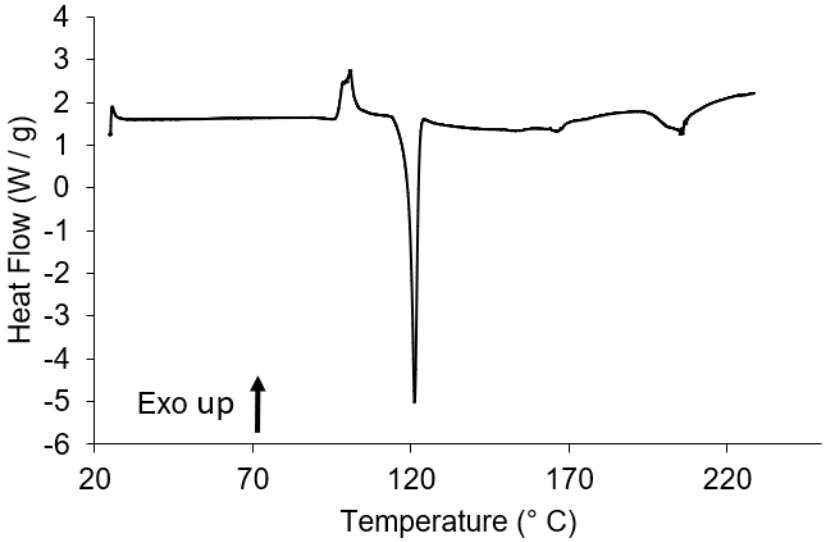

(a) TC1.8. Exothermic peak with an onset of 96.8 °C indicating a possible phase transition or recrystallisation. Endothermic event at 121.2 °C corresponding to a melt.

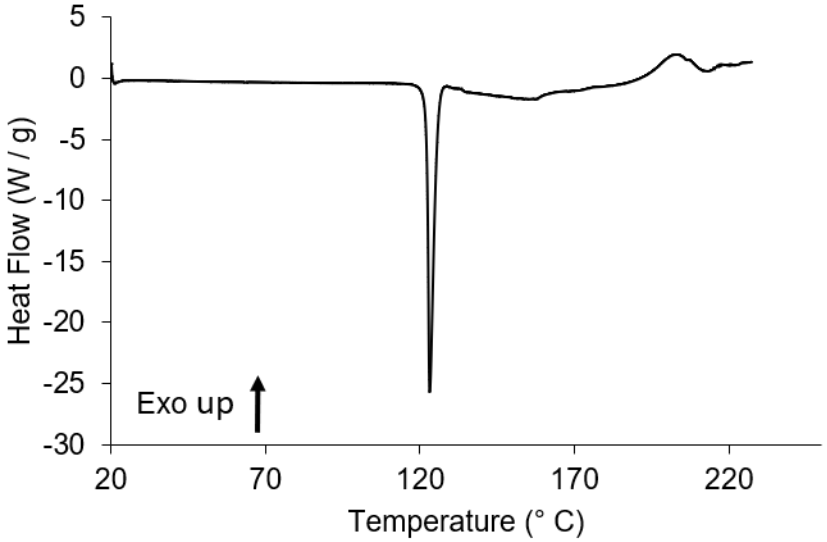

(b) TC1.7. Endothermic peak at 123.0 °C corresponding to a melting point.

Figure 5-15: DSC traces of TC1.8 and TC1.7

HSM of TC1.8 is shown in Figure 5-16, in which the sample was heated from 35 to 150 °C at 5 °C min^{-1}. During heating on the HSM, TC1.8 visibly undergoes a phase transition, passing through a melt and recrystallisation step at 92.5 to 100.9 °C. The sample then melts completely from 117.6 to 121.6 °C. The remaining colourless needle crystals correspond to the starting material 35DNBA, which displays a higher melting

point than the cocrystal (205.4 °C). Based on the results obtained, it is probable that the exothermic event in Figure 5-15a corresponds to a phase transition from **Cc5** to the colourless **Cc3** complex before the melt. This behaviour is slightly different from **Cc4**, as **Cc5** does not display the SCSC phase transition observed in **Cc4** from evaporation experiments and instead passes through a melt-recrystallisation phase transition. Potentially, **Cc5** could display the same SCSC behaviour, as the mechanism behind the phase transition from **Cc5** to **Cc3** is likely to be the same as that of **Cc4** to **Cc3** (i.e. proton transfer), but this has not been investigated further. However, the thermochromic behaviour of the **Cc5** to **Cc3** during the phase transition is discussed in Section 5.3.4.

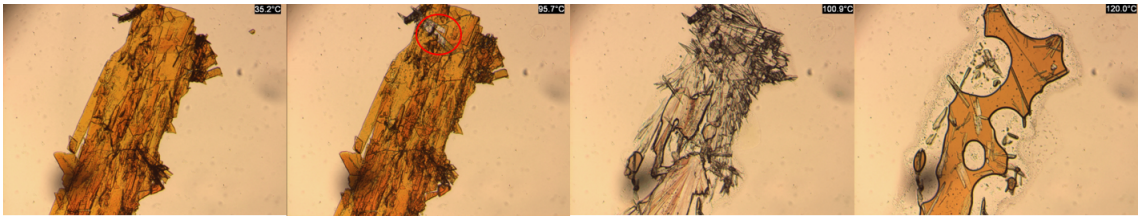

Figure 5-16: Thermal events during HSM of TC1.8. Phase transition occurs from 92.5 to 100.9 °C. The sample begins to melt at 117.6 °C

5.3 Continuous Crystallisation

Based on the results so far, the antisolvent approach could successfully reproduce both 4Br2MA:35DNBA complexes **Cc1** and **Cc2** as well as 4I2MA:35DNBA complex **Cc4** and the new complex, **Cc5**. Of particular interest was the production of **Cc2**, which had previously shown the irreversible thermochromic transition to **Cc1**, but could not be consistently produced by slow evaporation. In contrast, antisolvent crystallisation of 4I2MA:35DNBA did not readily produce thermochromic cocrystals. It was therefore deemed more beneficial to stick to 4Br2MA:35DNBA for production via flow crystallisation, as **Cc2** could be consistently produced unlike 4I2MA:35DNBA cocrystals; **Cc5** and **Cc4**. Therefore, efforts during continuous crystallisation aimed to reproduce **Cc2** in flow and test whether the thermochromic behaviour reported in evaporative crystallisation of single crystals of 4Br2MA:35DNBA could be replicated.

5.3.1 Platform Development

The batch antisolvent crystallisation tests, cross-referenced with previously reported slow evaporation experiments, suggested that high temperatures facilitated the formation of **Cc2**, while crystallisation at lower temperatures leads to the formation of **Cc1**.

Hence, the crystalliser platform must be capable of careful temperature control. In batch, the crystallisation process was rapid and the addition of the antisolvent resulted in precipitation of the solid within 1 to 3 minutes. Therefore the current conditions did not require the crystalliser to accommodate long residence times (RTs). Of further consequence was mixing as initial studies in the development of the antisolvent technique indicated that vigorous stirring or sonication during precipitation would result in the transition of **Cc2** to **Cc1**, even at high temperatures. Based on these observations, a gentle mixing regime was required. Therefore a temperature controlled segmented flow crystalliser based on the kinetically regulated automated input crystalliser (KRAIC) (described in Section 2.7.1) was developed to accommodate the elevated temperature antisolvent crystallisation. A schematic diagram of the segmented flow, antisolvent crystalliser is shown in Figure 5-17.

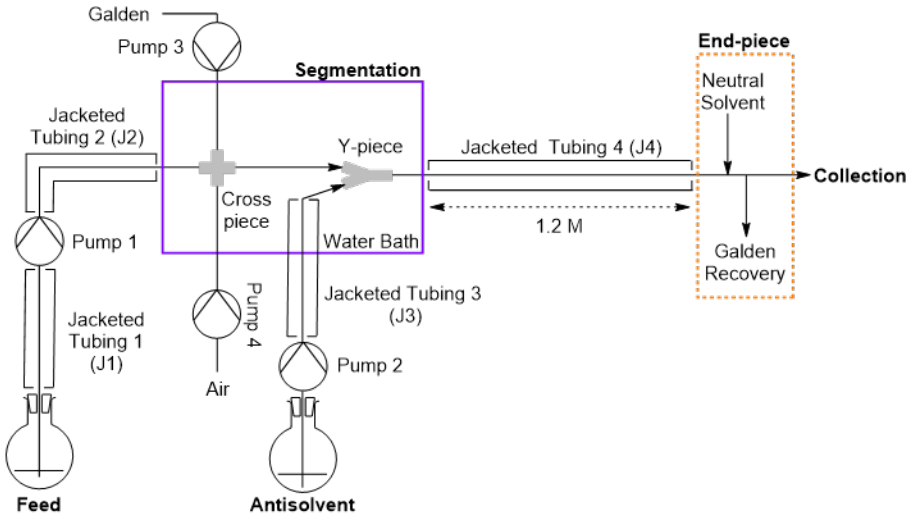

Figure 5-17: Schematic diagram for the segmented flow crystalliser for 4Br2MA:35D-NBA production. Photographs can be found in Appendix Figure 9-28.

5.3.2 Experimental

The air and carrier fluid (Galden SV110) were pumped using Ismatec (Reglo-Z series) gear pumps using perfluoroalkoxy alkane (PFA) (1 mm inner diameter (ID)) tubing. The feed and antisolvent were pumped using Vapourtec SF-10 peristaltic pumps or the Vapourtec R2$^+$ pump module. Jacketed tubing (1.5 mm ID) PFA was used to heat and transport the feed and antisolvent from the feedstock to the cross piece. The temperature of jacketed tubings 1 to 4 were controlled using a Grant R3 TX150 circulator unit. A polyether etherketone (PEEK) cross piece (1 mm ID) was used to

segment the feed by the addition of air and carrier fluid. Antisolvent was added to the segmented stream using a polypropylene (PP) Y-piece (2.8 mm ID) placed after the cross piece. The cross piece and Y-piece were submerged within a heated water (or ice) bath to control temperature. The segmented flow then moved into jacketed tubing 4 (J4), a fluorinated ethylene propylene (FEP) tube with a length of 1.2 m (3.2 mm ID). An end-piece was used to recover the carrier fluid. A neutral solvent (1:2 v/v%, MeOH:H_2O) was used to provide additional velocity for removal of any precipitated solid after carrier fluid recovery, without redissolving the product. In later runs, the feed solution was collected and stored in 20 mL glass sample vials for off-line extraction rather than direct filtration from the crystalliser outlet.

The parameters used in each experiment run are outlined in Table 5.5.

Table 5.5: Experimental parameters for antisolvent crystallisation in segmented flow

Experiment	Feedstock			Antisolvent	Segmentation[a]	J4 Tubing	Set Temperature
	[4Br2MA] ($mg\,mL^{-1}$)	[35DNBA] ($mg\,mL^{-1}$)	Flow Rate ($mL\,min^{-1}$)	Flow Rate ($mL\,min^{-1}$)	Air ($mL\,min^{-1}$)	RT (min:sec)	(°C)
TC2.1	30.00	34.80	1.00	2.00	4.18	01:13	20
TC2.2	30.00	34.80	1.00	2.00	4.18	01:02	40
TC2.3	15.00	17.40	1.00	2.00	8.40	00:55	4
TC3	30.00	34.80	1.00	2.00	6.30	00:45	40

Antisolvent = H_2O. *a* In segmentation, carrier fluid was always set to 1 increment or $2.1\,mL\,min^{-1}$ for every run.

5.3.3 Results and Discussion

TC2

In TC2 the aim was to determine if temperature could be used to form **Cc2** and **Cc1** selectively. Hence, experiments were run at controlled temperatures of 20 °C, 40 °C and 4 °C. Based on results from batch antisolvent experiments, it was expected to observe a switch from formation of **Cc2** at high temperatures to **Cc1** at low temperatures. In all three runs, the end-piece was present and a neutral solvent (1:2 v/v%, MeOH:H_2O) was used. The RT and run times for each experiment are shown in Table 5.6.

Table 5.6: RTs for TC2, antisolvent crystallisations in segmented flow

Experiment	RT (min:sec)	Run Time (min:sec)	Total No. of RTs
TC2.1	01:13	3:16	2.7
TC2.2	01:02	12:46	12.4
TC2.3	00:37	04:30	7.3

In TC2.1, the temperature of J4 was kept at 20 °C. The system ran for just 2.7 RTs before a blockage formed in the Y-piece. During this period, crystallisation occurred on addition of the antisolvent. Crystallisation was clearly seen to form the distinct orange colour of **Cc2** in-line. Collection was carried out using a Büchner filtration set-up. Interestingly, the typical orange colour associated with **Cc2** which was present within the J4 tubing jacket readily switched to the colourless form typically seen for **Cc1** on contact with the filter paper. This behaviour was similar to that observed in batch antisolvent experiments, where **Cc2** would sometimes switch to **Cc1** during removal of the solvent via filtration. A sample was thus collected after switching off the neutral solvent and removing the end-piece (to remove any triggering of the transition caused by the presence of **Cc1** encrustation in the outlet). For this sample, a collection vial was used. The precipitate initially remained orange, but gradually turned colourless on the benchtop, analogous to the behaviour observed in TCF1.4.

In TC2.2, the temperature of the tubing jackets (J1 to J4) and the water bath were increased to 40 °C. Crystallisation occurred rapidly after switching to the feedstock, with visible orange crystals forming within the second RT. Collection was carried out using sample vials periodically, three minutes into the run and continued until the run ended after twelve minutes. However, only colourless crystals formed in this case. This was revealed to be the result of encrustation in the Y-piece. As the Y-piece is the point of contact between the feedstock and antisolvent, back mixing may have led

to the formation of **Cc1** encrustation, which is likely to have seeded solution slugs and promote **Cc1** formation despite the higher temperatures. The encrustation was cleared by briefly switching the antisolvent feed to pure MeOH. After switching back to H_2O, orange crystals began to precipitate again, but they could not be isolated from collection without switching to colourless crystals.

Perhaps the most interesting result was observed during TC2.3, where all tubing jackets (J1 to J4) were lowered to 4 °C and the water bath was cooled with ice to 0.5 °C. Precipitation occurred within 1.5 RTs at the reduced temperature and to compensate, the air flow rate was increased to reduce the chance of a blockage forming. Crystallisation and collection started at the end of the first RT and continued until the end of the run. As was the case was TC2.1 and TC2.2 (after removal of the encrustation), orange crystals precipitated from the solution *in situ* (Figure 5-18).

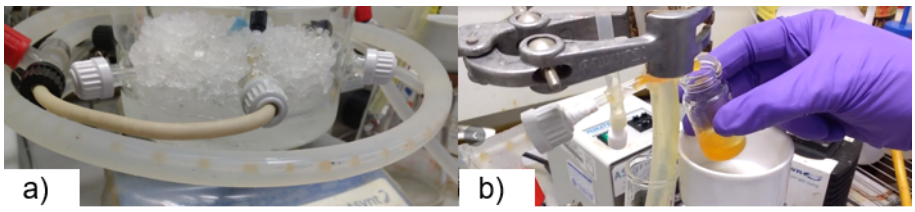

Figure 5-18: Photograph of 4Br2MA:35DNBA precipitation in a) segmented flow at 4 °C and b) at the crystalliser outlet

The formation of orange crystals at reduced temperature is in contrast to findings from batch antisolvent crystallisation tests, where precipitation below 10 °C favoured the formation of colourless crystals. Unfortunately, the orange crystals could not be isolated as they switched to colourless on hitting the filter paper. However, samples were taken every minute in glass vials and the observed colour was noted. These are shown in Table 5.7. J4 subsequently blocked five minutes into the run.

Table 5.7: Evaluation of observed colour with time for antisolvent crystallisation in segmented flow run TC2.3

Time[a] (min)	Observed colour
1	Orange
2	Orange
3	Orange/Colourless
4	Colourless

a Samples collected over 30 second periods

The clear trend is a switch over time from orange to colourless crystal formation. This is likely a consequence of the build-up of encrustation around the Y-piece and end-piece which begins to cause the transition from orange crystals to the colourless form. Even orange samples collected in glass vials which appeared to be uncontaminated to the naked eye, began to switch to colourless on the bench. Solid form analysis was carried out on the product isolated from TC2.1. The PXRD pattern is shown in Figure 5-19 and compared to TC1.5 (batch antisolvent crystallisation at 5 °C), showing good agreement. The result would therefore confirm that the colourless isolated crystals from flow match the structural arrangement of 4Br2MA:35DNBA in salt form (**Cc1**).

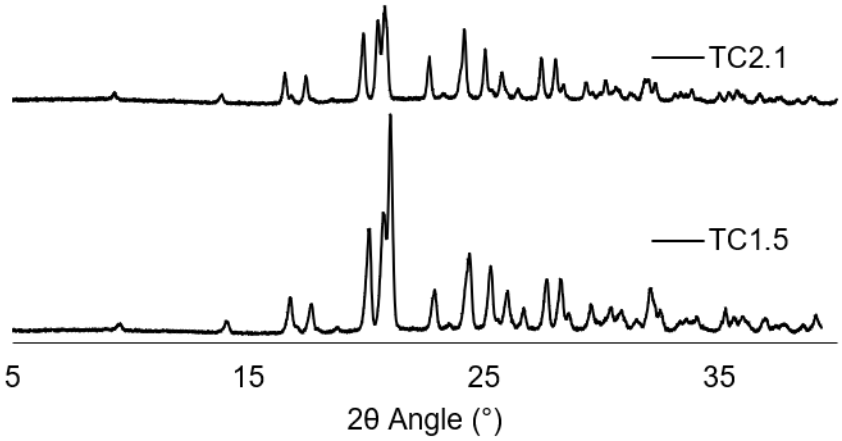

Figure 5-19: PXRD patterns of 4Br2MA:35DNBAisolated from antisolvent crystallisation in flow at 20 °C and batch antisolvent crystallisation at 5 °C

Based on the observations during the TC2 runs, it is interesting to note that the driving force for initial crystallisation of **Cc2** over **Cc1** is not temperature dependent in these segmented flow experiments. This is in contrast to batch antisolvent crystallisation, where temperature readily influenced the preference for precipitation of the salt or neutral form of 4Br2MA:35DNBA. This may suggest that the formation of **Cc2** is influenced by addition rate of the antisolvent. This was not investigated in TC2, but the addition rate of an antisolvent has been previously observed to affect both polymorphic selectivity and multi-component crystal formation in other systems.[205–207] In batch, it could be the case that the same trend is also present. It was observed that while temperature did have an strong influence on 4Br2MA:35DNBA formation in batch, sometimes **Cc2** could be formed at lower temperatures. However, this only occurred in rare cases. This may reflect the fact that the antisolvent was added manually, which could lead to variability in the addition rate and could be influencing nucleation and

growth rate. In this case, the advantage of using pumps and flow crystallisation would be to remove this inconsistency. Changing the addition rate should be considered in any future study concerning the antisolvent crystallisation of 4Br2MA:35DNBA or similar multi-component complexes.

TC3

In TC3, the system was set to 40 °C using the same concentration of feedstock as TC2.1, however the air flow rate was increased. This was to reduce encrustation around the Y-piece by increasing net flow and help prevent back mixing from occurring into the Y-piece. In TC3, the neutral solvent was switched to air only or off. The additional flow rate did reduce encrustation around the Y-piece, however encrustation around the tubing outlet continued to be a problem. Samples TC3.1 to TC3.5 were collected at the times indicated in Figure 5-20. A similar trend to TC2.3 was observed, where orange coloured crystals would form in-line and could initially be isolated without transitioning. The encrustation would build-up and cause the change from orange to colourless in all further samples. After 7 minutes, the outlet of the tubing was cleaned with acetone. The resultant isolated precipitate returned to the orange crystals (Figure 5-20).

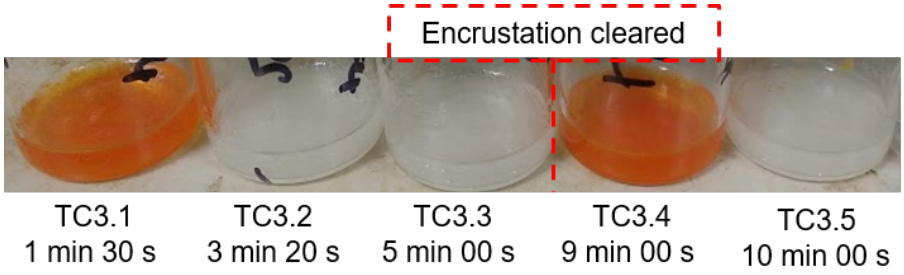

Figure 5-20: Sample vials from TC3

The orange crystals from sample TC3.4 were successfully isolated and analysed after collection from the continuous crystalliser. This was achieved by allowing the solvent to slowly evaporate instead of filtering. Solid form analysis was carried out to confirm the presence of **Cc2** and PXRD results are shown in Figure 5-21. TC3.1 crystals unfortunately transitioned to colourless before PXRD analysis was carried out. TC3.4 matched the PXRD pattern expected for **Cc2**. This was the first instance of successful work-up of the product extracted from flow and confirmed that the orange crystals observed in-line were the desired neutral 4Br2MA:35DNBA cocrystal, **Cc2**. TC3.1 remained **Cc2** after production in the flow crystalliser but transitioned to colourless crystals on filtration. PXRD also confirmed that the colourless crystals matched **Cc1**

and indicated that the observed transition is analogous to the thermochromic behaviour described by Jones *et al.*. As Jones *et al.* stated, the thermochromism displayed by 4Br2MA:35DNBA and other halo-aniline cocrystals is the result of a proton transfer from 35DNBA to the halo-aniline component.[109] This in turn, leads to changes in the crystal packing arrangement which causes the loss in colour. The results from antisolvent crystallisation experiments would indicate that the loss of colour in 4Br2-MA:35DNBA can be triggered by other external stimuli, not just temperature, which may help to explain the difficulty in isolating **Cc2** without switching to **Cc1**.

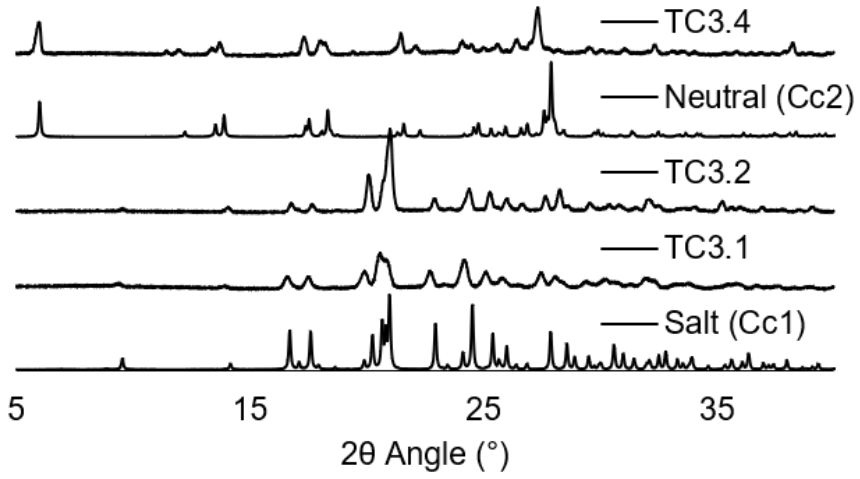

Figure 5-21: PXRD of TC3 vials in comparison to the simulated 4Br2MA:35DNBA cocrystals **Cc1** and **Cc2**

On the extraction of 4Br2MA:35DNBA

Other attempts were made to extract the metastable **Cc2** product directly from segmented flow, but the application of vacuum filtration or gravity-assisted filtration resulted in the transformation of **Cc2** to **Cc1**. As such, collection vials were the only way to successfully isolate **Cc2** from flow. However, filtration or oven drying (50 °C) often stimulated the transition, making isolation of the solid product particularly difficult. Oddly it was observed that material causing blockages in-line would often remain bright orange in colour, suggesting **Cc2** remained stable within the confines of the tubing/crystalliser or solvent, until dislodged (Figure 5-22). The most successful method for isolation was simply to leave the vials to evaporate under ambient conditions until dry. If undisturbed, the **Cc2** form remains stable, but this is both impractical and time consuming.

Figure 5-22: Blockage in the segmentation bath at 10 °C

The sensitive nature of **Cc2** means a careful work-up procedure is required for extraction and this provides a significant barrier to continuous processing. Further work should also consider raising the temperature of the water bath to prevent encrustation and blockages in the Y-piece. This would help reduce seeding **Cc1** formation. Ideally, back mixing into the Y-piece should be minimised, as the localised high antisolvent environment often caused encrustation build-up. Another difficulty was encrustation around the end-piece, this could be potentially improved by extending the RT in J4. The crystals would then have more time to grow in the controlled environment and hence nucleation on the end-piece would be less likely to occur. Regular switching of the neutral solvent or antisolvent to MeOH could also help to clean the problematic areas within the crystalliser design and prevent **Cc2** from switching to **Cc1**.

Thermochromic behaviour of TC3

HSM was carried out on samples TC3.1 and TC3.4. In the case of TC3.1, HSM was taken before the samples transitioned to **Cc1**. A selection of images are shown in Figure 5-23 depicting key thermal events. The samples were heated from 35 to 150 °C at 5 °C min^{-1}. As can be seen, a loss of colour begins to occur in TC3.1 from 69.5 to 114.5 °C. The sample also begins to lose crystallinity, but does not proceed through a melt until 130.5 °C. This indicated that **Cc2** crystals of 4Br2MA:35DNBA isolated from flow crystallisation can display the SCSC phase transition as displayed in evaporative samples isolated by Jones *et al.* However the transition occurs over a

longer temperature range than depicted in Figure 5-1 (67 to 84 °C). This may simply be reflecting the fact that analysis of evaporative methods looked at heating individual crystals whereas here, multiple crystals are heated simultaneously. Hence the more important comparison may be that the colour change onset temperature is very similar.

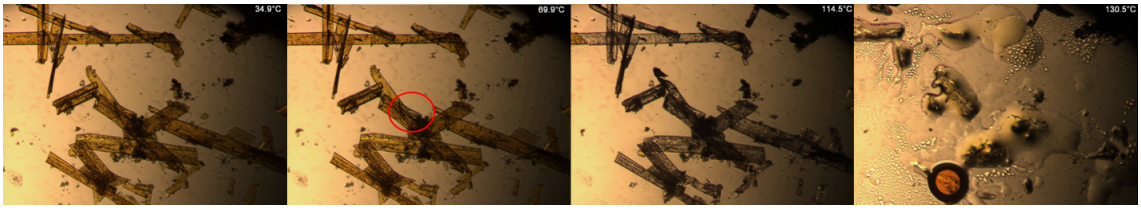

(a) TC3.1 (taken before sample transition to **Cc1**). Thermochromism occurred between 69.5 to 114.5 °C before a melt at 130.5 °C.

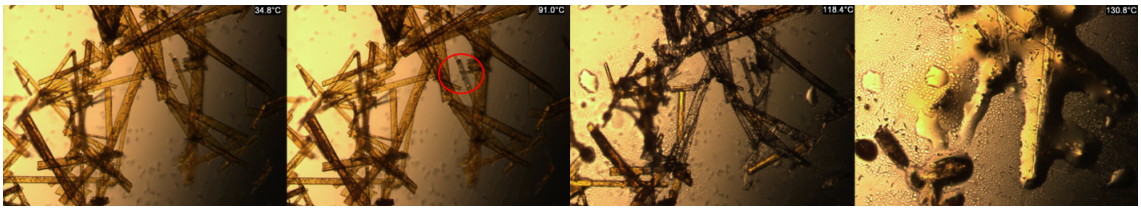

(b) TC3.4. Thermochromism occurs from 91.0 to 118.4 °C and a melt-recrystallisation transition occurs at 118.4 to 120.1 °C. Another melt occurs at 130.8 °C

Figure 5-23: HSM images of TC3.1 (before switching to **Cc1**), TC3.2 and TC3.4. Samples were heated from 35 to 150 °C at 5 °C min^{-1}

For TC3.4, the sample does not display thermochromic behaviour until 91 °C, after which crystals transition from yellow to colourless up to 118.4 °C. Unlike in TC3.1, some of the sample then subsequently undergoes a melt-recrystallisation phase transition at 118.4 to 120.1 °C followed by a second melt at 130.8 °C. This indicated that the thermochromic phase transition was more complex than first envisioned. Further thermal analysis was carried out using DSC to confirm the melt-recrystallisation phase change in TC3.4 (Figure 5-24). The DSC trace shows a sharp endothermic at 118.3 °C followed by an immediate exothermic peak at 121.6 °C. This is followed by another endothermic peak at 129.8 °C. The first exothermic and endothermic peaks closely match the melt-recrystallisation period depicted in HSM for TC3.4 and it is likely this corresponds to the transition from **Cc2** to **Cc1**. The second endothermic peak at 129.8 °C is close to the melt observed in Figure 5-23b. The major difference between TC3.1 and TC3.4 measurements was the time allowed for solvent evaporation after collection. For TC3.1, the sample was still wet, while TC3.4 was left to evaporate until dry. Further discussion of the effects of drying and the switching properties of 4Br2MA:35DNBA crystals isolated from antisolvent methods is continued in Section 5.3.4.

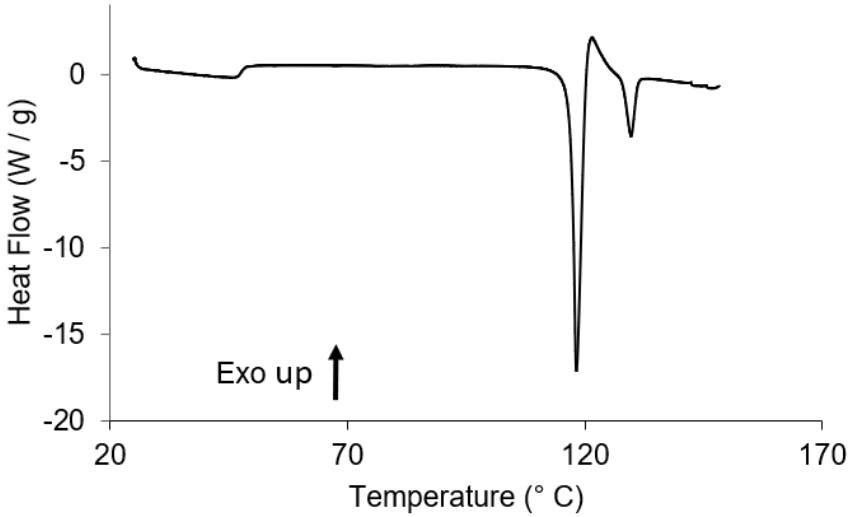

Figure 5-24: DSC of TC3.4, showing a melt and recrystallisation event at 117.5 °C followed by a second melting point at 129.8 °C

To summarise the work, segmented flow crystallisation was used to successfully produce the metastable **Cc2** *in situ* using antisolvent crystallisation methods. However, isolation of **Cc2** using traditional filtration techniques often led to the irreversible switching of **Cc2** to the non-thermochromic, stable **Cc1** form. Attempts were made to successfully isolate the product but the sensitivity of **Cc2** meant that the best method was to allow the sample to slowly evaporate after collection. This in turn was shown in TC3 to influence the thermochromic behaviour of 4Br2MA:35DNBA crystals and shifted the onset temperature for the colour change. Furthermore in TC3.4, the thermochromic phase transition was shown to occur via both a SCSC phase transition and via a melt-recrystallisation phase transition. In a broader context, the design of the small jacketed segmented flow crystalliser could facilitate rapid screening of temperature controlled antisolvent, flow crystallisations. Its application in non-ambient crystallisation experiments should be considered for other systems such as pharmaceuticals in future work.

5.3.4 Switching Properties of Isolated Multi-component Crystals

Jones *et al.* noted that block crystals of **Cc2** from slow evaporation will readily switch to **Cc1** and the transition can be facilitated by temperature. HSM was used to determine if similar behaviour is seen in the crystal from antisolvent crystallisation. This was confirmed to be the case for samples TC3.1 and TC3.4 isolated from flow crystallisation, however drying of the sample in TC3.4 led to a change in thermochromic phase

transition behaviour.

To investigate this further, batch antisolvent crystallisations were repeated using the same method described in Section 2.6.2; the results are shown in Table 5.8. However, the residual solvent following crystallisation was left to slowly evaporate, rather than extracting the precipitate via filtration, to better reflect the flow crystalliser sample conditions.

Table 5.8: Antisolvent crystallisation results at various temperatures

Experiment	Temperature (°C)	Complex[a]
TC4.1	20	**Cc2**
TC4.2	30	**Cc2**
TC4.3	40	**Cc2**
TC4.4	50	**Cc2**

a: Confirmation of neutral 4Br2MA:35DNBA form, **Cc2**, determined by PXRD. See Appendix Figure 9-30 for diffraction patterns

The samples were then subjected to DSC up to 150 °C and the resulting traces are shown in Figure 5-25.

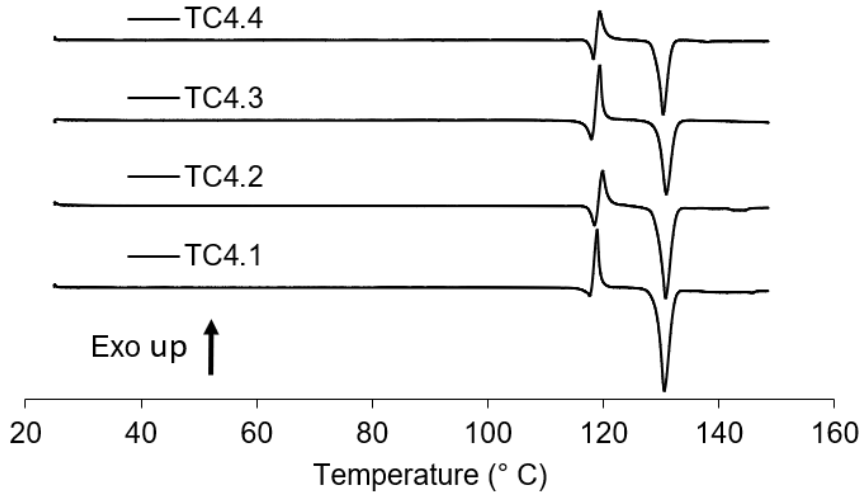

Figure 5-25: DSC traces for batch antisolvent crystallisation samples after drying

In all cases, the TCF4 samples show a clear melt-recrystallisation phase transition occurring at 118 °C, before the melting point at 130 °C. This is in agreement with TC3.4 (Figure 5-24) and in contrast to the sample reproduced from slow evaporation

(Figure 5-4), which did not show a melt-recrystallisation phase transition before the melting point. However, this does match the small transition at 117.9 °C in TC1.2 (Figure 5-11) during batch antisolvent crystallisation. Visual analysis of the phase transition was carried out using HSM however, the trend was less straightforward than the DSC traces. Figure 5-26 shows images from HSM analysis of TCF4.

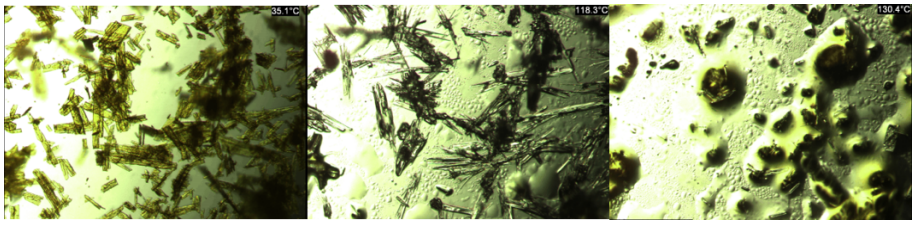

(a) TC4.1. Heated from 35 to 150 °C.

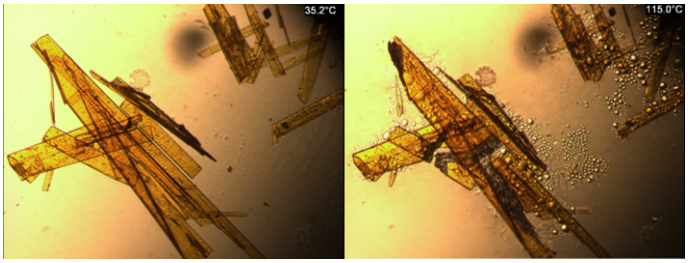

(b) TC4.2. Heated from 35 to 115 °C and held for 10 minutes before cooling.

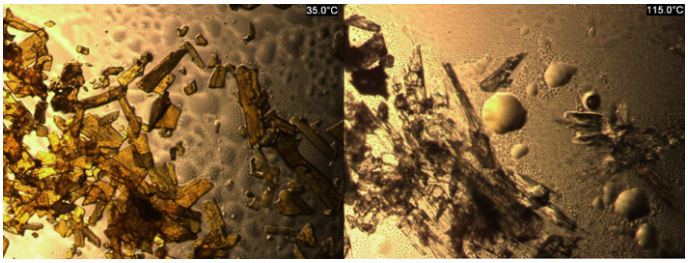

(c) TC4.3. Heated from 35 to 115 °C and held for 10 minutes before cooling.

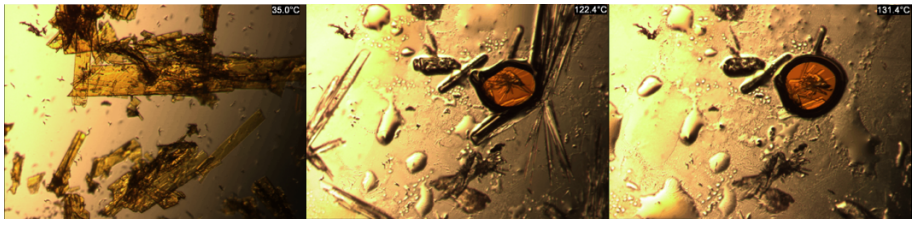

(d) TC4.4. Heated from 35 to 150 °C.

Figure 5-26: HSM images of TC4 thermal events. All samples were heated at 5 °C min^{-1}

For TC4.1 and TC4.4 the samples were heated from 35 to 150 °C. In both cases, a clear melt-recrystallisation transition occurred at 118.3 °C and 122.4 °C, respectively. This was followed by a full melt at 130.4 °C and 131.4 °C, respectively. In this case, the results reflected the thermal events observed in the TC4 DSC traces (Figure 5-25) very

well. For TC4.2 and TC4.3 HSM runs under the same conditions, different results were obtained. For TC4.2, the crystals began to decompose at 100 °C without recrystallising or melting, while TCF4.3 readily melted at 119 °C without recrystallising (Appendix Figure 9-31). Repeat analysis while holding at 115 °C (close to the transition point in the DSC) showed that both TC4.2 and TC4.3 could convert to the colourless form. However TC4.2 in particular, showed a resistance to change, only partially transitioning to the colourless form.

These observations from thermal analysis in combination with the behaviour difference seen in TC3.1 and TC3.4, suggested that the thermochromic phase transition may be influenced by macroscopic effects. Unlike TC3.1, samples from TC4 were allowed to dry similar to TC3.4. This resulted in the thermochromic transition occurring via a sharp melt-recrystallisation phase transformation, rather than a SCSC phase transition. As the major difference between TC3.1 and TC4 samples was the lack of moisture, H_2O may play a role in enabling the SCSC transition. To test the effects of solvent on the thermochromic phase transition in **Cc2**, a sample of TC4.2 was subjected to HSM after the addition of 20 µl of water. Images of thermal events in the HSM can be seen in Figure 5-27. The results show that a loss of colour via a SCSC transition in response to temperature from 72.0 to 80.5 °C. Furthermore, no visible melt-recrystallisation transition occurs at 118 °C in this case. This would indicate that the SCSC phase transition behaviour is enabled by the presence of water.

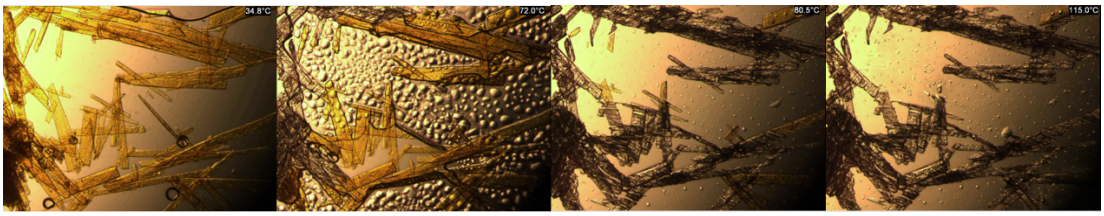

Figure 5-27: HSM images of TC4.2 thermochromic behaviour in the presence of water. Heated from 35 to 115 °C and held at 115 °C for 10 minutes.

In a further study, the HSM experiment was repeated with a sample of 4I2MA:35DN-BA, **Cc5** from TC1.8, which had previously shown a melt-recrystallisation event at 90 to 105 °C in thermal measurements (see Section 5.2.2 for full details). As with TC4.2, TC1.8 was subjected to 20 µl of water on a glass slide before heating. Figure 5-28 shows the thermal events observed on heating to 150 °C. As with TC4.2, TC1.8 shows that a SCSC phase change replaces the melt-recrystallisation transition. However, **Cc5** begins to transform slowly to colourless crystals even before the sample is actively heated, which reflects its lower stability compared to **Cc2**. In contrast to **Cc4** in literature,

which shows the thermochromic transition occurring from 45 to 65 °C, TC1.8 loses colour from 32.0 to 50.8 °C. Similar to **Cc4** however, is that the sample loses its colour as a wave, spreading from the highlighted area in Figure 5-28. This extends across the crystals at the physical point where they make contact. The sample then melts at 120 °C, similar to previous 4I2MA:35DNBA complexes. A link to the HSM videos discussed here can be found in the Appendix Section 9.3.

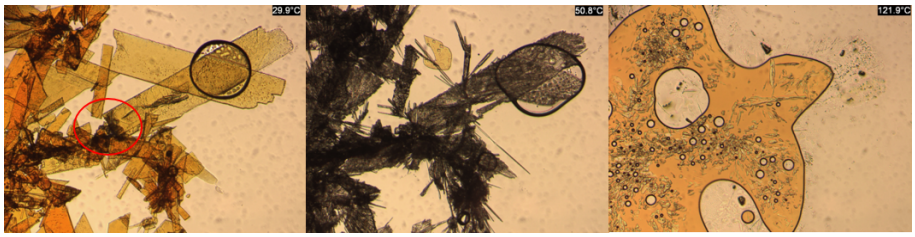

Figure 5-28: HSM images of TC1.8 thermochromic behaviour in the presence of water. Heated from 32 to 150 °C at 5 °C min^{-1}

The role of solvent in the thermochromism displayed by TC1.8 and TC4.2 is not well understood and significant further investigation is required. The results would suggest that the presence of moisture in the macroscopic domain facilitates SCSC phase transitions and lowers the transition temperature. Potentially, this could lead to 4Br-2MA:35DNBA or 4I2MA:35DNBA cocrystals whose thermochromic behaviour is 'dormant' at temperatures below 100 °C, until switched 'on' by moisture. This could lead to wider utility in their potential as switchable materials or humidity sensors, although effectively extracting the metastable chromatic crystals of **Cc2** and **Cc5** remains a considerable challenge.

5.4 Chapter Conclusions

In this chapter, the experimental investigation concerned the production of two halogenated multi-component cocrystal systems, 4Br2MA:35DNBA and 4I2MA:35DNBA, which displayed thermochromic properties in previous sample from slow evaporative crystallisation experiments. The aim of the work was to transfer the slow evaporation method to a more consistent and scalable crystallisation technique, in particular, the transfer from a batch process into a flow crystallisation platform would be desirable in terms of production and product consistency.

Initial work concentrated on replicating the cocrystal systems **Cc1** and **Cc2** (4Br2MA:35DNBA) and **Cc3** and **Cc4** (4I2MA:35DNBA) by replicating the batch evaporative methods used in their initial isolation. However, while the technique did produce the

multi-component complexes, the results were inconsistent in reproducing the desirable metastable **Cc2** and **Cc4** forms. Investigations extended to transferring the current evaporative crystallisation to a more reproducible method. In pursuit of this, it was found that H_2O was an effective antisolvent for producing the metastable cocrystal of 4Br2MA:35DNBA, however some difficulty was encountered in isolating the desired form. It was found that temperature controlled antisolvent methods were most effective in batch for isolating the orange 4Br2MA:35DNBA cocrystal. In pursuit of the metastable form of 4I2MA:35DNBA (**Cc4**), antisolvent crystallisation in MeOH produced a new polymorphic form (**Cc5**) which was isolated and characterised using thermal and X-ray diffraction methods. However its particularly low stability made it undesirable for transference into a flow crystallisation process at this stage.

For 4Br2MA:35DNBA, the batch antisolvent method was transferred to a temperature controlled segmented flow crystalliser platform which showed partial success in stabilising the form. Initial crystallisation produced the desired **Cc2** complex *in situ*, but the crystals were often seeded by **Cc1** encrustation within the end-piece or Y-piece. However, careful collection of the precipitate and evaporation of the solvent allowed isolation and characterisation of the orange coloured crystals. Results showed that isolated crystals from flow matched the **Cc2** crystal isolated from slow evaporation. While the flow crystallisation approach is significantly more robust and scalable than the initial evaporative method employed, the difficulty with isolating **Cc2** effectively provides a bottleneck in the work-up procedure. Considerable work in understanding the switchable behaviour of the neutral cocrystal, particularly on effective isolation, is required. A possible understanding may lie in the relationship between the effect of solvent on the thermochromic phase transition in the crystal structure. Results from thermal analysis of the dry cocrystal and the wet cocrystal of 4Br2MA:35DNBA, **Cc2** and 4I2MA:35DNBA **Cc5** indicates that the SCSC thermochromic phase transition first chracterised by Jones *et al.* may be facilitated by the presence of moisture, perhaps at the particle domain scale. In the absence of moisture, a melt-recrystallisation event is observed. The mechanism for this behaviour is beyond the scope of this work, but thermochromism that is mediated by moisture has been previously observed in polymeric films and inorganic structures.[106,208,209]

In terms of the crystallisation process, an antisolvent segmented flow crystallisation was successful in producing the 4Br2MA:35DNBA cocrystal form *in situ*. The temperature controlled segmented flow crystalliser, analogous to the KRAIC, was developed to facilitate antisolvent crystallisation under variable temperatures. The platform could be developed further and applied to other crystallisation processes to produce desirable

kinetic or metastable polymorphs that require careful temperature control. While integration with upstream processing was not attempted within this body of work, the segmented flow platform was developed from a holistic mindset and has the potential to be incorporated in a wider continuous manufacturing (CM) framework. Therefore, future work should consider the application of a small, high throughput, temperature controlled segmented flow crystalliser for cooling or antisolvent crystallisation processes which can be integrated with upstream flow technologies.

Chapter 6

Continuous Salt Crystallisation

6.1 Introduction

The work carried out in this chapter constitutes a three month placement at the AstraZeneca (AZ) Research and Development Department, Macclesfield, UK. The project was conducted under the supervision of Dr. Amy Robertson and Dr. Anna Jawor-Baczynska with the help of the Right Particle Team. The project aimed to evaluate the potential of continuous crystallisation for a commercially relevant active pharmaceutical ingredient (API). In particular, the process was under consideration for implementation of an integrated manufacturing process. The work in this chapter will describe the development and evaluation of the continuous crystallisation process of an API salt within this context. In order to protect the identity of the API no structural data can be given of the product. Instead, this chapter will concentrate on the process and possible benefits of working within a continuous framework.

The aim of the project is to investigate how effective a continuous crystallisation process would be at producing a commercially relevant API salt. The work was to demonstrate a continuous procedure for production of the salt form, without incurring any detriment to the desired physical properties. Therefore the design of the crystallisation processes needed to achieve physical characteristics of consistent, high quality which were within the acceptable production parameters. However, preserving crystal quality and key physical attributes when transferring from a batch to a continuous process is a challenging task.

Evaluation of the process was to be carried out by comparing a sample taken from the current batch process with that of a sample taken from the continuous crystallisation procedure. The merits of the continuous crystallisation process would be evaluated with respect to current manufacturing procedure. Optimisation of a process for production of an API is important step in meeting critical quality attributes (CQA) as well as for process efficiency. In particular, crystallisation of the API is important in ensuring the efficiency of downstream processing. For example, a wide particle size distribution may slow the filtration and drying procedure which can significantly impact the total time required for the manufacturing process.[91]

6.2 Background

During this work, two distinct approaches were carried out to produce the API salt. Initial investigations focused on using high throughput mixing in a tubular crystallisation procedure. The second approach involved the operation of continuous stirred

tank reactors (CSTRs) in periodic steady state operation. Tubular, high throughput crystallisers benefit from very high mass and heat transfer and can have a marked influence on the particle size, polymorphic behaviour and morphology of a crystallisation while also offering some of the highest process efficiency. In periodic steady state operation of a CSTR, addition and removal of suspensions is carried out at a high flow rate over short periods of time, rather than continuously. By using high slurry velocities in the transfer lines, problems such as blocking and fouling experienced with continuous CSTR can be avoided. The use of periodic CSTR operation for crystallisation has been previously demonstrated for paracetamol and the cocrystal system, urea:barbituric acid.[112,123]

The crystallisation process under consideration at AZ is shown in Figure 6-1. The crystalline product is produced by a reactive crystallisation between the free base API and the acid coformer succinic acid (SA). Upon mixing, spontaneous formation of the salt product in solution occurs, which rapidly precipitates. For the purposes of this thesis, the resultant product will be referred to as succinate salt (SAB) (where 'B' represents the API component).

Figure 6-1: Reaction for the production of the succinate salt

In the batch production of SAB the process proceeds by adding the free base to SA suspended in acetone. Crystallisation readily occurs during charging of the second component. As a consequence, the mixing environment is constantly changing during crystallisation and this results in the formation of excessive fines and a wide particle size distribution. It was noted that the filtration of SAB is slow during the washing stage and proved to a bottleneck in the overall process. As such, an improved crystallisation process could potentially enhance efficiency and productivity of the API salt. In this context the effectiveness of the two different continuous crystallisation approaches will be evaluated, with particular attention paid to changes in the crystal size, shape, distribution and filtration properties as well as the applicability of each set-up to a scaled-up crystallisation process. Furthermore, the work was produced from a holistic viewpoint and aimed to ensure that the development of the continuous crystallisation process could be integrated within a wider continuous manufacturing framework.

6.3 Experimental

6.3.1 Solubility

Solubility measurements for the API salt SAB were carried out using the Technobis Crystal 16 apparatus. The Crystal 16 employs turbidity measurements to measure dissolution. Samples are subjected in parallel to a heating and cooling temperature programme. For each sample, a transmission vs time plot is generated and analysed in order to determine clear and cloud points. The clear point is defined as the point at which 100 % of light is transmitted. This is assumed to indicate complete particle dissolution.

In this work, 1.5 cm^3 glass vials of varying concentrations of SAB in acetone were prepared with stirrer bars. The samples were heated using the same temperature profile. The samples were heated from 25 to 55 °C, held at 55 °C for 10 minutes and then cooled to 0 °C. The heating and cooling rate was set to 0.1 °C min^{-1} and the stirring speed was kept at 700 rpm throughout the run. Data was processed using CrystalClear (v.1.0.0) software. The clear point for each concentration was measured and the corresponding temperature reading was used to construct a solubility vs temperature plot.

6.3.2 Tubular Mixer Crystallisation

Continuous crystallisation experiments using a mixer piece were carried out at the AstraZeneca site in Macclesfield. The set-up is outlined in Figure 6-2. Stages 1 and 2 consisted of 500 mL jacketed feed vessels and stage 3 was a 1 L jacketed holder vessel. Two Masterflex peristaltic pumps, equipped with Masterflex tubing (3.1 mm inner diameter (ID)) were used to transfer the acid and base solutions from the feed vessels (stage 1 and 2 respectively). The flow rate for each pump was calibrated using pure acetone and Masterflex tubing (3.1 mm ID). A pump calibration curve of pump increments vs time was used to set the desired flow rates in all experiments (see Appendix 9-32). The acid and base solutions were combined in a Y or cross piece (3.1 mm ID) where the components are rapidly mixed. The output was then transferred to the holding vessel (stage 3) for 20 minutes before collection, stirring at 300 rpm throughout the experiment. After this dwelling period, the contents of stage 3 are removed and the resultant slurry was filtered under vacuum to isolate the solid for analysis. One further acetone wash was applied to the residual solid in stage 3 and isolated using filtration under vacuum. The samples were allowed to dry overnight and the yield is calculated from the total solid isolated.

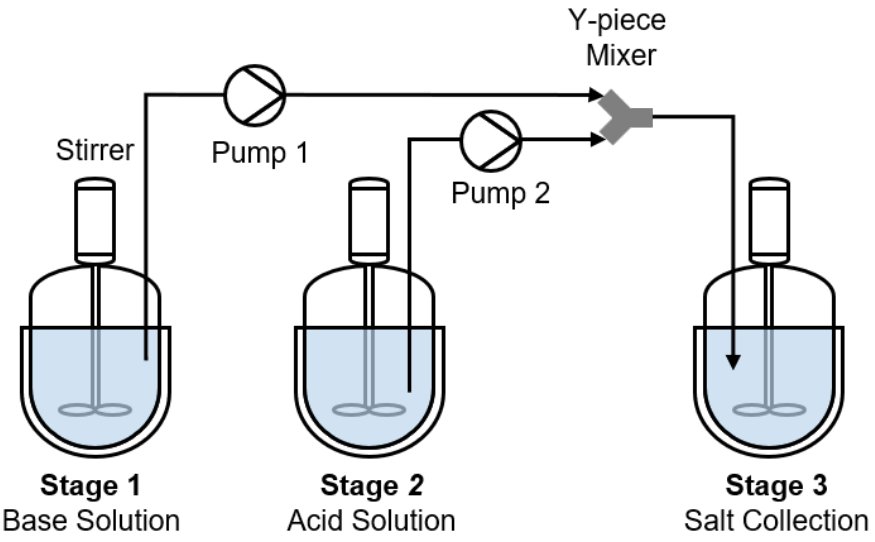

Figure 6-2: Schematic for the reactive crystallisation in a mixer piece

6.3.3 Continuous Stirred Tank Reactors

CSTR experiments were carried out using the system set-up at the AstraZeneca Research and Development site, Macclesfield (Figure 6-3 and Figure 6-3b). The periodic CSTR set-up consisted of two 500 mL jacketed feed vessels (stage 1 and stage 2) and two 160 mL jacketed CSTR vessels (stage 3 and 4). Each CSTR (stages 3 and 4) was operated at a working volume of 100 mL. Two Masterflex peristaltic pumps, equipped with Masterflex tubing (3.1 mm ID) were used to transfer the acid and base solutions from the feed vessels to the first CSTR (stage 3). Transfer between stages 3 and 4, as well as stage 4 and collection was facilitated by a controlled high vacuum system. The vacuum was applied manually at set intervals, by quickly opening and closing valves 2 (V2) and 3 (V3). Valve 1 (V1) was not used during these investigations. A dip tube was positioned between stages 3 and stage 4 as well as stages 4 and collection to allow the transfer of a calibrated volume (10 mL) of solution between vessels. The time between transfers was dictated by the residence time (RT) within each vessel. A total of ten transfers per CSTR per residence time were carried out. The temperature of each stage was controlled actively by three JULABO chiller units. One chiller was connected to stages 1 and 2 in tandem, while separate chillers were provided for stages 3 and 4. A thermocouple probe was installed in each vessel to maintain accurate temperature control.

A concentration of 10 w/w% base solution in acetone was prepared to 500 mL from a stock solution of 40 w/w%. A stoichiometric amount of the acid coformer was dissolved

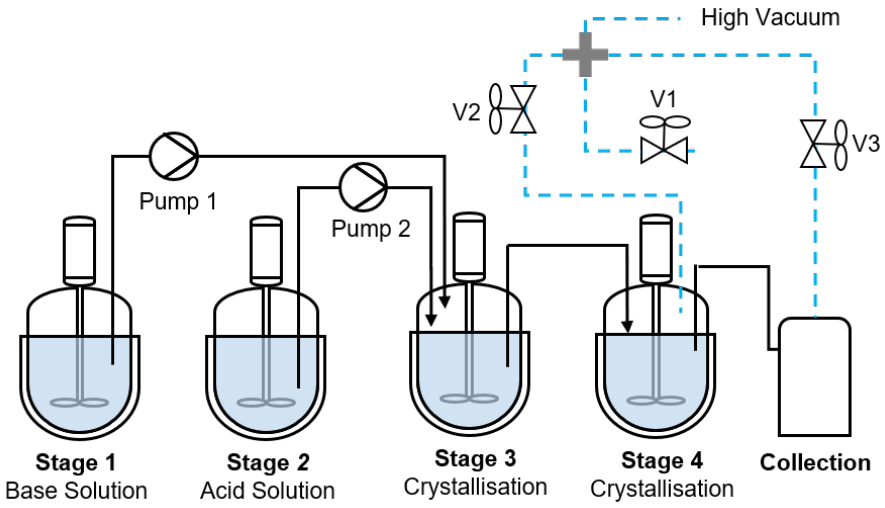

(a) Schematic for the reactive crystallisation in the CSTR system

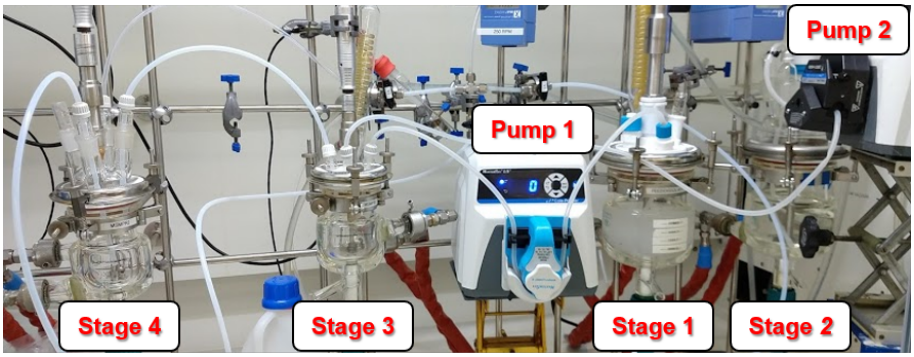

(b) Picture of the reactive crystallisation in the CSTR set-up

Figure 6-3: AstraZeneca periodic CSTR system

in 500 mL of acetone in stage 2. The temperature of both was actively controlled at a set stirring rate. Where seeds of the salt form were used, these were suspended in stage 1. Once equilibrated, each solution was pumped through the peristaltic pumps at a specified flow rate into stage 3. Once the volume of stage 3 reached 100 mL, V2 was opened and closed to transfer 10 mL of slurry to stage 4. This was repeated periodically until stage 4 reached the specified volume of a 100 mL. At this point, V2 and V3 are opened in tandem for the rest of the experiment. At the end of the experiment, the contents of stages 3, 4 and the collection vessel are combined and removed. The slurry is then filtered using vacuum filtration to isolate the solid for analysis. An acetone wash is applied in stages 3 and 4 to remove any residual solid in the system, a second filtration is applied and a total yield calculated for each run. The start-up calculations and operational parameters for the CSTR set-up are summarised in Table 6.1.

Table 6.1: Operating parameters and start-up calculations for the CSTR platform with a RT of 20 minutes

Operating Parameters					Start-up Calculations				
Vessel	V_{Max} (mL)	V_{Min} (mL)	Operating Volume (mL)	Flow Rate ($mL\,min^{-1}$)	Residence Time (min:sec)	Initial Pump Volume (mL)	Start-up Time (min)	Transfer Volume (mL)	Transfers per RT
Base Feed	500	200	500	5	100:00	-	-	-	-
Acid Feed	500	200	500	5	100:00	-	-	-	-
Stage 3	160	80	100	10	10:00	90.0	9:00	10	10
Stage 4	160	80	100	10	10:00	90.0	9:00	10	10

6.3.4 Particle Analysis

Particle Size

A method was devised for particle size analysis using a Malvern Mastersizer 3000 equipped with an Aero S dry powder dispersion. Dispersion of the powder is achieved by accelerating particles using compressed air. The particles are then pulled through to the Mastersizer 3000's laser diffraction chamber (using a vacuum source) for measurement. Sample feed rate is set using a vibrating feeder, which maintains a desired sample concentration. In experiments discussed below, the sample was first subjected to a molecular sieve with a 1 mm grid, in order to reject any large clumps of solid. Of the fine powder obtained, a small amount of sample was then transported to the Aero S feed tray. A method was developed using the Malvern Mastersizer software, the feed rate for all samples was set to 25 or 50, while the compressed air was applied at 2 or 3 bar. All samples were run in triplicate and the percentile particle size distribution values (Dv(10), Dv(50) and Dv(90)) are calculated from the average of these repeats.

SEM

High resolution scanning electron microscopy (SEM) images were collected using a Hitachi TM-1000 scanning electron microscope operating with an accelerating voltage of 15 kV. A small amount of sample was mounted onto an aluminium stub using a sticky carbon tab. The samples were coated with gold using a Quorum Q150R sputterer to a target thickness of 10 nm.

6.3.5 Filtration

Filtration times were analysed during collection. The following procedure was used to compare results. A 1 L Büchner flask with a 9 cm diameter filter area was equipped with a Whatman^{TM} filter paper. All filtrations were performed under a reduced pressure of approximately 0.7 bar. The filter paper was initially wet with a few drops of acetone to adhere the filter paper to the funnel. The slurry was then poured while shaking continuously to avoid settling, onto the filtration unit. Once there was enough slurry on the paper, the vacuum and a timer were started simultaneously. The filtration time (t) was recorded as the time taken for the filtrate to go below the cake surface. The total volume of the effluent (V) was measured with a 1 L graduated measuring cylinder. The weight of the solid extracted was measured after drying overnight.

Filtration analysis was carried out with the help of Dr. Claire MacLeod and Dr. Clare Mayes. The cake resistance (α) was calculated by simplifying the modified Darcy's

equation as shown in Equation 6.1.[210]

$$t = \frac{\mu C \alpha}{2A^2 \Delta P} V^2 + \frac{\mu R}{A \Delta P} V \tag{6.1}$$

The second component concerns the behaviour of the filter paper; as the resistance of the filter paper will be much smaller than the cake, this component can be ignored for simplicity. The equation can therefore be simplified to:

$$t = \frac{\mu C \alpha}{2A^2 \Delta P} V^2 \tag{6.2}$$

Where P is the pressure (Pa), μ the viscosity (Pa s), C is the mass fraction (kg m^3), V is the volume (m^3), A is the area of the filter (m^2) and t is time (seconds). In this comparison, the cake is assumed to be incompressible.

6.3.6 Thermal Analysis

Thermal analysis was investigated using a Thermal Advantage DSC Discovery instrument. Between 1.0 and 8.0 mg of sample was weighed into a Tzero aluminium pan. Samples were sealed by crimping an aluminium lid before being transferred to the autosampler. The heating and cooling profile was programmed and interpreted using the TRIOS Software (v4.2.1) under a stream of nitrogen gas.

Thermal gravimetric analysis (TGA) was investigated using a Thermal Advantage TGA Discovery instrument. Between 1.0 to 5.0 mg of sample was weighed into a TGA platinum 100 µL pan. Samples were loaded onto an autosampler for measurement. The pan was transferred to the furnace chamber and subjected to a heating profile programmed on using TRIOS software (v4.2.1) under an inert nitrogen atmosphere.

6.3.7 Process Analytical Technology

In situ measurements of the particle size and crystallisation induction time were monitored using process analytical technology (PAT), with the help of Dr. Anna Jawor-Baczynska, Dr. Lauren Agnew and Dr. Andre Powell at the AstraZeneca Research and Development site, Macclesfield.

Raman Spectroscopy

The method and data processing of Raman measurements was carried out by Dr. Andre Powell. A Raman (RXN1, Kaiser Optical Inc. series) immersion probe was

used to implement *in situ* steady state measurements and crystallisation induction times of SAB. Before the experiment, the laser was calibrated with a sample of SAB, succinic acid, acetone and free base solution. The spectra were compared and non-overlapping peaks were identified for measuring the SAB salt concentration. The probe was submerged in stage 3 CSTR and the crystallisation was monitored throughout the experiment between 804 and 1670 cm^{-1}. When fouling occurred, the probe was briefly removed from the CSTR and cleaned with ethanol before being re-submerged. Multivariate curve resolution was carried out in Matlab software to separate the pure components from the raw data. The output was plotted in Microsoft Excel.

Focused Beam Reflectance Measurements

The method and data processing of focused beam reflectance measurements (FBRMs) was carried out by Dr. Anna Jawor-Baczynska. A Mettler Toledo FBRM probe (S400 series) was mounted into stage 4 of the CSTR set-up. The probe was submerged below the solution suspension during the steady state experiment and particle size was tracked throughout the run. Data collection was carried out at a scan speed of $2\,m\,s^{-1}$. Data was interpreted using the Mettler Toledo iC FBRM V4.4 software and plotted in Microsoft Excel.

6.4 Results and Discussion

6.4.1 Solubility of the Salts

As SA is readily used in salt crystallisation experiments, its behaviour in a variety of solvents is well known. The solubility of SA in acetone from literature is shown in Figure 6-4.[211] As can be seen from the graph, SA has a relatively high solubility in acetone. At 20 °C SA is expected to dissolve up to $25\,mg\,mL^{-1}$. The equation generated from the solubility curve was used in later crystallisation experiments to prepare the SA concentration. This was to ensure that the acid coformer remained fully dissolved in the feed vessels and prevented precipitation in the feed line, which might lead to blockages in the peristaltic pump. The solubility of SAB was investigated using the Crystal 16 technology as outlined in Section 6.3.1. From the turbidity measurements taken, a solubility plot was generated. The results are depicted in Figure 6-5. The curve indicates that the solubility of SAB would double for every 10 °C rise in temperature. However, while SAB shows a high temperature dependence on solubility, it shows a very low overall solubility in acetone. The solubility curve indicates that even at 55 °C, less than $10\,mg\,mL^{-1}$ would be expected to dissolve.

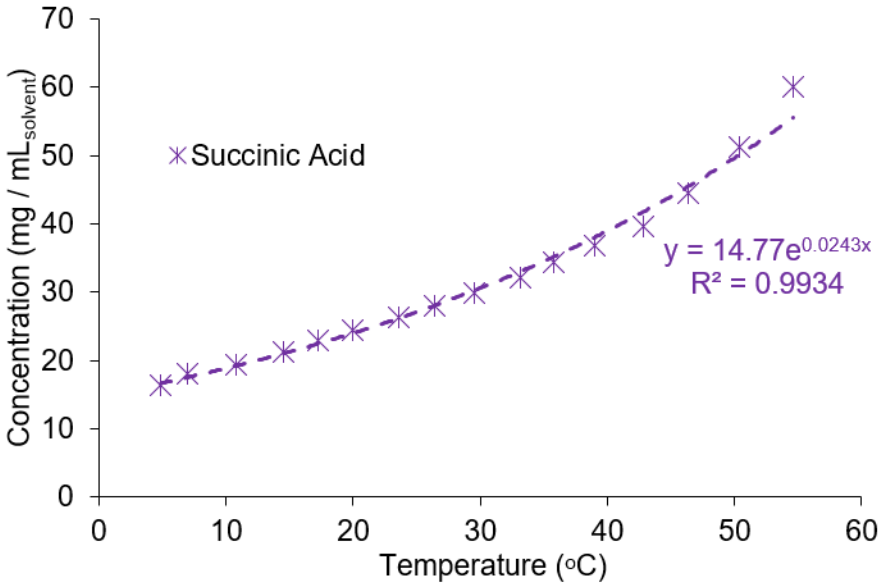

Figure 6-4: Solubility of the coformer succinic acid in acetone, values calculated from literature[211]

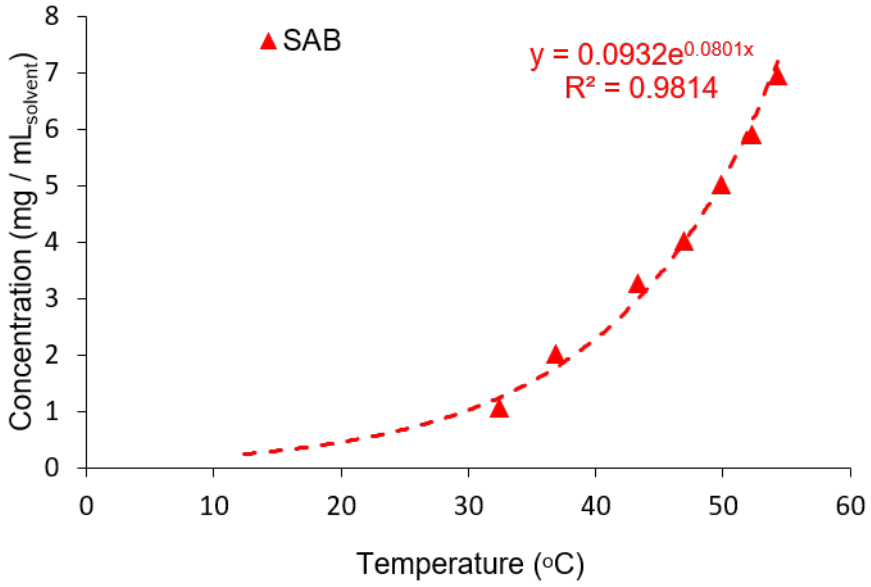

Figure 6-5: Solubility diagram of the SAB determined by turbidity measurements in the Crystal 16

Based on these results, it is clear that the solubility of the corresponding acid coformer is at least an order of magnitude higher than the salt form. As the free base API is also freely soluble in acetone, a relatively high concentration of the acid and base can be dissolved as a feed solution. In the context of moving production into a flow

environment, the reactive crystallisation will proceed readily when mixing the acid and base streams together. While mixing will cause some dilution of the resulting product concentration, the low solubility of the salt in comparison to the individual components will ensure there is a considerable drive towards precipitation within the expected working parameter range. Furthermore, the low solubility of the salt would be expected to minimise loss to the liquor. Flow crystallisation experiments in this work were developed to maintain undersaturation with respect to the acid and base components while ensuring a supersaturated environment for salt formation to drive precipitation.

6.4.2 Tubular Mixer Crystallisation

Initial experiments aimed to evaluate the effect of mixing on the crystallisation of SAB. A simple crystallisation platform was developed to perform the reactive crystallisation in flow. The set-up is outlined in Figure 6-2 and described in Section 6.3.2. The operating parameters for the mixer piece crystallisation runs are outlined in Table 6.2 and the experimental conditions and outputs are summarised in Table 6.3.

Table 6.2: Operating parameters for the mixer piece crystallisation and batch reference sample of SAB

Experiment	Method	Base Concentration (w/w%)	Base Flow Rate ($mL\,min^{-1}$)	Acid Flow Rate ($mL\,min^{-1}$)
Reference	Batch	40:60	-	-
AZ1	Low Flow Rate	20:80	9.89	19.87
AZ2	Low Flow Rate	10:90	20.33	19.89
AZ3	High Flow Rate	10:90	99.99	99.50

The concentration of SA was adjusted in each case so that at the point of mixing, regardless of flow rate, a 1:2 (Acid:Base) molar ratio was maintained

Table 6.3: Experimental conditions and outputs for continuous mixer experiments

Experiment	Feed Temperature[a] (°C)	Mixer Type[b]	Stage 3 (°C)	Run Time (min:sec)	Yield (%)	Relative Supersaturation[c]
AZ1	25	Cross	0	n/a	Blocked	155
AZ2	40	Y-Piece	0	8:00	86	23
AZ3	40	Y-Piece	0	3:00	86	23

a) Feed temperature refers to both Stage 1 and 2 in Figure 6-2 b) No active temperature control was applied to the mixer piece c) Relative supersaturation (σ), assuming the feed temperature remained unchanged at point of mixing

Platform Development

In comparison to a batch process, mixer pieces reduce the required time to homogenise a mixture. In the case of rapid crystallisation procedures, inefficient mixing can lead to a wide particle size range, which in turn can lead to problems with downstream processing.[212] In the batch production of SAB the process proceeds by charging the free base into a vessel of SA suspended in acetone. Crystallisation proceeds readily during addition of the base. During addition, the concentration and mixing environment is constantly changing, this results in a wide particle size distribution. As a result the filtration of SAB is slow, limiting the speed of the overall process. By combining the acid and base feeds simultaneously in a mixer piece, the consistency of the mixing environment and the concentration of the components would be maintained throughout the process. This could potentially improve the quality of the product.

The first attempt at crystallisation in flow (AZ1), used a cross piece for the mixing of the feeds (Figure 6-6). In this case, the acid feed was split and applied perpendicular to the base feed. The flow rate of the acid was applied at twice the feed rate of the base to ensure that at the cross piece, all flow rates would be the same. While the batch process uses a 40:60 w/w% free base:acetone solution, the equivalent amount of SA required to crystallise SAB exceeds the solubility of SA in acetone at 25 °C. As the feed lines from stages 1 and 2 cannot be actively heated, it was deemed necessary to dilute the stock base solution to half the concentration. This way, stoichiometric amounts of SA required should remain fully dissolved at room temperature. This prevented unwanted encrustation and blockages in the feed lines.

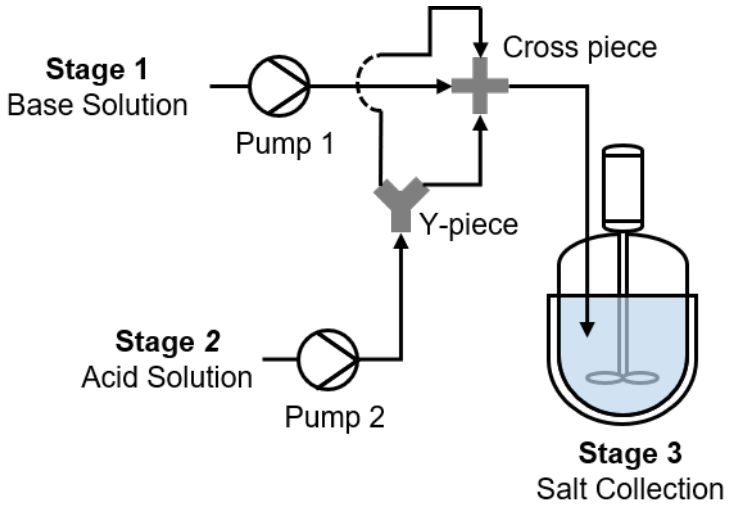

Figure 6-6: Schematic for the continuous reactive crystallisation using a cross piece

Unfortunately despite these precautions, the system almost immediately blocked upon combining the acid and base solutions in the cross piece. Formation of the salt was exceedingly rapid and blocked the mixer piece within a minute. While some sample could be isolated for analysis, the run could not continue and an accurate yield was not calculated. The rapid nucleation was the result of a high relative supersaturation. Using the equation from Figure 6-5 the saturation of SAB at room temperature is $0.69\,\mathrm{mg\,mL^{-1}}$. Using this value and by calculating the expected concentration of SAB after mixing, the relative supersaturation ratio (σ) of SAB was approximately 155, assuming the cross piece was at the same temperature as the feed (20 °C). This provides a huge drive towards precipitation, which leads to encrustation in the tubing before reaching the holding vessel (stage 3). It was also noted that splitting of the acid solution before the cross piece did not result in equal flow rates perpendicular to the base solution when reaching the cross piece. This was likely due to gravity and the positioning of the cross piece, which created one easier pathway for the fluid to travel along. While this could be overcome by careful design (introduction of a back pressure regulator (BPR)) or control of the flow rates and positioning of the cross piece, it would be difficult to accurately control. This would create unwanted inconsistencies in repeated runs.

In AZ2 and AZ3 the design was simplified to eliminate the cross piece, instead the feeds would be combined in a Y-piece mixer. The set-up is depicted in the experimental, Figure 6-2. To try to avoid immediate blockages, the concentration of the free base was reduced to 10:90 w/w% in acetone and equivalent molar amounts of SA were prepared in solution. The temperature of the feed vessels was raised to 40 °C to reduce relative supersaturation. While no active temperature control was applied to the Y-piece or tubing, the flow rates were likely sufficient to ensure the solution remained above room temperature upon mixing. The even addition of the flow rates in the Y-piece also aimed to improve consistency and help prevent back-mixing in the union which lead to crystal build-up in AZ1.

With these changes to the parameters, AZ2 was successful in running continuously until feed depletion. The slurry was held at 0 °C for 20 minutes to maximise crystallisation and solid recovery before filtration. The product was isolated with a total calculated yield of 86%. The yield is relatively good and based on the low solubility of SAB in acetone, the residual solid could be recovered with repeated washings. While the production of the process was improved significantly, a large amount of crystalline material was visible around the outlet of the tubing and within the transfer line from the mixer piece to holding vessel (Figure 6-7).

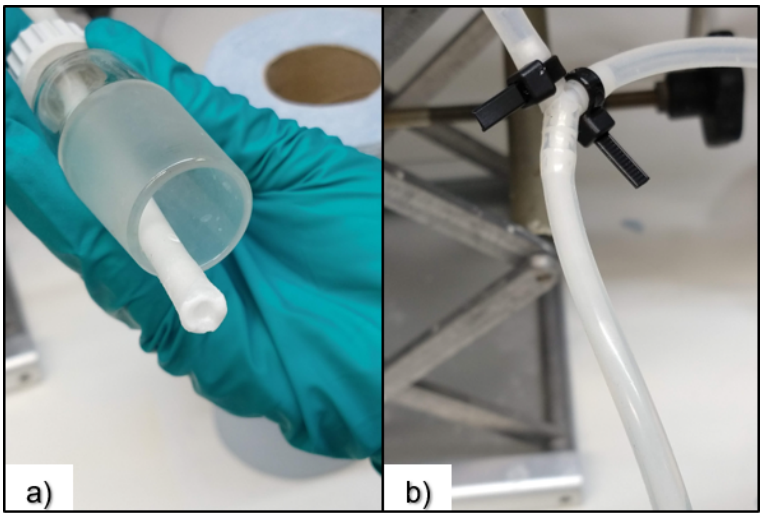

Figure 6-7: Photographs of crystal build-up around Y-piece and tubing outlet in AZ2

In order to try to improve the mixing and reduce encrustation further, AZ3 was run under the same parameters but at five times the overall flow rate. The experiment aimed to determine if turbulent mixing and high throughput could reduce particle size distribution and help to prevent encrustation in-line. Using the literature values for the dynamic viscosity and density of acetone, along with the experimental flow rate and mixer piece ID an approximate Reynolds number (Re) was determined for AZ1 to AZ3 using Equation 1.2. The calculated values for Re are depicted in Table 6.4.

Table 6.4: Approximate Reynold Numbers for AZ1, AZ2 and AZ3

Experiment	Re	Mixing
AZ1	509	Laminar
AZ2	688	Laminar
AZ3	3414	Transitional/Turbulent

Calculated from the combined flow rates in Table 6.2 using the dynamic viscosity and density of acetone at 25 °C

Based on these values, AZ1 and AZ2 would show a laminar mixing regime, while AZ3 would show transitional/turbulent mixing. As anticipated, the increased flow rates helped to reduce encrustation in the transfer line. Observations showed that unlike in previous runs, the internal diameter of the tubing remained clear and unobstructed, with the exception of some encrustation around the tubing outlet. However, the feed solution was depleted in only three minutes. These observation indicated that while production of the salt was possible in a continuous mixer platform, very high flow rates would be required to avoid blockages, which may not be applicable with larger scale

production. Furthermore, copious amounts of material would be required to run the system for an extended period to determine if encrustation would build-up significantly. As with AZ2, the slurry in AZ3 was held in stage 3 at 0 °C for 20 minutes before extraction. The total solid recovery was 86% which suggests that a high throughput can be maintained with the same overall yield. The high solid recovery, regardless of the flow rate, may be a consequence of the long holding time in stage 3, relative to the run time. Potentially, a larger difference in yield might be exhibited if after mixing the combined feed was directly filtered.

Crystal Morphology

Analysis of the crystal morphology in AZ1, AZ2 and AZ3 was carried out using SEM. A comparison is made with a sample supplied by AZ of SAB taken from the batch process. The images are shown in Figure 6-8.

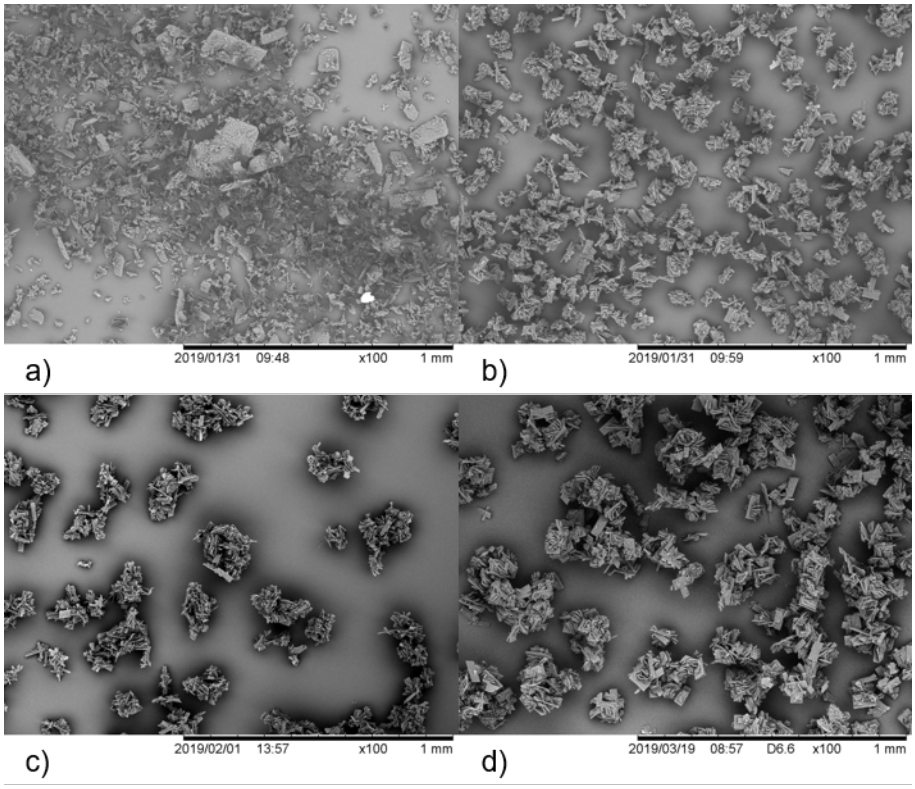

Figure 6-8: SEM images of SAB in a) Batch b) AZ1 c) AZ2 d) AZ3 after isolation at x100 magnification

As can be seen by comparing the batch and continuous samples, there is a clear change in morphology. The batch process consists of a series of platelets, with the largest

appearing to be over 300 µm in length. In contrast, samples isolated from AZ1 to AZ3 appear to show a spherical shape, around 100 µm in diameter. The size varies, but the general trend appears to indicate that AZ1 is smaller than AZ2 and AZ3, while AZ2 and AZ3 appear similar in size. Closer inspection of the spherical structures is shown in Figure 6-9.

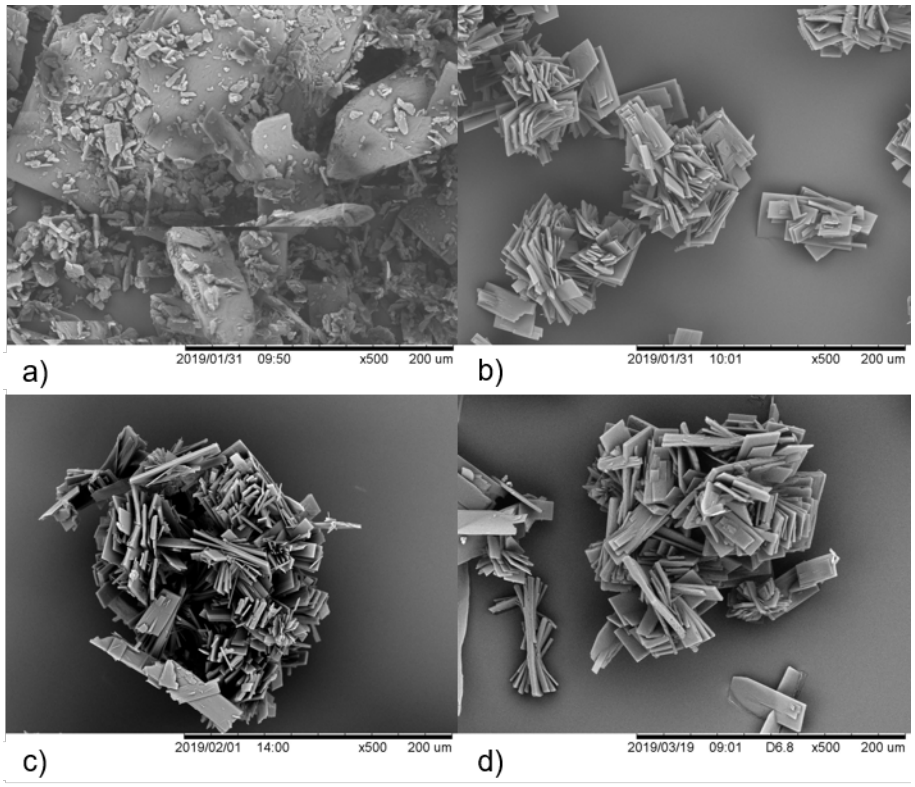

Figure 6-9: SEM images of SAB in a) Batch b) AZ1 c) AZ2 d) AZ3 after isolation at x500 magnification

As can be seen, the particles isolated from the mixer process appear to consist of agglomerates. Individual platelets can be identified within the agglomerate spheres and in general, it appears that the spherical structures consist of an assembly of crystalline platelets. From a visual perspective the individual platelets within these agglomerates show a similar morphology to the batch sample of SAB, which indicates the same crystalline form may be present. The structure of the agglomerates, along with the high supersaturation ratios during crystallisation, suggests that the change in structure compared to the batch sample may be a consequence of rapid crystallisation. Interestingly, the amount of visible fines is far lower in the continuous process than in the batch reference. In general, agglomerates are usually undesirable as the formation of agglomerates can trap solvent and other impurities within the structure, which can

compromise the purity of the dried product.[213] However, in some cases the formation of regular agglomerates can be advantageous, as these structures can display improved filtration properties compared to fines and needles, which increases the efficiency of the downstream operations. Inspection of the surface of each sample gives further indication of the low number of fines present compared to batch (Figure 6-10).

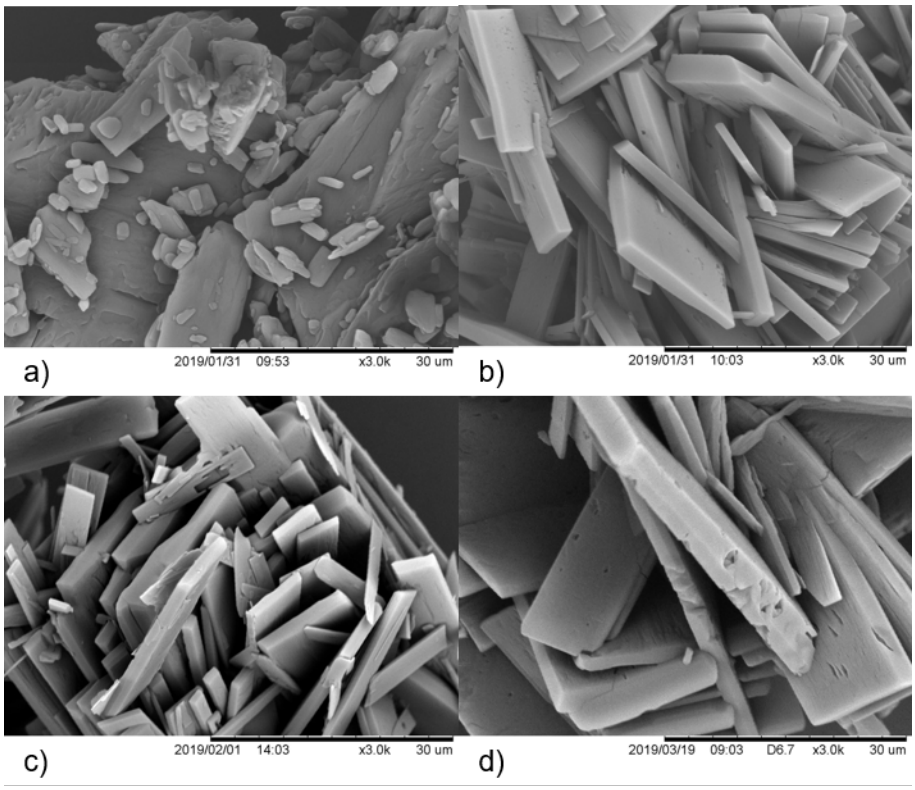

Figure 6-10: SEM images of SAB in a) Batch b) AZ1 c) AZ2 d) AZ3 after isolation at x3000 magnification

Many of the surfaces of the larger particles in the batch sample are littered with small, ill-defined particles. In contrast, the particles within the isolated agglomerates appear better defined and while some smaller fine particles can be seen within the agglomerate structure, they appear more clearly as plate-like structures. The surfaces and edges of the batch samples appear rougher and more coarse than the smoother surfaces visible in the continuous crystallisation samples. While it is difficult to discern the exact cause of the lack of agglomerates in the batch process without a fuller understanding of the procedure, the changes in size and shape in the continuous crystallisation can be attributed to the changes in the protocol. As the batch process is known to require long filtration times with agitation, this could potentially lead to breaking of the particles, which in turn leads to the rough surfaces observed. Without an extensive study of

the crystalline material before and after filtration, it is difficult to determine what influence the filtration step has on changes to the crystal shape in batch. However, the large ranges in plate sizes and non-uniformity of the particles in the batch sample do suggest that the supersaturation changes during crystallisation and is playing a role in crystal growth. The more consistent flow process produces a more uniform particle shape, albeit in the form of agglomerates. The agglomerates are likely formed as a consequence of the very high relative supersaturation levels.

Particle Size

Particle size analysis was carried out using the method described in Section 6.3.4. A dry method was used to quickly and reproducibly determine the sizes of the agglomerates to compare them to the batch particle size distribution (PSD). Initial observations indicated the sample had a tendency to clump together. This was observed as a peak in the PSD above 1000 µm which did not remain consistent during repeated scans of the same sample. Furthermore, SEM images indicated that agglomerate sizes did not exceed 1 mm. As such, the discrepancy was likely due to adherence of the solid sample during measurements. To avoid the anomaly, efforts were taken to eliminate the variable peak. A molecular sieve was used prior to measuring, to reject clumps larger than 1 mm. Measurements were taken in triplicate using a high feed rate and air pressure to separate the particles. Despite the precautions taken, the PSD should be taken as an approximation and general trend, rather than absolute values.

Example scans of the PSD of the batch, AZ1, AZ2 and AZ3 samples are shown in Figure 6-11. The batch sample shows a broad PSD typical of a sample with a range of crystal sizes. This corresponds well with the various sizes of plate-like crystals observed in the SEM images. The distribution is centred close to 10 µm which indicates a large number of fines present in the sample. In contrast, the continuous crystallisation samples show a bimodal distribution. The two peaks centre around 10 µm and 100 µm. Using the SEM images to interpret the data, it is likely the 100 µm peak represents the agglomerates. The smaller peak therefore corresponds to individual crystals broken off from the agglomerates or dispersed fines. Comparing the batch and continuous samples, in terms size range, the PSD of all samples taken from the continuous processes are within the scope of the batch reference. However, the samples produced continuously show a higher uniformity.

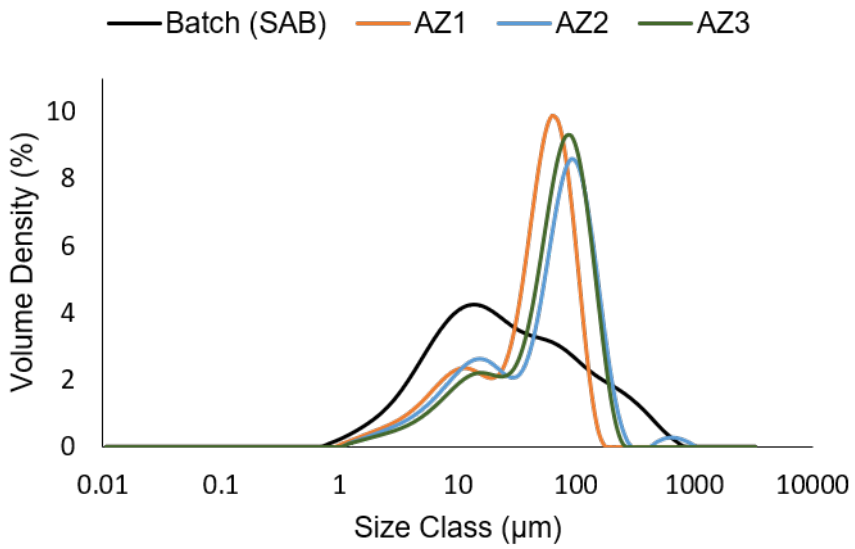

Figure 6-11: Particle size distribution in batch, AZ1, AZ2 and AZ3

The D-values (Dv(10), Dv(50) and Dv(90)) represent the intercepts in the size distribution at 10%, 50% and 90% of the cumulative volume density. For the batch and mixer samples, these are summarised in Table 6.5. The values quoted are calculated from the average and standard deviation of at least three repeats.

Table 6.5: Particle size distribution percentiles for samples of SAB taken from AZ1, AZ2, AZ3 and the batch reference

Experiment	Dv(10) (µm)	Dv(50) (µm)	Dv(90) (µm)
Batch	4.64 ± 0.26	25.0 ± 1.95	204 ± 21.0
AZ1	6.86 ± 1.00	47.8 ± 3.29	96.6 ± 1.62
AZ2	8.41 ± 0.13	70.2 ± 3.11	181 ± 32.7
AZ3	9.84 ± 0.14	65.5 ± 0.33	137 ± 1.1

D-values for the batch sample show a trend that favours the finer particles, as the Dv(50), or median value of the distribution is around 25 µm, while the Dv(90) value is close to 200 µm. The fact that the median value is relatively small compared to the Dv(90) value, is an indication of the broadness of the distribution, along with a favouring towards a smaller particle size. In the case of the flow samples, Dv(50) values are larger, with the cumulative volume lying more centrally compared to the Dv(90) value. Interestingly, AZ1 shows the smallest particles produced in flow. The values are significantly smaller than AZ2 and AZ3, this may reflect the difference in the mixer

type (cross piece vs mixer piece) or the difference in the supersaturation level upon salt formation. In terms of mixing, despite the difference in *Re* for AZ2 and AZ3, only a small change is observed in the Dv(50) value. However, the faster mixing in the AZ3 does provide a tighter distribution. As AZ1 particles were much smaller, it's likely that the type of mixer piece or the supersaturation level play a more significant role in the PSD than the flow rate under the current conditions.

Thermal Analysis

A comparison of the differential scanning calorimetry (DSC) and TGA traces for AZ3 and the reference sample of SAB can be seen in Figure 6-12. The scales are omitted in the interests of sample confidentially.

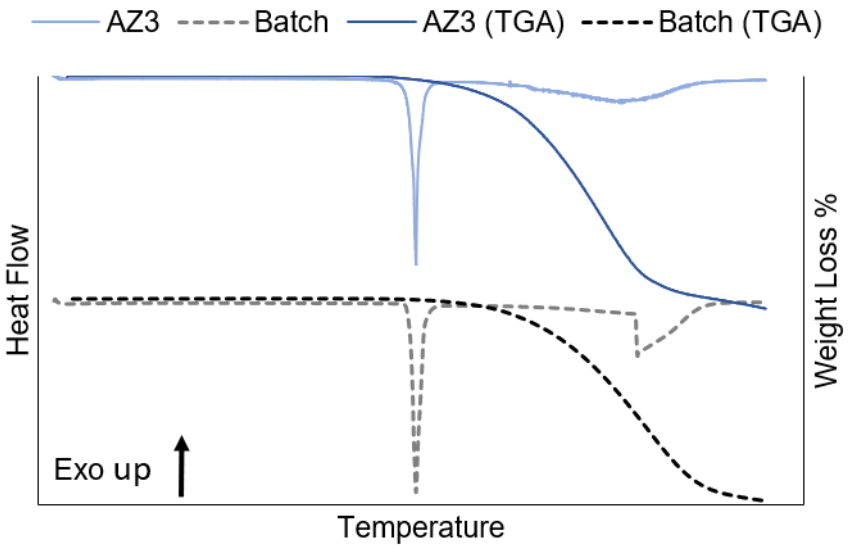

Figure 6-12: Comparison of DSC and TGA traces for AZ3 and the batch sample of SAB

The large peak in the DSC trace indicates the melting point of the salt. A good overlap is observed between the two samples produced in batch and flow. This is complemented by a similar change in the weight loss observed during the TGA trace. This provides confirmation that the product produced is the desired salt form and displays similar physical properties to the batch. A minor discrepancy is observed in the DSC trace of the batch sample above the melting point, corresponding to a sharp drop in heat flow and gradual return to the baseline. As this is not reflected in the TGA, it is likely a system error and can be ignored. A repeat would prbably remove the anomaly. The TGA also does not show any mass loss with respect to solvent trapped in the

agglomerates of AZ3. If this was the case, it would appear as a change in the mass loss trace that was not present in the batch sample. However, for the detection of very low concentrations of residual solvents, additional techniques would be needed to confirm the solvent/impurity level is within specification. TGA-mass spectrometry or high performance liquid chromatography (HPLC) would be effective ways to identify and compare the level of impurity retention in the agglomerate structures.[214]

Conclusions

In terms of platform development, the use of tubular mixing pieces allows consistent control over the mixing environment under high supersaturation concentrations. The process could be potentially integrated with upstream continuous manufacturing. For instance, the output from the free base synthesis could be directed into stage 1, with molar equivalents of SA prepared in stage 2. Downstream filtration could also be facilitated by automated and controlled withdrawing of the suspension from stage 3, either periodically or continuously. The use of a mixer piece allows rapid mixing of the acid and base solution which produces the desired SAB salt form. The solution crystallises with a high throughput forming a series of spherical agglomerates made from numerous well defined plate-like structures. The flow process results in a PSD that is significantly more uniform than the batch process, though the overall agglomerate structures are larger than the median batch crystal size. However this in turn, reduces the amount of fines in the filtered product. Despite the potential advantages of the more uniform PSD, the required flow rates to ensure no blockages occur during the run are difficult to maintain effectively, particularly over an extended period. The amount of encrustation around the tubular outlet within the short run time would eventually cause performance issues or blockages in-line. A possible alternative set-up would be to introduce temperature control to the feed-lines and mixer piece. This could reduce the amount of encrustation and allow a higher concentration of SA and the free base to be used, increasing production. However, as the solubility of SAB is very low in acetone the effectiveness of temperature control may be fairly limited. Based on the high supersaturation levels and encrustation observed, a mixer piece crystallisation process is unlikely to be practical. Therefore, a system capable of handling high solid loadings and encrustation was sought as an alternative.

6.4.3 Periodic Continuous Stirred Tank Reactor Crystallisation

CSTRs are the most common form of continuous crystallisers currently investigated. Compared to tubular crystallisers, they are much more reminiscent of batch crystallis-

ers and generally considered a more straightforward approach to transferring a batch process to a continuous process. The effectiveness of CSTRs on the crystallisation of pharmaceutical drugs has been previously demonstrated.[124] Furthermore, they have been successfully integrated into a end-to-end continuous production process for pharmaceutical production.[27]

A traditional CSTR is operated by the continual addition of the feedstock and removal of the slurry. But there has been recent examples showing the use of periodic CSTRs crystallisers.[123,215] In this mode of operation, periodic addition and removal of suspensions is carried out using a high flow rate over short periods of time. The advantages of using periodic operation are the extended dwelling periods within each vessel and the reduction in sedimentation within feed lines. In periodic operation, the system reaches a "controlled" steady state after an induction period, in which perturbations in the system have reached a minimum. The aim of this work was to evaluate the effectiveness of a periodic CSTR crystallisation process on the reactive crystallisation of SAB. The process developed in the mixer piece experiments was transferred to the CSTR set-up to allow for comparison between the two techniques.

Platform Development

The CSTRs set-up is outlined in Figure 6-3a and described in Section 6.3.3. The operating parameters for the CSTR crystallisation runs are outlined in Table 6.1. The experimental conditions and outputs for SAB are summarised in Table 6.6 and Table 6.7.

Table 6.6: Experimental conditions and outputs for SAB CSTR experiments

Experiment	Stirring Rate (rpm)	Seeding (w/w%)	Stage 1, 2 Temperature (°C)	Stage 3, 4 Temperature (°C)	Total Run Time (min:sec)	Productivity ($g\,h^{-1}$)	Yield (%)
AZ4	300	Unseeded	20, 20	20, 20	96:17	22.0	69.3
AZ5	300	0.5	20, 20	20, 20	80:00	26.40	75.9
AZ6	600	1.0	20, 20	20, 20	83:50	26.1	74.0
AZ7	300	1.0	40, 40	40, 20	80:00	26.5	75.4

Residence Time = 20 min, Total flow rate = 10.46 mL min^{-1}, Total feed volume = 1 L, Total operating volume = 200 mL, Seeds used from batch SAB sample

Table 6.7: Parameter investigations and outputs for SAB CSTR experiments

Experiment	Stirring Rate (rpm)	Parameter	Total Run Time (min)	Productivity ($g\,h^{-1}$)	Yield (%)
AZ8	300	Acid Start-Up	80:00	25.7	75.3
AZ9	300	Sonication	80:00	27.6	77.9
AZ10	600	Steady State	243:00	24.4	69.0

Residence Time = 20 min, Total flow rate = 10.46 mL min^{-1}, Total feed volume = 1 L, Total operating volume = 200 mL, 0.5 w/w% seeds used from batch SAB sample, temperature held at 20 °C in all runs

From the results of the solubility measurements and the initial mixer crystallisation experiments, it was determined that the reactive crystallisation experiments would be performed in the CSTR set-up at a set temperature of 20 °C across all stages. This would prevent a cooling profile from influencing the particle size. This was also the lowest possible temperature that could effectively dissolve the required molar equivalent amounts of the acid coformer. Furthermore, the low solubility of the API salt meant that maintaining a low temperature to maximise yield was not necessary, as the expected additional loss to liquor would be marginal, while the required energy to maintain a reduced temperature would be high. As the CSTR platform is more sophisticated than the previous approach, the simplified experimental parameters were also used to reduce the number of variables. As described in the experimental section 6.3.3, periodic transfer of the suspension was facilitated by a vacuum that was operated manually, while feed addition of the acid and free base was controlled by peristaltic pumps. This set-up was maintained throughout all experiments.

In AZ4, the acid and free base are added simultaneously. This approach was maintained throughout all experiments with the exception of AZ8 (acid start-up) and AZ10 (base start-up). AZ4 attempted to transfer the process which had shown promise in AZ3, into the CSTR set-up. As the periodic operation of a CSTR system is less prone to blockages, a slower flow rate could be used. The base and acid were combined within the vessel (stage 3), to avoid any potential encrustation in feed lines. Based on the combined flow rate and operating volume of the CSTR system, a total residence time of 20 minutes was maintained throughout the experiment. This ensured the process could be run steadily, over a longer period, while maintaining a similar total process time to mixer crystallisation experiments. The total run time for AZ4 was 96 minutes; equivalent to 4.8 residence times. Crystallisation occurred within seconds of combining the free base and acid in stage 3. During the operational period, a total of 48 vacuum transfers were performed. Under the conditions described in Table 6.6, AZ4 suffered no blockage in-line. Transfer between vessels was rapid and the suspension did not adhere to the walls of the tubing. A small amount of residual product was noted to be left behind, however, at no point did the solid residue accumulate during the operational period. After extraction of the suspension, it was noted that extensive encrustation occurred in stage 3 of the CSTR platform, while almost no observable encrustation was present in stage 4 (Figure 6-13)

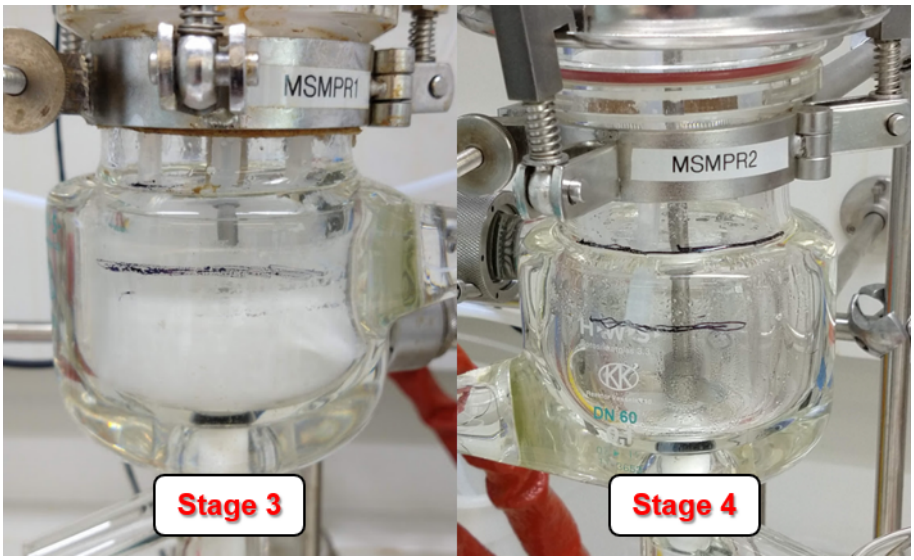

Figure 6-13: Encrustation in stage 3 and 4 after SAB production in the CSTR set-up

The high encrustation in the first vessel is the result of the high supersaturation levels and is analogous to encrustation observed within the tubing lines seen in the mixer experiments. However, the lack of noticeable encrustation in stage 4 indicates that nucleation occurred predominantly in stage 3, while stage 4 promoted crystal growth. Despite the large amount of encrustation, no noticeable drop in performance was observed during the run, though visibility in stage 3 was substantially reduced. The total solid recovery after washing was calculated to be 69.3%. As the encrustation in stage 3 could not be removed during the acetone washing stage, this likely corresponds to the missing yield. Overall, the process proved much more effective than the mixer piece experiments, as the process was robust enough for an extended operational period. The major issue observed was the high amounts of encrustation exhibited in stage 3. While this did not impede the crystallisation over the operational period, it could eventually cause issues in transfer of the suspension or effect the quality of the crystalline product. As such, investigations focused on controlling the amount of encrustation, whilst analysing any changes in the extracted product particle size and shape.

In AZ5, SAB seeds were introduced to the system. The addition of seeds has been shown to be an effective method for controlling salt crystallisation and particle size.[216] In order to effectively deliver seeds to the CSTR, the free base solution was used as a suspension vessel. The seeds used were taken from the batch SAB reference. As the salt is only weakly soluble in acetone, the 10:90 w/w% free base:acetone solution could be easily saturated with SAB at the required temperature. The w/w% of seed added was

calculated as a percentage of the expected output of SAB. In order to keep the crystals suspended without entangling the feed lines, stage 1 was continuously stirred at a low speed (25 - 50 rpm). The free base solution provided a convenient medium for transfer of the seeds in flow, the low solid loading was compatible with the peristaltic feed pumps and kept within the process specifications. As with AZ4, the process proceeded well, with no notable obstruction in the feed delivery or transfer during the crystallisation. The solid recovery was 75.9%, indicating the addition of seeds to the free base solution increases the crystallisation yield by more than 5%. The process had a similar run time of 80 minutes. No noticeable change was perceived in the amount of encrustation visible in stage 3, despite the addition of seeds. Most likely the low seed loading could not offset nucleation on the walls of the vessel.

In AZ6, the stirring rate and seed loading was increased to 600 rpm and 1 w/w% respectively. The faster stirring rate and higher seed loading were used to determine if encrustation could be mitigated by increasing seed loading and reducing sedimentation. The higher stirring rate also aimed to ensure the suspension was more evenly distributed, so that transfer between Stages 3 and 4 was not preferentially removing smaller, better suspended crystals. This was notable when comparing PSD between the main collection and the acetone washing stage of the process for AZ4. The difference between the PSD of the sample from the main collection and the wash are clearly visible in Figure 6-14.

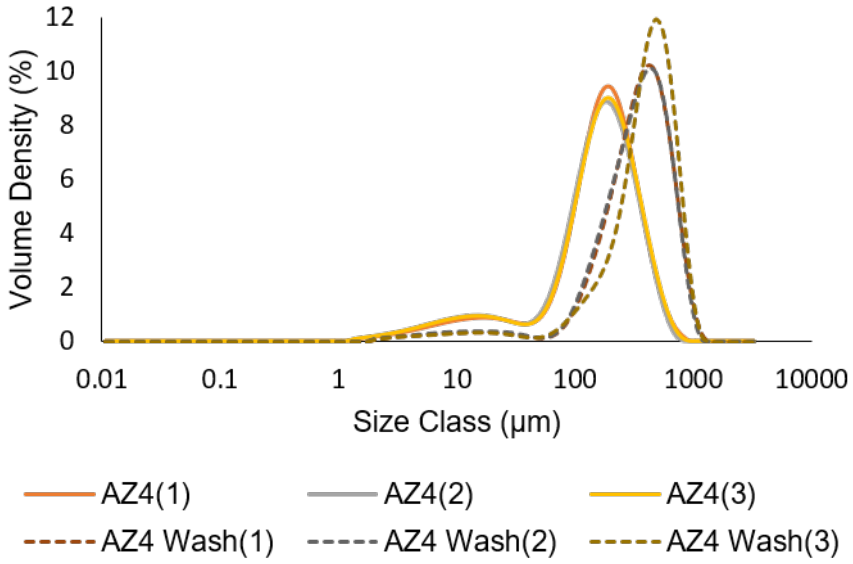

Figure 6-14: Particle size distribution difference between the main collection and wash stage in AZ4

In comparison with AZ5, AZ6 had a similar overall yield suggesting that the additional seed loading did not increase solid recovery. However, the sedimentation was deemed much improved at 600 rpm with a visibly more uniform suspension observed during the run. As a consequence, very little solid was collected from the acetone wash after removal of the main collection. The fraction of product collected in the washing step in AZ4 and AZ5 was 10.2 % and 2.8 % respectively, while in AZ6, this was reduced to 1.7 %, reflecting the reduction in sedimentation.

Despite the minor improvements in AZ6, a reduction in encrustation in stage 3 was not discernible from previous runs. In AZ7, stages 1, 2 and 3 were heated to 40 °C, while stage 4 remained at 20 °C. The stirring rate was held at 300 rpm and a seeding loading of 1 w/w% was used. As the nucleation vessel was heated, the initial crystallisation should be less supersaturated. The high seed loading and temperature aimed to help mitigate the encrustation in the vessel. Initial relative supersaturation was reduced from 124 to 24. Solid recovery remained at 75.4 %, close to the value achieved in AZ5 and AZ6. The yield therefore was not majorly effected by the higher initial temperature. A small reduction in the onset of encrustation was observed, but no major improvement was seen by the end of the run. The slower stirring speed did lead to sedimentation in the vessel after an extended period. Future experiments could potentially investigate whether increasing the initial temperature further might improve encrustation, (i.e. heating to 55 °C would reduced the relative supersaturation to 7) but as the solubility of the API salt is low in acetone, it is unclear how much of a difference this would make to encrustation over extended periods. Furthermore the current set-up has no method of controlling the temperature in the feed-lines. This capability could be incorporated in later designs to improve control, but could not be carried out within the scope of this work. As such alternative methods were sought to influence nucleation.

In AZ8, the start-up procedure was investigated. The seed loading and stirring rate used were the same as AZ5. However, rather than filling stage 3 with the acid and base solutions simultaneously, the vessel was allowed to half-fill with the SA solution first. The SA pump was then switched off and the free base added. Once stage 3 had filled, both pumps were switched on and the run continued in the same manner as the other periodic CSTR experiments. The idea was to provide a more dilute system at the beginning of operations, thereby reducing the likelihood of excessive nucleation on the walls of the vessel. The more gradual increase in supersaturation compared to previous runs may help to decrease encrustation and promote nucleation via seeding (Figure 6-15).

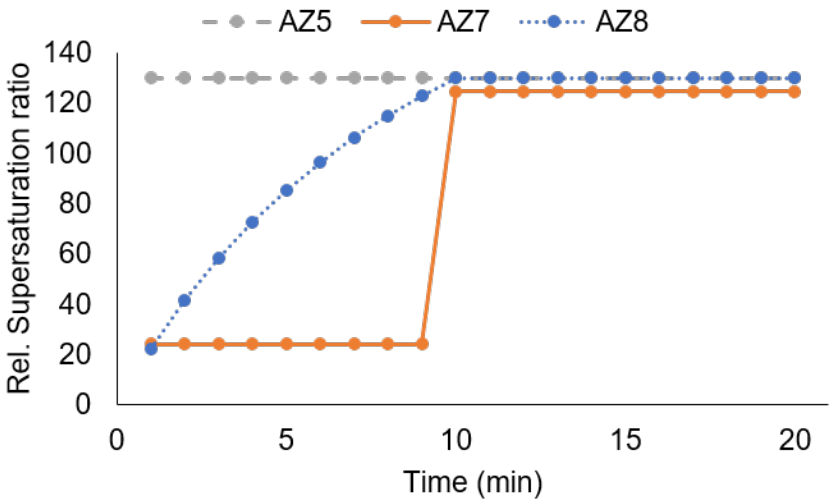

Figure 6-15: Calculated relative supersaturation ratios in AZ5, AZ7 and AZ8 during the start-up procedure, assuming 100% production of SAB

Using this approach, encrustation appears to have been improved during the initial stages of the process. This was maintained for the first residence time (Figure 6-16). However, after 30 minutes there was little visible difference between the amount of encrustation observed in previous runs. It is possible that encrustation could have been reduced inside the vessel, but this is difficult to tell without *in situ* monitoring. The overall yield was maintained at 75%.

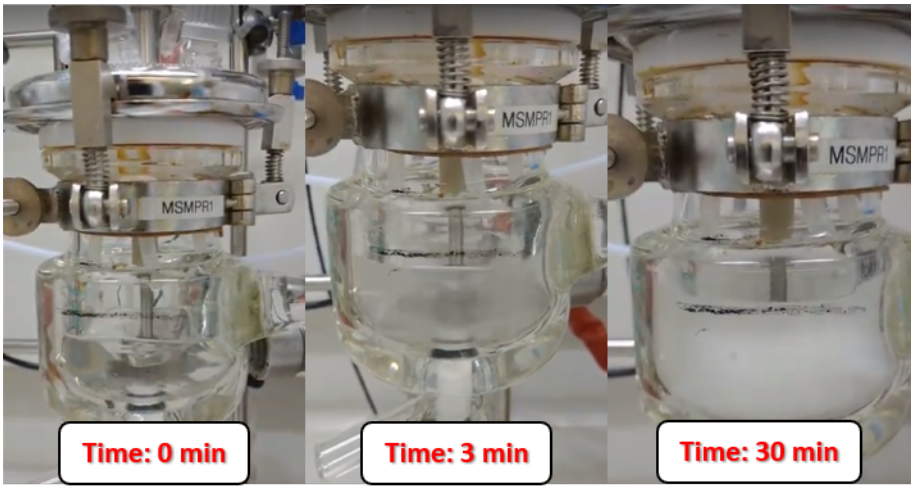

Figure 6-16: Encrustation in AZ8 at time 0, 3 and 30 min

Crystal Morphology

Images of AZ4, AZ5, AZ6 and AZ7 are shown in Figure 6-17. AZ8 SEM images are included in the Appendix (Figure 9-33) but showed little difference to AZ5, so have been omitted for clarity. As can be seen from the images obtained, the isolated samples show the same spherical agglomerates observed in the mixer experiments. However, the size is more variable. AZ4, representing the unseeded experiment, appears to show agglomerates larger than those observed in AZ5 and AZ6 where seeding was used. AZ6 appears to show a larger proportion of fines than AZ5 which is unsurprising as the high shear rates generated by the increased stirrer speed may be causing the agglomerates to break. In the case of AZ7, the particles are much more varied in size.

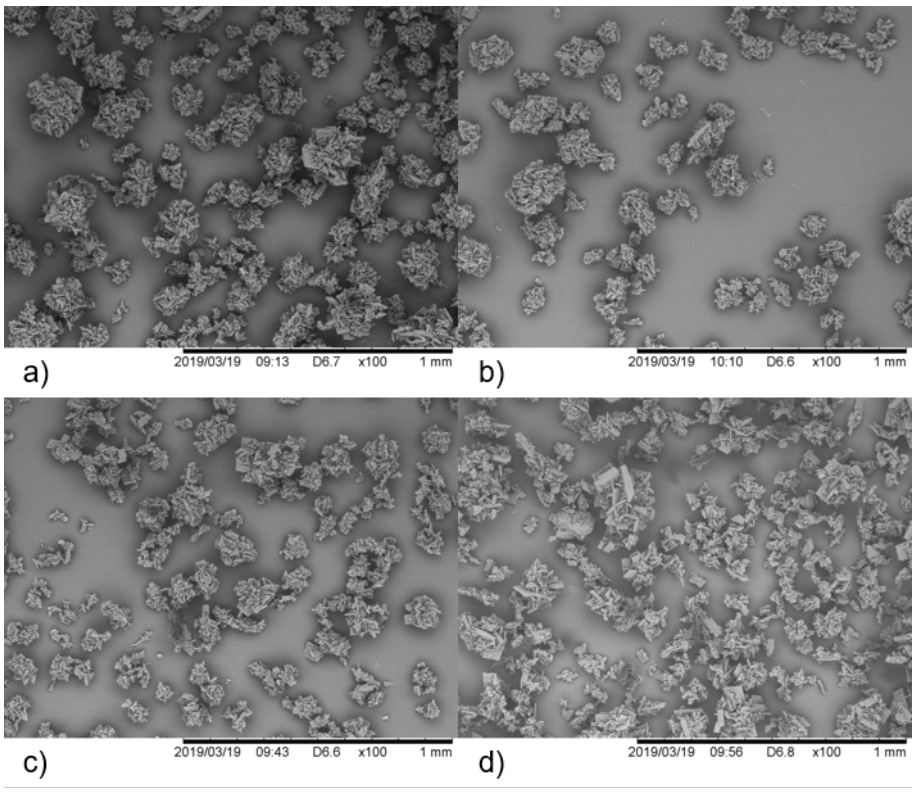

Figure 6-17: SEM images of SAB in a) AZ4 b) AZ5 c) AZ6 d) AZ7 after isolation at magnifications of x100

As was the case with the mixer experiments, the agglomerates consist of the individual platelets of various sizes (Figure 6-18). The plate-like morphology of the agglomerate components is consistent with the morphology of the batch process sample. Since the relative supersaturation ratio is similar to the mixer piece experiments, it is unsurprising that the morphology is unchanged in the CSTR runs. There are however, visibly

more fines in samples taken at higher stirring rates and seeding experiments than the unseeded runs. The agglomerates also appear larger than those visualised from the mixer experiments. The trend appears to indicate that a higher stirring speed reduces the size of the agglomerates (AZ6), while a heightened temperature on the initial crystallisation widens the distribution of size of the agglomerates (AZ7).

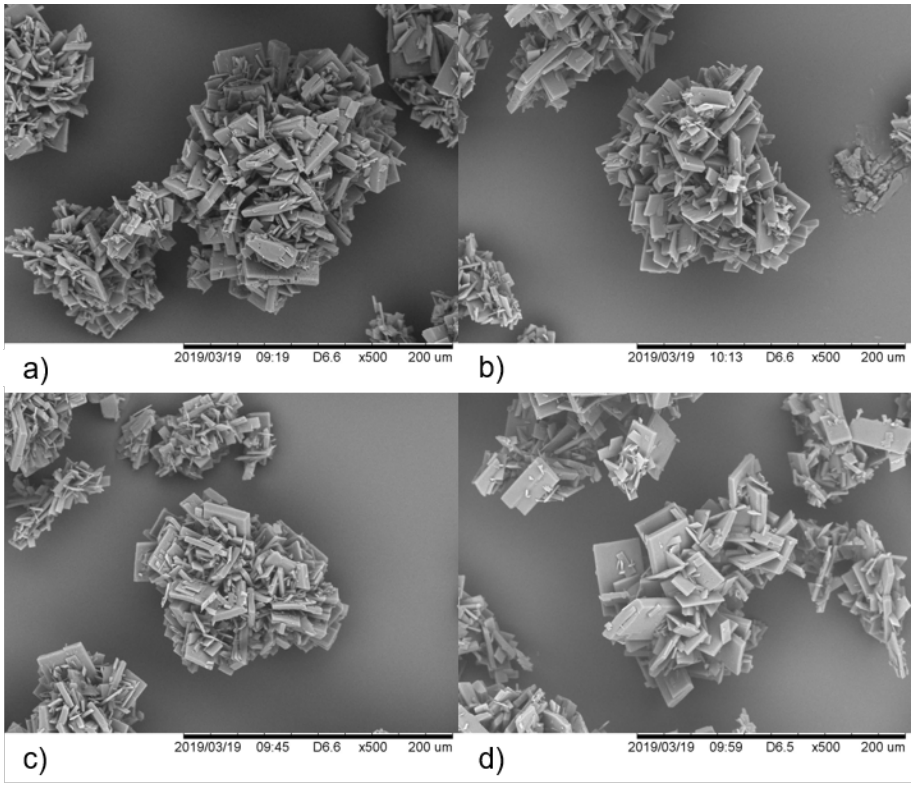

Figure 6-18: SEM images of SAB in a) AZ4 b) AZ5 c) AZ6 d) AZ7 after isolation at magnifications of x500

The particulates within the isolated agglomerates from continuous CSTR runs appear as well defined as previously noted in mixer experiments (Figure 6-19). Even with the changes in the apparatus and parameters, the surfaces and edges of the samples all exhibit similarly smooth faces and edges to the mixer experiments. As isolation in all runs has resulted in agglomerates, this may reflect a preference for the formation of agglomerates regardless of the crystalliser. However, these structures are not present in the batch sample so particle size and shape should be controllable by careful selection of the crystallisation and extraction procedure.

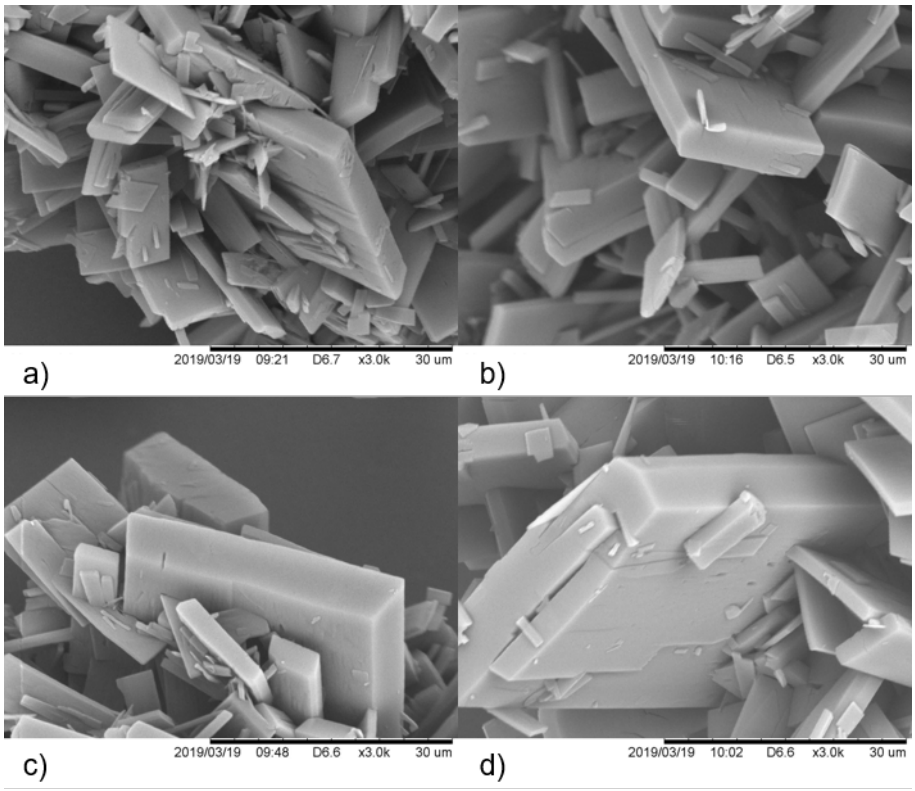

Figure 6-19: SEM images of SAB in a) AZ4 b) AZ5 c) AZ6 d) AZ7 after isolation at magnifications of x3000

Particle Size

An example scan of the PSD of the AZ4, AZ6, AZ7 and AZ8 are shown in Figure 6-20. The periodic CSTR samples show a bimodal distribution reminiscent of the mixer piece experiments. However, while the general shape of the PSD is similar, broadening is particularly prominent for AZ7. In the case of the fines peak, AZ6 shows the highest proportion of smaller particles, which corresponds well with the SEM images and would be expected considering the higher stirring rate and seed loading used. The isolated particles remain within the range of sizes isolated from the batch reference. The uniformity is good in the cases of AZ4 and AZ6, though AZ7 shows a broadening of the size range, with a trace similar to the batch. This could indicate that temperature plays a significant part in the size distribution. Maintaining a constant temperature may promote more uniform particles, but in the form of spherical agglomerates.

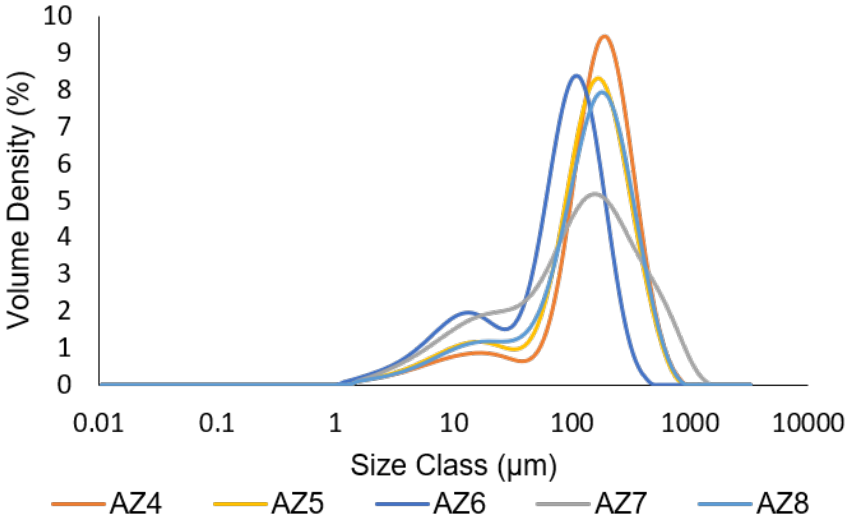

Figure 6-20: Particle size distribution of AZ4 to AZ8

The D-values for experiments A4Z to AZ8 are summarised in Table 6.8. The values quoted are calculated from the average and standard deviation of at least three repeats. Comparison of the D-values with the mixer experiments indicates that the agglomerates from the CSTR are generally larger than the mixer piece samples. The D-values with the exception of AZ6 show a median of between 130 and 170 µm, while the median for AZ6 is below 100 µm and approaches the values observed in AZ2 and AZ3. This perhaps indicates that a higher stirring rate promotes a mixing regime that is similar to that from the mixer piece unions.

Table 6.8: Particle size distribution percentiles for samples of SAB taken from AZ4 to AZ8 and the batch reference

Experiment	Dv(10) (µm)	Dv(50) (µm)	Dv(90) (µm)
AZ4	22.3 ± 2.26	167 ± 4.76	366 ± 8.46
AZ5	15.4 ± 0.17	143 ± 4.51	330 ± 3.06
AZ6	9.28 ± 0.29	85.5 ± 1.10	198 ± 7.27
AZ7	13.4 ± 1.65	127 ± 8.38	492 ± 17.4
AZ8	19.7 ± 0.95	161 ± 11.4	391 ± 28.3

Comparison between AZ4 and AZ5 suggests that seeding causes a slight shift in the distribution to a lower value, but only has a marginal effect, making a larger difference to the overall yield. While the change in Dv(90) values is only moderate in AZ4 and

AZ5, there is a clear difference with AZ6 and AZ7. Based on this, the likely outcome is that higher stirring speeds favours smaller agglomerate formation, while higher initial temperatures favour larger agglomerate formation. This in contrast to AZ1, AZ2 and AZ3 where the change in temperature and *Re* caused little change in the particle distribution. Here the effect of stirring speed and temperature is far more pronounced.

Based on these studies, the spherical agglomerate size could be potentially tuned to a desired size and distribution by adjusting mixing, temperature and seeding. As the stirring rate is independent of the flow rate in a CSTR, this provides an advantage over the mixer piece process. Furthermore, the use of CSTRs in series provides better mixing and temperature control than an equivalent sized batch process, allowing greater control over crystal size distribution.

Filtration

The agglomerates produced during the continuous flow experiments have been observed to filter quickly. In all cases with the exception of AZ4, the filtrate passes through the cake in less than a minute. As a comparison, the batch sample was suspended in acetone to an equivalent mass fraction. The time taken to filter each solution was measured and the results are summarised in the Appendix Table 9.5. From the data acquired experimentally, the cake resistance was calculated using Darcy's Law as outlined in the experimental section 6.3.5. The results are summarised in Figure 6-21.

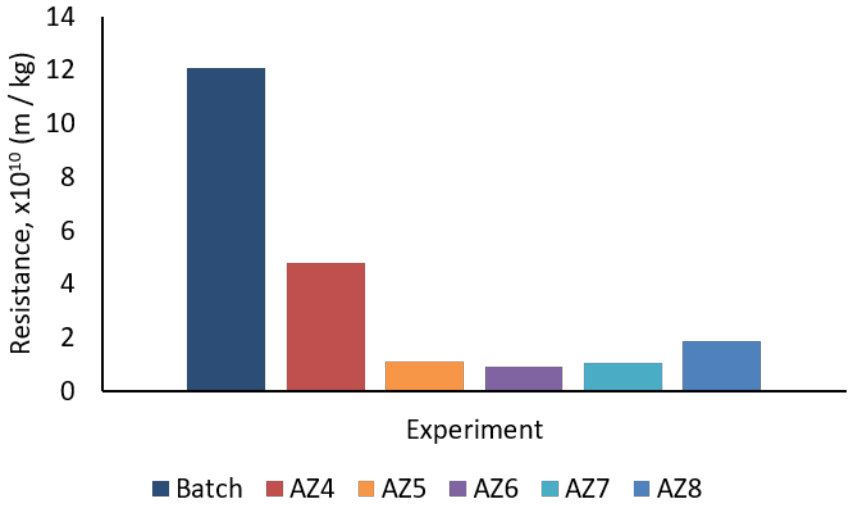

Figure 6-21: Cake resistance for AZ4 to AZ8 and the batch sample of SAB

As can be observed from the graph, the specific cake resistance of the batch sample was

an order of magnitude larger than the values calculated for the periodic CSTR runs. The only exception is AZ4, however a poor vacuum seal lead to higher cake resistance than anticipated and this would likely be rectified in a repeat measurement. While this clearly shows an improvement in small scale filtration experiments, further investigation would be required to confirm whether the particles would perform better at scale. This is important as the compressibility of agglomerates under pressure filtration can lead to performance issues. This is particularly the case when agitation is introduced to the cake layer.[217] While a low cake resistance is only one factor that contributes to the performance of a particle during filtration, clearly the agglomerates in flow display measurably faster filtration that could be of benefit. Of particular interest would be whether agglomerates might be useful in integrated processes, where continuous crystallisation feeds directly into a continuous extraction unit. Often filtration is a bottleneck, in looking to integrate continuous manufacturing, a slow filtration could have a detrimental effect on the upstream methodology. If the agglomerates are free of unwanted impurities, it is possible that spherical shape may be more effective in a integrated continuous processes than finer crystals.

Sonication

AZ9 aimed to investigate the effect of ultrasound on the encrustation noted to occur regularly in stage 3 during crystallisation. While AZ8 showed that this could be reduced by initially filling the vessel with SA solution to reduce early supersaturation, it did not provide a long term solution. The encrustation is excessive on the walls of the vessel and is typical of crystallisation processes with a high supersaturation and rapid nucleation process. This can be detrimental to the system in the long term, leading to blocking issues, reduced solid form control and extended washing and cleaning periods. While this has not been a problem with the current operational time frame, ideally this should be reduced as much as possible. To counter the encrustation, an additional ultrasound system was installed into stage 3. The ultrasound was submerged halfway into the vessel and switched on at 50% power output before pumping the solution. Sonication was applied throughout the experiment. A comparison of the stage 3 after the run in AZ5 and AZ9 is shown in Figure 6-22.

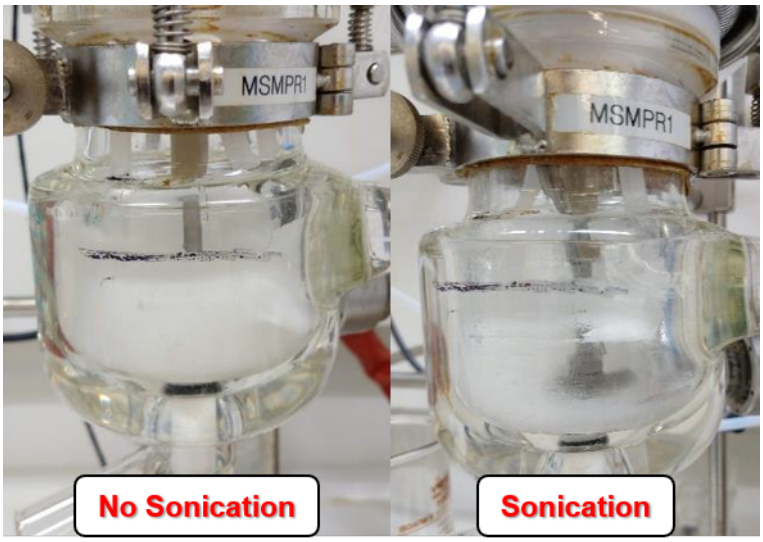

Figure 6-22: Effect of ultrasound on encrustation in stage 3

As can be seen, there is a visible reduction in encrustation around the interior of the vessel when sonication is applied and therefore ultrasound was effective at reducing encrustation. During observation of the run the suspension of solids was also improved, which would suggest that smaller particles are being formed. This would be expected as sonication has previously been shown to be effective at reducing particle size and encrustation.[130,218] The addition of sonication also slightly increased the overall yield by 2 to 3%. This is likely due to a better suspension leading to easier extraction and reduction in residual solid in the vessel. However the application of ultrasound had an adverse effect on the agglomerates. This was observed as significant increase in filtration time. SEM images confirm that breakdown or a reduction in agglomerate formation occurred, as more fines were present (Figure 6-23). The addition of sonication likely prevented the forming or facilitated the breakdown of the agglomerates. As a consequence the filtration time was increased. The reduction of agglomerate formation due to ultrasound has been previously demonstrated by Narducci *et al.* for adipic acid.[219]

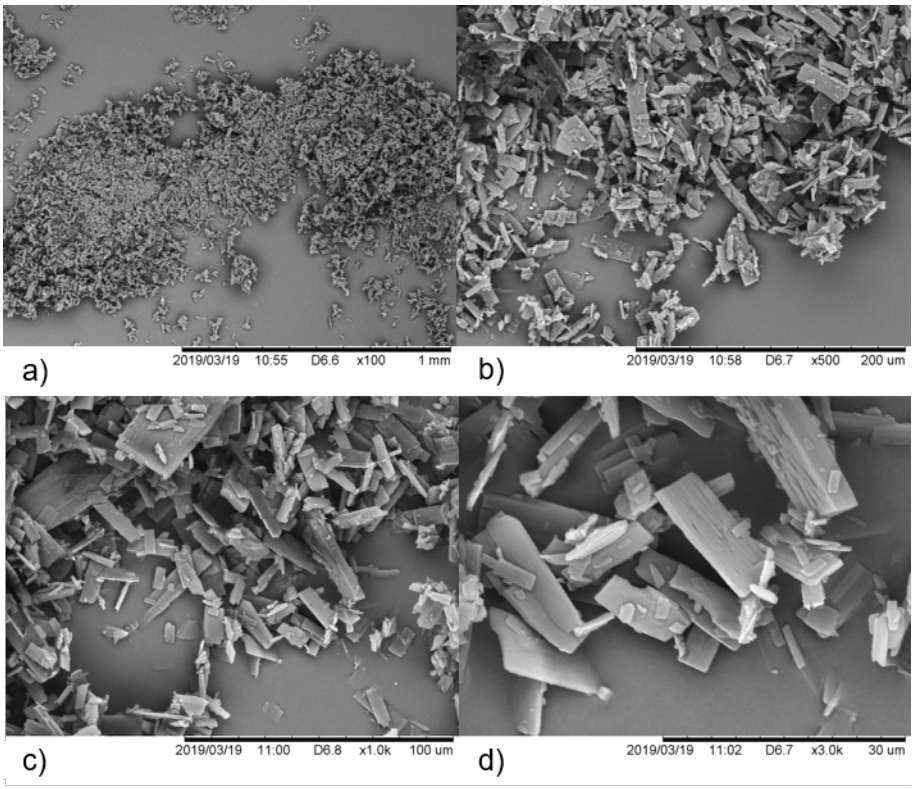

Figure 6-23: SEM images of SAB in AZ9 at a) x100 b) x500 c) x1000 and d) x3000 magnifications

The overall pattern for the PSD is changed compared to previous runs. (Figure 6-24). The typical bimodal distribution is lost in favour of a much higher volume density of fine crystals. The D-values from laser diffraction measurements are summarised in Table 6.9. The median volume density (Dv50) indicates that at least 50% of particles detected were smaller than 12.3 µm. While a very broad distribution (Dv(90) = 762 µm) is indicated, based on the SEM and lack of agglomerates it likely this was an anomaly, caused by adhesion of the smaller particles which failed to break-up before detection. In this case, an alternate methodology could be developed to give better measurements, such as suspending the sample in a solvent medium before detection.

Table 6.9: Particle size distribution percentiles after sonication

Experiment	Dv(10) (µm)	Dv(50) (µm)	Dv(90) (µm)
AZ9	3.49 ± 0.02	12.3 ± 0.10	762 ± 33.2

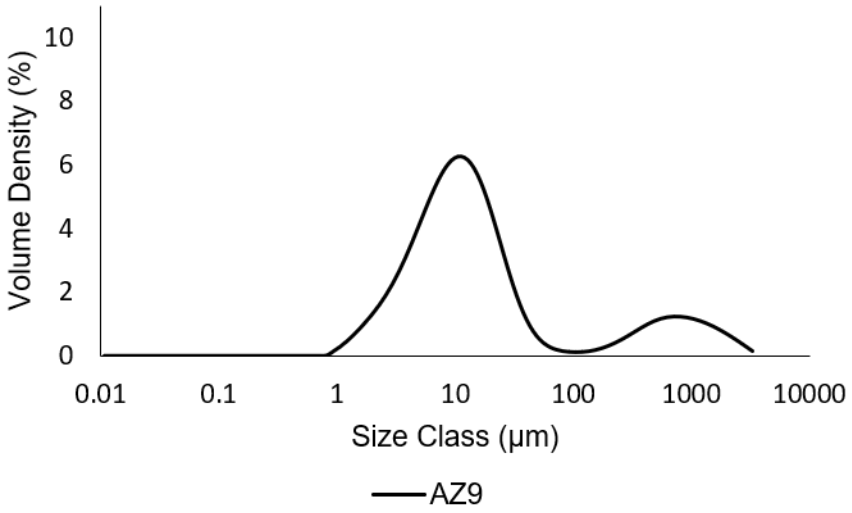

Figure 6-24: Particle size distribution of AZ9

Overall, sonication did effectively reduce the amount of encrustation present in stage 3, however this had an adverse effect on the agglomerate structures. As a consequence of the much smaller particles formed, an increase in filtration time was observed. If the faster filtration time associated with the spherical agglomerates was to be desired, ultrasound would need to be kept to a minimum. A possible alternative approach might be to apply sonication periodically, rather than continuously. In this manner, the agglomerate structure may remain intact, while still reducing the amount of encrustation. However, a further issue with ultrasound is the long term scale-up.[220] This is due to the fact that while ultrasound probes deliver a very high intensity at the point of delivery, the sound energy density rapidly decreases with distance. As such, their effectiveness becomes increasingly non-homogeneous as vessels are scaled-up. Therefore, the cost benefit of ultrasound generally decreases for larger vessels. As SAB is currently produced on a multi-kilogram scale, the application of this technology for continuous crystallisation scale-up is fairly limited. The experiment does highlight that encrustation and agglomerate reduction controls can be introduced and may be applicable to some smaller scale processes, particularly where the agglomerate structures are not advantageous.

Steady State

Up to this point, the work has demonstrated that using a periodic CSTR system may be a feasible approach for the crystallisation of SAB. However, some encrustation and

sedimentation issues have been encountered, particularly in the stage 3 CSTR. Based on the results thus far, an optimised process was considered to overcome these issues. The results from AZ5 indicated that the addition of seeds to the free base was an effective and simple method for boosting solid recovery. AZ6 showed that a higher stirrer speed would help to suspend particles and reduce agglomerate sizes without causing excessive breakage. AZ8 indicated that pre-filling with the SA solution resulted in a initial reduction in encrustation with little immediate impact on the filtration speed.

AZ10 aimed to demonstrate that the system could be run over a longer period without issue. The conditions are described in Table 6.7. In this case, AZ10 was run at 600 rpm, with a 0.5 % seed loading in order to reduce sedimentation and maximise the yield respectively. Rather than pre-fill with the acid as in AZ8, AZ10 tried pre-filling the first CSTR with the free base/seed solution. This more closely reflected the batch production method, reduced the initial supersaturation ratio and ensured that a larger proportion of SAB seeds were present at the beginning of the salt crystallisation. To determine when a controlled state of operation was reached, steady state behaviour of the periodic CSTR was investigated using process analytical technology (PAT). An immersible Raman probe was placed in stage 3 and FBRM probe in stage 4. The Raman probe would measure the onset of crystallisation, while the FBRM probe would determine particle size *in situ*. In this way, a better understanding of the system could be carried out while also evaluating the performance and productivity over an extended period. During the run, crystallisation proceeded over the 4 hour period with no blockages or issues occurring with the transfer of the slurry. Initial filling with the base solution resulted in a reduction in encrustation initially, but fouling was still high after 4 hours. Despite this no notable drop in performance was observed. The system was run for over 12 RTs, with an overall 69% yield achieved (Table 6.10).

Table 6.10: Sample yield per collection period in AZ10

Sample	Collection Time (min)	Yield per Collection Period (%)	Residence Times
A	60:00	83.9	1 - 3
B	37:00	51.8	3 - 5
C	58:00	74.5	5 - 8
D	58:00	76.0	8 - 11
E	20:00	30.4	12
Total	243:00	69.0	12

A graph of the Raman data of relative concentration vs absolute time is depicted

in Figure 6-25. As can be seen from the graph, initially, a high amount of natural light is seen, this is during the base charging phase. As the acid is added, the light rapidly decreases and the number of counts for the solid phase of SAB rises. After 30 minutes the signal has stabilised, indicating that steady state has occurred in stage 3. Unfortunately, after an hour, the probe becomes fouled by encrustation and the proportion of signal from the solution phase is lost. The probe was later cleaned during switching of the collection vessels, where the signal can be seen to return to the same level as before fouling. Unfortunately, fouling of the probe meant a large proportion of the signal was lost. The fact that the signal returned to the same level after cleaning is a good indication that a steady state was achieved.

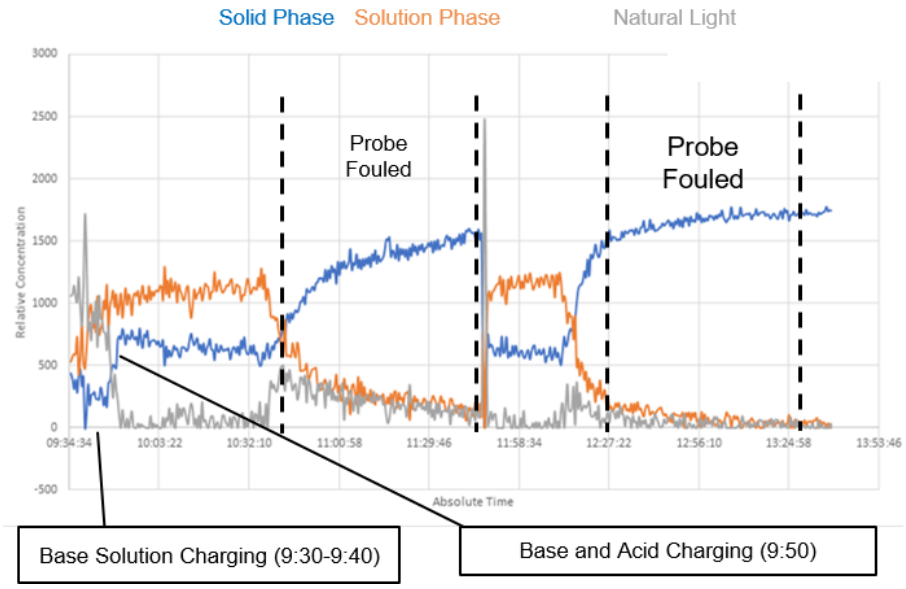

Figure 6-25: Raman monitoring and probe fouling in AZ10

The signals gathered for the FBRM probe in stage 4 are shown in Figure 6-26. Over the course of the run, each trace shows a distinct oscillating wave pattern. There are also some fouling issues, but these are less pronounced than in the Raman tracking. This would be expected, as nucleation and encrustation are more pronounced in the first vessel. The oscillating pattern does suggest that some minor disturbance to the system is occurring, however this is not unexpected as transfer to and from the vessel is occurring at regular intervals. Overall disturbances become minimised after 1 hour of operation, which suggest the system has reached a controlled state of operation.

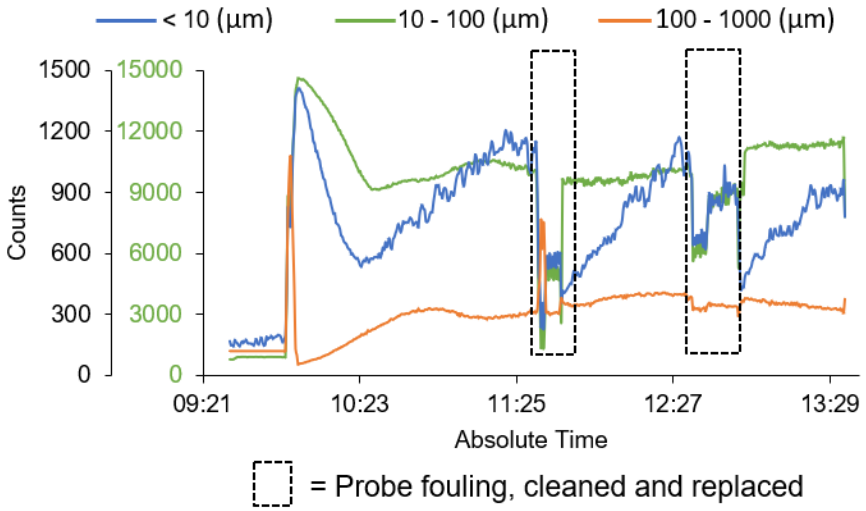

Figure 6-26: Particle tracking and probe fouling in AZ10

In terms of particle size, an interesting trend emerges when comparing the chord lengths at different time stamps (Figure 6-27).

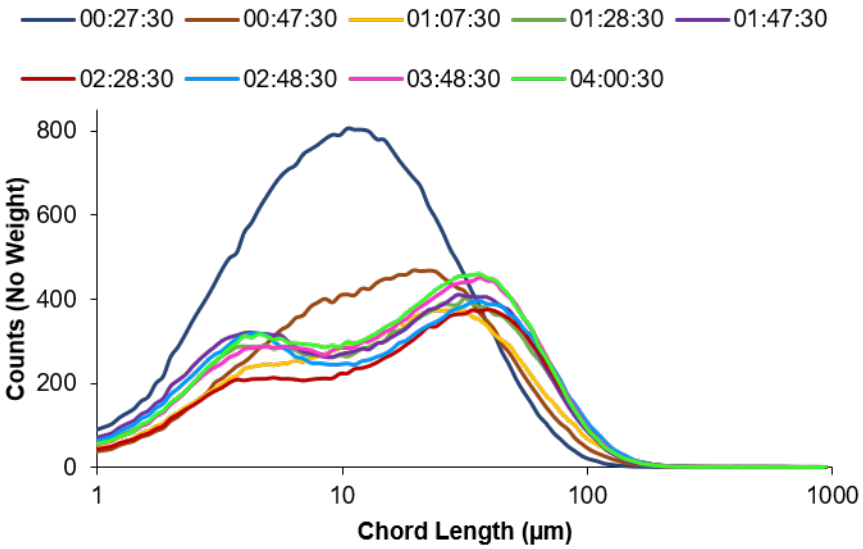

Figure 6-27: Chord length changes with time in AZ10

At the beginning of the run, the chord lengths show a broad distribution, centred close to 10 - 20 µm. As the run proceeds, this gradually changes to a bimodal pattern, with two peaks centred on 4 - 5 µm and 40 - 50 µm. While the exact values are lower than those previously encountered in off-line PSD measurements, the pattern observed is

reminiscent of the measurements taken on the laser diffractometer. According to the data, the bimodal pattern is formed and maintained throughout the run after 1 hour. This is a clear indication that the system reached steady state within this time period.

Offline analysis was carried out using SEM and laser diffraction measurements. A comparison of the crystals in sample A (before steady state) and sample C (steady state reached) clearly shows that the fine crystals are predominately formed in the early stages of the crystallisation process (Figure 6-28). The agglomerates are preferred once the system has reached steady state. Previous runs therefore consisted of a mixture of the two preferred structural arrangements. It would be interesting to determine if the preference for fine structures in the early stages of the run is an effect of the initial dilution, or whether the formation of the agglomerates is related to the encrustation build-up on the interior walls.

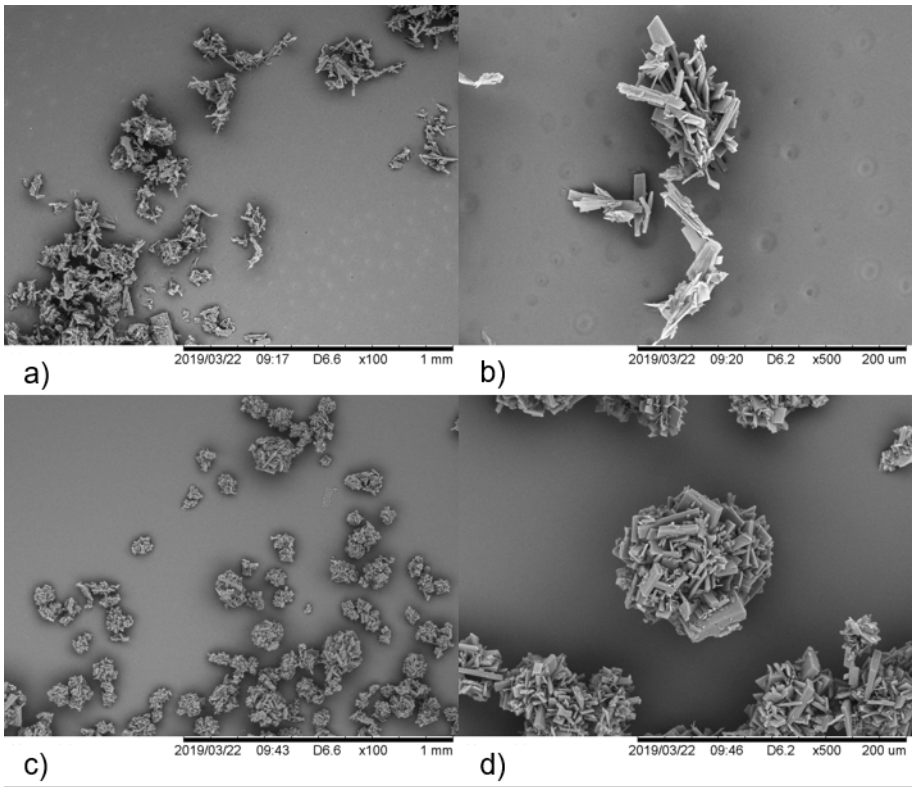

Figure 6-28: SEM images at x100 and x500 magnification for AZ10 samples: A, (a) and (b) and C (c) and (d)

The offline PSD pattern and the corresponding D-values for each collection are shown in Figure 6-29 and Table 6.11 respectively. Based on the results, the Dv(90) values are close in size to those found in AZ6, reflecting the effect of the higher stirring rate. The

PSD traces are reminiscent of those seen in Figure 6-27, with a preference for smaller particles in sample A, followed by the typical bimodal distribution thereafter. The median D-value shifts as the run progresses, from 34.5 µm in Sample A to around 70 to 90 µm in Sample B to E, are in agreement with chord length measurements.

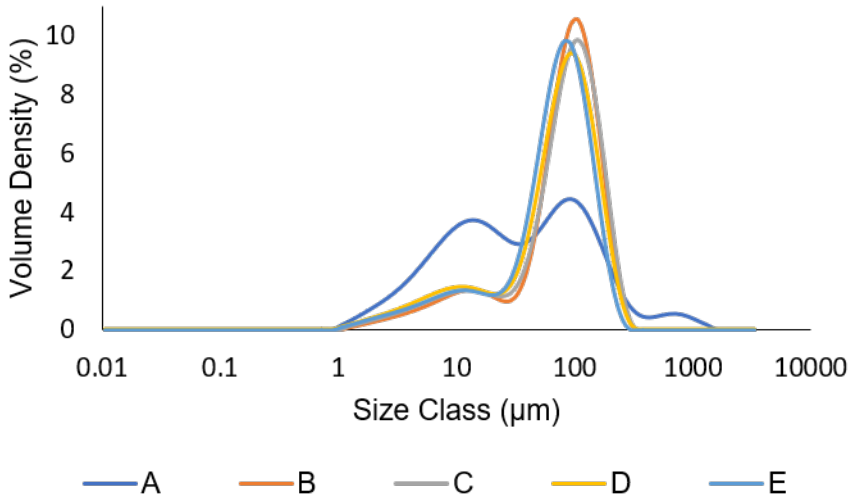

Figure 6-29: Offline PSD traces across AZ10 samples

Table 6.11: Particle size distribution percentiles in AZ10

Sample	Dv(10) (µm)	Dv(50) (µm)	Dv(90) (µm)
A	4.96 ± 0.08	34.5 ± 1.13	187 ± 14.9
B	12.3 ± 0.39	87.0 ± 1.45	172 ± 11.5
C	10.9 ± 0.45	85.8 ± 1.25	172 ± 4.34
D	9.01 ± 0.12	76.6 ± 0.42	160 ± 2.21
E	9.71 ± 0.34	72.2 ± 3.40	157 ± 25.7

AZ10 showed clear indication that particle size changes with time, with a preference for agglomerates once the system reached a controlled state of operation. Despite encrustation on the interior of stage 3 continuing to occur, AZ10 ran until feed depletion without any pump or blockage issues. PAT techniques confirmed that steady state was achievable within 1 hour. While further filtration analysis was not carried out, it would be expected that sample A would show a higher cake resistance due to its lower uniformity.

6.5 Conclusions

In this work, a case study was carried out on the continuous crystallisation of a commercially relevant API salt. During the course of this study two continuous processes approaches were considered; a tubular mixer system and a two-stage CSTR system operating in periodic withdrawal mode. Based on the early work with the mixer pieces, the tubular reactor set-up was concluded to be effective for salt crystallisation only at high velocity flow rates. In comparison periodic CSTR production showed better potential for continuous crystallisation scale-up and integration. In the latter, all experiments ran for at least 80 minutes (4 residence times) without issues, giving an appreciable yield between 70-80%. In AZ10, the system was shown to be capable of running for 12 RTs without downtime. AZ10 confirmed that steady state was achieved in 1 hour using PAT. From the data generated, a 0.5% w/w seed, 600 rpm stirring rate, with equal pumping regimes and a set temperature of 20 °C shows the most promise for further development. During the course of the project, the isolated product was noted to form spherical agglomerates with high uniformity that filtered rapidly. The agglomerate structures were replicated in the tubular mixer piece and CSTR set-up, indicating there formation was a consequence of the high relative supersaturation, rather than crystalliser equipment. The cake resistance of the agglomerates tested was shown to be lower than the batch reference, indicating a possible benefit of reduced extraction times using the flow process. However, further analysis of the compressiblity is required, particularly with the use of the conventional industrial techniques, such as pressure filtration and agitation.

A number of potential issues still remain, however. A top priority is the encrustation, which was noted to be very high in the first CSTR (stage 3) but almost non-existent in stage 4. Sonication was shown to reduce encrustation in stage 3 but prevented agglomerate formation, which impacted filtration times. A possible solution would be to raise the temperature in stage 3 and pre-fill with the free base solution/seed suspension. This might reduce the amount of encrustation, but a high stirrer rate may be necessary to avoid broadening of the particle sizes. Furthermore, the feed lines would need to be temperatures controlled. This would also facilitate safely increasing the concentration of the free base and acid; improving productivity. While TGA measurements did not indicate the inclusion of solvent into the agglomerate structure, a more sensitive technique might be needed to ensure that solvent inclusion levels do not affect product quality.

In terms of integration with upstream and downstream technologies, the periodic CSTR

system would be well placed for in-tandem process design. Stages 1 and 2 could be fed from a designed flow synthesis platform, with continuous withdrawing into stage 3. An in-line filter has previously been demonstrated in stage 4 of the periodic CSTR set-up and this could be incorporated for isolation of the product.[221] The current set-up still requires manual operation of the valves to control periodic transfer, for integration with other technologies, aspects of the system would need to be automated to allow greater accuracy when transferring the solid suspension. Even so, the periodic CSTR platform has proven to be versatile in observing and controlling particle size for a relevant commercial product. Ultimately, the use of periodic CSTRs in crystallisation shows promise in integrated manufacturing and would be a useful tool for the production of a commercial API from a continuous manufacturing perspective.

Chapter 7

Conclusions

The pressure from societal and environmental factors to deliver green processes while meeting consumer demand is an increasingly challenging issue, requiring complex and comprehensive improvements across the industrial supply chain. In Chapter 1, continuous manufacturing (CM) was outlined as a cleaner and more efficient manufacturing procedure which is likely to be a key fixture in replacing batch manufacturing methods for pharmaceutical and fine chemical production. However, pharmaceutical and fine chemical production is a multi-step procedure, with a complex supply chain under strict regulatory control measures. Therefore, delivering green processing using CM is a challenging problem. To overcome current limitations it is necessary to develop new technologies and processes and a deeper understanding of the scope of CM from a pharmaceutical and fine chemical production perspective. A key problem is bridging the perceived gaps in CM, such as between upstream synthesis and downstream crystallisation technologies. This is a current bottleneck in CM and forms the primary motivation for the research presented in this thesis. A greater understanding along with the development of continuous crystallisation and other downstream processes that can be integrated with upstream flow synthesis platforms will contribute to the adoption of novel end-to-end continuous sustainable chemical production.

In Chapter 3, the development of an integrated continuous synthesis and crystallisation process for paracetamol (PCM) was pursued. A one-pot synthetic method starting from the key intermediate 4-hydroxyacetophenone (4HAP) was replicated in batch and investigated for transfer into a flow environment. The most effective method involved flowing the starting material through a packed bed column, filled with the key reactant and catalyst hydroxylamine hydrochloride (HOA). The process showed high selectivity to the PCM product, with reaction monitoring showing a conversion of 72% and selectivity of 97% at peak performance. However, issues occurred with leaching of the HOA component into the reaction stream which caused blockages. To overcome this, the reaction was separated into two distinct steps; oximation of 4HAP to 4-hydroxyacetophenone oxime (4HAPO) and a subsequent Beckmann rearrangement of 4HAPO to PCM. Oximation of 4HAP was successfully implemented in a tubular flow reactor using HOA and sodium acetate (NaAc) which had previously been demonstrated in batch. This approach showed potential for integration as the product could be crystallised directly from the reactor output. The extracted product (4HAPO) from the oximation step was then be redissolved and combined with the homogeneous organocatalyst trifluoroacetic acid (TFA) in flow to produce PCM in 70 to 80 % isolated yield. In effect, a possible route to PCM from 4HAP was developed which translates the important chemical steps into a continuous environment. However, the need for the development of *in situ* separation and extraction technologies limited the integration

of flow synthesis steps and downstream crystallisation in the procedure. A continuous crystallisation profile was designed for the intermediate 4HAPO in ethanol/water mixtures. A compact segmented crystalliser (mini-KRAIC (m-KRAIC)) was designed that reduced reactor space footprint and allowed integration between the crystallisation and synthetic procedures for 4HAPO production. A cooling crystallisation profile was tested for 4HAPO in the m-KRAIC with partial success, but controlled nucleation within the tubular crystalliser proved difficult. A semi-batch model did show the direct crystallisation of high purity 4HAPO from the flow chemistry effluent, which opens the door to potential coupling of the flow process with a series of continuous stirred tank reactors (CSTRs). This was determined to be a more suitable route to a successful integration of flow synthesis and continuous crystallisation for 4HAPO.

In Chapter 4 a novel bench-top scale coupling for the flow chemical synthesis of the drug substance pyrazinamide (PZA) was integrated with a segmented flow crystalliser (kinetically regulated automated input crystalliser (KRAIC)). Initial research resulted in poor crystallisation processing, however, the introduction of a controlled cooling step resolved blockage issues and raised productivity to $1\,\mathrm{g\,h^{-1}}$. The rapid cooling was shown to induce nucleation and reduce crystal size by an average of 80%. The resultant crystalline PZA showed better processability and improved solid suspension. As a consequence of the crystallisation technique, the γ polymorph of PZA was selectively obtained. γ-PZA shows enhanced dissolution and solubility properties compared to the thermodynamically stable α form.[198] This work demonstrated the first cooling crystallisation to selectively produce the γ polymorph from a purely aqueous solution without additives. However, the mechanism for the selection of metastable γ polymorph is poorly understood. The development of in-line structural analysis for continuous crystallisation would be key in understanding the crystal growth and polymorph selectivity observed and would enable greater control and understanding in integrated CM processes. The potential of *in situ* structural analysis of crystals produced in segmented flow crystallisation procedures is currently under investigation in a collaboration between the University of Bath, Chick Wilson group and the Diamond Light Source facility and may be applied to the crystallisation of PZA in the future.

Chapter 5 investigated the production of two thermochromic multi-component complexes, 4-bromo-2-methylaniline (4Br2MA):3,5-dinitrobenzoic acid (35DNBA) and 4-iodo-2-methylaniline (4I2MA):35DNBA. The neutral cocrystal form of 4Br2MA:35DNBA and 4I2MA:35DNBA could not be consistently replicated using batch evaporative methods. In pursuit of a scalable and more reliable method, H_2O was found to be an effective antisolvent. Temperatures 20 °C, 30 °C and 40 °C in antisolvent crystallisation

experiment were shown to selectively produced the desired orange, 4Br2MA:35DNBA cocrystal. The thermochromic metastable form of 4I2MA:35DNBA could not be reproduced using antisolvent crystallisation, but a new polymorphic form of 4I2MA:35DNBA was isolated and characterised using thermal and X-ray diffraction methods. For 4Br2MA:35DNBA, the batch antisolvent method was transferred to a temperature controlled segmented flow crystalliser platform. Antisolvent crystallisation produced the desired chromatic cocrystal *in situ*. However, the crystals were often seeded by encrustation within the outlet or during extraction, leading to the irreversible transition to the non-thermochromic salt form of 4Br2MA:35DNBA. Careful collection of the precipitate and evaporation of the solvent allowed characterisation of the orange coloured crystals from flow. Results showed that isolated crystals matched the desired neutral cocrystal of 4Br2MA:35DNBA. However, discrepancies were observed in the isolated cocrystal thermochromic behaviour, with an observed melt-recrystallisation event present that superseded the previously observed single-crystal-to-single-crystal (SCSC) phase transition. Results from thermal analysis of the dry and wet cocrystals of 4Br2MA:35DNBA and the new form of 4I2MA:35DNBA, showed that the thermochromic transition may be enabled by the presence of moisture on the particle domain scale. The mechanism for this behaviour is not fully understood and future work should look to develop a deeper understanding of this phenomenon. The results of this study would help to establish an effective mechanism for the isolation of the metastable cocrystals. This could be then fed into a continuous isolation or work-up procedure which could be integrated with the flow crystallisation procedure developed during this work.

Finally, Chapter 6 consisted of a case study developing a continuous crystallisation procedure for a commercially relevant active pharmaceutical ingredient (API) salt. Particular emphasis was placed on the development of a crystallisation procedure which could fit within an integrated continuous manufacturing process. During the course of this study, two continuous processes were considered; a continuous flow tubular mixer system and a two-stage CSTR system operating in periodic withdrawal mode. The tubular reactor set-up suffered from large amounts of encrustation as a result of the rapid supersaturation in the formation of the salt and was concluded to be only effective at high velocity flow rates. In comparison, periodic CSTR production showed better potential for continuous crystallisation scale-up and integration. The latter operated consistently for twelve residence times (RTs) without downtime and an overall solid recovery of 70 % was achieved for the API salt. Steady state measurements were taken using process analytical technology (PAT) and a psuedo-steady state was shown to be established within three RTs. From the data generated, a 0.5% w/w seed loading, 600 rpm stirring rate, set temperature of 20 °C and equal pumping regimes for the acid and

base solutions produced an isolated product in the form of spherical agglomerates. The spherical agglomerates showed a high uniformity and as a consequence, filtered rapidly. The cake resistance of the agglomerates tested was shown to be one order of magnitude lower than the batch reference, indicating a possible benefit in the form of reduced extraction times using the flow process over the batch. However, encrustation during nucleation of the salt remained an issue. Sonication was shown to reduce encrustation, but prevented agglomerate formation, which caused filtration times to increase. Even so, production of the API using periodic CSTRs crystallisation showed considerably promise due to the high consistency and potential for spherical agglomerate control. In terms of development, the current CSTR set-up requires manual operation and would benefit from automation and integration with other technologies. This would allow for greater accuracy when transferring the solid suspension. By improving the ease of use, the attractiveness of continuous processes will lead to the adoption of continuous manufacturing in early research development work flows. This will help to curb the retention of outdated batch technologies in fine chemical and pharmaceutical industry, improving long term sustainability.

The work presented in this thesis highlights how the application of flow technology can be used to facilitate significant improvements and control in the production of fine chemicals, ranging from well established pharmaceutical compounds such as PCM and PZA to novel multi-component complexes such as 4Br2MA:35DNBA and 4I2MA:35DNBA and a current commercial API salt. During this research, the direct crystallisation from flow synthetic production of 4HAPO and direct continuous crystallisation of PZA was shown. These provide examples of how green chemistry practices and efficient synthetic procedures can facilitate the direct integration of upstream and downstream processing in CM. This avoids the need for in-line work up or separation and helps to simplify complex processes. However, purification and separation cannot always be avoided, as was the case for the amidation of PCM from 4HAPO. A major challenge in integration is the design and development of continuous separation and extraction technologies. The development of more technologies than can separate complex reaction mixtures would overcome some of the limitations of coupling between flow synthesis and crystallisation procedures.

Another consideration is the development of procedures from a holistic viewpoint. It is often the case that reaction optimisation and crystallisation procedures are developed independently and without consideration of the downstream or upstream implications. Taking a wider view and developing a work flow that encompasses end-to-end manufacturing may be an important step in speeding up the development of integrated

continuous manufacturing. Workflows and guides have begun to appear for flow chemistry[29] and continuous crystallisation[222] independently, but a framework for end-to-end or integrated production is not common practice.

While the application and development of flow synthesis is becoming increasingly more pronounced and versatile, continuous crystallisation is less well established. Here the continued optimisation of novel crystallisers will increased understanding and adoption of CM practices. Future work should consider establishing a segmented flow crystalliser design that can accommodate non-ambient temperatures. The design used in Chapter 5 for the thermochromic multi-component complexes could be scaled up, providing a more versatile segmented flow crystalliser. The KRAIC could also be developed to deliver seeds to the system. One of the limitations in the crystallisation of 4HAPO using the m-KRAIC was the lack of nucleation. If a reliable seed dosing feed could be applied consistently to each slug solution, then greater control could be exerted over the crystallisation procedure.

Finally, the continued development of cheap, modular and versatile continuous processes and platforms will accelerate the engineering of end-to-end or multi-step CM on the lab scale. This will promote a base understanding of CM and lead to the wider adoption of continuous and sustainable chemical production.

Chapter 8

References

(1) P. T. Anastas and J. C. Warner, *Green Chemistry: Theory and Practice*, Oxford University Press, Oxford, 2nd edn., 2000.

(2) P. T. Anastas and J. B. Zimmerman, *IEEE Engineering Management Review*, 2007, **35**, 16.

(3) D. J. Constable, P. J. Dunn, J. D. Hayler, G. R. Humphrey, J. L. Leazer, R. J. Linderman, K. Lorenz, J. Manley, B. A. Pearlman, A. Wells, A. Zaks and T. Y. Zhang, *Green Chemistry*, 2007, **9**, 411–420.

(4) United Nations, *The Sustainable Development Agenda*, `https://www.un.org/sustainabledevelopment/development-agenda/`, Accessed 25/06/2019.

(5) C. Jackson, *ICCA Report Highlights Chemical Industry's Contribution to Global Economy*, `https://sdg.iisd.org/news/icca-report-highlights-chemical-industrys-contribution-to-global-economy/`, Accessed 26/06/2019.

(6) CSCT, *Multidisciplinary Research*, `www.csct.ac.uk/research`, Accessed 25/06/2019.

(7) S. L. Lee, T. F. O'Connor, X. Yang, C. N. Cruz, S. Chatterjee, R. D. Madurawe, C. M. V. Moore, L. X. Yu and J. Woodcock, *Journal of Pharmaceutical Innovation*, 2015, **10**, 191–199.

(8) A. S. Travis, in *Nitrogen Capture*, Springer International Publishing, Cham, 2018, pp. 93–127.

(9) S. A. May, *Journal of Flow Chemistry*, 2017, **7**, 137–145.

(10) T. Kandemir, M. E. Schuster, A. Senyshyn, M. Behrens and R. Schlögl, *Angewandte Chemie - International Edition*, 2013, **52**, 12723–12726.

(11) C. L. Burcham, A. J. Florence and M. D. Johnson, *Annual Review of Chemical and Biomolecular Engineering*, 2018, **9**, 253–281.

(12) A. Cybulski, J. Moulijn, M. Sharma and R. Sheldon, in *Fine Chemicals Manufacture*, Elsevier Science B.V., 2007, pp. 15–58.

(13) A. A. Lapkin and P. K. Plucinski, in *Chemical Reactions and Processes under Flow Conditions*, Royal Society of Chemistry, Cambridge, 2009, ch. 1, pp. 1–43.

(14) A. S. Myerson, M. Krumme, M. Nasr, H. Thomas and R. D. Braatz, *Journal of Pharmaceutical Sciences*, 2015, **104**, 832–839.

(15) S. Kawano, K. Ito, K. Yahata, K. Kira, T. Abe, T. Akagi, M. Asano, K. Iso, Y. Sato, F. Matsuura, I. Ohashi, Y. Matsumoto, M. Isomura, T. Sasaki, T. Fukuyama, Y. Miyashita, Y. Kaburagi, A. Yokoi, O. Asano, T. Owa and Y. Kishi, *Scientific Reports*, 2019, **9**, 8656.

(16) B. Munos, *Nature Reviews Drug Discovery*, 2009, **8**, 959–968.

(17) K. S. Elvira, X. C. I Solvas, R. C. Wootton and A. J. Demello, *Nature Chemistry*, 2013, **5**, 905–915.

(18) I. R. Baxendale, R. D. Braatz, B. K. Hodnett, K. F. Jensen, M. D. Johnson, P. Sharratt, J. P. Sherlock and A. J. Florence, *Journal of Pharmaceutical Sciences*, 2015, **104**, 781–791.

(19) N. Kockmann, M. Gottsponer, B. Zimmermann and D. M. Roberge, *Chemistry – A European Journal*, 2008, **14**, 7470–7477.

(20) B. Gutmann, D. Cantillo and C. O. Kappe, *Angewandte Chemie - International Edition*, 2015, **54**, 6688–6728.

(21) S. V. Ley, *Chemical Record*, 2012, **12**, 378–390.

(22) B. Gutmann and C. O. Kappe, *Journal of Flow Chemistry*, 2017, **7**, 65–71.

(23) P. McKenzie, S. Kiang, J. Tom, A. E. Rubin and M. Futran, *AIChE Journal*, 2006, **52**, 3990–3994.

(24) R. A. Sheldon, *Chemical Society Reviews*, 2012, **41**, 1437–1451.

(25) L. Rogers and K. F. Jensen, *Green Chemistry*, 2019, **21**, 3481–3498.

(26) P. Zhang, N. Weeranoppanant, D. A. Thomas, K. Tahara, T. Stelzer, M. G. Russell, M. O'Mahony, A. S. Myerson, H. Lin, L. P. Kelly, K. F. Jensen, T. F. Jamison, C. Dai, Y. Cui, N. Briggs, R. L. Beingessner and A. Adamo, *Chemistry - A European Journal*, 2018, **24**, 2776–2784.

(27) S. Mascia, P. L. Heider, H. Zhang, R. Lakerveld, B. Benyahia, P. I. Barton, R. D. Braatz, C. L. Cooney, J. M. Evans, T. F. Jamison, K. F. Jensen, A. S. Myerson and B. L. Trout, *Angewandte Chemie - International Edition*, 2013, **52**, 12359–12363.

(28) D. G. H. V. Darvas Ferenc, in *Flow Chemistry, Volume 1 - Fundamentals*, De Gruyter, Berlin, 1st edn., 2014, ch. 2, pp. 8–58.

(29) M. B. Plutschack, B. Pieber, K. Gilmore and P. H. Seeberger, *Chemical Reviews*, 2017, **117**, 11796–11893.

(30) J.-i. Yoshida, *Basics of Flow Microreactor Synthesis*, Springer Japan, Tokyo, 1st edn., 2015.

(31) J. Wegner, S. Ceylan and A. Kirschning, *Chem. Commun.*, 2011, **47**, 4583–4592.

(32) F. E. Valera, M. Quaranta, A. Moran, J. Blacker, A. Armstrong, J. T. Cabral and D. G. Blackmond, *Angewandte Chemie - International Edition*, 2010, **49**, 2478–2485.

(33) R. E. Hayes and J. P. Mmbaga, *Introduction to chemical reactor analysis, second edition*, CRC Press, Boca Raton, 2nd edn., 2012, pp. 1–529.

(34) S. Klutz, S. K. Kurt, M. Lobedann and N. Kockmann, *Chemical Engineering Research and Design*, 2015, **95**, 22–33.

(35) M. Jiang and R. D. Braatz, *CrystEngComm*, 2019, **21**, 3534–3551.

(36) M. H. Reis, T. P. Varner and F. A. Leibfarth, *Macromolecules*, 2019, **52**, 3551–3557.

(37) T. McGlone, N. E. Briggs, C. A. Clark, C. J. Brown, J. Sefcik and A. J. Florence, *Organic Process Research and Development*, 2015, **19**, 1186–1202.

(38) J. Khinast and J. Rantanen, *Continuous Manufacturing of Pharmaceuticals*, ed. P. Kleinebudde, John Wiley & Sons, Ltd, Chichester, UK, 1st edn., 2017.

(39) W. L. Luyben, in *Chemical Reactor Design and Control*, John Wiley & Sons, 1st, 2007, ch. 1, pp. 1–30.

(40) M. Damm, T. N. Glasnov and C. O. Kappe, *Organic Process Research and Development*, 2010, **14**, 215–224.

(41) A. Nagaki, N. Takabayashi, Y. Tomida and J. I. Yoshida, *Beilstein Journal of Organic Chemistry*, 2009, **5**, 16.

(42) N. G. Anderson, *Organic Process Research and Development*, 2012, **16**, 852–869.

(43) Y. Mo and K. F. Jensen, *Reaction Chemistry and Engineering*, 2016, **1**, 501–507.

(44) S. Lawton, G. Steele, P. Shering, L. Zhao, I. Laird and X. W. Ni, *Organic Process Research and Development*, 2009, **13**, 1357–1363.

(45) J. Chen, B. Sarma, J. M. Evans and A. S. Myerson, *Crystal Growth and Design*, 2011, **11**, 887–895.

(46) D. Zhang, S. Xu, S. Du, J. Wang and J. Gong, *Engineering*, 2017, **3**, 354–364.

(47) M. D. Johnson, S. A. May, J. R. Calvin, J. Remacle, J. R. Stout, W. D. Diseroad, N. Zaborenko, B. D. Haeberle, W. M. Sun, M. T. Miller and J. Brennan, *Organic Process Research and Development*, 2012, **16**, 1017–1038.

(48) E. L. Paul, V. A. Atiemo-Obeng and S. M. Kresta, *Handbook of industrial mixing: science and practice*, John Wiley & Sons, Ltd, Hoboken, 1st edn., 2004.

(49) J. C. Pastre, D. L. Browne and S. V. Ley, *Chemical Society Reviews*, 2013, **42**, 8849–8869.

(50) J. I. Yoshida, A. Nagaki and D. Yamada, *Drug Discovery Today: Technologies*, 2013, **10**, 53–59.

(51) M. Fekete and T. Glasnov, in *Flow Chemistry - Fundamentals*, ed. F. Darvas, G. Dormán and V. Hessel, De Gruyter, Berlin, 1st edn., 2014, vol. 1, ch. 4, pp. 95–140.

(52) K. F. Jensen, B. J. Reizman and S. G. Newman, *Lab on a Chip*, 2014, **14**, 3206–3212.

(53) A. J. Alvarez and A. S. Myerson, *Crystal Growth and Design*, 2010, **10**, 2219–2228.

(54) P. Watts and C. Wiles, *Journal of Chemical Research*, 2012, **36**, 181–193.

(55) D. M. Roberge, L. Ducry, N. Bieler, P. Cretton and B. Zimmermann, *Chemical Engineering and Technology*, 2005, **28**, 318–323.

(56) P. M. Valencia, O. C. Farokhzad, R. Karnik and R. Langer, *Nature Nanotechnology*, 2012, **7**, 623–629.

(57) D. Cantillo and C. O. Kappe, *ChemCatChem*, 2014, **6**, 3286–3305.

(58) M. Irfan, T. N. Glasnov and C. O. Kappe, *ChemSusChem*, 2011, **4**, 300–316.

(59) T. Junkers and B. Wenn, *Reaction Chemistry and Engineering*, 2016, **1**, 60–64.

(60) B. D. A. Hook, W. Dohle, P. R. Hirst, M. Pickworth, M. B. Berry and K. I. Booker-Milburn, *The Journal of Organic Chemistry*, 2005, **70**, 7558–7564.

(61) K. Watts, A. Baker and T. Wirth, *Journal of Flow Chemistry*, 2014, **4**, 2–11.

(62) T. N. Glasnov and C. O. Kappe, *Macromolecular Rapid Communications*, 2007, **28**, 395–410.

(63) A. Polyzos, M. O'Brien, T. P. Petersen, I. R. Baxendale and S. V. Ley, *Angewandte Chemie - International Edition*, 2011, **50**, 1190–1193.

(64) R. Porta, M. Benaglia and A. Puglisi, *Organic Process Research and Development*, 2016, **20**, 2–25.

(65) L. Malet-Sanz and F. Susanne, *Journal of Medicinal Chemistry*, 2012, **55**, 4062–4098.

(66) T. Schwalbe, D. Kadzimirsz and G. Jas, *QSAR and Combinatorial Science*, 2005, **24**, 758–768.

(67) T. Gustafsson, F. Pontén and P. H. Seeberger, *Chemical Communications*, 2008, 1100–1102.

(68) A. R. Bogdan, S. L. Poe, D. C. Kubis, S. J. Broadwater and D. T. McQuade, *Angewandte Chemie - International Edition*, 2009, **48**, 8547–8550.

(69) D. R. Snead and T. F. Jamison, *Angewandte Chemie - International Edition*, 2015, **54**, 983–987.

(70) D. Kopetzki, F. Lévesque and P. H. Seeberger, *Chemistry - A European Journal*, 2013, **19**, 5450–5456.

(71) M. D. Hopkin, I. R. Baxendale and S. V. Ley, *Chemical Communications*, 2010, **46**, 2450–2452.

(72) B. J. Deadman, M. D. Hopkin, I. R. Baxendale and S. V. Ley, *Organic and Biomolecular Chemistry*, 2013, **11**, 1766–1800.

(73) M. Viviano, T. N. Glasnov, B. Reichart, G. Tekautz and C. O. Kappe, *Organic Process Research and Development*, 2011, **15**, 858–870.

(74) D. J. Watson, E. D. Dowdy, J. S. DePue, A. S. Kotnis, S. Leung and B. C. O'Reilly, *Organic Process Research and Development*, 2004, **8**, 616–623.

(75) T. L. LaPorte, M. Hamedi, J. S. DePue, L. Shen, D. Watson and D. Hsieh, *Organic Process Research and Development*, 2008, **12**, 956–966.

(76) M. Baumann and I. R. Baxendale, *Beilstein Journal of Organic Chemistry*, 2015, **11**, 1194–1219.

(77) L. Pellegatti and J. Sedelmeier, *Organic Process Research and Development*, 2015, **19**, 551–554.

(78) J. A. Rincón, C. Mateos, P. García-Losada and D. J. Mergott, *Organic Process Research and Development*, 2015, **19**, 347–351.

(79) Y. Lv, Z. Yu and W. Su, *Organic Process Research and Development*, 2011, **15**, 471–475.

(80) P. Poechlauer, J. Manley, R. Broxterman, B. Gregertsen and M. Ridemark, *Organic Process Research and Development*, 2012, **16**, 1586–1590.

(81) Z. Brennan, *FDA calls on manufacturers to begin switch from batch to continuous production*, `http://www.in-pharmatechnologist.com/Processing/FDA-calls-on-manufacturers-to-begin-switch-from-batch-to-continuous-production`, Accessed 07/09/2019.

(82) G. McDonald, *Janssen working on other continuous processes post US FDA OK for Prezista*, `https://www.in-pharmatechnologist.com/Article/2016/04/13/Janssen-working-on-other-continuous-processes-post-US-FDA-OK-for-Prezista`, Accessed 07/09/2019.

(83) J. M. Vargas, S. Nielsen, V. Cárdenas, A. Gonzalez, E. Y. Aymat, E. Almodovar, G. Classe, Y. Colón, E. Sanchez and R. J. Romañach, *International Journal of Pharmaceutics*, 2018, **538**, 167–178.

(84) K. J. Carpenter and W. M. Wood, *Advanced Powder Technology*, 2004, **15**, 657–672.

(85) J. Ulrich and C. Strege, *Journal of Crystal Growth*, 2002, **237-239**, 2130–2135.

(86) A. Mersmann, *Crystallization Technology Handbook*, CRC Press, New York, NY, 2nd edn., 2001.

(87) R. Davey and J. Garside, *From Molecules to Crystallizers: An Introduction to Crystallization*, Oxford University Press, Oxford, 2000, pp. 1–52.

(88) W. Beckmann, *Crystallization: Basic Concepts and Industrial Applications*, Wiley-VCH Verlag GmbH & Co. KGaA, Weinheim, Germany, 1st edn., 2013.

(89) D. Erdemir, A. Y. Lee and A. S. Myerson, *Accounts of Chemical Research*, 2009, **42**, 621–629.

(90) A. K. El-Zhry El-Yafi and H. El-Zein, *Asian Journal of Pharmaceutical Sciences*, 2014, **10**, 283–291.

(91) R. Beck and J. P. Andreassen, *AIChE Journal*, 2012, **58**, 107–121.

(92) J. Lu and S. Rohani, *Current Medicinal Chemistry*, 2009, **16**, 884–905.

(93) A. Y. Lee, D. Erdemir and A. S. Myerson, *Annual Review of Chemical and Biomolecular Engineering*, 2011, **2**, 259–280.

(94) J. Bauer, S. Spanton, R. Henry, J. Quick, W. Dziki, W. Porter and J. Morris, *Pharmaceutical Research*, 2001, **18**, 859–866.

(95) S. R. Chemburkar, J. Bauer, K. Deming, H. Spiwek, K. Patel, J. Morris, R. Henry, S. Spanton, W. Dziki, W. Porter, J. Quick, P. Bauer, J. Donaubauer, B. A. Narayanan, M. Soldani, D. Riley and K. McFarland, *Organic Process Research and Development*, 2000, **4**, 413–417.

(96) D. Chakraborty, N. Sengupta and D. J. Wales, *Journal of Physical Chemistry B*, 2016, **120**, 4331–4340.

(97) C. H. Gu and D. J. Grant, *Journal of Pharmaceutical Sciences*, 2001, **90**, 1277–1287.

(98) P. Upadhyay, A. K. Dantuluri, L. Kumar and A. K. Bansal, *Journal of Pharmaceutical Sciences*, 2012, **101**, 1843–1851.

(99) G. R. Desiraju, *Journal of Chemical Sciences*, 2010, **122**, 667–675.

(100) Z. Gao, S. Rohani, J. Gong and J. Wang, *Engineering*, 2017, **3**, 343–353.

(101) S. L. Childs, G. P. Stahly and A. Park, *Molecular Pharmaceutics*, 2007, **4**, 323–338.

(102) A. Karagianni, M. Malamatari and K. Kachrimanis, *Pharmaceutics*, 2018, **10**, 18.

(103) S. Aitipamula, P. S. Chow and R. B. Tan, *CrystEngComm*, 2014, **16**, 3451–3465.

(104) S. Karki, T. Friščić, L. Fábián, P. R. Laity, G. M. Day and W. Jones, *Advanced Materials*, 2009, **21**, 3905–3909.

(105) D. K. Bučar, S. Filip, M. Arhangelskis, G. O. Lloyd and W. Jones, *CrystEngComm*, 2013, **15**, 6289–6291.

(106) J. Lin, M. Lai, L. Dou, C. S. Kley, H. Chen, F. Peng, J. Sun, D. Lu, S. A. Hawks, C. Xie, F. Cui, A. P. Alivisatos, D. T. Limmer and P. Yang, *Nature Materials*, 2018, **17**, 261–267.

(107) C. G. Granqvist, P. C. Lansåker, N. R. Mlyuka, G. A. Niklasson and E. Avendaño, *Solar Energy Materials and Solar Cells*, 2009, **93**, 2032–2039.

(108) A. Seeboth, D. Lötzsch, R. Ruhmann and O. Muehling, *Chemical Reviews*, 2014, **114**, 3037–3068.

(109) C. L. Jones, C. C. Wilson and L. H. Thomas, *CrystEngComm*, 2014, **16**, 5849–5858.

(110) C. L. Jones, J. M. Skelton, S. C. Parker, P. R. Raithby, A. Walsh, C. C. Wilson and L. H. Thomas, *CrystEngComm*, 2019, **21**, 1626–1634.

(111) D. K. Bučar, R. W. Lancaster and J. Bernstein, *Angewandte Chemie - International Edition*, 2015, **54**, 6972–6993.

(112) K. A. Powell, G. Bartolini, K. E. Wittering, A. N. Saleemi, C. C. Wilson, C. D. Rielly and Z. K. Nagy, *Crystal Growth and Design*, 2015, **15**, 4821–4836.

(113) T. Lee, H. R. Chen, H. Y. Lin and H. L. Lee, *Crystal Growth and Design*, 2012, **12**, 5897–5907.

(114) W. Beckmann, *Organic Process Research and Development*, 2000, **4**, 372–383.

(115) V. Svoboda, P. MacFhionnghaile, J. McGinty, L. E. Connor, I. D. Oswald and J. Sefcik, *Crystal Growth and Design*, 2017, **17**, 1902–1909.

(116) M. W. Park and S. D. Yeo, *Chemical Engineering Research and Design*, 2012, **90**, 2202–2208.

(117) M. Kakran, N. G. Sahoo, L. Li and Z. Judeh, *Powder Technology*, 2013, **237**, 468–476.

(118) E. L. Paul, H. H. Tung and M. Midler, *Powder Technology*, 2005, **150**, 133–143.

(119) H. H. Tung, *Organic Process Research and Development*, 2013, **17**, 445–454.

(120) N. Rodríguez-Hornedo, S. J. Nehm, K. F. Seefeldt, Y. Pagán-Torres and C. J. Falkiewicz, *Molecular Pharmaceutics*, 2006, **3**, 362–367.

(121) S. T. Kim, J.-H. Kwon, J.-J. Lee and C.-W. Kim, *International Journal of Pharmaceutics*, 2003, **263**, 141–150.

(122) K. A. Powell, A. N. Saleemi, C. D. Rielly and Z. K. Nagy, *Organic Process Research and Development*, 2016, **20**, 626–636.

(123) K. A. Powell, A. N. Saleemi, C. D. Rielly and Z. K. Nagy, *Chemical Engineering and Processing: Process Intensification*, 2015, **97**, 195–212.

(124) A. J. Alvarez, A. Singh and A. S. Myerson, *Crystal Growth and Design*, 2011, **11**, 4392–4400.

(125) S. Ferguson, F. Ortner, J. Quon, L. Peeva, A. Livingston, B. L. Trout and A. S. Myerson, *Crystal Growth and Design*, 2014, **14**, 617–627.

(126) L. R. Agnew, T. McGlone, H. P. Wheatcroft, A. Robertson, A. R. Parsons and C. C. Wilson, *Crystal Growth and Design*, 2017, **17**, 2418–2427.

(127) D. M. Hobbs and F. J. Muzzio, *Chemical Engineering Journal*, 1997, **67**, 153–166.

(128) D. Douroumis and A. Fahr, *European Journal of Pharmaceutics and Biopharmaceutics*, 2006, **63**, 173–175.

(129) Kenics, *KM Mixer*, `https://www.chemineer.com/products/kenics/km-mixers.html`, Accessed 16/08/2019.

(130) R. J. P. Eder, S. Schrank, M. O. Besenhard, E. Roblegg, H. Gruber-Woelfler and J. G. Khinast, *Crystal Growth and Design*, 2012, **12**, 4733–4738.

(131) K. Robertson, P. B. Flandrin, A. R. Klapwijk and C. C. Wilson, *Crystal Growth and Design*, 2016, **16**, 4759–4764.

(132) N. E. Briggs, U. Schacht, V. Raval, T. McGlone, J. Sefcik and A. J. Florence, *Organic Process Research and Development*, 2015, **19**, 1903–1911.

(133) C. J. Brown, J. A. Adelakun and X. w. Ni, *Chemical Engineering and Processing: Process Intensification*, 2015, **97**, 180–186.

(134) A. Chanda, A. M. Daly, D. A. Foley, M. A. LaPack, S. Mukherjee, J. D. Orr, G. L. Reid, D. R. Thompson and H. W. Ward, *Organic Process Research and Development*, 2014, **19**, 63–83.

(135) S. Chada, D. Mandala and P. Watts, *Journal of Flow Chemistry*, 2017, **7**, 37–40.

(136) L. Dalla-Vechia, L. S. M. Miranda, R. O. M. A. De Souza, B. Reichart, T. Glasnov and C. O. Kappe, *Organic and Biomolecular Chemistry*, 2013, **11**, 6806–6813.

(137) P. F. Carneiro, B. Gutmann, R. O. De Souza and C. O. Kappe, *ACS Sustainable Chemistry and Engineering*, 2015, **3**, 3445–3453.

(138) A. E. Cervera-Padrell, S. T. Morthensen, D. J. Lewandowski, T. Skovby, S. Kiil and K. V. Gernaey, *Organic Process Research and Development*, 2012, **16**, 888–900.

(139) A. Adamo, P. L. Heider, N. Weeranoppanant and K. F. Jensen, *Industrial and Engineering Chemistry Research*, 2013, **52**, 10802–10808.

(140) P. H. Seeberger, *Nature Chemistry*, 2009, **1**, 258–260.

(141) A. G. O'Brien, Z. Horváth, F. Lévesque, J. W. Lee, A. Seidel-Morgenstern and P. H. Seeberger, *Angewandte Chemie - International Edition*, 2012, **51**, 7028–7030.

(142) R. Godawat, K. Brower, S. Jain, K. Konstantinov, F. Riske and V. Warikoo, *Biotechnology Journal*, 2012, **7**, 1496–1508.

(143) R. L. Hartman, J. R. Naber, S. L. Buchwald and K. F. Jensen, *Angewandte Chemie - International Edition*, 2010, **49**, 899–903.

(144) P. L. Heider, S. C. Born, S. Basak, B. Benyahia, R. Lakerveld, H. Zhang, R. Hogan, L. Buchbinder, A. Wolfe, S. Mascia, J. M. Evans, T. F. Jamison and K. F. Jensen, *Organic Process Research and Development*, 2014, **18**, 402–409.

(145) B. P. Loren, M. Wleklinski, A. Koswara, K. Yammine, Y. Hu, Z. K. Nagy, D. H. Thompson and R. G. Cooks, *Chemical Science*, 2017, **8**, 4363–4370.

(146) P. Bana, R. Örkényi, K. Lövei, Á. Lakó, G. I. Túrós, J. Éles, F. Faigl and I. Greiner, *Bioorganic and Medicinal Chemistry*, 2017, **25**, 6180–6189.

(147) A. Balogh, A. Domokos, B. Farkas, A. Farkas, Z. Rapi, D. Kiss, Z. Nyiri, Z. Eke, G. Szarka, R. Örkényi, B. Mátravölgyi, F. Faigl, G. Marosi and Z. K. Nagy, *Chemical Engineering Journal*, 2018, **350**, 290–299.

(148) J. L. Quon, H. Zhang, A. Alvarez, J. Evans, A. S. Myerson and B. L. Trout, *Crystal Growth and Design*, 2012, **12**, 3036–3044.

(149) A. Adamo, R. L. Beingessner, M. Behnam, J. Chen, T. F. Jamison, K. F. Jensen, J. C. M. Monbaliu, A. S. Myerson, E. M. Revalor, D. R. Snead, T. Stelzer, N. Weeranoppanant, S. Y. Wong and P. Zhang, *Science*, 2016, **352**, 61–67.

(150) K. P. Cole, J. M. C. Groh, M. D. Johnson, C. L. Burcham, B. M. Campbell, W. D. Diseroad, M. R. Heller, J. R. Howell, N. J. Kallman, T. M. Koenig, S. A. May, R. D. Miller, D. Mitchell, D. P. Myers, S. S. Myers, J. L. Phillips, C. S. Polster, T. D. White, J. Cashman, D. Hurley, R. Moylan, P. Sheehan, R. D. Spencer, K. Desmond, P. Desmond and O. Gowran, *Science*, 2017, **356**, 1144–1151.

(151) S. Ottoboni, C. J. Price, C. Steven, E. Meehan, A. Barton, P. Firth, A. Mitchell and F. Tahir, *Journal of Pharmaceutical Sciences*, 2019, **108**, 372–381.

(152) E. Rancan, F. Aricò, G. Quartarone, L. Ronchin, P. Tundo and A. Vavasori, *Catalysis Communications*, 2014, **54**, 11–16.

(153) G. G. Tokmadzhyan, *Russian Journal of Organic Chemistry*, 2011, **47**, 1746–1749.

(154) G. Quartarone, E. Rancan, L. Ronchin and A. Vavasori, *Applied Catalysis A: General*, 2014, **472**, 167–177.

(155) C. L. Jones, Ph.D. Thesis, University of Bath, Bath, 2015.

(156) W. Clegg, *X-ray crystallography*, Oxford University Press, Oxford, 2nd edn., 2015.

(157) W. Clegg, A. J. Blake, J. M. Cole, J. S. O. Evans, P. Main, S. Parsons and D. J. Watkin, *Crystal Structure Analysis*, Oxford University Press, Oxford, 2nd edn., 2009.

(158) W. Clegg, *Crystal structure determination*, Oxford University Press, Oxford, 1st edn., 1998.

(159) A. R. West, *Basic solid state chemistry*, John Wiley & Sons, Ltd, Chichester, UK, 1988.

(160) P. J. Hore, *Nuclear magnetic resonance*, Oxford University Press, Oxford, 1995.

(161) P. J. Hore, *Nuclear magnetic resonance*, Oxford University Press, Oxford, 2nd edn., 2015.

(162) J. I. Goldstein, D. E. Newbury, P. Echlin, D. C. Joy, C. E. Lyman, E. Lifshin, L. Sawyer, J. R. Michael, J. I. Goldstein, D. E. Newbury, P. Echlin, D. C. Joy, C. E. Lyman, E. Lifshin, L. Sawyer and J. R. Michael, in *Scanning Electron Microscopy and X-ray Microanalysis*, Springer US, Boston, MA, 2011, pp. 21–60.

(163) A. Ul-Hamid, in *A Beginners' Guide to Scanning Electron Microscopy*, Springer International Publishing, Cham, 2018, pp. 233–264.

(164) P. Kippax, *Paint and Coatings Industry*, 2005, **21**, 42–47.

(165) H. G. Merkus, in *Particle Size Measurements*, Springer Netherlands, Dordrecht, 2009, pp. 259–285.

(166) R. A. Moore and N. Moore, *European Journal of Hospital Pharmacy*, 2016, **23**, 187–188.

(167) R. Joncour, N. Duguet, E. Métay, A. Ferreira and M. Lemaire, *Green Chemistry*, 2014, **16**, 2997–3002.

(168) L. Zou, Y. Cui and W. Dai, *Chinese Journal of Chemistry*, 2014, **32**, 257–262.

(169) T. Zhang, J. Jiang and Y. Wang, *Organic Process Research and Development*, 2015, **19**, 2050–2054.

(170) S. C. Mitchell, P. Carmichael and R. Waring, in *Kirk-Othmer Encyclopedia of Chemical Technology*, John Wiley & Sons, Ltd, Hoboken, NJ, USA, 2003, vol. 2, pp. 652–678.

(171) A. A. Lapkin, P. K. Heer, P. M. Jacob, M. Hutchby, W. Cunningham, S. D. Bull and M. G. Davidson, *Faraday Discussions*, 2017, **202**, 483–496.

(172) F. Aricò, G. Quartarone, E. Rancan, L. Ronchin, P. Tundo and A. Vavasori, *Catalysis Communications*, 2014, **49**, 47–51.

(173) F. P. Byrne, S. Jin, G. Paggiola, T. H. M. Petchey, J. H. Clark, T. J. Farmer, A. J. Hunt, C. Robert McElroy and J. Sherwood, *Sustainable Chemical Processes*, 2016, **4**, 7.

(174) I. R. Baxendale, S. V. Ley, A. C. Mansfield and C. D. Smith, *Angewandte Chemie - International Edition*, 2009, **48**, 4017–4021.

(175) M. O'Brien, P. Koos, D. L. Browne and S. V. Ley, *Organic and Biomolecular Chemistry*, 2012, **10**, 7031–7036.

(176) D. E. Crawford, C. K. Miskimmin, J. Cahir and S. L. James, *Chemical Communications*, 2017, **53**, 13067–13070.

(177) R. X. Ren and W. Ou, *Tetrahedron Letters*, 2001, **42**, 8445–8446.

(178) D. P. Luo, Y. F. Huang, X. Y. Hong, D. Chen, G. X. Li, X. B. Huang, W. X. Gao, M. C. Liu, Y. B. Zhou and H. Y. Wu, *Advanced Synthesis and Catalysis*, 2019, **361**, 961–964.

(179) L. Liu, Z. Li, C. Chen, H. Li, L. Xu and Z. Yu, *Tetrahedron*, 2018, **74**, 2447–2453.

(180) S. Y. Wang, A. A. Kossoy, Y. D. Yao, L. P. Chen and W. H. Chen, *Thermochimica Acta*, 2017, **655**, 319–325.

(181) W. Zhang, S. Yang, Q. Lin, H. Cheng and J. Liu, *The Journal of Organic Chemistry*, 2019, **84**, 851–859.

(182) X. Mo, T. D. R. Morgan, H. T. Ang and D. G. Hall, *Journal of the American Chemical Society*, 2018, **140**, 5264–5271.

(183) J. K. Maurin, *Acta Crystallographica Section C Crystal Structure Communications*, 1994, **50**, 1354–1357.

(184) Y. Gao, J. Liu, Z. Li, T. Guo, S. Xu, H. Zhu, F. Wei, S. Chen, H. Gebru and K. Guo, *The Journal of Organic Chemistry*, 2018, **83**, 2040–2049.

(185) J. Zhang, C. Dong, C. Du and G. Luo, *Organic Process Research and Development*, 2015, **19**, 352–356.

(186) J. Zhang, Y. Lu, K. Wang and G. Luo, *Industrial and Engineering Chemistry Research*, 2013, **52**, 6377–6381.

(187) C. E. Bernardes and M. E. Da Piedade, *Crystal Growth and Design*, 2012, **12**, 2932–2941.

(188) C. Battilocchio, S.-H. Lau, J. M. Hawkins and S. V. Ley, *Organic Synthesis*, 2017, **94**, 34–45.

(189) R. A. Castro, T. M. Maria, A. O. Évora, J. C. Feiteira, M. R. Silva, A. M. Beja, J. Canotilho and M. E. S. Eusébio, *Crystal Growth and Design*, 2010, **10**, 274–282.

(190) K.-T. Liu, M.-H. Shih, H.-W. Huang and C.-J. Hu, *Synthesis*, 1988, **1988**, 715–717.

(191) K. Yamaguchi, Y. Wang, H. Kobayashi and N. Mizuno, *Chemistry Letters*, 2012, **41**, 574–576.

(192) C. Battilocchio, J. M. Hawkins and S. V. Ley, *Organic Letters*, 2014, **16**, 1060–1063.

(193) W. Holzer, G. A. Eller, B. Datterl and D. Habicht, *Magnetic Resonance in Chemistry*, 2009, **47**, 617–624.

(194) K. Nakata and Y. Takaki, *Memoirs of Osaka Kyoiku University, Series*, 1987, **3**, 93–97.

(195) G. Rø and H. Sørum, *Acta Crystallographica Section B Structural Crystallography and Crystal Chemistry*, 1972, **28**, 1677–1684.

(196) Y. Takaki, Y. Sasada and T. Watanabé, *Acta Crystallographica*, 1960, **13**, 693–702.

(197) S. Cherukuvada, R. Thakuria and A. Nangia, *Crystal Growth and Design*, 2010, **10**, 3931–3941.

(198) M. W. Hermanto, A. Yeoh, B. Soh, P. S. Chow and R. B. Tan, *Organic Process Research and Development*, 2015, **19**, 1987–1996.

(199) K. Zhang, S. Xu, S. Liu, W. Tang, X. Fu and J. Gong, *Crystal Growth and Design*, 2018, **18**, 4874–4879.

(200) C. Ge, J. Liu, X. Ye, Q. Han, L. Zhang, S. Cui, Q. Guo, G. Liu, Y. Liu and X. Tao, *Journal of Physical Chemistry C*, 2018, **122**, 15744–15752.

(201) K. Wittering, J. King, L. H. Thomas and C. C. Wilson, *Crystals*, 2014, **4**, 123–140.

(202) A. Y. Sheikh, S. A. Rahim, R. B. Hammond and K. J. Roberts, *CrystEngComm*, 2009, **11**, 501–509.

(203) A. Paradkar, R. S. Dhumal, A. L. Kelly, P. York and P. D. Coates, *Pharmaceutical Research*, 2010, **27**, 2725–2733.

(204) P. B. Flandrin, Ph.D. Thesis, University of Bath, Bath, 2019.

(205) M. Kitamura, *CrystEngComm*, 2009, **11**, 949–964.

(206) M. R. Thorson, S. Goyal, Y. Gong, G. G. Z. Zhang and P. J. A. Kenis, *CrystEngComm*, 2012, **14**, 2404–2412.

(207) S. A. Raza, U. Schacht, V. Svoboda, D. P. Edwards, A. J. Florence, C. R. Pulham, J. Sefcik and I. D. Oswald, *Crystal Growth and Design*, 2018, **18**, 210–218.

(208) M. G. Baron and M. Elie, *Sensors and Actuators, B: Chemical*, 2003, **90**, 271–275.

(209) Y. H. Lin, Y. S. Hsiao, H. C. Lu, P. Chen and W. T. Whang, *Journal of Polymer Research*, 2016, **23**, 196.

(210) S. Murugesan, D. M. Hallow, J. P. Vernille, J. W. Tom and J. E. Tabora, *Organic Process Research and Development*, 2012, **16**, 42–48.

(211) F. Wang, Y. Li, Z. Ning, C. Jiang and X. Wang, *Journal of Chemical and Engineering Data*, 2016, **61**, 3059–3068.

(212) A. F. Blandin, D. Mangin, V. Nallet, J. P. Klein and J. M. Bossoutrot, *Chemical Engineering Journal*, 2001, **81**, 91–100.

(213) E. Simone, R. Othman, G. T. Vladisavljević and Z. K. Nagy, *Pharmaceutics*, 2018, **10**, 17.

(214) C. B'Hymer, *Pharmaceutical Research*, 2003, **20**, 337–344.

(215) R. Peña and Z. K. Nagy, *Crystal Growth and Design*, 2015, **15**, 4225–4236.

(216) S. Kim, B. Lotz, M. Lindrud, K. Girard, T. Moore, K. Nagarajan, M. Alvarez, T. Lee, F. Nikfar, M. Davidovich, S. Srivastava and S. Kiang, *Organic Process Research and Development*, 2005, **9**, 894–901.

(217) C. S. MacLeod and F. L. Muller, *Organic Process Research and Development*, 2012, **16**, 425–434.

(218) P. P. Apshingekar, S. Aher, A. L. Kelly, E. C. Brown and A. Paradkar, *Journal of Pharmaceutical Sciences*, 2017, **106**, 66–70.

(219) O. Narducci, A. G. Jones and E. Kougoulos, *Chemical Engineering Science*, 2011, **66**, 1069–1076.

(220) G. Ruecroft, D. Hipkiss, T. Ly, N. Maxted and P. W. Cains, *Organic Process Research and Development*, 2005, **9**, 923–932.

(221) I. I. Onyemelukwe, A. R. Parsons, H. P. Wheatcroft, A. Robertson, Z. K. Nagy and C. D. Rielly, *Crystal Growth and Design*, 2019, **19**, 60–80.

(222) C. J. Brown, T. Mcglone, S. Yerdelen, V. Srirambhatla, F. Mabbott, R. Gurung, M. L. Briuglia, B. Ahmed, H. Polyzois, J. Mcginty, F. Perciballi, D. Fysikopoulos, P. Macfhionnghaile, H. Siddique, V. Raval, T. S. Harrington, A. D. Vassileiou, M. Robertson, E. Prasad, A. Johnston, B. Johnston, A. Nordon, J. S. Srai, G. Halbert, J. H. Ter Horst, C. J. Price, C. D. Rielly, J. Sefcik and A. J. Florence, *Molecular Systems Design and Engineering*, 2018, **3**, 518–549.

Chapter 9

Appendix

9.1 Paracetamol

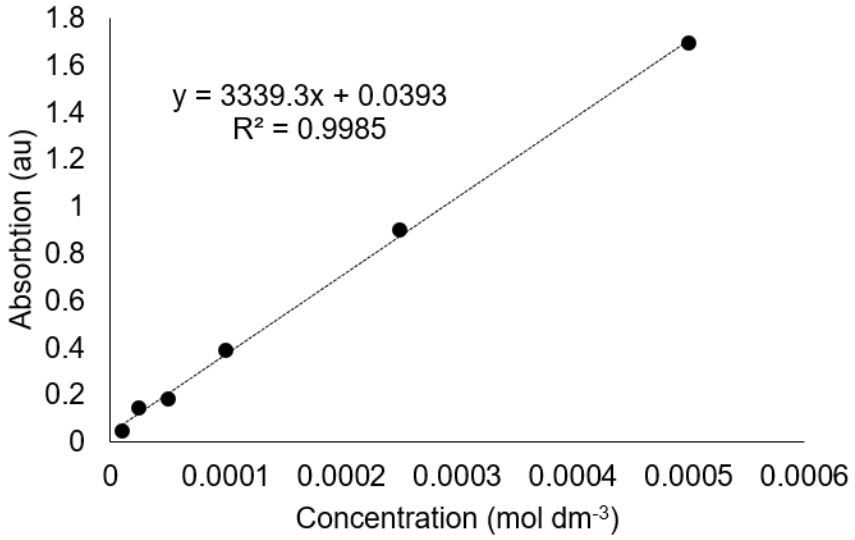

Figure 9-1: Calibration curve for the absorption vs concentration measurements for Eosin Y in ethanol (EtOH) at a fixed wavelength of 478 nm

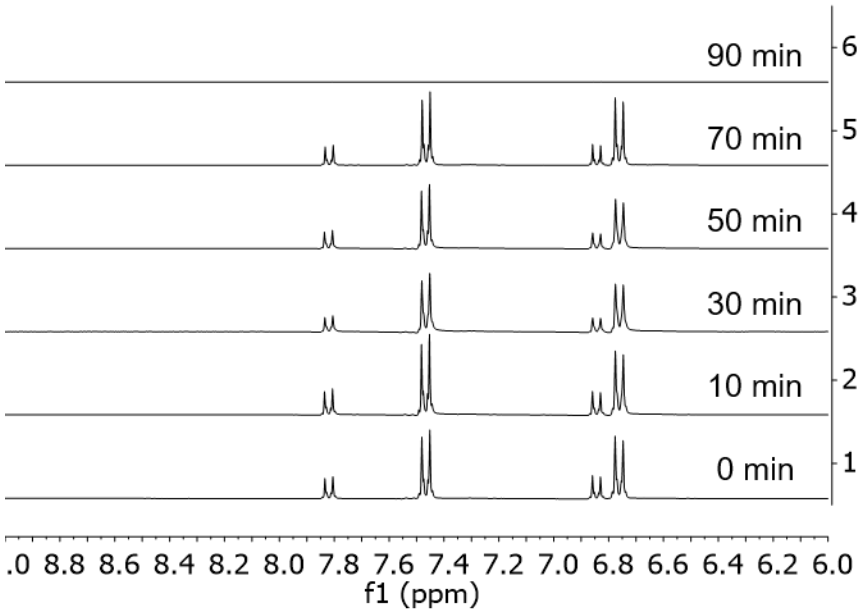

Figure 9-2: NMR spectra from reaction monitoring of PCM10, 4-hydroxyacetophenone (4HAP) = 7.81 to 7.84 ppm and 6.84 to 6.86 ppm, 4-hydroxyacetophenone oxime (4-HAPO) = 7.44 to 7.49 ppm and 6.74 to 6.79 ppm

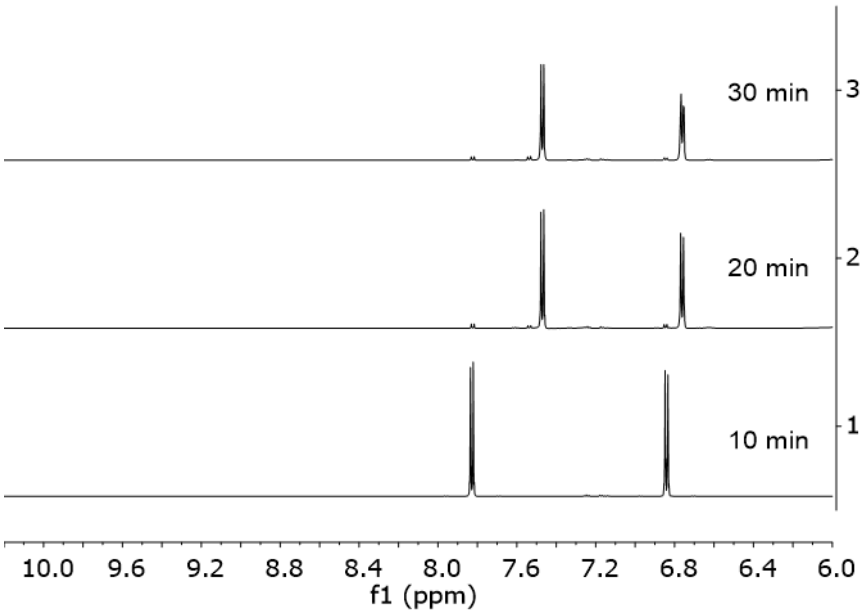

Figure 9-3: Nuclear magnetic resonance (NMR) monitoring between 6 to 10 ppm for 4HAPO production in PCM11.1

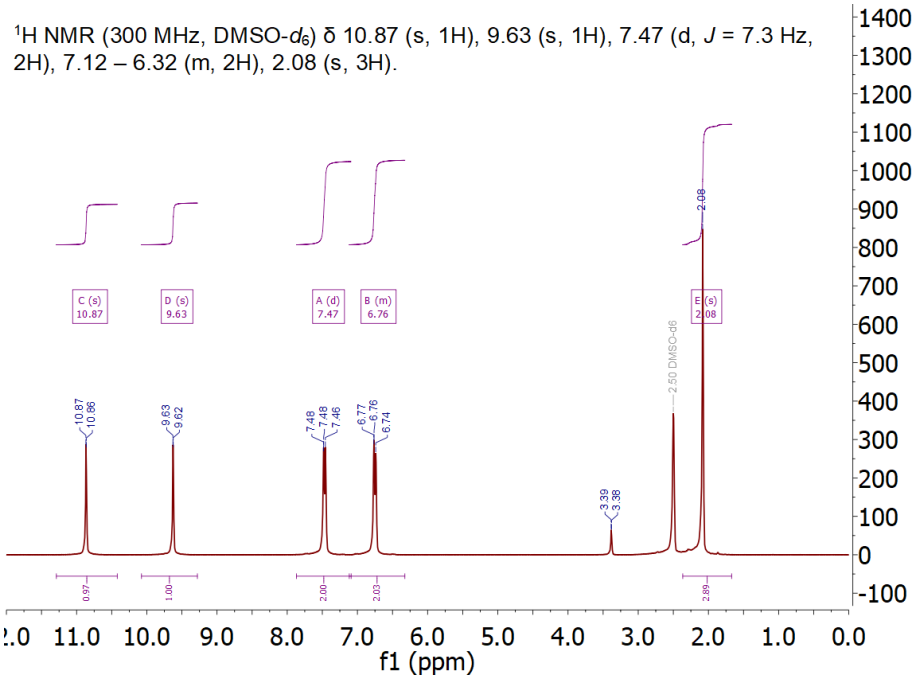

Figure 9-4: NMR spectrum for PCM12 product after recrystallisation

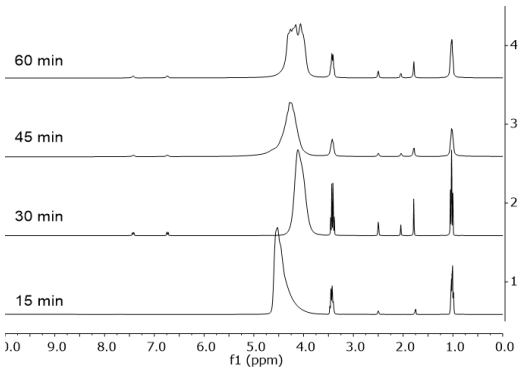

(a) PCM14.1

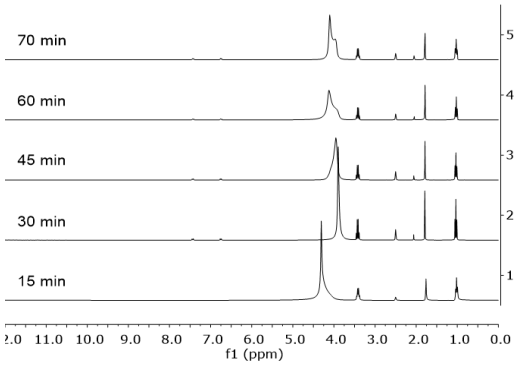

(b) PCM14.2

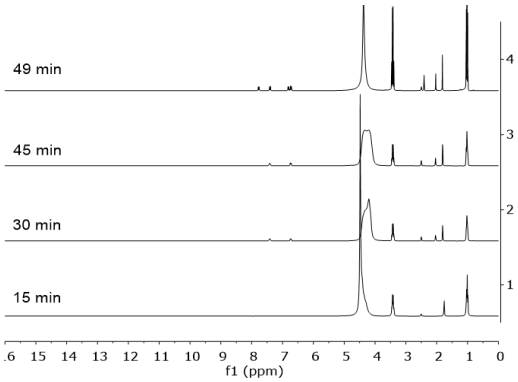

(c) PCM14.3

Figure 9-5: NMR monitoring of 4HAPO in PCM14

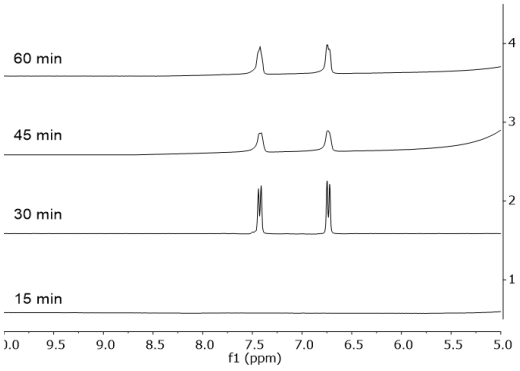

(a) PCM14.1 (6 to 10 ppm)

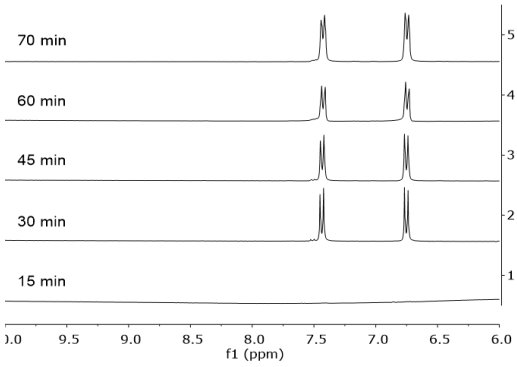

(b) PCM14.2 (6 to 10 ppm)

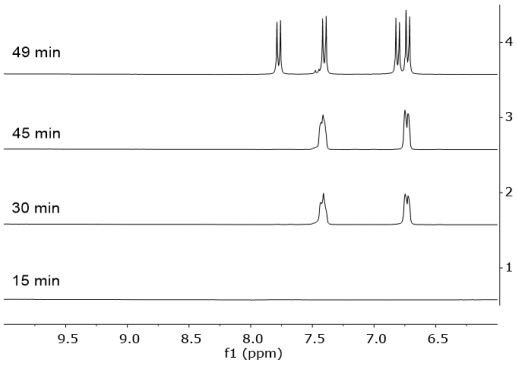

(c) PCM14.3 (6 to 10 ppm)

Figure 9-6: NMR monitoring between 6 to 10 ppm for 4HAPO production in PCM14

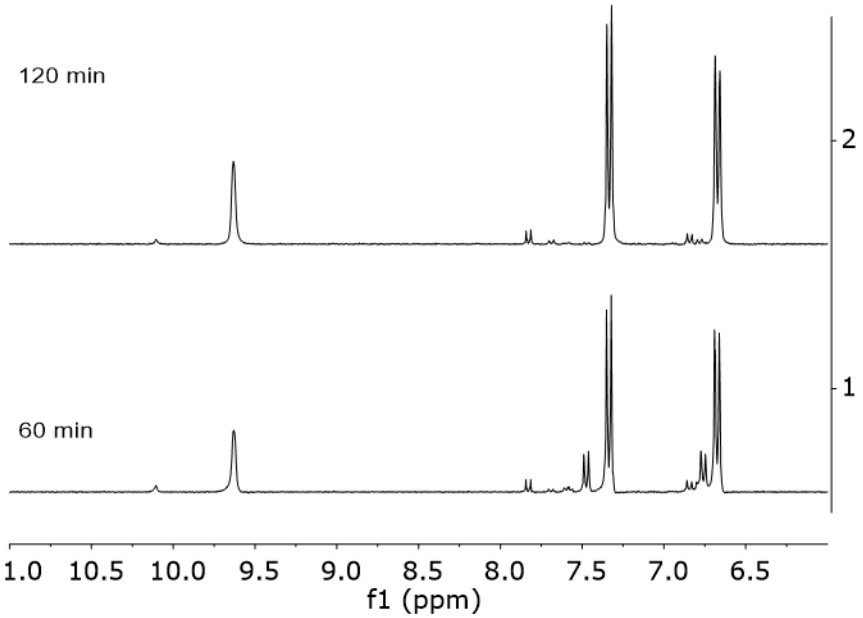

Figure 9-7: PCM15.2 (6 to 11 ppm)

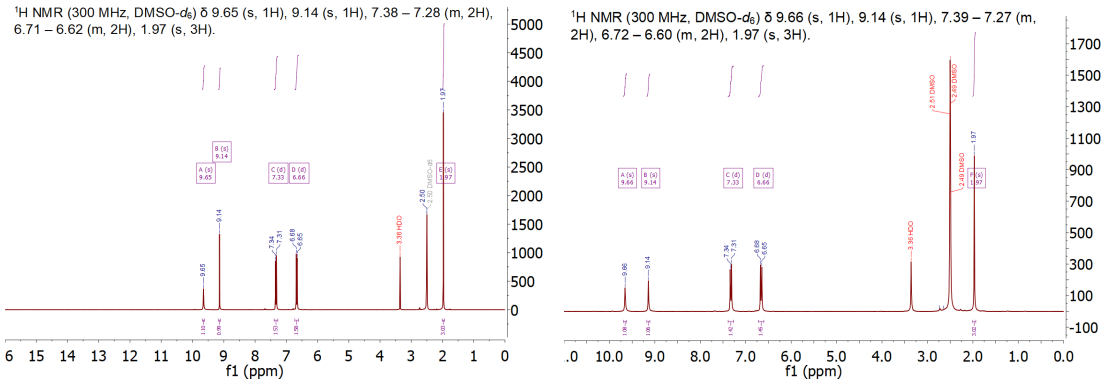

(a) PCM15.1 (b) PCM15.2

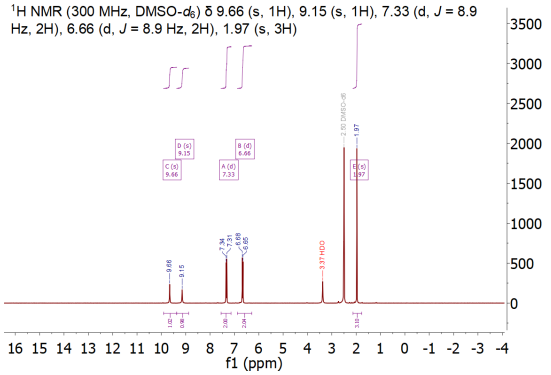

(c) PCM15.3

Figure 9-8: NMR spectrum of the isolated product in PCM15

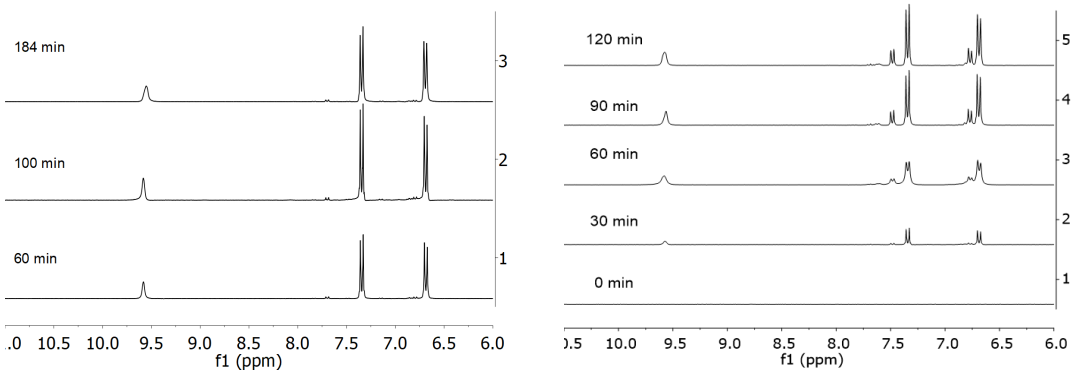

(a) PCM16.1 (6 to 11 ppm) (b) PCM16.2 (6 to 10 ppm)

Figure 9-9: NMR monitoring for the flow synthesis of paracetamol (PCM) in PCM16

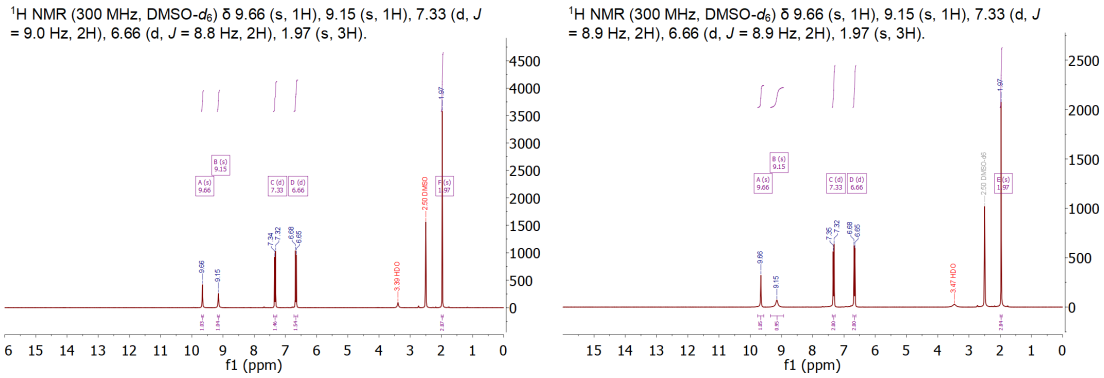

(a) PCM16.1 (b) PCM16.2

Figure 9-10: NMR spectra for the isolated product from PCM16

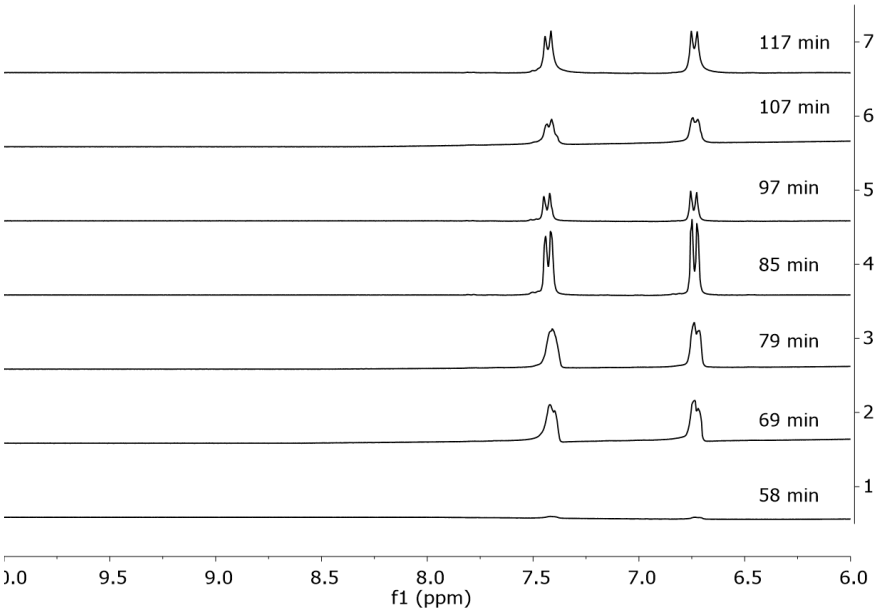

Figure 9-11: NMR spectra between 6 and 10 ppm at different time stamps during HAPO1

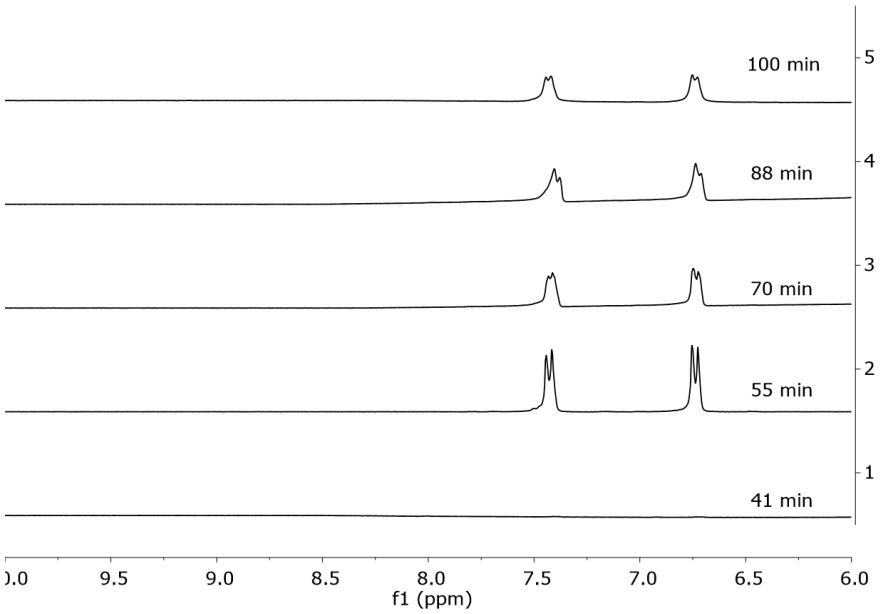

Figure 9-12: NMR spectra between 6 and 10 ppm at different time stamps during HAPO2

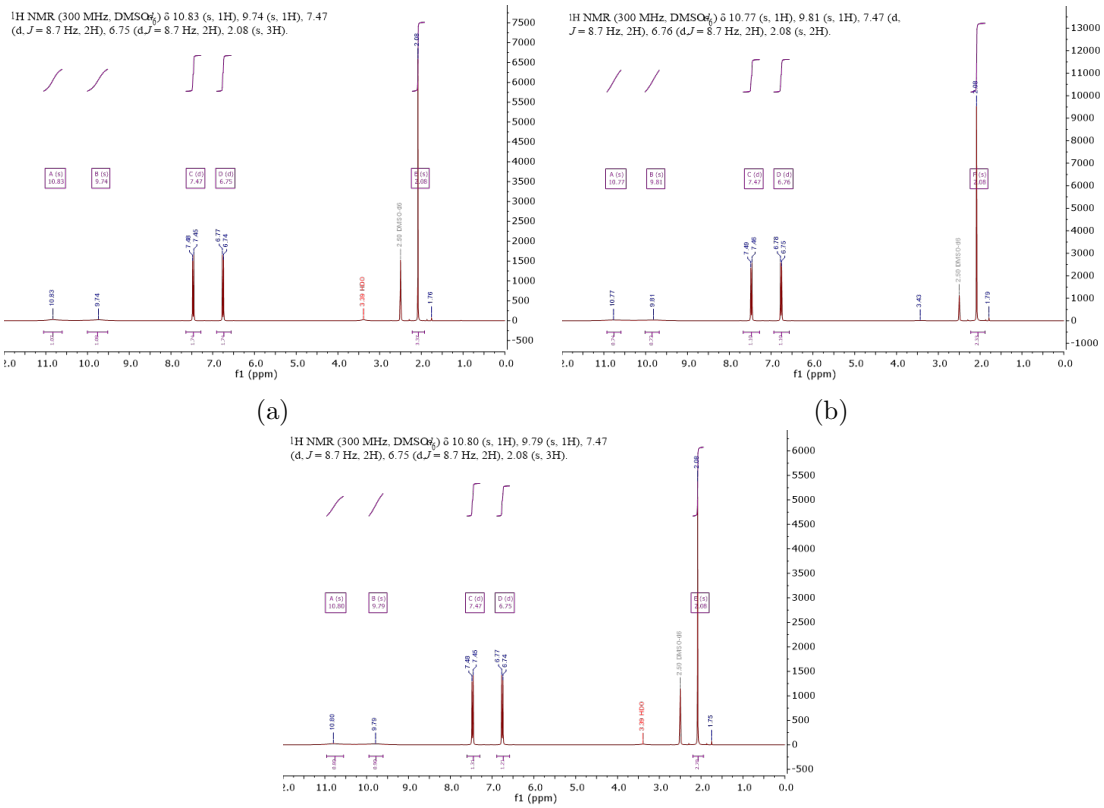

Figure 9-13: NMR spectra of the isolated product from HAPO8 a) Start-up b) Steady state and c) Shutdown

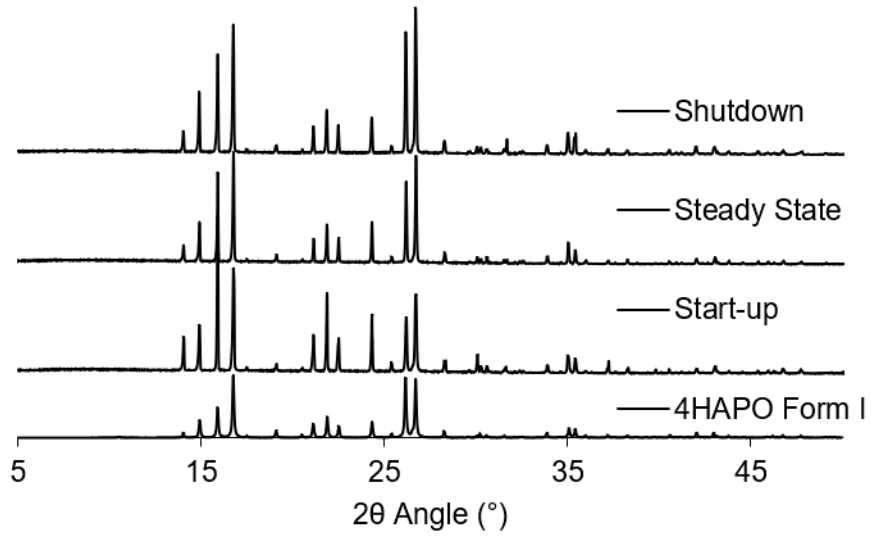

Figure 9-14: Powder X-ray diffraction (PXRD) spectra of HAPO8 and HAPO Form I from simulated single crystal X-ray diffraction (SCXRD) data

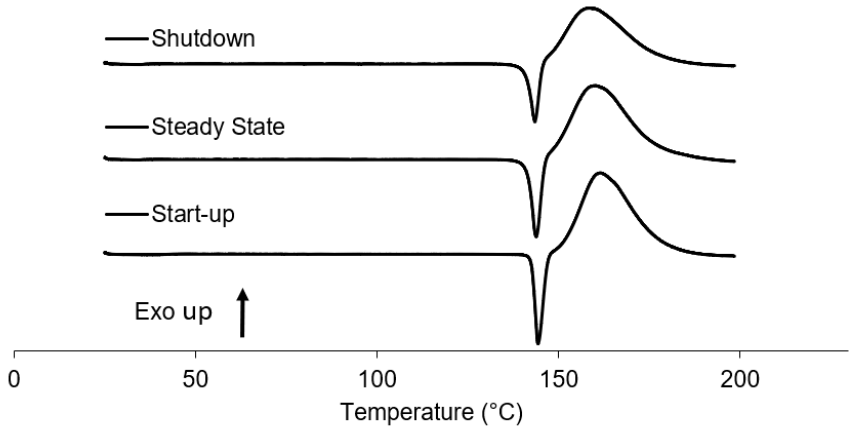

Figure 9-15: Differential scanning calorimetry (DSC) trace of HAPO8 samples

9.2 Pyrazinamide

Table 9.1: Set pump rates for pyrazinamide (PZA) coupling experiments

Experiment	Feed ($mL\,min^{-1}$)	Air ($mL\,min^{-1}$)	Galden ($mL\,min^{-1}$)
PZA1	1.00	-	-
PZA2	1.00	2.1	2.1
PZA3	1.00	6.3	2.1
PZA4	1.00	6.3	2.1
PZA5	1.00	6.3	2.1
PZA6	1.00	6.3	2.1
PZA7	1.00	6.3	2.1
PZA8	1.00	6.3	2.1
PZA9	1.00	6.3	2.1
PZA10	1.00	6.3	2.1
PZA11	1.00	6.3	2.1

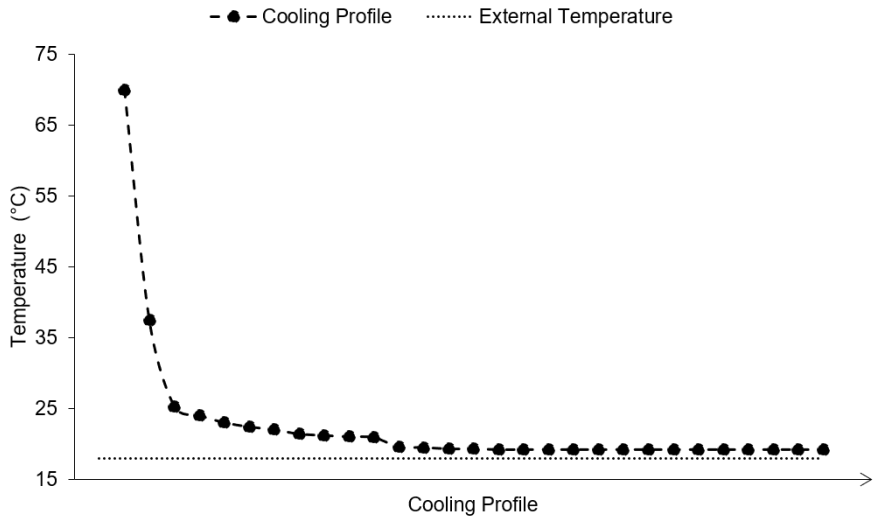

Figure 9-16: Typical cooling profile in PZA, uncontrolled nucleation experiments

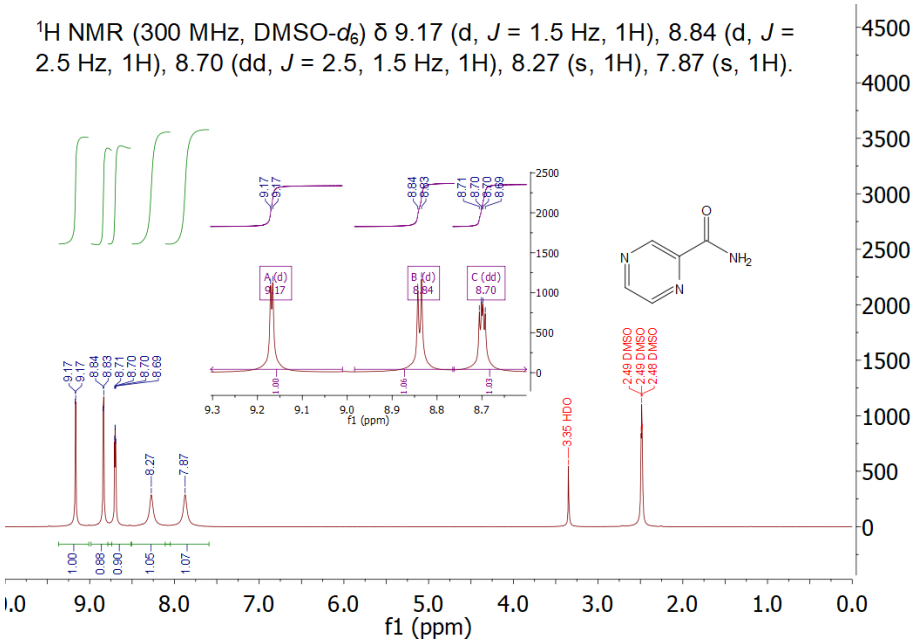

Figure 9-17: NMR of PZA1, showing the NMR shifts for the isolated pyrazinamide sample

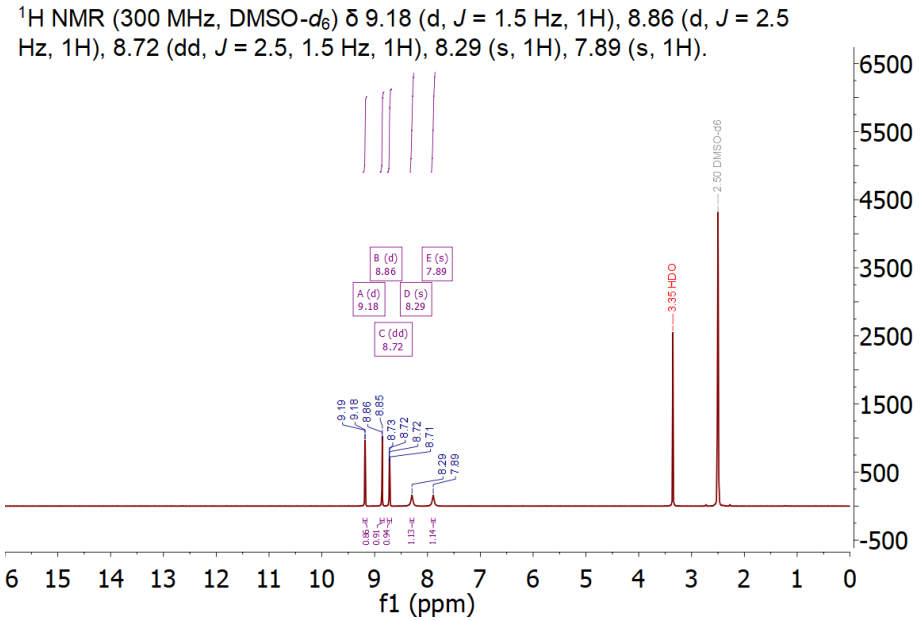

Figure 9-18: NMR spectrum for PZA2 after isolation from continuous synthesis and crystallisation

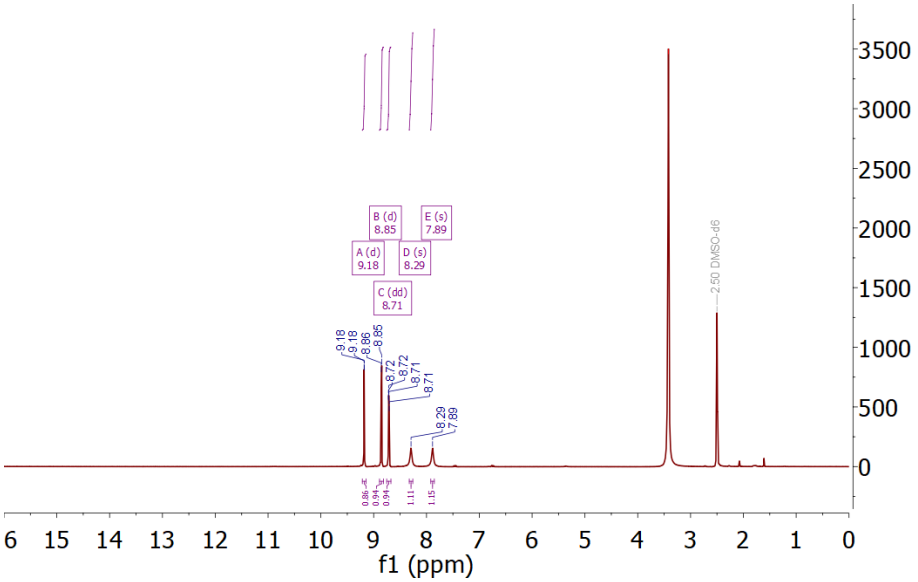

Figure 9-19: NMR spectrum for PZA5 after isolation from continuous synthesis and crystallisation

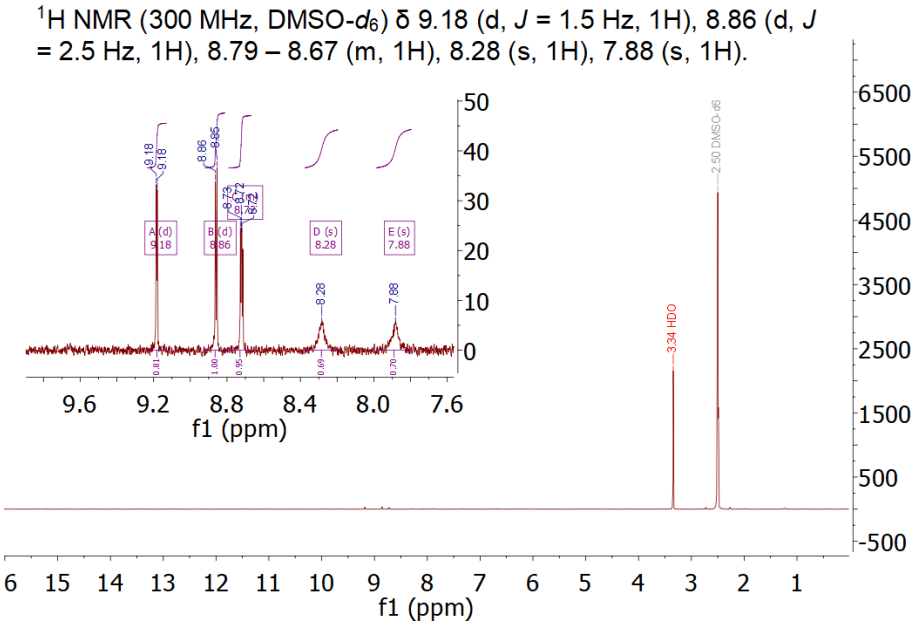

Figure 9-20: NMR spectrum for PZA6 after isolation from continuous synthesis and crystallisation

Table 9.2: Average solution volume per slug and crystal appearance in the PZA6

No. of Slugs	Start Volume (mL)	End Volume (mL)	Change in Volume (mL)	Average Slug Volume (mL)
28	0	2.0	2.0	0.07
12	4.4	5.4	1.0	0.08
10	5.6	6.4	0.8	0.08
10	6.6	7.4	0.8	0.08
13	7.4	8.6	0.8	0.06
12	8.8	9.6	0.8	0.06
27	0	2.0	2.0	0.07
13	2.4	3.6	1.2	0.09
12	3.8	4.8	1.0	0.08
10	5.0	5.8	0.8	0.08
13	6.0	7.0	1.0	0.08
			Total Average Slug Size	0.08 ± 0.01

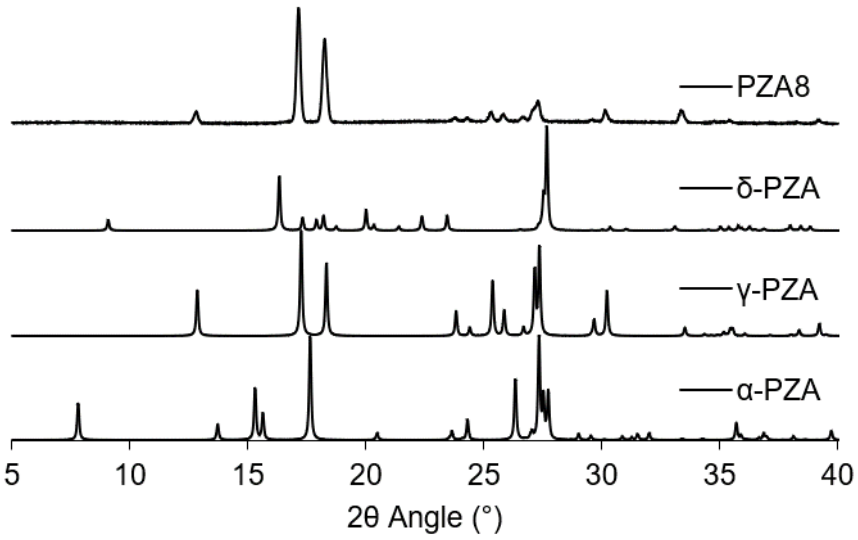

Figure 9-21: PZA8 PXRD pattern compared to accessible polymorphs of PZA

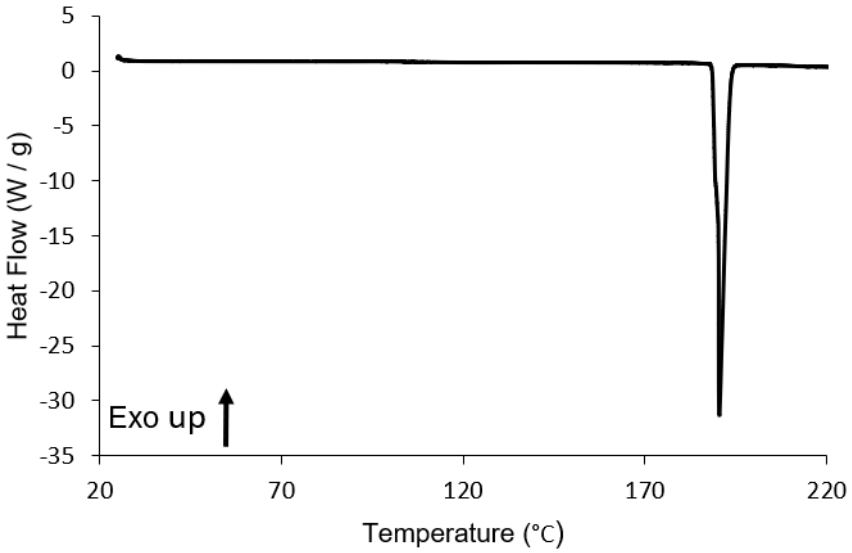

Figure 9-22: PZA8 DSC trace, endothermic peak at 190 °C corresponds to the product melting point

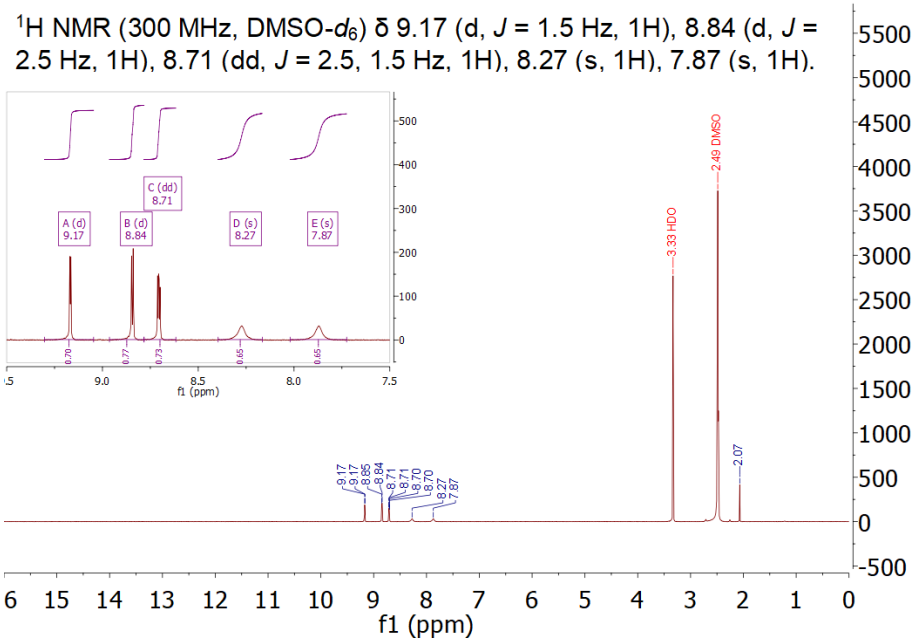

Figure 9-23: NMR spectrum for PZA10 sample after integrated continuous synthesis and crystallisation

9.3 Thermochromics

Hot Stage Microscopy Videos

A link has been provided for access to the hot stage microscopy (HSM) videos for samples TC1.8, TC3, TC4 and Figure 5-6:

`https://www.dropbox.com/s/fdqqsf8j1y9xdvq/Scott_Daniel_ThesisAppendix_HSM.zip?dl=0`

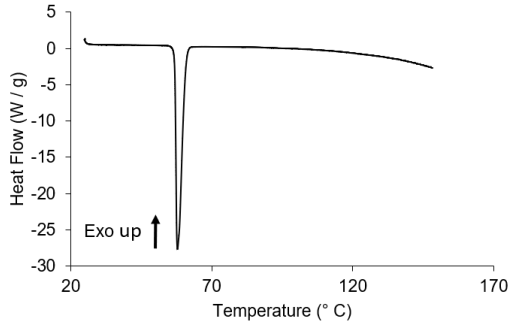

(a) DSC trace of 4-bromo-2-methylaniline (4-Br2MA)

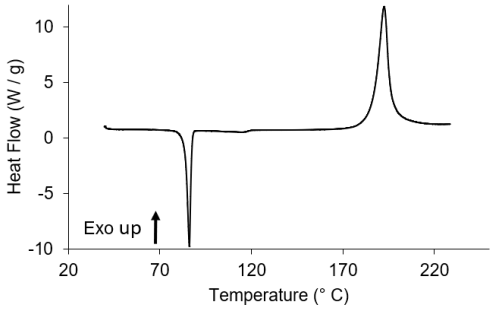

(b) DSC trace of 4-iodo-2-methylaniline (4I2-MA)

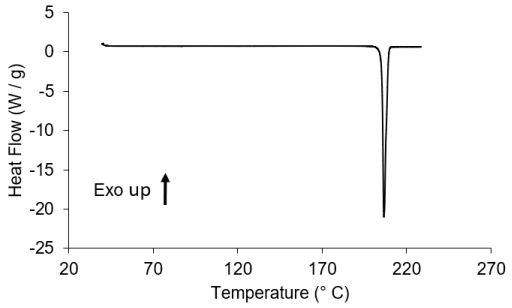

(c) DSC trace of 3,5-dinitrobenzoic acid (35D-NBA)

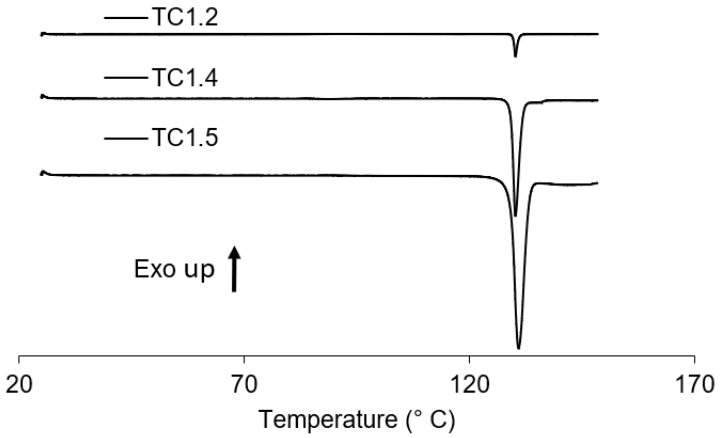

Figure 9-25: DSC of antisolvent crystallisation samples of 4Br2MA:35DNBA in batch

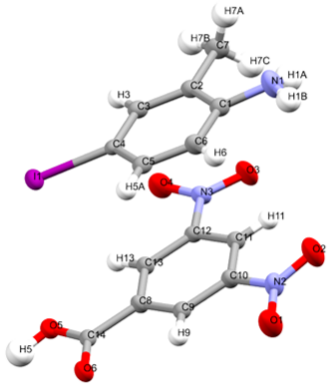

Figure 9-26: Asymmetric unit for 4I2MA:35DNBA, **Cc5** crystal structure

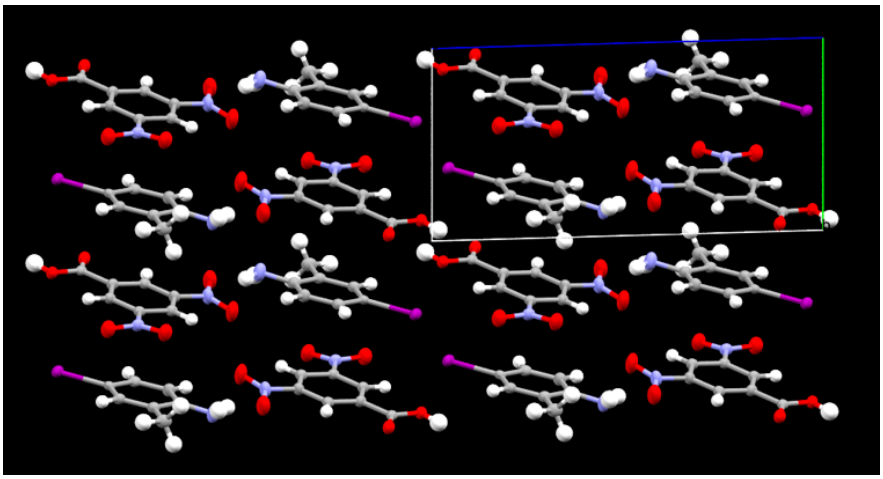

Figure 9-27: Crystal packing along the *c* axis for 4I2MA:35DNBA, **Cc5** structure

Table 9.3: Hydrogen bonding in TC1.8, 4I2MA:35DNBA, **Cc5** structure

Atoms	Bond Distance (Å)	Bond Angle (°)	Bond Type
O5–H5 $\cdots$ O6	2.694(7)	172(8)	Hydrogen
N1–H1B $\cdots$ O1	3.13(1)	163(9)	Hydrogen
C7–H7C $\cdots$ O2	3.59(1)	162.8	Hydrogen
I1 $\cdots$ O4	3.190(4)	-	Halogen
I1 $\cdots$ O4	3.654(4)	-	Halogen
C4 $\cdots$ C14	3.365(9)	-	$\pi \cdots \pi$

Table 9.4: Crystal data and structure refinement for 4-iodo-2-methylaniline:3,5-dinitrobenzoic acid (4I2MA:35DNBA), **Cc5** crystal

Sample	TC1.8
Compound	4I2MA:35DNBA
Formula	$[C_7\,H_8\,I\,N][C_7\,H_4\,N_2\,O_6]$
Formula weight	445.17
T (K)	150.00
Radiation	Cu-Kα ($\lambda = 1.541\,84$ Å)
Crystal system	Triclinic
Space Group	$P\bar{1}$
a (Å)	7.2067(3)
b (Å)	7.3426(2)
c (Å)	14.9307(5)
α (°)	88.380(2)
β (°)	88.649(3)
γ (°)	89.199(3)
V (Å^3)	789.47(5)
Z	2
ρ_{calc} (g cm^{-3})	1.873
μ (mm^{-1})	16.292
F(000)	436.0
Crystal size (mm^3)	$0.29 \times 0.104 \times 0.015$
2θ range for data collection (°)	5.924 to 136.378
Index ranges	$-8 \leq h \leq 7, -8 \leq k \leq 8, -17 \leq l \leq 17$
Reflections collected	12256
Independent reflections	2715 [$R_{\mathrm{int}} = 0.0570$, $R_{\mathrm{sigma}} = 0.0338$]
Data/restraints/parameters	2715/168/218
Goodness-of-fit on F^2	1.215
Final R indexes [I>=2σ (I)]	$R_1 = 0.0442$, $wR_2 = 0.1111$
Final R indexes [all data]	$R_1 = 0.0457$, $wR_2 = 0.1117$
Largest diff. peak/hole (e Å^{-3})	1.45/-1.07

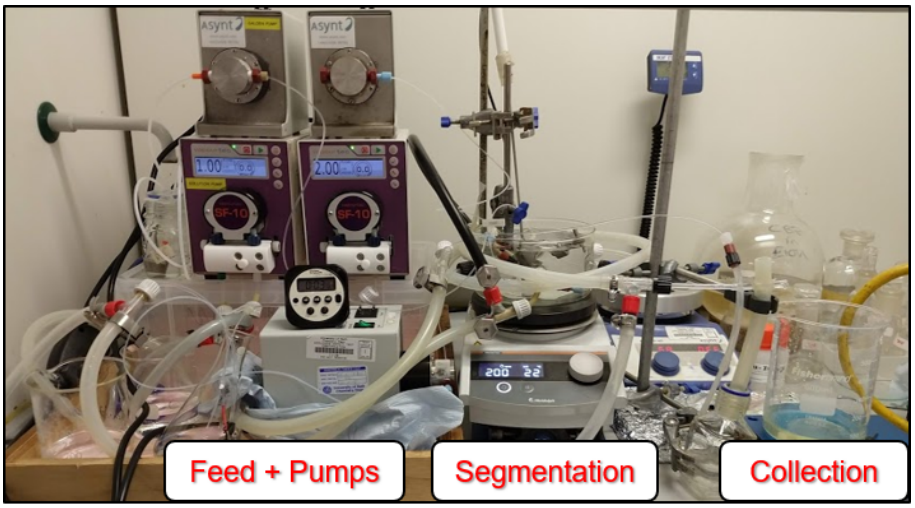

(a) Crystalliser Set-up

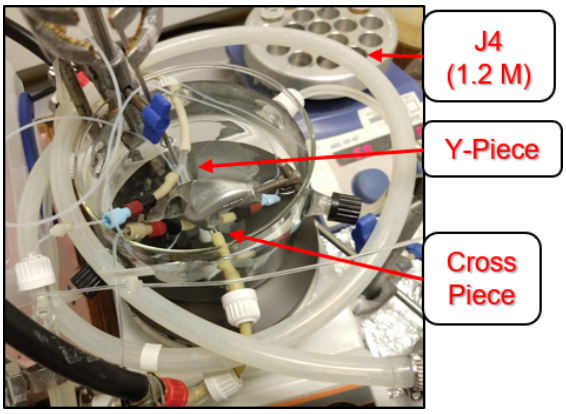

(b) Segmentation and antisolvent addition in a water bath

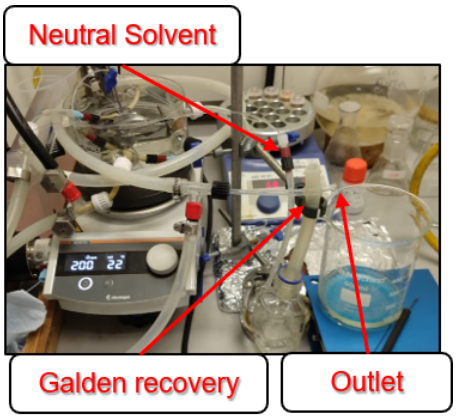

(c) Crystalliser outlet and carrier fluid recovery

Figure 9-28: Photographs of the jacketed segmented flow crystalliser used in Chapter 5 antisolvent crystallisation experiments

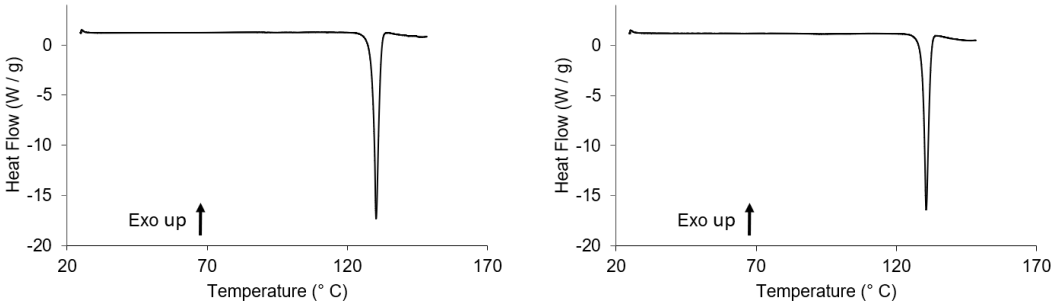

(a) TC3.1 (taken after sample transitioned to **Cc1**).

(b) TC3.2

Figure 9-29: DSC traces of TC3 4Br2MA:35DNBA samples

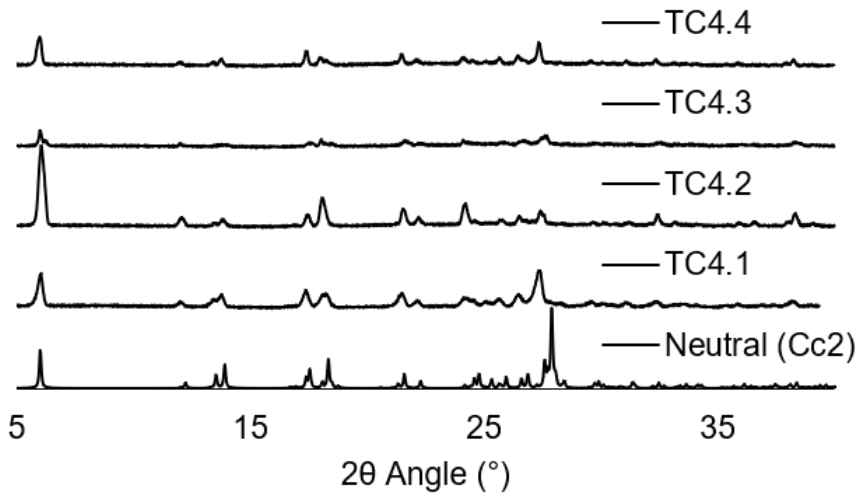

Figure 9-30: PXRD pattern for TC4, produced from batch antisolvent crystallisation and compared to the simulated pattern for the neutral 4Br2MA:35DNBA complex, derived from SCXRD acquired by Jones *et al.*

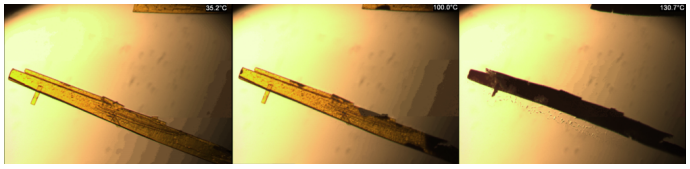

(a) TC4.2

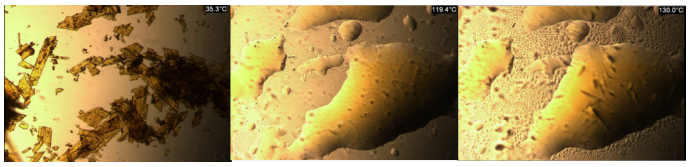

(b) TC4.3

Figure 9-31: HSM images of TC4.2 and TC4.3 heated from 35 to 150 °C at 5 °C min^{-1}

9.4 Continuous Salt Crystallisation

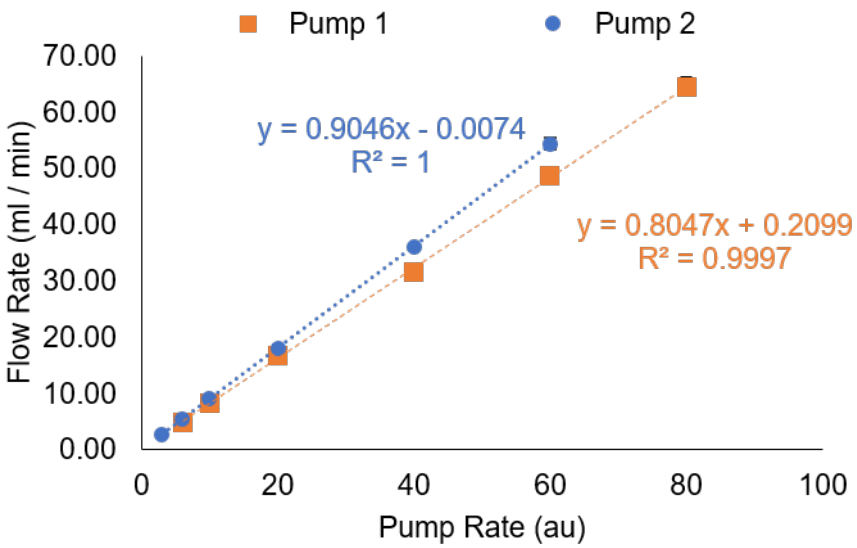

Figure 9-32: Calibration plot for Masterflex pumps in Chapter 6

Table 9.5: Evaluation of filtration times of SAB isolated from AZ4 to AZ8 and the batch reference

Experiment	Mass (g)	Volume (mL)	Time (sec)	Mass Fraction ($g\,mL^{-1}$)
Batch	17.39	430	51	40
AZ4[a]	35.34	940	90	38
AZ5	35.20	500	11	70
AZ6	36.42	860	16	42
AZ7	35.26	820	17	43
AZ8	34.22	840	30	41

Filter diameter = 9 cm, 0.7 bar reduced pressure

[a] Poor seal led to incomplete vacuum

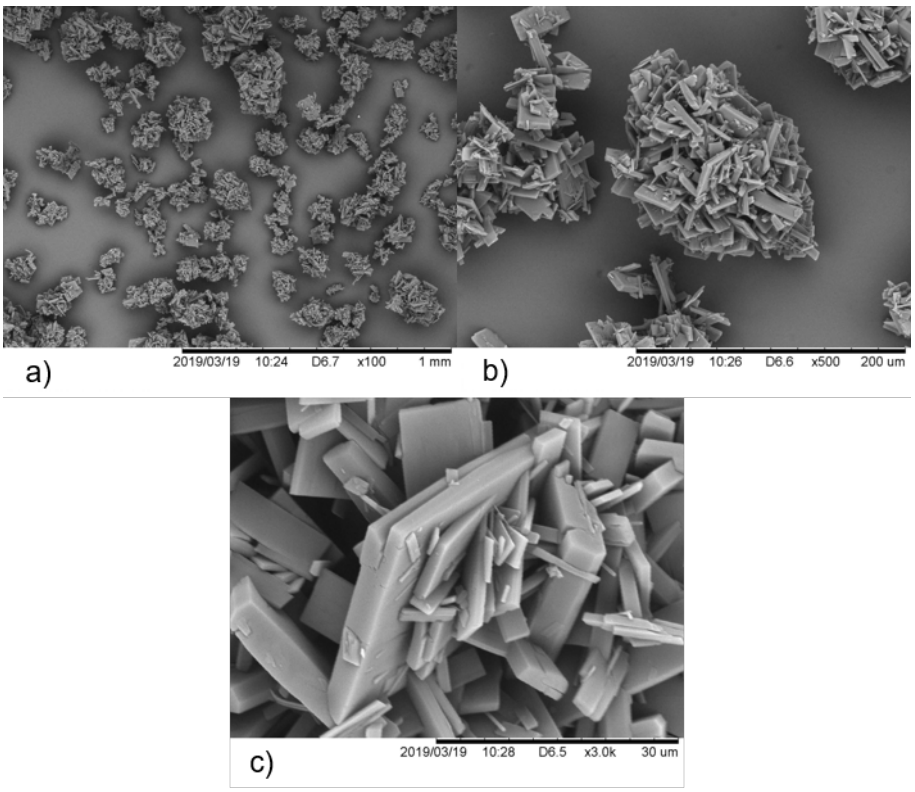

Figure 9-33: Scanning electron microscopy (SEM) images of succinate salt (SAB) in AZ8 at magnifications of a) x100 b) x500 c) x3000